Quantification of the influence of directional sea state parameters over the performances of wave energy converters

Rémy Pascal

A thesis submitted for the degree of Doctor of Philosophy.
The University of Edinburgh.
May 8, 2012

Abstract

Accurate predictions of the annual energy yield from wave energy converters are essential to the development of the wave industry. The current method based on power matrices uses only a small part of the data available from sea state estimations and it is consequently prone to inaccuracies. The research presented in this work investigates the issue of energy yield prediction and questions the power matrix method. This is accomplished by quantifying the influence of several directional sea states parameters on the performances of wave energy converters.

The approach taken was to test several wave energy converters in the Edinburgh Curved tank with a large set of sea states. The selected wave energy converters are a fix OWC, a set of two OWCs acting as a weak directional device and the desalination duck model. Uni-modal and bi-modal sea states were used. For the uni-modal sea states, parameters related to the wave system shape were considered. For the bi-modal sea states, the relative position of the wave system peaks was investigated and the uni-modality index was introduced to quantify the degree to which sea states could be considered bi-modal. For all sea states, the significant wave height was kept constant.

The experimental work required good spectral estimates. The MLM and MMLM were adapted to deterministic waves to improve their stability and accuracy. A routine to isolate wave systems was also developed in order to estimate parameters with respect to each wave systems.

For uni-modal spectra, parametric models of the observed performances of the devices could be devised. The frequency spreading and its interaction with the energy period proved to be as important as the energy period itself, which suggests that the frequency spreading should be used for energy production prediction. For bi-modal spectra, evidence of the duck sensitivity to directionality was found while the OWCs were not affected.

Declaration of originality

I hereby declare that the research recorded in this thesis and the thesis itself has been conducted and written entirely by myself, unless otherwise stated. The work has not been submitted in any previous application for a degree.

Remy Pascal

6 May 2012

Acknowledgements

I would like to acknowledge the Engineering and Physical Science Research Council for funding this thesis. I would also like to address a special thanks to the person involved in the Supergen Marine Doctoral Training Program and all the person that organised the short courses of the program.

Pr. Ian Bryden supervised me during thesis. I am thankful to him to let me work on my own project and ideas. Ian has always been supportive but he made sure that I reached the crucial milestones of my PhD.

A great part of this work would not have been possible without the Matt Folley consent for me to use his devices in my experiments. Matt spent a large amount of time ensuring that his devices were safely shipped from Belfast to Edinburgh. The assistance of Jorge was also very helpful and I greatly value the work he did in developing the Duck model that I used.

To two persons I am very grateful. They helped me solve most of my technical problems, assisted me in the workshop when required and maintained the Edinburgh Curved tank in optimal condition for my tests. Without Gregory Payne and Jamie Taylor experience, most of the design and experimental work conducted during this thesis would have been of much lower quality.

I am very thankful to the old slowly decaying portacabin and its joyful, enthusiastic, kind and helpful inhabitants. I am sadly aware that I am probably the last student to complete its entire PhD in this historic place of wave energy. This place was very inspirational and I hope its spirit will be transferred to the next home of the Wave Power Group. So great thanks to Gareth, Jorge, Greg, Jamie, Thomas, Sam, Dave, Giovanni, Sylvia, João and Julien for making this office a great place to be. The laughs were good, the coffee was the best in campus and the biscuits never scarce (sort off...).

Merci a mes parents. Cette thèse est le premier pas que je réalise sans me reposer sur leurs épaules. Pour autant, je ne l'ai pas accompli avant mes 28 ans. Merci de m'avoir toujours encouragé et soutenu au cours de mes études et de m'avoir forcé un peu quand j'en ai eu besoin.

Finally, I can not finish this page without a word for Joana. She showed me how to finish a thesis and made sure I stayed in Edinburgh long enough so I could start this one. She kept my motivation alive through this project and always believed in me. With her help I can now close this book but we will keep adding new chapters to our common book.

Contents

Appendix

List of figures

List of tables

Nomenclature and notations

General Notations:

vector from origin to point A	$\overrightarrow{A}$
complex number z	$\underline{z}$
average value of x	$\overline{x}$
integral part of x	$\lfloor x \rfloor$
Oscillating water column	OWC
Wave energy converter	WEC
tank depth	d

Notation related to energy spectra, wave elevation and wave amplitudes:

wave length	λ
wavenumber vector	$\overrightarrow{k}$
group velocity	G_g
relative phase	ϕ
absolute phase	Φ
pulsation	ω
direction of a regular wave	θ
reflection coefficient as ratio of amplitude	R_{coeff}
JONSWAP peak enhancement factor	γ

For some notations, the distinction is made between their continuous and discrete notations:

	Continuous	Discrete
wavenumber-circular frequency energy spectrum	$S(\overrightarrow{k},\omega)$	$S_{\overrightarrow{k},\omega}$
frequency-direction energy spectrum	$S(f,\theta)$	$S_{f,\theta}$
Omnidirectional frequency spectrum	$S(f)$	S_f
Directional Spreading function	$D(f,\theta)$	$D_{f,\theta}$
Cross-spectra between two points M and N	$\Phi_{nm}(\omega)$	$\Phi_{nm,\omega}$
wave amplitude related to the *frequency-direction* energy spectrum	$a(f,\theta)$	$a_{f,\theta}$
wave elevation at a point A at an instant t	$\eta(A,t)$	$\eta_{A,u}$

When needed, the incident and reflected quantities will be distinguished with a I or R superscript. For example, the Incident *frequency-direction* energy spectrum is noted $S^I_{f,\theta}$ in its discrete from.

The estimated form of the previous quantities are noted with and overhead hat. For example, the estimated *frequency-direction* energy spectrum is noted $\hat{S}(f, \theta)$.

Notation related to wave spectrum parameters

significant wave height	H_{m0}
energy period	T_E
zero-crossing period	T_Z
peak period	T_P
mean direction at each frequency	$\theta_{m,p}$
variation of $\theta_{m,p}$ along the frequency axis	β_Θ
integrated mean direction over the frequencies	Θ_M
frequency spreading parameter	f_s
angular spreading factor at each frequency	θ_{sp}
integrated angular spreading factor	Θ_S
uni-modality index	μ
energy period Difference	δT_E
Mean direction difference	$\delta\theta_M$
energy ratio	$H_{m0,r}$
peak energy ration	max_r

This work intent to explore the influence of the shape of wave systems and of multi-modal spectra over the performances of WECs. For multi-modal sea states, the parameters of Table 2.1 can be defined with respect to each wave system of a multi-modal sea state. The parameters defined that way are noted with an extra subscript, ordered by decreasing importance of the wave system: the energy period T_E of the dominant wave systems becomes $T_{E,1}$. The wave systems are sorted using their peak value. When parameters are estimated with respect to the wave system only, the same mathematical expressions as in Table 2.1 are used, but the spectral estimates outside of the isolated system (see Section 4.4.2 on page 66) are set to 0.

Notation related to wave generation

Frequency resolution of the directional spectrum	ΔF
Sub-frequency of the directional spectrum used for the single summation generation	Δf
Angular resolution of the directional spectrum used for the single summation generation	$\Delta\Theta$
Period of generated sea states	T
Low frequency cut off of the spectrum	F_{min}
High frequency cut off of the spectrum	F_{max}

Notation related to performance assessment of the probe layouts and the wave measurement methods.

principal angle of the isosceles triangle used to measure wave direction	α
length of the equal sides of the isosceles triangle	l
average uncertainty over all angles in the measure of the direction of propagation	$\overline{\delta_\theta}$
Uncertainty in the wave direction of propagation	ϵ_d
Error in the probe coordinates	ϵ_p
Mean distance between each pair of probes	m_L
Area of the probe layout for directional spectrum estimation	A
Normalised area of the probe layout for directional spectrum estimation	A_n
Standard deviation of the distance between each pair of probes	m_{std}
Normalised standard deviation of the distance between each pair of probes	$m_{n,std}$
Normalised difference between $\hat{\Theta}_{S,1}$ and $\Theta_{S,1}$	$\epsilon_{n,\Theta}$
Total difference between estimated and target spectra	ϵ_T
Weighted total difference between estimated and target spectra	$\epsilon_{w,T}$
Normalised difference between $\hat{H}_{m0,1}$ and H_{m0}	$\epsilon_{n,H_{m0}}$
Smoothing window for the spectral estimates	W_S
Window steepness coefficient for smoothing spectral estimates	C_s
Side length of the smoothing window of spectral estimates	l_s

Notation related to wave energy converters measurements

Inner OWC diameter	$D_{o,I}$
Outer OWC diameter	$D_{o,O}$
Duck model length	L_D
Volume flow rate through the OWC orifice	Q
wave elevation inside the OWC	η_o
wave gauge reading inside each OWC	$\eta_{o,n}$
Pressure differential across OWC orifice	$P_{d,o}$
Pressure differential across Duck partition	$P_{d,d}$
Calibrated damping of the duck partition	K_d
normalized power	P^n
Power of the single OWC, where relevant	P_{1owc}
Power of the double OWC, where relevant	P_{2owc}
Power of the Duck, where relevant	P_D
Wave power per meter of crest length	P_w
relative capture width	Cw
Duck relative capture width, where relevant	Cw_D
single OWC relative capture width, where relevant	Cw_{1owc}
double OWC relative capture width, where relevant	Cw_{2owc}
interaction factor between the OWCs	I_f

Chapter 1
Introduction

1.1 The need to get better at understanding WEC performances

Which hurdles do the wave energy community faces if it is to significantly contribute to the energy mix of our future societies?

There are obvious engineering, environmental and public acceptance challenges. The current and future devices must become more efficient, more robust, easier to deploy and maintain. To gain public acceptance of those devices, the industry must demonstrate that their global environmental benefit outweigh the disturbance to the local environment, it must engage with the wider sea community and clearly show that positive effects can overcome the problems generated by large scale development of wave energy converters. While it is not specific to the wave energy community, electricity grids must evolve to accommodate an ever increasing part of local generation and they must strengthen their links between sources of renewable energy and consumption hotspots.

The economic and financial aspect are not to be disregarded. The industry must secure resilient sources of public support before reaching the stage of maturity needed to compete head to head with long standing and established energy generation industries, such as fossil fuel or nuclear powered plants. However, private investment is key at every stage of an industry development. Significant efforts are required to continuously ease the way of the private sector into the wave energy industry. One of them is the development of standards in order to bring clarity and visibility to the sector. Several project are currently ran with this objective, such as *EquiMar*[1] and the development of standards by IEC/TC 114 Marine Energy committee or The European Marine Energy Centre Ltd (EMEC).

A specific aspect of this effort is the development of standardized, reliable procedures to estimate the performances of wave energy converters prior to deployment. It is a crucial element for the cost-benefit break down of a project, and it is also vital to provide fair comparison between devices for a site developer. Such a procedure should not be specific to a device, but care must be taken that no bias against any type of devices is introduced.

---

[1] http://www.equimar.org/

With this point of view, this procedure cannot be based solely on estimations provided by developers themselves. The different stage of development and the varied experience of each development team means that such estimations, while very valuable internally for the device understanding and optimisation, could be subject to different hypotheses and limitations.

To this day, the procedure fitting the requirement pre-cited is the combination of scatter diagram and wave energy converter power matrices as used in Babarit *et al.* (2006). Reports such as Smith & Taylor (2007) have integrated this method into official guidance for electricity production estimation, and is is currently widely accepted as a standard across the industry.

This method is not exempt of limitations and very little real sea experience over long periods are available to asses its long term reliability. It is only based on a wave period parameter and wave significant wave height. Consequently, lots of valuable information about wave climate are averaged out during the process. The shape of the wave systems and the occurrence of multi-modal sea states are discarded. By simplifying the sea state description, this process could first introduce a bias as devices will not have the same sensitivity to other parameters, and it also questions to reliability of the method. Holmes & Barrett (2007) demonstrated that large variation of the energy output of a device can be expected for the same combination of wave period a wave height, leading to energy production lower than expected.

Test and improvement on this method is thus needed and waited by the different actors of the industry. Those improvements will have to aim mainly at reducing the financial risk taken while investing on the development of a wave energy project by reducing the uncertainty linked to the estimation of energy production from WECs. By introducing new parameters linked to other aspect of the wave climate into the method, the uncertainty on the electricity generation could be reduced and the confidence of private investors raised. This will also increase the fairness of the comparison between devices. However, increasing the number of parameters will also increase the method complexity, the number of tests needed to fully characterise device performance and could finally make the method unusable out of academia.

The research presented in this thesis aims to help these improvements by quantifying the influence of some key wave climate parameters over a range of wave energy converters. It is complementary to studies conducted by other groups such as Saulnier *et al.* (2010). The tests presented are designed to get a clearer picture of which parameters are essential. It might be that the significant wave heigh and a period parameter is all what is needed to get reasonable estimate, or each device might prove to need a set of different parameters to be correctly described. Either way, the results of this research will bring understanding of the method currently in use by the industry and it should contribute to the development of the wave energy industry by working toward removing one of the hurdle the wave energy industry is facing.

1.2 Expected outcomes

It is important to clarify the possible outcome of this work. By quantifying and comparing the influence of several sea states parameters over the performances of three wave energy converters, three possible outcomes were thought possible when starting this work.

First, it could be that on the three devices, none of the currently discarded parameters, such as the spectral bandwidth and the directional spreading, was to be found to be significant by comparison to the energy period or the significant wave height. Such results, while apparently negative, would be welcomed as they will reinforce the current reliance on those two parameters only for the estimation of power production from wave energy converters.

Second, several of those discarded parameters could prove to have a influence of comparable magnitude with the influence of the established parameters. If these new parameters are common to all three devices, it would be a clear sign that those parameters should be included in a generic extension of the current method for the estimation of performances of wave energy converters. However, if the significant parameters are different for each considered device, this could signify that a reliable method applicable to all sort of wave energy converters might be impossible to reach, and that customized method for each type of wave energy converter should be sought for.

1.3 The statistical approach

The chosen approach for this work is to evaluate statistically the influence of sea state parameters over the performance of wave energy converters. While this approach might not provides insight into how each parameters contributes to the performance of the wave energy converters, it is seen as a way to handle multiple sea states parameters fairly between multiple devices. A statistical approach gives the possibility the measure the significance of each observed effect and interactions between variables can be assessed. Thus the statistical approach should allow a global view on the influence of the sea states parameters over the performances of wave energy converters.

Practically, the average power output of three devices (see Section 5 on page 110) representing different type of wave energy converters are measured as a function of a wide range of sea state parameters (see Section 6.1.2 on page 123). Statistical models utilising the sea state parameters for explanatory variable are fitted to the observed performances. With this method, it is possible to assess the significance of each parameters used in the model, and to quantify its effect (see Section C on page 211).

Three devices is not enough for generalisation over all types of WECs. This number was only limited by the time constraint of this work. However, by using the same set of parameters, tests on other models could extent the presented results. If nothing else, those results will provide a better understanding of the base method currently in use and should help interpret the results of electricity production estimation of wave energy converters from power matrices and scatter diagrams.

1.4 Justifying physical model tests

Only physical model tests are used in this work. This decision was taken mainly over the concern not to introduce limiting hypothesis over the behaviour of devices. Trying to assess the influence of directional sea state parameters, it is thought that none of the effects such as sloshing, rolling or viscosity that hard difficult to include in numerical models should be neglected. The moorings arrangement had to be taken into account. Those are the physical phenomenon that might introduce sensitivity of the wave energy converters to directional sea state parameters. While numerical modelling of devices has shown positive progress in the past years, this level of complexity is still difficult to achieve and it is extremely computationally intensive. The statistical approach itself requires a large number of tests, each tests needing long time series (at least half an hour at full scale) to be realistic. Providing this amount of data numerically was just unrealistic in the time frame of this work, let alone the time needed to build and tests the numerical models themselves. The physical model approach is providing the means to acquire large amount of time domain data in complex sea states and no simplification on the devices behaviour has to be made.

1.5 The Edinburgh Curved Wave tank: a presentation

The Edinburgh Curved tank is the central experimental facility that is utilised during this work. As the facility is at the centre of the work presented, a brief presentation is provided and a more complete presentation is available in Taylor *et al.* (2003).

The tank was commissioned in 2003, following the decommissioning of the previous deep-water ocean basin. Its main feature is to be built as a quarter of a circle, with 48 absorbing type wave-makers aligned on its curved side. Due to the limited space, the use of sloped beaches was prohibited and *wedged* beaches composed of several grades of open-cell foam material are used instead on the long edge. Finally, the short edge of the tank is fitted with a glass panel allowing intimate visual contact with the experiments taking place. Fig. 1.1 gives a schematic representation of the tank and a photography of it taken in 2003.

The depth of the tank is constant at $1.2\,\mathrm{m}$, allowing deep water waves at the nominal frequency of $1\,\mathrm{Hz}$. The usable range of frequencies extends from $0.4\,\mathrm{Hz}$ up to $2\,\mathrm{Hz}$. The stroke of the wavemakers (low frequency waves) prevents the generation of longer waves, and the narrower wavemakers would be needed to produce good quality wave fronts at higher frequencies. The deep water assumption $2d > \lambda$ with d the tank depth and λ the wave-length is only respected for waves frequencies higher than $0.8\,\mathrm{Hz}$. Waves a lower periods should be treated as intermediate depth or even shallow water depth. However, during the course of this work, only deep water wave theory is considered. An assessment of the tank capabilities was done during the course of this work and outcomes are presented in Section 3.3 on page 26.

1.6 The selected WECs

The selection of WEC models used during this thesis has to satisfy multiple goals. Primary, they should represent a broad range of WEC concepts for the results to be as generic as possible. Second, the comparison of the effect of directional spectrum parameters over directional and omnidirectional device is of particular interest, so the chosen devices must range from purely omnidirectional (mooring included) to strongly directional. Finally, the Edinburgh Curved tank can only accommodate deep water devices, and reliable models from prior work were favoured as this thesis is not focused into developing new models.

Aside of this constraints, outstanding performances are not required for those models. As the

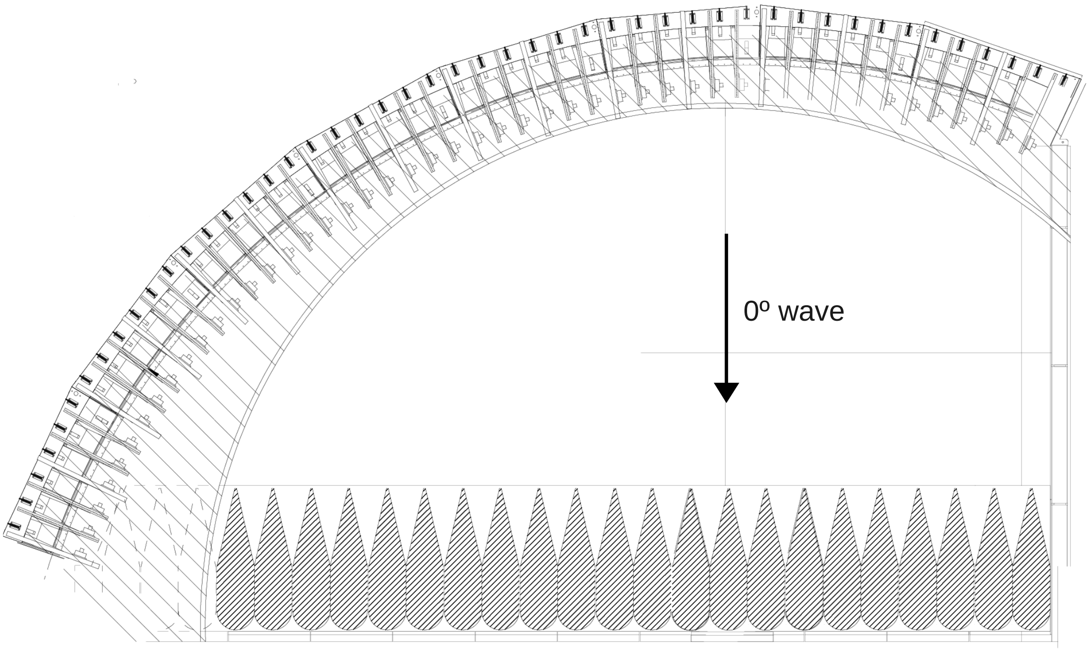

(a) Schematic view of the Edinburgh curved tank

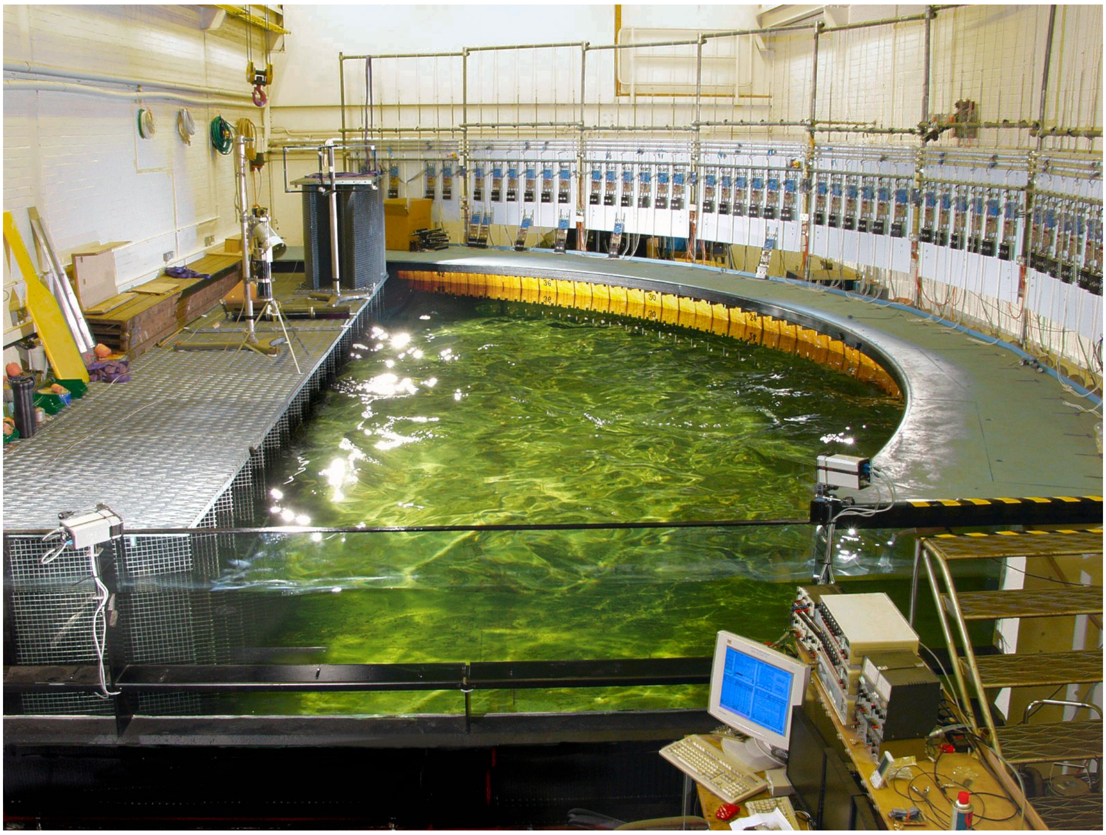

(b) 2003 photography of the Edinburgh curved tank

Figure 1.1: *Photographic and schematic representations of the Edinburgh Curved tank.*

main goal is to study their performance variation relatively to the spectral parameters, absolute performance is not a strong concern, and emphasis is put on the repeatability and precision of the performance measurements.
Three WEC models are chosen according to those constraints and considering practical issues.

- A single fixed OWC model. The model utilised was developed by Queen's University Belfast, so it has been tested and validated before being used in this study. The single fixed oscillating water column is a generic omnidirectional device. It is expected that its performances will not be much affected by the effect of wave directionality.
- Two fixed OWCs. They are two identical instances of the previous model. By being considered as a single device, the two OWCs are standing for a weakly directional device that cannot align itself with the main direction of propagation.
- The desalination duck model. This model is an evolution of the Edinburgh Duck and it has been developed and tested continuously at the University of Edinburgh during the last four years (Pascal, 2006), (Salter *et al.*, 2007), (Lucas *et al.*, 2008) and (Lucas *et al.*, 2009). The desalination duck model is a fully directional device that can align itself with the waves. As well as providing data for this study, the extensive testing in directional seas will provide some valuable knowledge of the model behaviour in directional waves.

The time frame associated to a PhD work do not allow the use of more models. This work should be extended in the future with other types of WECs to generalize the results.
No theoretical performance characteristics of the devices are provided. This work intended to use previously developed models, hence no time was dedicated towards theoretical analysis or numerical modelling. To the knowledge of the author, contents from previous studies of such type of analysis with the selected device configurations for these tests were not published yet, and subsequently cannot be referenced in this work. Further publication based on the material presented in this work will hopefully includes such type of content to help understand and discuss the observed experimental results.

1.7 Outlines of the thesis

This thesis is sectioned into seven main chapters describing the important section of the work accomplished, or supporting its understanding. An initial chapter is focused on providing some background on the concepts used to described sea states and introduces the main sea states parameters. The two following chapters are focused on the wave measurement and generation in the Edinburgh Curved tank. The three following chapters are presenting in details the WEC models, the test plan and the results of the tests. The main conclusions of this work are given in a separated chapter, and supporting material is provided in appendices. The outlines of the thesis is presented below:

- Chapter 2: Sea State Representation and Directional spectrum

  A short introduction to the main hypothesis underlying the concepts utilised in this thesis. The wave linear theory is presented as the main concept behind the description of a sea state into its directional spectrum. Some consideration on spectrum discretisation are given. The main concept of sea state modelling through standard spectral shape are exposed and the sea states parameters used in this work are presented.

- Chapter 3: Generating Waves

  This chapter describes how waves are generated during this work. The possibilities of the Edinburgh tank are assessed to verify that the tank is capable of generating the required sea states.

- Chapter 4: Measuring the directional spectrum

  A description of the adaptation of the Maximum Likelihood Method and its derivative, the MMLM, to the experimental set up is provided. The adapted method performances are then assessed with simulated waves and a comparison with the industry standard is provided.

- Chapter 5: Wave Energy Converters description and characteristics

  The Duck and OWC models are presented, with some of their essential characteristics.

- Chapter 6: Experimental plan

  This chapter first describes and discusses the set of sea states parameters selected in this work. It then describes the experimental plan set up to measure the influence of the selected parameters. Tank measurements of the planned sea states are also provided.

- Chapter 7: Results

  The presentation of the results from the WEC tests in the tank and their statistical analysis. The influence of the selected parameters over the model performances is described and compared. Discussion about the test results and their validity is provided.

- Chapter 8: Conclusion

  Conclusion of this work and main results are presented. A section on future work and outcome is added.

- Appendices

  Some point of method and extra material to the thesis are presented in Appendices. Material presented in Appendices is referenced in the body of the text.

1.8 Disclaimer on the results

While implementing the corrections to the thesis requested by the examiner, an error in the directional spectrum estimation appeared. In the time frame allowed for the corrections, it was not possible to estimate again with the corrected method all the spectra and their associated parameters, therefore the values presented on this thesis are uncorrected and based on the method used before the viva. However, rapid checks have shown that while all the sea state parameters values are slightly different when computed from the corrected spectra, the main conclusions of this thesis remain valid. Particularly, the method used to assess the influence of the the sea state parameters still perform as well and puts in evidence the crucial role of the interaction between parameters. The possibility to devise parametric models of the devices performances is also confirmed with the corrected versions of the sea state parameters.

Chapter 2
Sea State Representation and Directional spectrum

This chapter is intended to give a short summary of the concepts used in this thesis to mathematically represent sea states. It first presents the basics of linear wave theory underlying all further development, and then it describes in more details the decomposition into directional spectra of real sea states. Different forms of the directional spectrum are presented and the link between wave amplitude and spectra is detailed. The basics of sea state modelling through standard spectral shapes is outlined with reference to the main functions used. Finally, the description of the directional sea states parameters used in this work are given, with their mathematical description.

2.1 Linear wave theory

Underlying all sea state descriptions in this work is the assumption that any given sea state can be described as an infinite sum of regular waves (Stokes, 1847; Bryden *et al.*, 1990) of different directions of propagation, frequencies and amplitudes.
For each of these components, the wave elevation η at a point $M(x, y)$ at any instant t can be written:

$$\eta(x, y, t) = a \cdot \cos(-\omega t + k(x \cos\theta + y \sin\theta) + \phi) \tag{2.1}$$

with

$$\omega^2 = kg \cdot \tanh(kd) \tag{2.2}$$

$a =$ amplitude of the wave

$\phi =$ phase of the wave

$\theta =$ direction of propagation the wave

$d =$ water depth

Defining the wave-number vector $\overrightarrow{k} = k(\cos\theta \cdot \overrightarrow{x} + \sin\theta \cdot \overrightarrow{y})$, Eq. 2.1 can also be written as $\eta(x, y, t) = a \cdot \cos(\overrightarrow{k} \cdot \overrightarrow{M} - \omega t + \phi)$.

In a real sea state, the phase ϕ of each component is assumed to be random. Eq. 2.2 is known as the *dispersion relation*. It is a relation particular to gravity waves that links the wave frequency and its wave number. This decisive relation in wave theory is first stated formally for water of finite depth d in Airy (1841). During this work, only deep water waves were considered and all following equations are given with the assumption that $d \to \infty$.

2.1.1 The directional spectrum

With only three non-random parameters defining each single components, a sea state can be described in a 3-dimensional space. The representation of a sea state in this space is known as its directional energy spectrum and was introduced by Pierson & Marks (1952). The decomposition in single waves of a complex sea state is commonly done using tools based on Fourrier transformation. A more in depth review of such tools is presented in Chapter 4 on page 48.

This decomposition assumes an infinite period of the considered sea state an that its characteristics are stationary. In practice, samples of an half an hour to an hour are done during which the sea state is considered constant. While this hypothesis is acceptable in most cases, works such as Liu (2000) use time sensitive tools to show that sea states characteristics can vary significantly during the course of a samples, specially during the building up or decay of a storm event. This is a clear limitation to this concept but no convincing alternative is currently available.

The assumption of infinite period leads to continuous frequency and angular decompositions. Thus, the wave elevation $\eta(x, y, t)$ is modelled as:

$$\eta(x, y, t) = \int_0^\infty \int_{-\pi}^{\pi} a(\omega, \theta) \cos\left[-\omega t + k(\omega)(x \cos\theta + y \sin\theta) + \phi(\omega, \theta)\right] d\omega d\theta \tag{2.3}$$

The finite length duration and discrete nature of the samples induces a finite and discrete frequency and angular decomposition of Eq. 2.3. The wave elevation η can then be written at any point $M(x, y)$ of the considered area and at any instant t as:

$$\eta(x, y, t) = \sum_p^M \sum_q^N a_{pq} \cos(-\omega_p t + k_p(x \cos\theta_q + y \sin\theta_q) + \phi_{pq}) \tag{2.4}$$

In the context of tank testing, only the discrete version of the spectrum is considered.
Three main forms of directional spectra can be found in the literature. They are all three easily related but it is good practice to precise which ones will be used in this research. Most early contributions Barber (1963); Capon *et al.* (1967) treating of directional spectral estimates are based on the *wavenumber-circular frequency spectra* $S(\overrightarrow{k},\omega)$ (also known as *wavenumber-frequency spectrum*). Those studies are not focused on gravity waves, so there is no dispersion relation linking the wavenumber to the frequency and this form became more intuitive. However, in the case of ocean waves, the dispersion relation (see Eq. 2.2) renders the description of the directional spectrum as a function of ω and $\overrightarrow{k}$ contra-intuitive as it is sufficient to talk of the amplitude, frequency and direction of a wave to fully characterise it. Henceforth, the directional spectrum of ocean waves is more commonly expressed in the *frequency-direction* form $S(f,\theta)$ or in the *circular frequency-direction* form $S(\omega,\theta)$.
The link between the two last forms is straightforward

$$S(f,\theta) = 2\pi \cdot S(\omega,\theta) \tag{2.5}$$

and assumes that $S(\omega,\theta)$ is already expressed only for the positive frequencies. When computing a spectral density $S(\omega)$, the initial results are expressed for $\omega \in]-\infty,+\infty[$. In that case, Eq. 2.5 must be transformed in $S(f) = 4\pi S(\omega)$ with $f \in [0,+\infty[$ (see Newland (2005) page 52).

Benoit *et al.* (1997) give the link between the *wavenumber-frequency spectrum* and the *frequency-direction* forms as:

$$S(f,\theta) = \frac{2\pi k}{G_g} S(k_x,k_y) \tag{2.6}$$

with G_g the group velocity as defined by the linear theory.

In this work, everything related with the spectrum estimation is based on the *wavenumber-frequency* spectrum as all the equations are using this notation. However, the parts focusing on the wave generation or the computation of the statistical parameters of the directional spectrum are using the *frequency-direction* form as it is more intuitive. Wave amplitudes of Eq. 2.3 are directly related to the *frequency-direction* spectrum as in Eq. 2.7:

$$a(f,\theta) = \sqrt{2\,df \cdot d\theta \cdot S(f,\theta)} \tag{2.7}$$

In the discrete form, Eq. 2.7 is transformed into $a_{pq} = \sqrt{2\,\Delta f \cdot \beta_\Theta \cdot S_{f_p,\theta_q}}$.
Finally, the directional energy spectrum is often split into an omnidirectional energy spectrum S_{f_p} and a normalised directional spectrum D_{f_p,θ_q} following:

$$S_{f_p,\theta_q} = S(f) \cdot D_{f_p,\theta_q} \tag{2.8}$$

$$\text{with} \sum_q D_{f_p,\theta_q} \cdot \beta_\Theta = 1 \tag{2.9}$$

2.1.2 Limitation of linear wave theory

First, all the wave components are assumed to be independent in the linear theory. This is an approximation, and it has been shown that interaction between wave components can be responsible for the build of extreme waves. This sort of phenomenon will not be accounted for by linear theory.
Second, the linear theory assumed that propagating waves can be modelled as perfect sinusoidal waves. While this is acceptable for waves which amplitude is much smaller than their wave length, it is not the case for steeper waves. The actual form of propagating gravity waves is cnoidal. The cnoidal wave form can be approximated by using higher order theory, but these higher order theories are not compatible with the frequency analysis required to build the directional spectrum. By simplifying the wave form, the linear theory looses some properties of the waves, such as the induced drift force on structure. Additionally, trying to reproduce pure sinusoidal waves in a tank is not possible. One can observe that ”bound” and ”free” harmonic are always generated with the main component of a regular wave. It is therefore difficult to reproduce perfectly a spectrum in a tank: the harmonics of the lower frequency components of the spectra ass themselves to the higher frequency components of the spectrum in the frequency analysis, but the ”bound” harmonic part of the wave travels at the velocity of the component it is bound too.

2.2 Modelling of the directional spectrum

2.2.1 Models for spectral shape

Several attempt were conducted to model the directional spectrum in order to obtain a standard shape that could be use in engineering applications. Some studies such as Pierson & Marks (1952) focused on the omnidirectional spectrum, concentrating on the wave energy repartition as a function of the frequency. Empirical models were devised, usually taking one to three parameters. The most used spectral shape used in the wave energy community are the Bretschneider spectrum (also called Modified or Generalized Pierson-Moskowitz) and the JONSWAP spectrum (Hasselmann *et al.*, 1973). Those spectral shape are very convenient to the experimenter as they allow the recreation of the omnidirectional from the peak period T_p and the significant wave height H_{m0} (see Section 2.3.3 for the definition of these parameters). The Bretschneider spectrum required only an wave height and period parameters as input while the JONSWAP spectrum requires a third parameters, γ, to control the broadness of the spectrum. For $\gamma = 1$, the JONSWAP and the Bretschneider are identical and by increasing γ, the JONSWAP get narrower.

find ref

The directional distribution D_{f_p,θ_q} was also the subject to several studies. Cartwright (1963) introduced the most widely used representation of D_{f_p,θ_q} as in Eq. 2.10:

$$D_{f_p,\theta_q} = F(s)cos^{2s}(\frac{\theta_q - \theta_{m,p}}{2}) \tag{2.10}$$

with $\theta_{m,p}$ the mean direction of propagation at the frequency f_p and $F(s)$ the coefficient required to satisfy Eq. 2.9. Later on, specific work on the variation of the parameter s of Eq. 2.10 with respect to the frequency were published. Mitsuyasu *et al.* (1975); Hasselmann *et al.* (1980) present different empirical models for fully developed seas. However, in both case s is increasing from 0 to a maximum at $f = 1.05 f_m$, with f_m the modal period defined as the peak of the omnidirectional spectra. s decreases for higher frequencies with $s \rightarrow \approx 1$ for $f >> f_m$. In this work, the wave generation method (see Section 3.2 on page 20) uses a constant s value for all frequencies. This is commonly done in engineering application to simplify the process and this simplification has been applied by Edinburgh Design Ltd in their wave generation software. Alternatives to the Cartwright formula are mentioned by (Tucker & Pitt, 2001) such as the *wrapped-normal* and the cos^n formula. However, those are seldom used in practice and will not be considered in this work.

2.2.2 Multi-modal sea states

In this work, it is often referred to the terms of bi-modal or multi-modal sea states. Those terms refers to the fact that the wave observed in a real sea states can often have been created by more than one meteorological system. Waves created by different meteorological system will exhibits different characteristics such as direction, period or spectral shape. The waves issued from a single meteorological system are grouped into a wave system. When many wave systems are present in a real sea state, it is described as multi-modal. Kerbiriou *et al.* (2007a) has quantified for a specific location the number of observed multi-modal sea states. It appears that over 65% of the observed sea states during the course of this study could be characterized as multi-modal.

In the directional spectrum, multi-modal sea states are characterized by the presence of more than one peak of energy in the (f, θ) plan. Such sea states cannot be represented directly using the classical spectral shape and directional distribution presented in the previous section. The modelling of such sea states is commonly done by the decomposition of the observed spectrum into its different wave systems. Each wave system can then be modelled using the standard spectral shapes (Guedes Soares, 1984; Guedes Soares & Nolasco, 1992; Kerbiriou *et al.*, 2007a; Boukhanovsky & Guedes Soares, 2009; Mackay, 2011).

2.3 Sea state parameters

From the spectral representation of sea states, it is often useful to derive a set of parameters that will be used to form statistics about the wave climate of a location. It is commonly accepted that it is better to get statistics on the parameters, and then to recreate the desired spectra by using the standard spectral shape described in Section 2.2 than to try to obtain a representative spectral shape specific to the considered site. The standard spectral shapes have indeed been defined over larger range of observations and theoretical considerations.

Sea state parameters are used in this work both the evaluate the performances of the directional spectrum estimation method (see Section 4 on page 48) and to question and maybe evolve the common approach to estimate power production from WECs. This sections gives the definition off all the parameters used in this work, and justify the choice of the selected bandwidth indicator. Finally, the nomenclature associated to the isolated wave systems (see Section 4.4.2 on page 66) is explained.

2.3.1 Selecting a bandwidth parameter

Numerous parameters related to the bandwidth of omnidirectional frequency spectra have been proposed in the past. Saulnier *et al.* (2010) present an extensive list of those, as well as a first study of the correlation between such parameters and the performance of WECs. There is currently no widespread consensus on which of these parameters are the most pertinent. The decision was made to use f_s (known as *frequency spreading* in Pascal & Bryden (2011); Pascal *et al.* (2011)) as its physical meaning is obvious: it is the weighted average of the distance to the energy frequency $\frac{1}{T_E}$ and its definition is given in Table 2.1. Fig. 2.1 shows the evolution of f_s with γ, the peak enhancement parameter in the JONSWAP formula. It shows that f_s varies substantially for a range of values of γ between 1 and 5. The most commonly used values of γ are within that range ($\gamma = 1$ corresponds to a Bretschneider spectrum, and $\gamma = 3.3$ is the standard value for JONSWAP (Tucker & Pitt, 2001)). As will be explained further on in more detail in Section 6 on page 122, these two frequency spectra are the ones retained for testing the scaled WECs, which makes f_s relevant for this study as it should allow a clear distinction between the generated sea states.

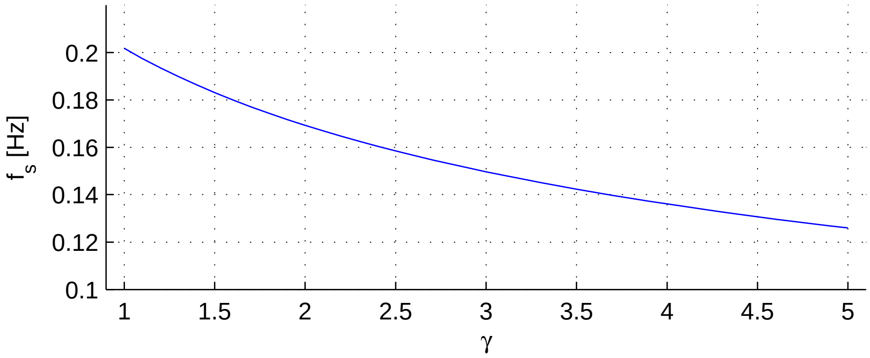

Figure 2.1: *f_s as a function of γ the peak enhancement parameter of JONSWAP spectra for a* $T_E = 1\,\mathrm{s}$.

As f_s is a weighted average by S_f of the distance each frequency bin to the energy frequency, it is expected that f_s will not be very sensitive to the higher frequency component of the spectra. This is indeed a seek after characteristics and an advantage over other bandwidth related parameters as the high frequency components of the spectra will be first chopped during the wave generation process (see Section 3.2 on page 20) and then wave systems are isolated by a method that is often discarding the tail of the spectra (see Section 4.4.2 on page 66).

Finally, while this work will only use f_s as a bandwidth indicator and will not enter into comparison between the different parameters related to the bandwidth of omnidirectional spectra, it is expected that conclusion relative to the influence of f_s should be transferable to those other parameters.

2.3.2 Parameter linked to the variability of the mean direction of propagation

The possibility of variation in the mean direction of propagation $\theta_m(f)$ with respect to frequency f was also considered. Such a phenomenon could be observed if the wind system generating a wave system is moving, such as a fast moving storm (Ochi, 2003). As waves of different period travel at different speeds, an observer at one point in space and time will observe waves of different periods coming from different direction. The parameter β_Θ was introduced in this study as an attempt to account for such phenomena. β_Θ is defined as the coefficient of the linear regression fitted to the observed values of $\theta_m(f)$. It was thought to be a relevant parameter as there is no prior knowledge of how a self aligning device such as the Duck would align itself when exposed to wave systems with $\beta_\Theta \neq 0$.

2.3.3 Sea state parameters related to uni-modal sea states

The spectral density S_f is computed from the directional spectra as $S_f = \sum_q S_{f_p,\theta_q} \cdot \Delta\theta$. Table 2.1 shows all the sea states parameters used trough this work for the tests of the wave energy converters, the definition of the sea states and the characterisation of the wave measurement method. Those parameters are normally conceptualised with respect to a uni-modal sea states, but can be computed for any spectral shape. θ_{sp} and Θ_S are the discrete version of the second definition of those parameters as presented in Frigaard *et al.* (1997). The subset of these parameters which effect on WEC performances will be tested is presented in Table 6.1 on page 124 alongside the description of the test plan.

2.3.4 Parameters of isolated wave systems

This work intent to explore the influence of the shape of wave systems and of multi-modal spectra over the performances of WECs. For multi-modal sea states, the parameters of Table 2.1 can be defined with respect to each wave system of a multi-modal sea state. The parameters defined that way are noted with an extra subscript, ordered by decreasing importance of the wave system: the energy period T_E of the dominant wave systems becomes $T_{E,1}$. The wave systems are sorted using their peak value. When parameters are estimated with respect to the wave system only, the same mathematical expressions as in Table 2.1 are used, but the spectral estimates outside of the isolated system (see Section 4.4.2 on page 66) are set to 0.

With parameters defined for each wave system, it is possible to define relational parameters

Symbol	Physical meaning	Unit	Equation
H_{m0}	the significant wave height	[m]	$H_{m0} = 4\sqrt{m_0}$
T_E*	the energy period	[s]	$T_E = \dfrac{m_{-1}}{m_0}$
T_p	The peak period	[s]	the period of the most energetic bin of S_f. $T_p = \frac{1}{f_m}$
T_Z	The zero crossing period	[s]	$T_Z = \dfrac{m_2}{m_0}$
$\theta_{m,p}$	the mean direction at each frequency	deg(°)	$\theta_{m,p} = \dfrac{\sum_q S_{f_p,\theta_q}\theta_q}{\sum_q S_{f_p,\theta_q}}$
β_Θ*	the variation of $\theta_{m,p}$ along the frequency axis	deg(°)/[Hz]	the coefficient of the linear regression of $\theta_{m,p}$ as a function of the frequency.
Θ_M	the integrated mean direction over the frequencies	deg(°)	$\Theta_M = \dfrac{\sum_p S_{f_p}\theta_{mean,p}}{\sum_p S_{f_p}}$
f_s*	frequency spreading parameter	[Hz]	$f_s^2 = \dfrac{\sum_p S_{f_p}(f_p - \frac{1}{T_E})^2}{\sum_p S_{f_p}}$
θ_{sp}	angular spreading factor at each frequency	deg(°)	$\theta_{sp}^2 = \dfrac{\sum_q S_{f_p,\theta_q}(\theta_q - \theta_{m,p})^2}{\sum_q S_{f_p,\theta_q}}$
Θ_S*	the integrated angular spreading factor	deg(°)	$\Theta_S = \dfrac{\sum_p S_{f_p}\theta_{sp}}{\sum_p S_{f_p}}$

Table 2.1: *List of parameters related to the spectral shape. The parameters marked by a * are the parameters which effect on WEC performances will be tested.*

between the different wave systems. Those are defined in Table 2.2 for the bi-modal case.

Symbol	Physical meaning	Unit	Equation
μ	uni-modality index	-	$\mu = \dfrac{T_{E,1} \cdot H_{m0,1}^2}{\sum_i T_{E,i} \cdot H_{m0,i}^2}$
δT_E	Period Difference	second	$\delta T_E = T_{E,1} - T_{E,2}$
$\delta \theta_M$	Mean direction difference	deg(°)	$\delta\theta_M = \lvert\theta_{M,1} - \theta_{M,2}\rvert$

Table 2.2: *List of relational parameters between wave systems.*

δT_E and $\delta\theta_M$ are related to the relative position of the two wave systems in the (f, θ) plan. The uni-modality index μ is introduced in order to classify sea state from completely bi-modal to uni-modal. When both wave systems carry the same amount of energy, $\mu = 0.5$. As the ratio of energy between the dominated and dominant wave system decreases, μ increases from 0.5 to 1. Through the uni-modality index μ, it is possible to explore the possibility that a threshold could be defined: it would be indeed be interesting if multi-modal sea states with $\mu > threshold$ could be considered as uni-modal for the purpose of estimation of WEC performances.

Finally, the isolation method can be applied to uni-modal sea states. Isolating the wave system from the rest of the spectra makes the measures more robust to noise and could separate the incident and the reflected part of the wave system. While the parameters defined on the isolated system and on the entire spectra corresponds to the same physical phenomenon, their value are likely to be different due to the isolation. It is therefore needed that the notation allows the differentiation between the *isolated* and *non-isolated* parameters. In this work, the *isolated* parameters will be noted with an extra 1 subscript, as the dominant wave system of multi-modal sea states. Uni-modal sea states are therefore treated as bi-modal sea state with insignificant second wave system.

Chapter 3
Generating Waves

3.1 Introduction

A novel implementation of the single summation method was used to generate the sea states in the Edinburgh Curved tank during this thesis. This technique was first described by Jefferys (1987) but it has been seldom used since. It differs from the common implementation standard method described by (Rogers & King, 1996) and incorporated into *Ocean*, the wave programming language provided by Edinburgh Designs Ltd as it ensures both a deterministic frequency spectrum and directional distribution. Hence, it allows the exact specification of sea structure required for this work, especially in the generation of bi-modal sea states.
The following sections discuss the use of this specific method and describe its implementation. Then, a review of the tank characteristics is given. Emphasis was given to ensuring that the experimental set up was able to sustain the generation method.

3.2 The deterministic approach

3.2.1 Rational for deterministic waves

Experimentalists need to consider whether their tests will be better served by using deterministic or random wave generation. This question has generated a healthy debate in the tank testing community since the early eighties, as discussed, for example, by J. Ploeg (1987).

In the context of wave energy research, tank tests are used for both survivability and performance characterisation. For the later at least, exploring a large range of sea states is necessary, implying that shorter run times are desirable, with a tight control of the incident wave field.

A disadvantage of true random wave generation is that the target spectrum is not entirely realised unless an infinite time series is generated. The generated sea states using this method are truly random and do not repeat themselves. By increasing the length of the time series, the experimenter reduces the theoretical variance between the generated and the target spectra, as described by Miles & Funke (1989) and Jefferys (1987). In practice, it means that even using the same target spectrum, variability of the results between runs is expected as the spectrum realised in each run will be different. With a random wave generation method, it is always a trade off between long time series and control of the generated sea state.

On the contrary, sea states generated with a deterministic method will repeat themselves over the *repeat time* of the sea state. If an integer number of repeat time of the sea states is generated and recorded, a deterministic method is thus offering a better control of the incident wave field if ones only focused on its spectral characteristics.

However, waves generated with deterministic methods generally do not exhibit statistical properties identical to those of ocean waves that they should modelled. This is because they do not simulate random Gaussian processes. The quantities measured using deterministic sea states will only exhibit similar characteristics to what could be expected in a truly random sea state when the number of spectral components utilised for the wave synthesis $\rightarrow \infty$. Therefore, quoting Tucker *et al.* (1984), *statistics of wave groups are certainly affected* while synthesising sea states with a deterministic method (denoted random phase method in the work mentioned above).

Significantly, Elgar *et al.* (1985) have shown that the condition mentioned above can be considered as satisfied if at least a 1000 spectral components are used. Their study reveals that when the number of spectral component is $\gtrsim 1000$, the difference in the average length of runs is less than 2%.[1]

Additionally, Saulnier *et al.* (2009) demonstrated that deterministic waves do not introduce any bias on the observed performances of wave energy converters compared with more realistic random waves. This later study consequently dismiss the main reason not to use deterministic wave generation method for the purpose of this work. Finally, the body of evidence designates deterministic wave generation techniques as the most appropriate for the purpose of tank testing of wave energy converters as far as power generation is concerned.

---

[1] in this work, around 1200 spectral components are used, see Section 3.2.2.

3.2.2 Single summation implementation for this thesis

The legacy at the University of Edinburgh imposes to use of a deterministic approach as all the equipment is designed for it. According to Section 3.2.1, this is also the most appropriate approach for this study.

The intuitive method to generate deterministic waves is to use Eq. 2.4 with the a_{ij} coming directly from the target directional spectrum. For every element of the discrete directional spectrum, a regular wave is added to the final signal with the required amplitude, frequency and direction and a random phase. This methods is commonly referred to as the *double summation* method. The repeat period of the generated wave sequence equals the inverse of the frequency resolution ΔF of the target spectrum.

However, it has its shortcomings as constructive interactions between regular waves travelling in different directions but with an identical frequencies generate spatial patterns across the tank (Miles & Funke, 1989; Jefferys, 1987). This phenomenon is known as *phase-locking*, and can also be observed between the incident and reflected spectra (see Section 4.2.2 on page 50).

The method used in this study is the direct implementation of the method described by Jefferys (1987). It avoids the *phase locking* problem by splitting every frequency band into N (number of angles) sub-frequencies $\Delta f = \Delta F/N$ so that no wave components are generated with exactly the same frequency across the tank. Jefferys *et al.* (1981) demonstrated the benefit that a small gap in frequencies between waves provides in respect to the directional resolution of the Maximum Likelyhood Method (MLM). In Fig. 3.1, the resolution of the MLM is greatly increased by introducing a small frequency gap between two wave fronts. Eq. 2.4 becomes:

$$\eta(x,y,t) = \sum_{i=0}^{M\cdot N-1} a_i \cos(-\omega_i t + k_i(x\cos\theta_i + y\sin\theta_i) + \phi_i) \qquad \text{with} \quad \omega_i = 2\pi i\Delta f \tag{3.1}$$

For each frequency band ΔF, there is no formal recommendation about how to distribute the N components into the sub-frequencies in the initial publication. In this study, an organised repartition was arranged into each frequency band. The sub-frequencies are allocated incrementally to waves which are sorted in an ascending order in respect of their direction of propagation. Fig. 3.2 shows graphically the evolution from the target directional spectrum to the single summation method implemented in this study. This repartition lead to a formal expression of θ_i as:

$$\theta_i = \theta_{min} + \Delta\theta \cdot i^{'} \qquad \text{with} \quad i^{'} \equiv i\ mod(N) \tag{3.2}$$

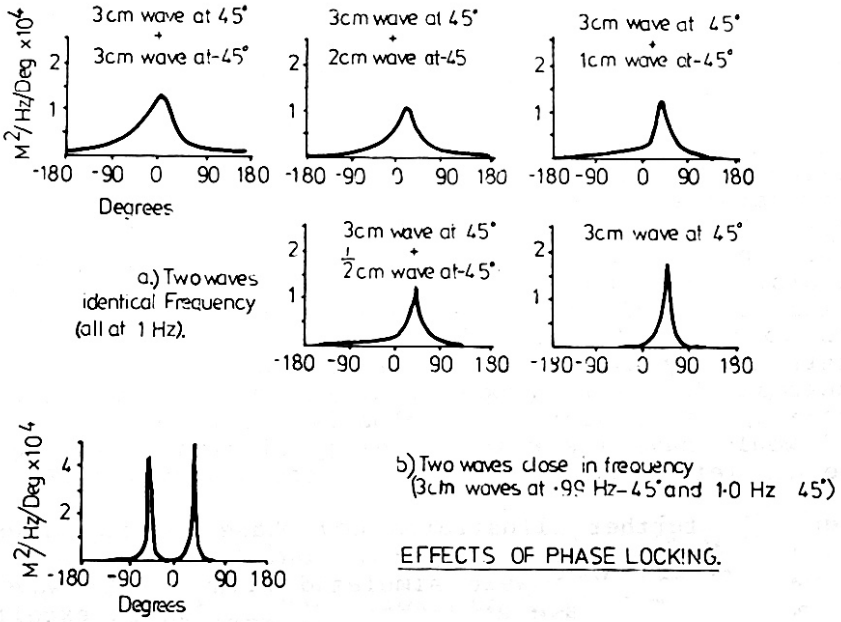

Figure 3.1: Figure extracted from Jefferys et al. *(1981) showing the benefit to the MLM estimate of introducing a small frequency gap between wave components.*

The underlying hypothesis behind the directional spectrum definition is that regular waves are propagating independently without interaction (see Section 2.1 on page 10). However, previous experiences in wave tanks has shown the limit of this hypothesis. A phenomenon called tooth breeding reported by Salter (1981) and Keller (1984) exemplifies such interactions. In this experiment, a sea states composed of two fronts with very close frequency is generated. the resulting waves are measured at regular spacing from the wavemakers and it can be seen that as the wave travel away from the wave makers, more and more components appear in the measured spectrum. Thus, wave repartition inside each frequency band was selected as it provides the largest possible gap along the frequency axis between waves propagating in the same direction, in order to reduce the probability of wave interaction altering the generated spectrum. Section 3.3.1 explores the tank capabilities regarding this issue.

Fig. 3.3 shows the resulting auto-spectrum of virtual wave elevation generated from a very narrow directional spectrum. The spacing between each bin equals Δf, and the spacing between each peak equals ΔF.

The values related to the wave generation are summarised in Table 3.1

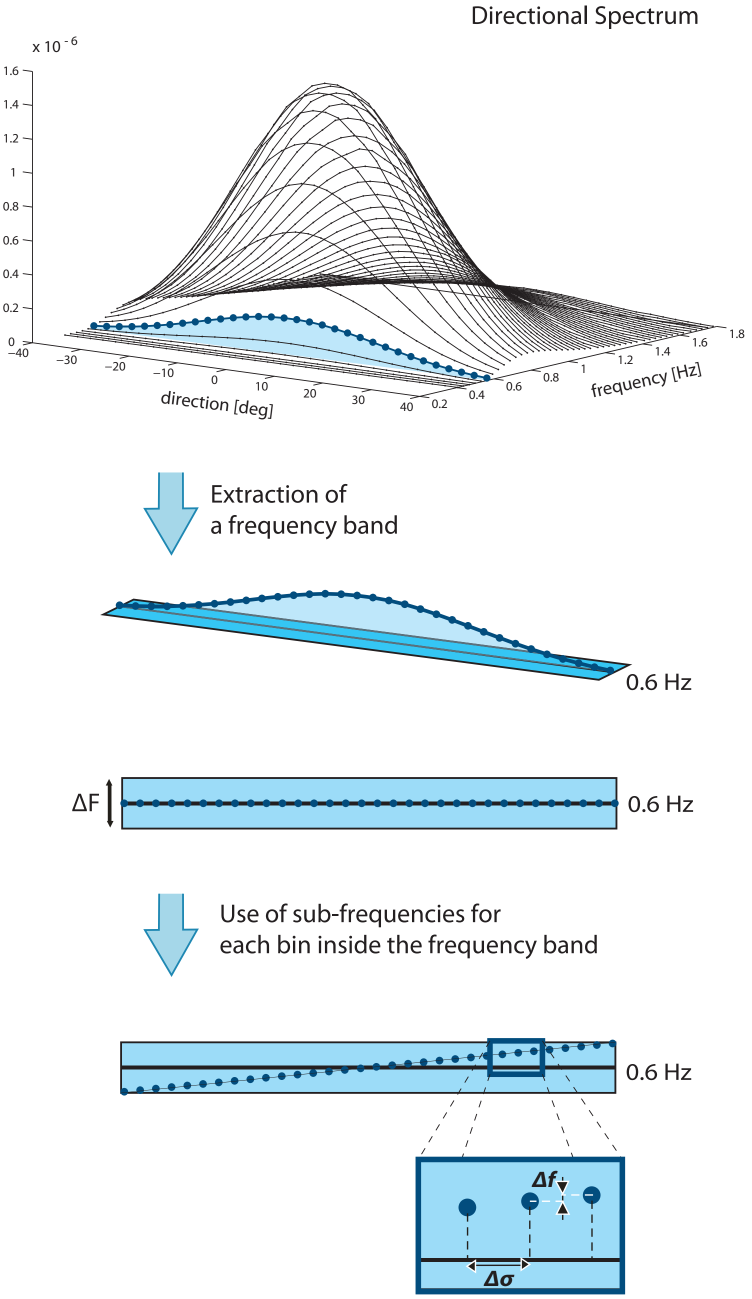

Figure 3.2: *From the directional spectrum to the single summation wave front repartition in the* (f,θ) *plan.*

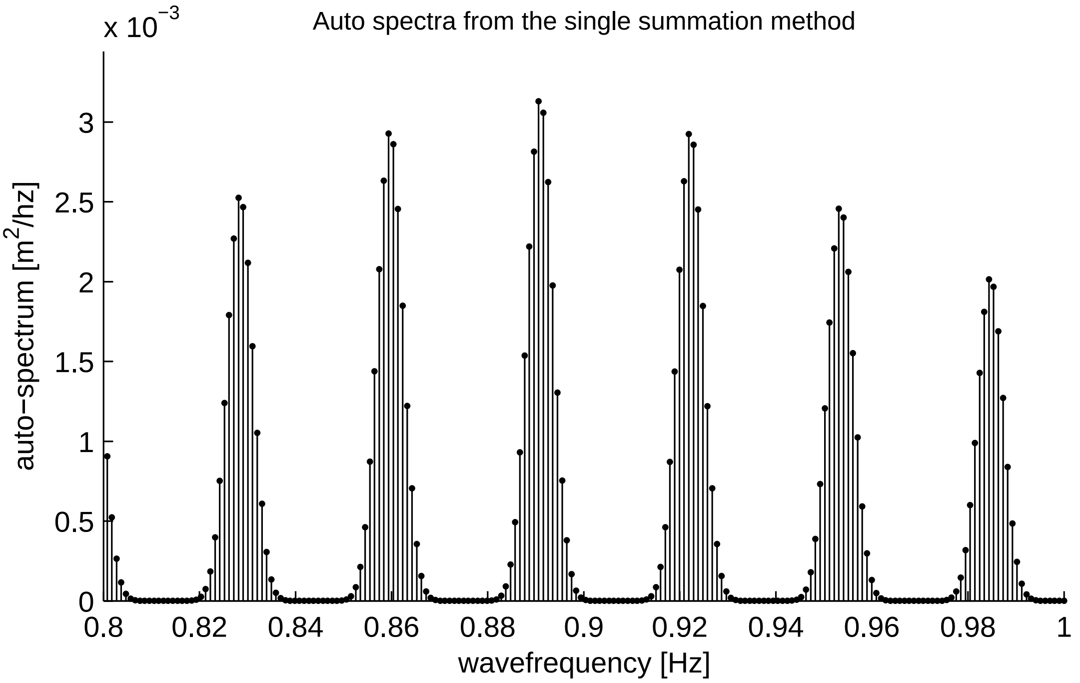

Figure 3.3: *Auto-spectrum from a perfect virtual wave elevation generated with the implemented version of the single summation method.*

Symbols	Value	Description
F_{min}	$0.375\,\mathrm{Hz}$	start of the lowest frequency band.
F_{max}	$1.75\,\mathrm{Hz}$	start of the highest frequency band.
M	45	number of frequency band.
N	32	number of direction of propagation per band.
ΔF	$1/32\,\mathrm{Hz}$	frequency resolution of the directional spectrum.
Δf	$1/(32 \cdot \mathrm{N})\,\mathrm{Hz}$	sub-frequency of the directional spectrum used for the single summation generation.
θ_{min}	$-40\,^{\circ}$	minimum wave direction of propagation.
θ_{max}	$40\,^{\circ}$	maximum wave direction of propagation.
$\Delta\theta$	$80/32\,^{\circ}$	angular resolution of the directional spectrum.

Table 3.1: *Values used for the generation of complex seas using the single summation method*

3.2.3 Determining the amplitudes of each bin

After specifying the location of each bin in the (f, θ) plan, its spectral density has to be estimated. In the most generic case, many wave systems (or mode, if referring to multi-modal sea states) can contribute to the density in one bin.
For each wave system, its frequency spectrum is first defined at the frequency resolution ΔF using a parametric spectral shape such as JONSWAP or Bretschneider. The energy in each band is then spread between the different sub-frequencies Δf of the band using a $\cos^{2s}$ spreading function of integral equals to one over the considered range.

There is two possibilities to handle the bins for which more than one wave system has a non zero contributions. One can either take the sum of the contribution from each wave system, or take the maximum contribution. The latest solution was initially preferred as it would have yield clearer separation between wave systems (The trough between two systems would be deeper by only choosing the max of the contributions and not their sum). However, the *Ocean* language does not provide any conditional statement which make it impossible to select the maximum between two values. Selecting the sum of the contributions had to be the practical choice[2]. It is not ideal for the purpose of separating the wave systems in bi-modal sea states, but it will be the directional estimation method to a stronger tests. Finally, the obtained energy spectrum is converted into an amplitude spectrum using Eq. 2.7 on page 12. For uni-modal and bi-modal wave systems, examples of the *Ocean* code used to generate the sea state are shown in Appendix A.1 on page 187.

3.3 The tank characteristics

To sustain the proposed generation method, the wave tank must be able to generate wave fronts with sufficient precision, both in terms of frequency and direction of propagation. While the Edinburgh Curved Wave Tank has demonstrated over the years that it can generate waves at accurate frequencies, data were needed to verify the directional characteristics of the tank as well as the possibility of wave interaction affecting the frequency resolution during wave propagation from the wave-makers to the measurement zone.
Measurements of the wave reflections were conducted during this work. These used mixed seas

---

[2] In afterthought, it appeared that Matlab could have been used to do the computation, writing into Ocean a list of front to generate with all their characteristics already computed. This would have allowed the use of the maximum of the contributions instead of their sum

and add to the understanding of the processes taking place in the tank.

Finally, some remark over the tank calibration are presented at the end of this section. The calibration of the tank revealed to have a significant impact over the spectral shape produced during the course of this work.

3.3.1 Wave front distinction

As the proposed frequency resolution for the wave generation was very fine ($\Delta f = 0.00098\,\mathrm{Hz}$), it was thought necessary to verify the capability of the Edinburgh Curved tank to generate distinct wave fronts at the required frequency resolution. Two measurement were taken, one involving a sea state made of two wave fronts separated by the minimal frequency step Δf of the proposed wave generation method, and the minimum angular step $\Delta\theta$, and another sea state composed of two wave fronts travelling in the same direction but with the larger frequency step ΔF.

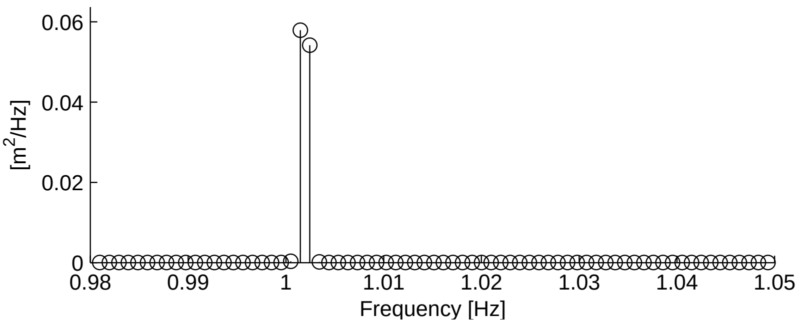

(a) Spectrum of the record of two wave fronts separated by Δf and $\Delta\theta$.

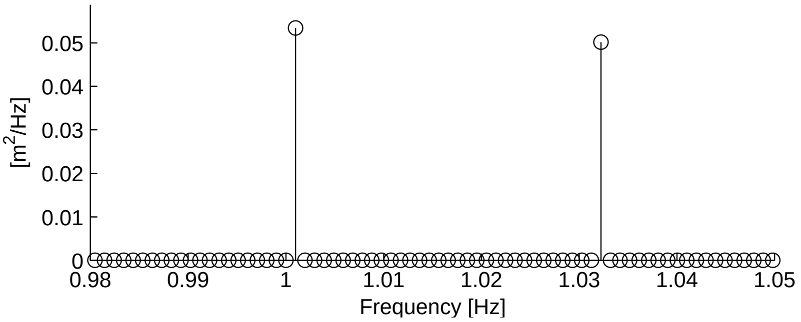

(b) Spectrum of the record of two wave fronts separated by ΔF and propagating in the same direction.

Figure 3.4: *Wave tank records of two waves separated only by a) Δf and $\Delta\theta$ and b)ΔF. The wave gauge was located $\simeq 2\,\mathrm{meter}$ from the wave makers along the axis of the tank (see Fig. 1.1a on page 6).*

While measuring the waves, it was clear that in both cases the tank was generating different fronts as a envelope of a very long period was clearly visible in the tank. Fig. 3.4a and Fig. 3.4b demonstrate this by exhibiting very sharp frequency spectra, with the energy clearly limited to the two specified wave fronts. It shows that the tank can effectively generate the required wave fronts and that little wave interaction occurs between the wavemakers and the measurement area.

3.3.2 Direction of propagation

An assessment of the wave directional accuracy was motivated by the wave generation technique presented in the above section. Complex directional seas are created using the single summation method (Miles & Funke, 1989) with wave fronts separated by only $\Delta\theta = \frac{80}{32} = 2.58\,^{\circ}$. This relatively small angular gap between two theoretical consecutive wave fronts raised the issue of the tank capability to generate singular wave front with the required angular precision.

The chosen process for this study was to measure the wave front direction of propagation of each regular wave components one after the other. A method based on the phase differences between three wave elevation gauges (PTPD method, Fernandes *et al.* (2000)) was chosen. Due to the $2.58\,^{\circ}$ angle step used between wave fronts, the method must be accurate and precise enough to measure a wave direction of propagation to $\pm\,1\,^{\circ}$.

3.3.2.1 Computing the Angle from Three Probes

The three probes are set in the tank forming a triangle. The influence of their position on the method's performance is discussed later in this section.

The method relies on the measured phase differences between probes. It relates the wave phase speed to the distance between probes to estimate the wave direction of propagation. The location of the three probes is denoted as M_1, M_2 and M_3.

Depending on the wave angle relative to the triangle orientation, more than one wave length can fit between two probes, imposing the use of the absolute phase Φ_i instead of the relative phase ϕ_i related by $\Phi_i = \phi_i + 2\pi m_i$. m_i corresponds to the number of wavelengths fitting entirely between two probes. By convention, the phase at the first probe $\Phi_1 = \phi_1 = \Phi_0$, implying $m_1 = 0$.

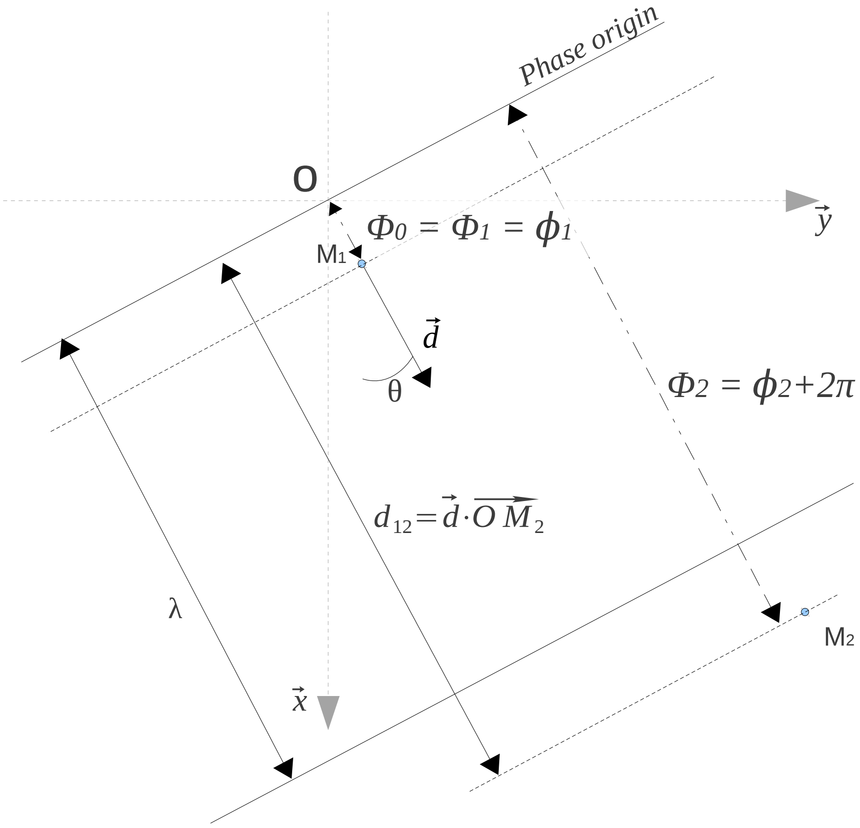

Figure 3.5: *schematic for the calculation of the* Φ_i

m_2 and m_3 are first estimated using the known target angle θ_t of the wave. As shown in Fig. 3.5, they are computed as the integral part of the ratio of the distance between the phase origin and the points $M_2(x_2, y_2)$ and $M_3(x_3, y_3)$ to the wave length λ. This ratio is computed through the scalar product between $\overrightarrow{d}$, the vector collinear to the wave direction of propagation and unit length, and the vectors $\overrightarrow{OM_2}$ and $\overrightarrow{OM_3}$ between the phase origin and the considered point:

$$m_i = \left\lfloor \frac{\overrightarrow{d} \cdot \overrightarrow{M_i'}}{\lambda} \right\rfloor \text{with} \quad \lambda = \frac{k}{2\pi} \tag{3.3}$$

$$m_i = \left\lfloor \frac{\overrightarrow{d} \cdot (\overrightarrow{OM_1} + \overrightarrow{M_i})}{\lambda} \right\rfloor \tag{3.4}$$

$$m_i = \left\lfloor \frac{\Phi_0}{2\pi} + \frac{x_i \cos\theta_t + y_i \sin\theta_t)}{\lambda} \right\rfloor \tag{3.5}$$

The wave angle θ is then estimated by relating the wave elevation observed at the probes η_o and the wave elevation η as predicted by the linear theory. a_o, ω_o and ϕ_{io} are the parameters computed by Fourier transform of the signal. Eq. 2.1 on page 10 is modified to take into account the absolute phase. The error term in η_o is neglected. The wave elevation at a point $M_i(x_i, y_i)$ of the study area can be written has:

$$\eta(x_i, y_i, t) = a\cos(-\omega t + k(x\cos\theta + y\sin\theta) + \Phi_0) \tag{3.6}$$

$$\eta_o(x_i, y_i, t) = a_o\cos(\omega_o t + \phi_{i,o}) = a_o\cos(-\omega_o t - \phi_{i,o}) \tag{3.7}$$

η and η_o are equalized at each probe. Using the absolute phases leads to:

$$\begin{cases} -\phi_{1,o} = \Phi_1 = \Phi_0 \\ -(2\pi m_2 + \phi_{2,o}) = \Phi_2 = k(x_2\cos\theta + y_2\sin\theta) + \Phi_0 \\ -(2\pi m_3 + \phi_{3,o}) = \Phi_3 = k(x_3\cos\theta + y_3\sin\theta) + \Phi_0 \end{cases} \tag{3.8}$$

$$\Leftrightarrow \begin{cases} \Phi_1 = \Phi_0 \\ \Phi_2 - \Phi_1 = k(x_2\cos\theta + y_2\sin\theta) \\ \Phi_3 - \Phi_1 = k(x_3\cos\theta + y_3\sin\theta) \end{cases} \tag{3.9}$$

$$\Leftrightarrow \begin{cases} \Phi_1 = \Phi_0 \\ \Phi_2 - \Phi_1 = k(x_2 \cos\theta + y_2 \sin\theta) \\ \cos\theta = \dfrac{\frac{\Phi_3 - \Phi_1}{k} - y_3 \sin\theta}{x_3} \end{cases} \tag{3.10}$$

$$\Leftrightarrow \begin{cases} \Phi_1 = \Phi_0 \\ \Phi_2 - \Phi_1 = k\left(x_2 \dfrac{\frac{\Phi_3 - \Phi_1}{k} - y_3 \sin\theta}{x_3} + y_2 \sin\theta\right) \\ \cos\theta = \dfrac{\frac{\Phi_3 - \Phi_1}{k} - y_3 \sin\theta}{x_3} \end{cases} \tag{3.11}$$

$$\Leftrightarrow \begin{cases} \Phi_1 = \Phi_0 \\ \dfrac{\Phi_2 - \Phi_1}{k} - \dfrac{x_2}{x_3}\dfrac{\Phi_3 - \Phi_1}{k} = \sin\theta\left(y_2 - y_3 \dfrac{x_2}{x_3}\right) \\ \cos\theta = \dfrac{\frac{\Phi_3 - \Phi_1}{k} - y_3 \sin\theta}{x_3} \end{cases} \tag{3.12}$$

$$\Leftrightarrow \begin{cases} \Phi_1 = \Phi_0 \\ \sin\theta = \dfrac{x_3(\Phi_2 - \Phi_1) - x_2(\Phi_3 - \Phi_1)}{k(y_2 x_3 - y_3 x_2)} \\ \cos\theta = \dfrac{\frac{\Phi_3 - \Phi_1}{k} - y_3 \sin\theta}{x_3} \end{cases} \tag{3.13}$$

$$\Leftrightarrow \begin{cases} \Phi_1 = \Phi_0 \\ \sin\theta = \dfrac{x_3(\Phi_2 - \Phi_1) - x_2(\Phi_3 - \Phi_1)}{k(y_2 x_3 - y_3 x_2)} \\ \cos\theta = \dfrac{\frac{\Phi_3 - \Phi_1}{k} - y_3 \frac{x_3(\Phi_2 - \Phi_1) - x_2(\Phi_3 - \Phi_1)}{k(y_2 x_3 - y_3 x_2)}}{x_3} \end{cases} \tag{3.14}$$

$$\Leftrightarrow \begin{cases} \Phi_1 = \Phi_0 \\ \sin\theta = \dfrac{x_3(\Phi_2 - \Phi_1) - x_2(\Phi_3 - \Phi_1)}{k(y_2 x_3 - y_3 x_2)} \\ \cos\theta = \dfrac{y_2(\Phi_3 - \Phi_1) - y_3(\Phi_2 - \Phi_1)}{k(y_2 x_3 - y_3 x_2)} \end{cases} \tag{3.15}$$

θ, the wave angle of propagation, is finally estimated in three different ways using the reverse trigonometric functions (Eq. 3.16). The precision associated with each solution is discussed in the next section.

$$\begin{cases} \theta_1 = \arccos(\cos\theta) \\ \theta_2 = \arcsin(\sin\theta) \\ \theta_3 = \dfrac{\theta_2 + \operatorname{sgn}(\theta_2)\cdot\theta_1}{2} \end{cases} \tag{3.16}$$

If the estimated angle differs radically from the target angle, the error probably comes from one of the m_i. An difference between θ_t and θ can lead to an error while estimating the m_i in critical cases when the absolute phase is close to a multiple of 2π. This is solved by iterating the method, changing one of the m_i at a time until the right set is found.

3.3.2.2 Precision and final probe layout

As stated in the previous section, the precision of the method must be below $\pm 1\,°$. The angle estimation is a function of the probe layout and the measured phases. Measurement errors in those quantities (dx, $d\phi$) generate errors in the wave angle estimation. The method's precision and the probe layout performances are investigated with a formal error estimations using the mathematics package *Maple^{TM}*.

Maple study For any quantity $f(x_1..x_n)$,, the error inherited from $x_1..x_n$ is computed as:

$$df = \sum_n \left|\frac{\partial f}{\partial x_i}\right| \cdot dx_i. \tag{3.17}$$

This formula is applied to θ_1, θ_2 and θ_3 of Eq. 3.16. The magnitude of the errors is assumed to be similar for each probe: $d\phi_1 = d\phi_2 = d\phi_3 = d\phi$, and $dx_1 = dy_1 = dx_2 = dy_2 = dx_3 = dy_3 = dx$. While no formal assessment of the errors are available, a reasonable estimation leads to $d\phi = 5\,°$ and $dx = 5\,\mathrm{mm}$.

The formal derivation of Eq. 3.17 for each θ is shown in Appendix A.2 on page 195. Each solution results in a different pattern of error in respect of the incident wave direction of propagation. A generic representation of those patterns is represented on Fig. 3.6.

From the patterns, the best solutions for each wave angle was extracted, and the performance of the probe layout is evaluated by computing the average error $\overline{\delta_\theta}$ and the its standard deviation σ_θ as a measure of the pattern curvature.

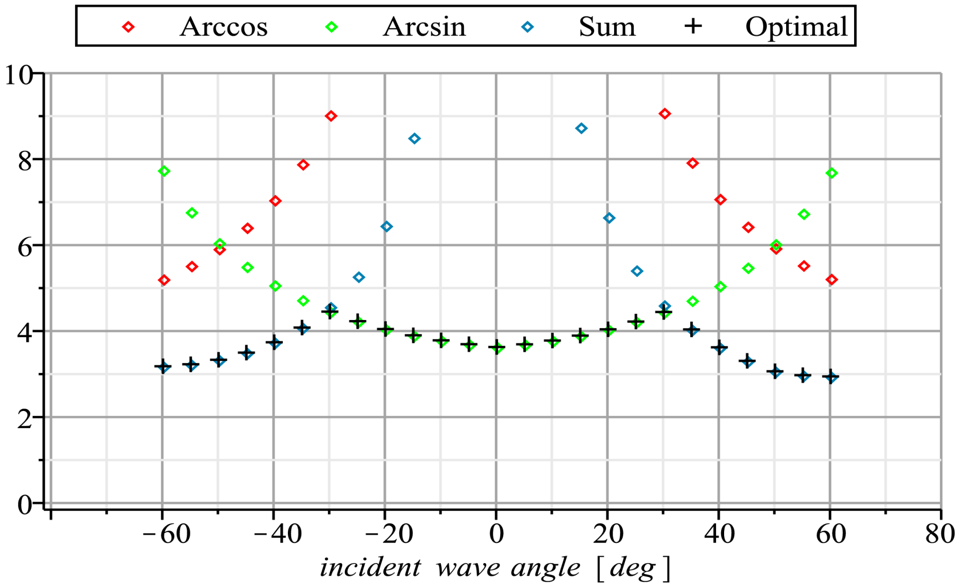

Figure 3.6: *Generic pattern of angle estimation error with the 3 possible solutions as a function of the incident angle. Depending the the incident angle, the solution which is least sensitive to the measurement errors is not always the same.*

For symmetry reasons, the probes are set in an isosceles triangle with the symmetry axis corresponding to the 0° direction of propagation. Using this, the probes layout is fully determined by the main angle α of the triangle and the length of the arms l. Fig. 3.7 shows the generic layout.

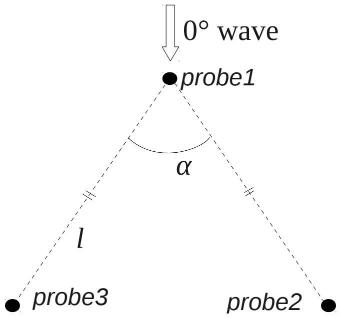

Figure 3.7: *Schematic of the probe layout*

The influence of l and α over the method performance is explored systematically with a full factorial design, using three values of α (60°, 90° and 120°) and three values of l ($0.9\,\mathrm{m}$, $1.1\,\mathrm{m}$ and $1.3\,\mathrm{m}$). The results are presented in Fig. 3.8.

The interaction plots in Fig. 3.8c shows that there is little or no interaction of the investigated parameter (lines are nearly parallel) so each of them can be optimised independently. Looking at Fig. 3.8b, a larger l generate both smaller $\overline{\delta_\theta}$ and smaller σ_θ. The largest l is consequently

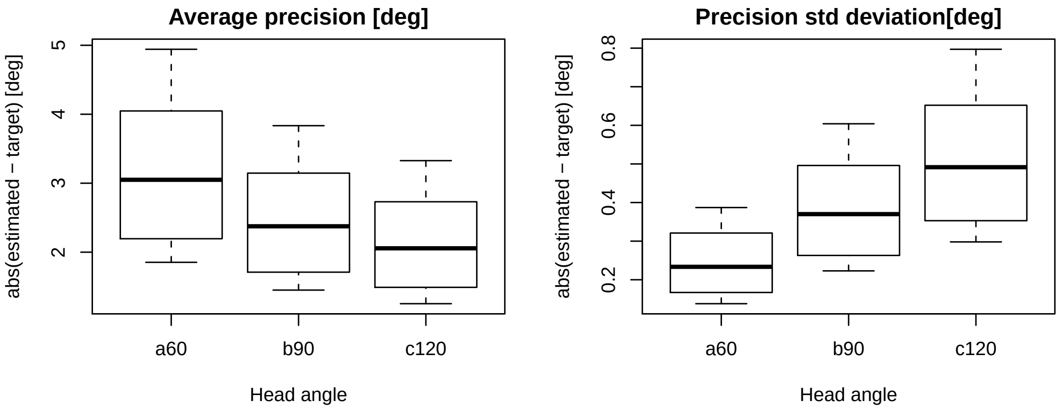

(a) angle box plot

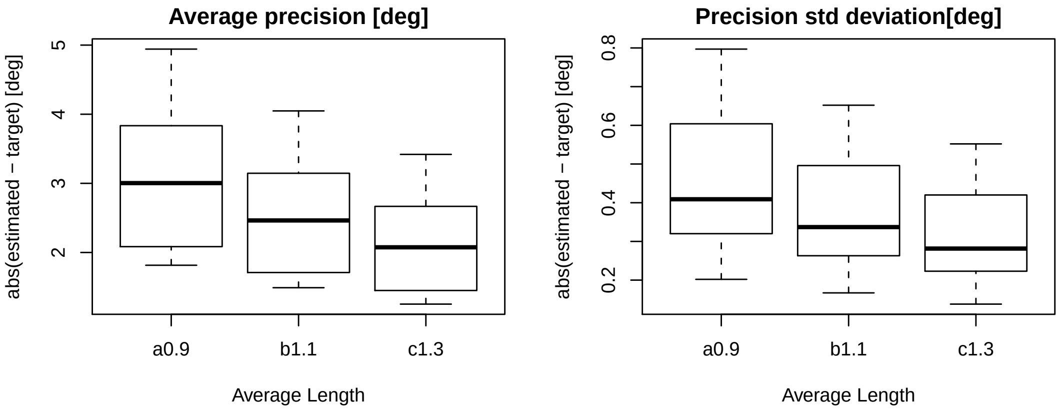

(b) side length box plot

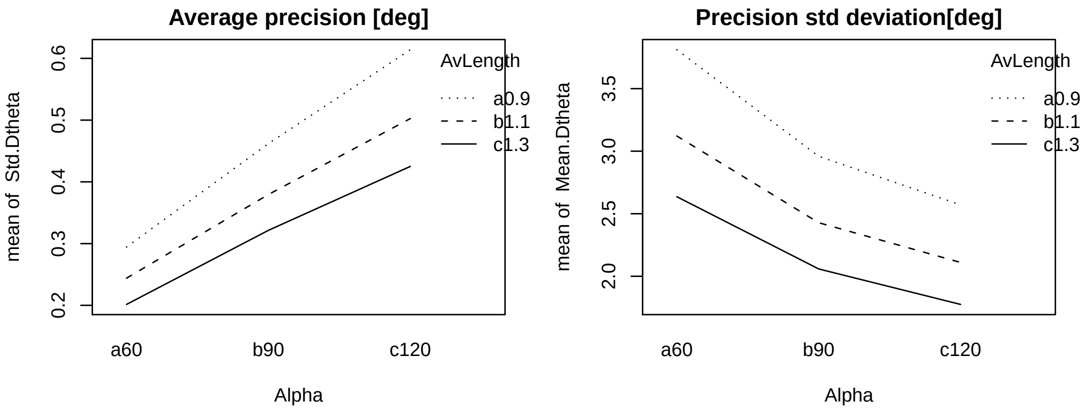

(c) interaction plot

Figure 3.8: *Graphic representation of the full factorial design experiment used to study the probe layout for the angle precision estimation study. A description of boxplots and the interaction.plots is provided in Appendix C on page 211.*

chosen for the optimal probe layout. One of the possible explanation is that as the ratio $\frac{dx}{l}$ get smaller, the method is less sensitive to the probe position error.

On the contrary, Fig. 3.8a shows that there is no optimal α for $\overline{\delta_\theta}$ and σ_θ together. The intermediate level (90 °) is chosen to get an acceptable performance in respect to both criteria.

Finally, taking into account the geometrical constraint of the tank, the final probe layout had a side length $l = 1.2\,\mathrm{m}$ and a head angle $\alpha = 90\,°$. Its error level was formally investigated and the results are shown in Fig. 3.9.

The method achieves a precision of $1.9\,°$ for a $0\,°$ wave direction up to $2.5\,°$ at $\pm 40\,°$ incident angle.

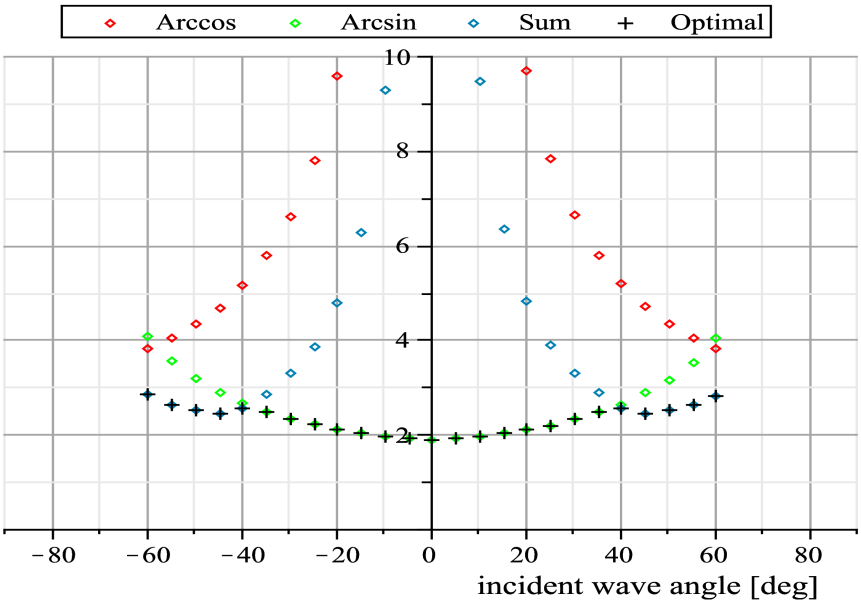

Figure 3.9: *Error level of the final probe layout as a function of the incident wave angle.*

Assessing the probe positions before every measurement is not practical. As a consequence, it is difficult to average out the resulting error by repeating measurements. However, the errors on phase measurements are due to the reflection pattern inside the tank, and some external random factor. Hence, it is possible to take them into account by repeating measurements. Studying the contribution of each factor to the total error bring a better understanding of the method's precision.

Fig. 3.10 shows the contribution of both sources of error for the [60 °; +60 °] range of incident wave angles. Error contribution from the probes' position are revealed to be small relatively to the contribution from the error in phase measurement (1/3 at $0\,°$) and never higher than $0.5\,°$. This part of the study shows that a minimum error of $0.5\,°$ have to be accepted from the error

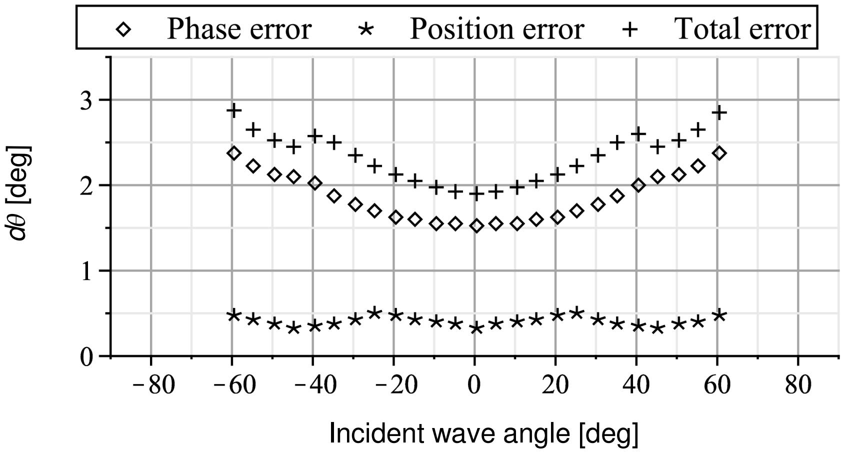

Figure 3.10: *Contribution of the phase error $d\phi$ and the position error dx to the total error of the method*

in probe positions measurement, and replications of each measurement will be used to bring down the total error below the target $1\,°$.

The error due to probe position are assumed to be independent of frame location. Measurements were made on two different days, each day in a different position inside the tank working area in order to allow averaging of the results and to provide some knowledge about the tank repeatability and spatial variability. Finally, to reduce the number of runs needed for position comparison, 6 probes were used forming two independent triangles. Fig. 3.11 shows the experimental set up in the tank during the experiments.

3.3.2.3 Measures, Results and Conclusions

For the first set of measurement, wave elevations for wave angles in the $[-30\,°; +30\,°]$ nominal range with $5\,°$ interval were recorded. 5 measurements were made for each angle, in a random order to minimise any variation due to daily variations. The results are presented in Fig. 3.12a. Results from each triangle are not in agreement for wave angles less than $\pm 25\,°$, probably due to reflection from the side glass. For wave angles equal to or higher than $30\,°$, results were not conclusive as the method fails to compute the angle in some cases. Otherwise, measurements were encouraging, with good consistency between each run, and variations around $1\,°$ between the triangles. This later value is slightly higher than the $0.5\,°$ maximum systematic error due to the error in probe position but less than the estimated error for the method.

The second set of measurements were made more than a month later. Waves with directions of

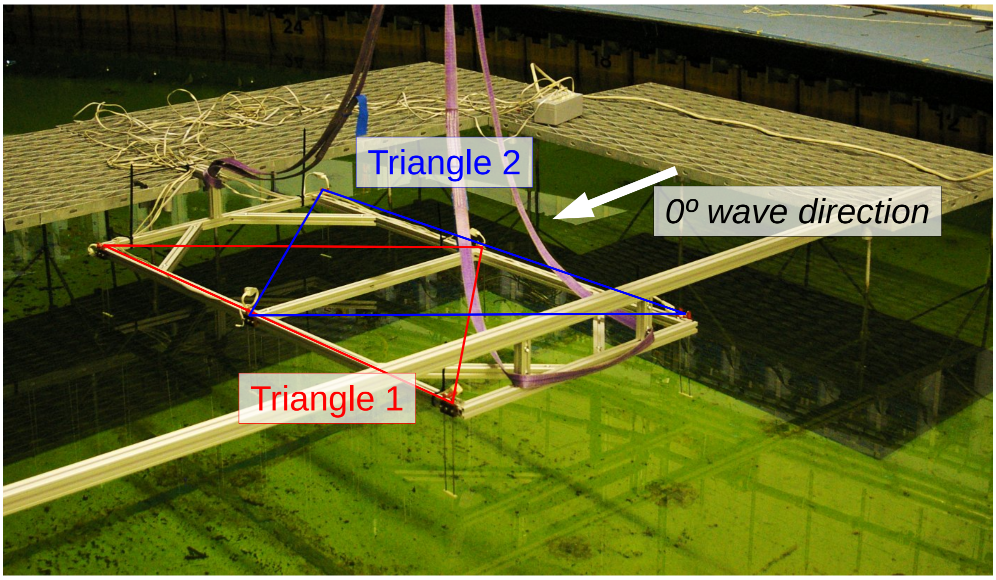

Figure 3.11: *Final probe layout as set in the Edinburgh Curved Tank during the measurements*

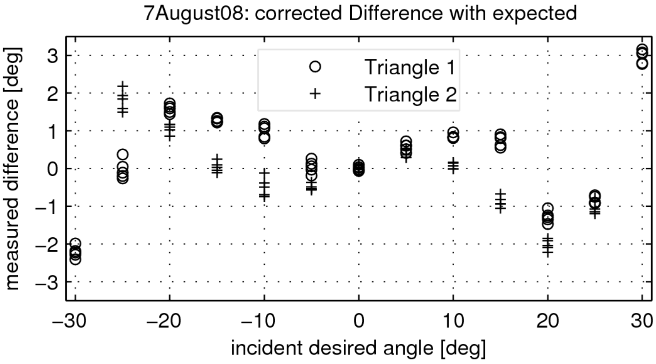

(a) Measure of wave direction of propagation - 1^{st} day.

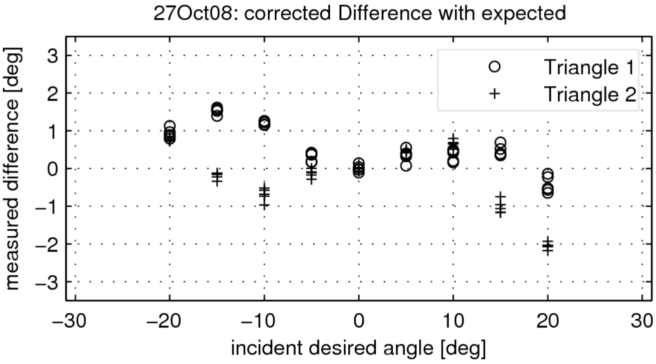

(b) Measure of wave direction of propagation - 2^{st} day.

Figure 3.12: *Measure of wave direction of propagation. The values represent the difference between the corrected measured angle and the target angle. The measures from each triangle are corrected separately by subtracting the average value measured for the* 0° *wave for each triangle.*

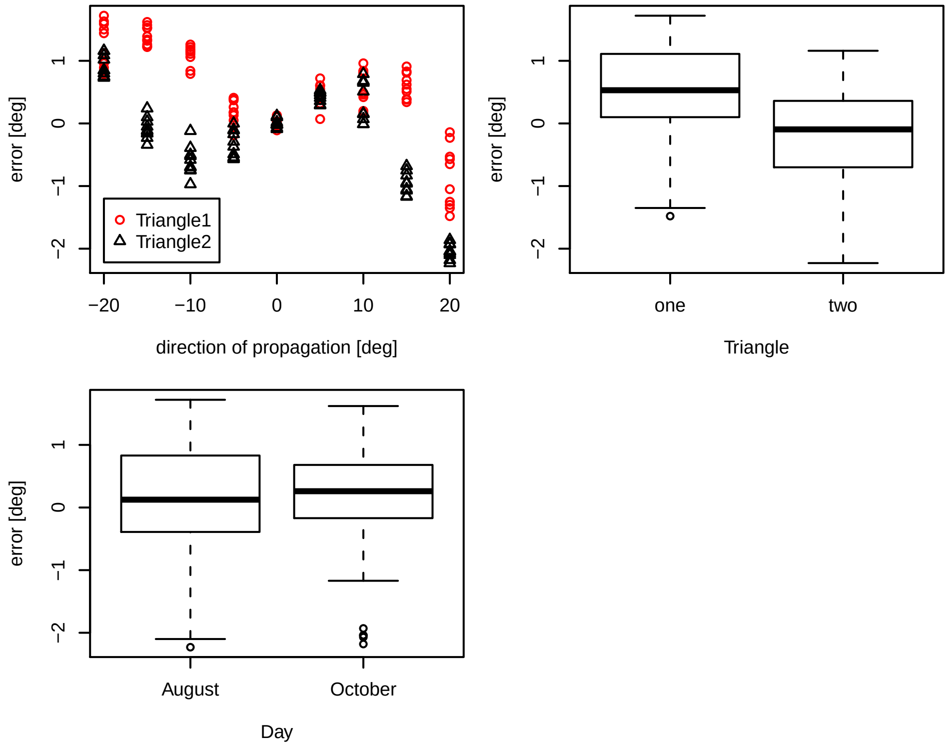

Figure 3.13: *Mean effect of factors Day, Triangle and Angle on the error in direction of propagation*

propagation in the [−20 ° ; +20 °] range were recorded. The measurement method is identical as the one used for the first test. The frame supporting the probes was located at a similar position, so some measured difference could come from the difference in triangle position. Measurements are shown in Fig. 3.12b.

Measurements from both days are summarized in Fig. 3.13 and Fig. 3.14. The first observations is that the factor *Day* do not seems to have any influence. The difference of the mean between each day is likely to be insignificant as shown by the box plot, and there is little interaction between *Day* and *Triangle* or *Day* and *Angle*. On the contrary, the factor *Triangle* is likely to have a significant effect on the observations, both as a difference in mean values of error (see box plot) and in interaction with the *Angle* continuous explanatory variable.

These results confirm the very good repeatability and low spatial variability of the tank (factor Day does not influence the results) already shown by previous studies such as Cruz *et al.* (2006). It can be concluded that the tank can generate regular waves with an error in their direction of propagation below ±1 ° in a range of ±20 ° around its main axis. Compared to the 2.5 ° angular gap needed between each wave front of the generated spectra, it means that the tank

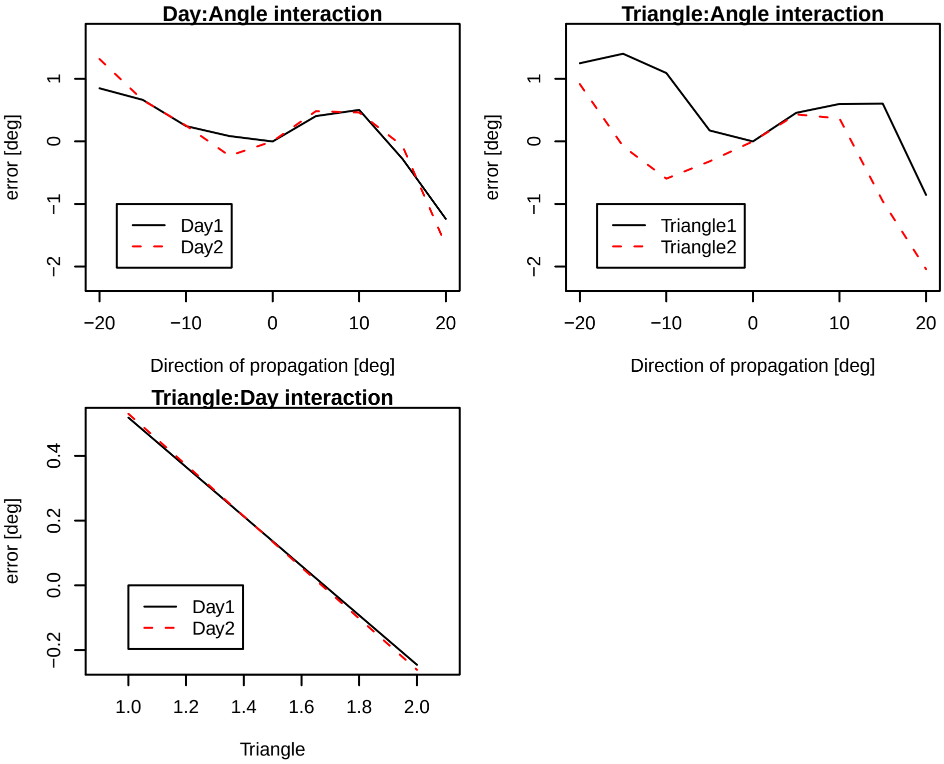

Figure 3.14: *Effect of interactions between factors Day, Triangle and Angle on the error in direction of propagation*

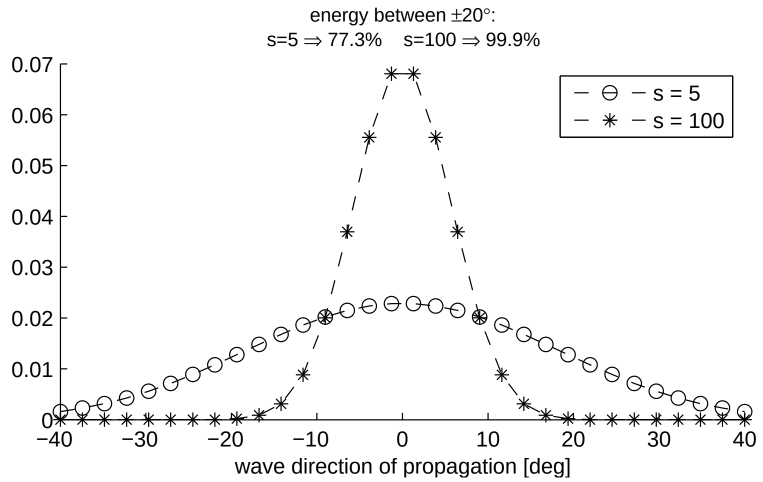

Figure 3.15: *Angular energy distribution of the 32 wave direction per frequency band.*

can successfully generate distinct wave fronts in this range. However, out of the $\pm 20\,^\circ$ range, the accuracy of the wave angle of propagation cannot be guaranteed due to wave diffraction ($\theta < -20\,^\circ$) or reflection on the glass ($\theta > 20\,^\circ$). This makes it desirable to generate spectra for which most of the energy will be contained in the $\pm 20\,^\circ$ range, thus limiting the type of spectra to rather narrow angular distributions.

For the remainder of this work, the 32 wave fronts per frequency band will be generated in the range $\pm 40\,^\circ$, which effectively constricts most of the energy to the desired range after applying a spreading function. Fig. 3.15 shows the energy repartition as a function of the direction of propagation for two different spreading parameters. The angular spreading function is $\cos^{2s}(\theta)$ and the curves are normalised so that their integral is equal to 1. Even in the widest spreading case used in this study (s=5), 77% of the energy is concentrated in the $\pm 20\,^\circ$ range.

3.3.3 Wave reflection assessment

Wave reflection in a multi-directional wave tank is a major concern with regard to the wave quality, and the methodology used to conduct tests. Large amounts of reflection induce significant reflected spectrum, which in turn affects the model performance in ways that can be difficult to quantify. Thus, a study of the reflections coefficient of the beaches that has been specially designed for the Edinburgh Curved Wave tank was conducted.

The work presented in this section was carried out jointly with Jorge Lucas and was published in a conference (Pascal *et al.*, 2009) during the course of this PhD. It included additional results to those presented in Lucas *et al.* (2008), focusing on the variation of the reflection coefficient with wave amplitude. The beach reflection coefficient is computed as $R_{coeff} = a_r/a_i$ with a_i the incident wave amplitude and a_r the reflected wave amplitude.

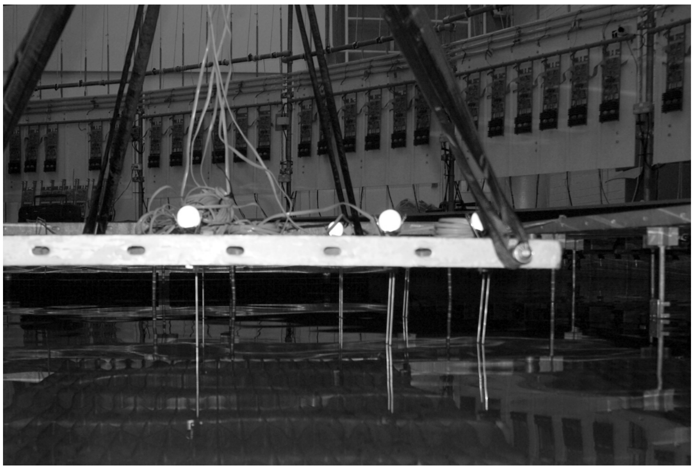

Figure 3.16: *Detail of the lines of probes used to measure the reflection coefficients. The Qualysis balls (optical tracking system) that can be observed on top of the platform were used to keep track of the probes' position. in this photo, the wave direction is parallel to the visible face of the suspended platform*

3.3.3.1 Layout and Precision

The reflection coefficients were calculated using the method introduced by Mansard & Funke (1980). It uses three measurements points in line with the wave direction of propagation and introduces a noise parameter in the computation process. For the best accuracy and in order to avoid specific singularities, the probes should respect the distances suggested by the authors:

$$x_{12} = \lambda/10 \quad \text{and} \quad \lambda/6 < x_{13} < \lambda/3 \tag{3.18}$$

with: $x_{13} \neq \lambda/5 \neq 3/10\lambda$

x_{ij} the distances between the i and j probes

λ: the incident wave length

The amplitudes of the incident and reflected waves are obtained by minimising the error through least squares. The method allows the measurement of the reflections coefficient for each frequency across a discrete frequency spectrum. Hence, simultaneous records of polychromatic waves can be taken to reduce the time of experiment for each amplitude setting.

The spacing between the probes is necessarily a compromise as the wave length λ is not constant. For this study, the probe distances were based on the 1 Hz wave as it is the design frequency of the tank. The corresponding $\lambda = 1.56\,\mathrm{m}$ gives an optimal $x_{12} = 156\,\mathrm{mm}$. Given the physical constraints of the experimental facility, the final set up is $x_{12} \approx 165\,\mathrm{mm}$ and $x_{13} \approx 510\,\mathrm{mm}$.

As remeasuring those distances before every test is not practical, any error in the probe relative distances induces an imprecision in the results that cannot be averaged out by repeating the measurement. The first step to mitigate this effect is to use two lines of probes closely located and with the same geometry. However, to evaluate the maximum possible imprecision, we tested the method's implementation in Matlab against virtual data, introducing random errors in the probe relative distances of up to $5\,\mathrm{mm}$. The virtual wave elevations were generated using linear theory, and they include a 10% R_{coeff}. The frequency range investigated corresponds to the working range of the tank. Fig. 3.17 presents the extreme boundaries of the induced error for both lines at each frequency for a 1000 runs.

The final probe spacing of both lines were measured and found to be very similar. Consequently, the imprecision level is assumed to be nearly equal. Fig. 3.17 shows that in the worth case, the error induced by errors on the probe relative distances is $<1.5\%$, with a tendency to larger errors at higher frequencies. Altogether, the error level was considered to be small and controlled. A $\pm 1\%$ error was therefore assumed for the results of these reflection experiments.

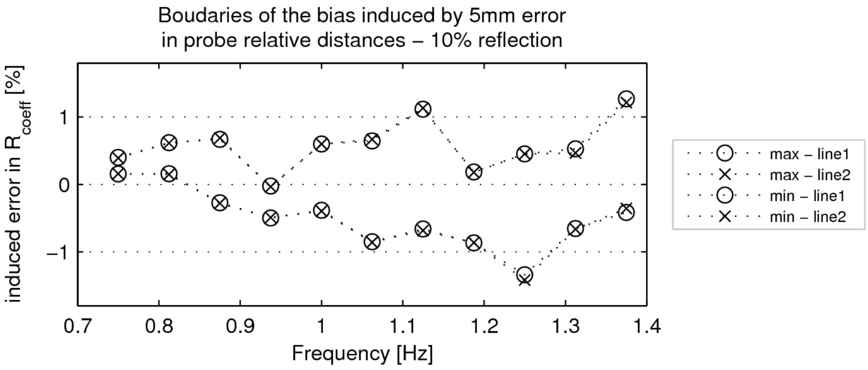

Figure 3.17: *Precision study of the reflection estimation study assuming a* $5\,\mathrm{mm}$ *error on probe position*

3.3.3.2 Measurements and Results

The Edinburgh Curved Wave tank is designed for optimal operation at $1\,\mathrm{Hz}$. We investigated the reflection coefficients for waves propagating normally to the beaches over a [0.75Hz ; 1.375Hz] range, with a $0.0625\,\mathrm{Hz}$ step.

Three polychromatic waves were used for these measurements. Each wave is composed of 11 components equally spaced in the considered frequency range. The amplitude of each component in a wave had a constant target value: $7.5\,\mathrm{mm}$ for the High wave, $6\,\mathrm{mm}$ for the Medium wave and $4\,\mathrm{mm}$ for the Low one.

Records of wave elevation from regular wave at $1\,\mathrm{Hz}$ were also done to provide a point of comparison and further validation of the method.

For both set of measurements each records lasted $16\,\mathrm{s}$, and two sets of three probes were used. Two extra set of five measurements of the High amplitude wave were recorded at two different positions to assess the tank spatial variability.

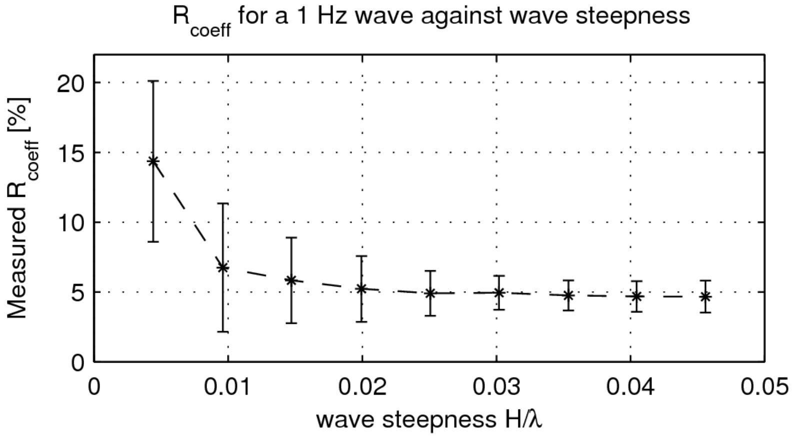

Figure 3.18: *Measures of the reflection coefficient against the wave steepness for a monochromatic* $1\,\mathrm{Hz}$ *wave.*

Monochromatic results Fig. 3.18 shows the measures of the reflection coefficient for the monochromatic $1\,\mathrm{Hz}$ wave. R_{coeff} for each amplitude is plotted against the wave steepness, H/λ with $H = 2a_i$, instead of the wave amplitude to allow easier comparison with earlier studies (Jefferys, 1987; Lin, 1999). The plotted values are the average of the results given by the two lines and the error bars are the standard error given by $s/\sqrt{n}$ (where s is the sample standard deviation and n the number of measurements).

As expected, the measured R_{coeff} is inversely related with the wave steepness, ranging from around 21% for $H/\lambda \approx 0.005$ (wave amplitude of $4\,\mathrm{mm}$) to less than 7.5% for $H/\lambda \geq 0.02$ (wave amplitudes higher than $20\,\mathrm{mm}$) tanking into account the measured error and the 1% error from probe position. The errors are also better controlled for higher wave steepness.

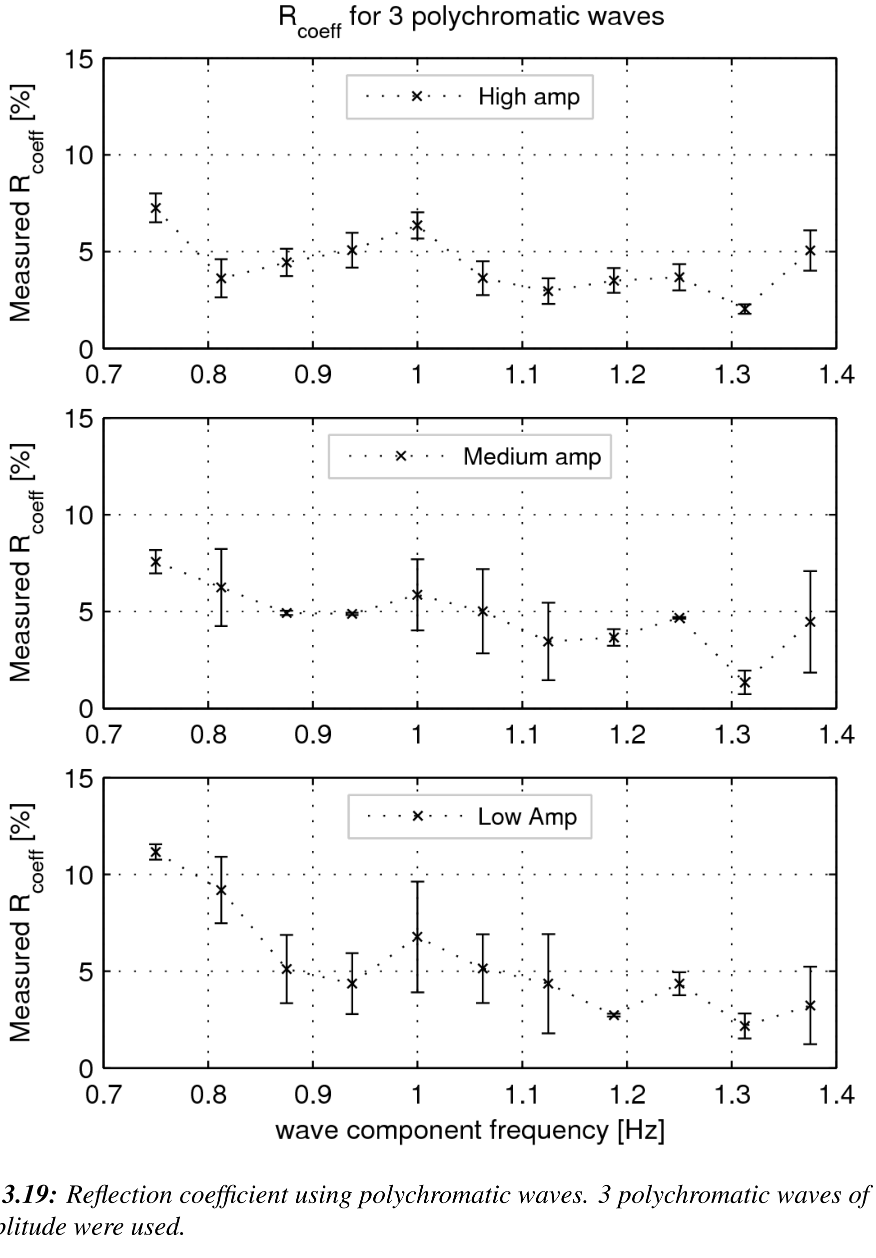

Figure 3.19: *Reflection coefficient using polychromatic waves. 3 polychromatic waves of different amplitude were used.*

Polychromatic results In Fig. 3.19, it is more difficult to distinguish a clear pattern. This figure represents the average R_{coeff} measured from the records of polychromatic waves. Each graph corresponds to one amplitude setting of the components, and generally smaller reflection coefficient are observed at higher frequencies. This could be explained by the higher wave steepness of the waves at higher frequencies. The error bars associated with the high amplitude records are also smaller than the ones associated with the medium and small amplitudes, which agrees with the results observed in Fig. 3.18. Taking into account those error bars, the results from both series of test appear to be in agreement at 1 Hz, even if the average values from the polychromatic wave records are constantly lower than the one from the monochromatic wave records.

To formalise the data analysis, an analysis of variance (ANOVA) has been done using R Development Core Team (2009) over a linear model fitted to the data (see Appendix A.3 on page 202). The factors used in this linear model are Position, Amplitude, Line and Frequency. Looking at the normality plot of residuals, the best model proved to be the one including no interaction between those factors.

The test showed that the null hypothesis (hypothesis that a particular factor does not affect the average results) can only be statistically rejected for the factor Frequency. This is encouraging as it validates the method robustness to the use of different lines of probes (no significant influence of the factor Line), and it (see Appendix A.3 on page 202)confirms the low spatial variability of the tank characteristics.

Interestingly, accepting the null hypothesis for the factor Amplitude also suggests that in the case of a polychromatic waves, the amplitude of each bin does not have an effect over the beach reflection coefficients.

Further testing by increasing the number of amplitudes tested are necessary to strengthen this observation. It might also be interesting to monitor a wave height parameter such as H_{m0} for the polychromatic waves as a more appropriate parameter than the wave height of each individual component.

Overall, the measured reflection coefficients are satisfactory with values generally well under 10%, which compare favourably with values published in previous studies.

Discussion on the results These measures of reflection coefficient in the Edinburgh Curved Wave tank show the good performances of the beaches with waves propagating normally to them. The agreement between results from monochromatic and polychromatic waves validate the utilisation of polychromatic waves, which is by nature less time consuming. From the monochromatic tests, recommendations of a minimum wave amplitude could be given in order to keep reflection under as acceptable level. In the case of the Edinburgh curved wave tank, a minimum of 7 mm wave amplitude (corresponding to a steepness of 0.01) should be used with a 1 Hz wave to keep the reflection coefficient under 10%.

On the contrary, in the case of polychromatic waves, the results suggest that the amplitude do not affect the R_{coeff}. This is a markedly different to what was commonly observed with monochromatic waves in this study and reported in other wave tanks (Jeffrey *et al.*, 1978). It is of particular interest while considering directional spectra as they are composed of a large number of wave components, resulting in relatively low amplitude for any single one. It would indeed be useful to experimentally confirm that the reflection characteristics of the Edinburgh Curved Wave Tank do not degrade while using directional spectra.

3.3.4 The tank calibration

Calibrating a multi-directional tank is a difficult task. While it is rather simple to separate the incident and reflected spectra using mono-directional waves, this is a much more complex tasks when using directional waves. Some effort are currently done at the university (Reich, 2010) to adapt a method described by Masterton & Swan (2008) which aim to avoid the reflection issues with the use of focused waves. However, this work is not yet advanced enough to produce the required calibration. Instead, the current calibration is based on the work of Lucas *et al.* (2008), which only concerns the calibration of the waves propagation at 0 °. During the work, the gains associated to the waves around 1 Hz were substantially diminished and the gains associated to waves propagating in other direction were untouched.

It went unnoticed at the time but the wave measurement in the first phase (see Section 6.2 on page 126) revealed that this modification introduced some unbalance between the gains around the 1 Hz, 0 ° waves. This appears in the spectral estimation as a recognizable dip in the shape of the spectra around this area. The effect is best seen when observing the average spectra over the 5 runs of a wave as shown in Fig. 3.20. Instead of the long ridge along the 0 ° line that should be observed, one can observe a small recession specially around 1 Hz.

This effect was only realised after the waves for the first phase of the tests had been generated, recorded and used with the different devices. It would have been to time consuming to redo all those tests using the old calibration file that does not exhibit this unbalance. This should results in spectra broader than expected but as spectral shape is not crucial to this project, it was thought to be acceptable. However, as the second phase of testing was not already started, the calibration file was reverted to the previous tank transfer function for those tests.

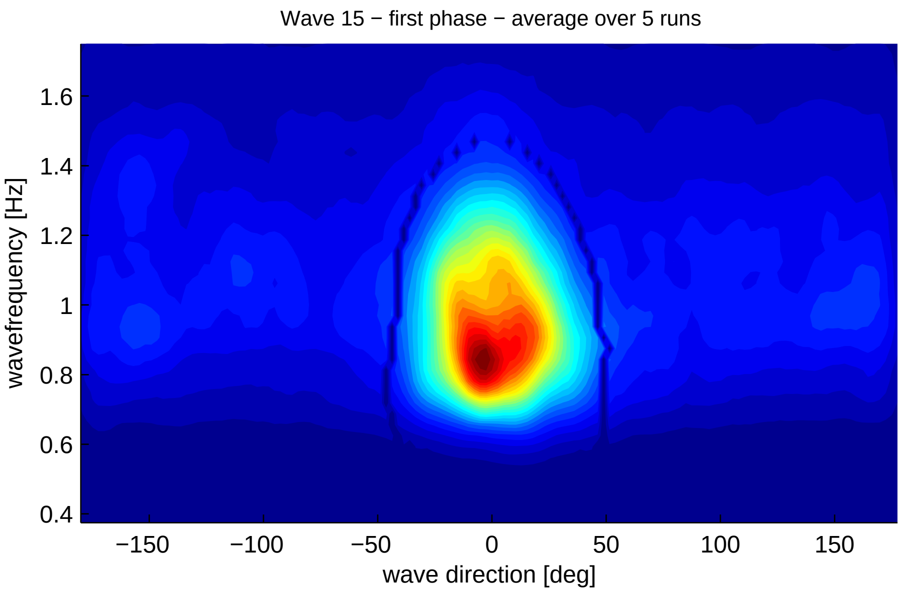

Figure 3.20: Average spectral estimate over the 5 runs of wave 15 of the first phase tests.

Chapter 4
Measuring the directional spectrum

4.1 Introduction

Good knowledge of the incident wave field is an important aspect of tank testing. This aspect is emphasised in the context of this work where many sea state parameters influence will be jointly evaluated. Indeed, in order to successfully separate the effect of each parameter and get statistically significant estimates, good quality input is an absolute requirement. As a new wave generation method is used (see Section 3.2.2) and directional wave measurement never took place in the Edinburgh Curved tank previously, it was crucial to properly implement a measurement method adapted to the directional sea state generated in the tank. Tests also require the estimation of parameters relative not only to the complete directional spectrum, but relative to different wave systems composing a directional spectrum. An wave system isolation technique was required to allows those measures.

As a new probe layout had to be set up in the tank and the available measurement techniques were investigated, it appeared they were all designed for ocean waves and were not using the discrete nature of deterministic waves to optimise the estimates. Hence, the Maximum Likelihood Method and one of its derivative, the Modified Maximum Likelihood Method that should be able to take into account the wave reflection from the beach, was adapted to the generated waves.

A method to isolate the wave systems was implemented to satisfy the testing requirement. It is inspired from previous methods but differs significantly in its philosophy: it does not part the full spectrum into wave systems but tries to isolate the identified wave systems from the non significant part of the spectrum. This minimises the influence of the spectrum estimate background noise in the estimated spectral parameters.

In this chapter, the underlying theory beyond the MLM is presented, and the developed method including the wave system isolation is thoroughly tested with virtual wave elevations to assess its performances. For this purpose, virtual data are generated in order to replicate the conditions in the wave tank. An in depth description of the virtual data is given. Sources of degradation of the method resolution such as wave reflection and uncertainty in the wave front direction of propagation are taken into account. Considerations into array design are developed, and the sensitivity of the method towards to sources of errors is assessed using the final probe payout arrangement, . Finally, some element of comparison between the implemented method and the industry standard are given in order to judge the benefits of adapting the method to the nature of the waves.

4.2 Theory of the MMLM

4.2.1 Introduction on directional spectrum estimation

Several methods to estimate the directional wave spectrum have been published and referenced since the interest about this topic raised in the sixties. Benoit *et al.* (1997) gave a good overview of the different generic methods available to analyse ocean waves. Of these methods, the Maximum Entropy Method (MEM), the Maximum Likelyhood Method (MLM) and the Bayesian method and their derivatives are the most generic as they do not assume the shape of the directional spectrum prior of the measurement. They are consequently the only methods adapted to measure spectra made of several wave systems.

In the later years, a new generation of tools based on wavelet transform and not on Fourier Transform as been introduced. They are mainly used for 2D spectral analysis (Liu, 2000; Massel, 2001) but it has been extended to directional spectra measurement using techniques of Phase-Path Difference method (Donelan *et al.*, 1996; Fernandes *et al.*, 2000). The principal advantage of wavelet measurement is that time variation of the spectra can be studied as well as the frequency and directionality dimension, allowing a better understanding of non-stationary processes such as time varying sea-state. However, Donelan *et al.* (1996) specify that the extra information on non-stationarity is gained at the expense of frequency resolution of the final directional spectra. As waves in the tank, contrary to ocean waves, are stationary (see Section 4.2.4.1) there will be no theoretical gain in using a wavelet based method, but only loss in the frequency resolution. This latest point is critical with regard to the objective of the directional spectral measurement for this study where the method must be able to identify multi peak spectra.

4.2.2 Focusing on the MLM and its derivative, the MMLM

Much less work has been published on methods adapted to wave field that cannot be considered random. The methods mentioned above are based on the assumptions of random phase between the wave components. Close to a reflector or in a wave tank, a minimal level of wave reflection cannot be avoided as shown by numerous such as Ouellet & Datta (1986); Lucas *et al.* (2008); Pascal *et al.* (2009). This induces phase locked components described by Miles & Funke (1989) in the wave field that affect the precision of the generic methods as discussed by Huntley & Davidson (1998). In order to retain method accuracy in such cases, the Modified Maximum Likelihood Method (MMLM) was presented by Isobe & Kondo (1984). Further works on this method were published by Davidson *et al.* (1998) and Huntley & Davidson (1998). Taking into account the geometric characteristics of the tank (see Section 4.2.5) and the level of reflection, a version of the MMLM adapted to the wave characteristics was identified as the best way to accurately measure directional wave spectra in the Edinburgh Curved Wave tank. The following section describes the fundamental theoretical concepts associated with the MLM methods and its derivatives.

4.2.3 Maximum Likelihood method: general concepts

The mathematical steps of the Maximum Likelihood method applied to gravity waves can be followed in details in Davis & Regier (1977). It is useful to remind here the main concepts and equations of the development.

4.2.3.1 spectrum to cross-spectrum relation

The generic MLM is based on the established relation under the linear wave theory between the *wavenumber-frequency* spectrum $S(\overrightarrow{k},\omega)$ and the spatially lagged cross-spectrum $\Phi(\overrightarrow{\zeta},\omega)$:

$$\Phi(\overrightarrow{\zeta},\omega) = \int S(\overrightarrow{k},\omega)\cdot e^{i\overrightarrow{k}\cdot\overrightarrow{\zeta}}\cdot d\overrightarrow{k} \tag{4.1}$$

$$\text{or}\qquad S(\overrightarrow{k},\omega) = \frac{1}{(2\pi)^2}\int \Phi(\overrightarrow{\zeta},\omega)\cdot e^{-i\overrightarrow{k}\cdot\overrightarrow{\zeta}}\cdot d\overrightarrow{\zeta} \tag{4.2}$$

4.2.3.2 Data adaptive spectral estimators

Eq. 4.2 gives the relation between the directional spectrum and the cross-spectrum. However, by sampling the wave elevation in a limited number of points, one can only get an estimate of the spatially legged cross-spectrum $\hat{\Phi}_{nm}(\omega)$ between each pair of points (A_n, A_m) , leading only to an estimate of the *wavenumber-frequency* spectrum $\hat{S}(\overrightarrow{k}, \omega)$. From Eq. 4.2, the spectrum estimate is naturally searched as a linear combination of the estimated cross-spectra:

$$\hat{S}(\overrightarrow{k}, \omega) = \sum_{n,m} \alpha_{nm}(\overrightarrow{k}, \omega) \cdot \hat{\Phi}_{nm}(\omega) \tag{4.3}$$

Assuming that the cross-spectra estimates are unbiased, Eq. 4.3 is used to derive a fundamental relation between the estimate of the spectral estimate and the spectrum itself:

$$\begin{gathered} < \hat{S}(\overrightarrow{k}, \omega) >= \int S(\overrightarrow{k}', \omega) \cdot W(\overrightarrow{k}, \overrightarrow{k}') \cdot d\overrightarrow{k}' \\ \text{with} \quad W(\overrightarrow{k}, \overrightarrow{k}') = \sum_{n,m} \alpha_{nm}(\overrightarrow{k}, \omega) \cdot e^{i\overrightarrow{k}'(\overrightarrow{A_n} - \overrightarrow{A_m})} \end{gathered} \tag{4.4}$$

The function $W(\overrightarrow{k}, \overrightarrow{k}')$ is the wavenumber window function. Determining $W(\overrightarrow{k}, \overrightarrow{k}')$ at each wave number is equivalent to know what are the α_{nm} coefficients and the spectral estimates $\hat{S}(\overrightarrow{k}, \omega)$.

Then, a second assumption is done to characterise the window function: the α_{mn} coefficients are factorisable as $\alpha_{mn} = \underline{\gamma}_n \cdot \underline{\gamma}_m^*$, which in turn forces the window function to be always positive.

At this point of the development, Davis & Regier propose two different options for computing the spectral estimates from the cross-spectrum. The first one called the Maximum Likelihood Estimator (MLE) follows the path set by Capon *et al.* (1967), and the second is referred to as the Data-Adaptive Spectral Estimator (DASE).

The MLE imposes the constraint

$$W(\overrightarrow{k}, \overrightarrow{k}) = 1 \tag{4.5}$$

physically meaning that in the absence of noise and considering a wave field composed of a single wave train propagating with a wavenumber vector $\overrightarrow{k_0}$, the spectral estimate is directly linked to the signal variance $E(\overrightarrow{k_0})$ in the form:

$$\begin{cases} \hat{S}(\overrightarrow{k},\omega) = \dfrac{E(\overrightarrow{k_0})}{d\overrightarrow{k}\cdot d\omega} \quad \text{for } \overrightarrow{k} = \overrightarrow{k_0} \\ \hat{S}(\overrightarrow{k},\omega) = 0 \quad \forall \overrightarrow{k} \neq \overrightarrow{k_0}. \end{cases} \tag{4.6}$$

In the case of a complex sea state, the directional spectrum estimator for each discrete wavenumber is computed by considering the observed wave field as a simple wave train of the same wavenumber plus noise corresponding to all the other single wave train forming the sea state. This finally come down to minimise the convolution between the window function and the remnant noise spectrum, which is equivalent to minimising the variance estimator $\hat{E}(\overrightarrow{k_0})$ itself. This leads to compute the variance estimator as a function of the cross-spectrum:

$$\hat{E}(\overrightarrow{k_0}) = \left[\sum_n \sum_m \hat{\Phi}_{nm}(\omega)^{-1} \cdot e^{i\overrightarrow{k_0}\left(\overrightarrow{A_n}-\overrightarrow{A_m}\right)}\right]^{-1} \tag{4.7}$$

and the spectral estimates $\hat{S}(\overrightarrow{k},\omega)$ are directly computed from this using Eq. 4.6.

The DASE imposes a looser constraint on the window function:

$$\int_{\overrightarrow{k'}} W(\overrightarrow{k'},\overrightarrow{k}) \cdot d\overrightarrow{k'} = 1. \tag{4.8}$$

This physically mean that the DASE estimator does not compute $\hat{S}(\overrightarrow{k_0},\omega)$ only from the signal variance at $\overrightarrow{k} = \overrightarrow{k_0}$, but as a weighted average of the contribution from wavenumbers in the vicinity of $\overrightarrow{k} = \overrightarrow{k_0}$. This is arguably a much more elegant solution when it comes to compute discrete estimates of a process inherently continuous.

From this point, Davis & Regier show that the problem can be reduced to an eigenvalue problem where the optimal estimate is:

$$\hat{S}(\overrightarrow{k_0},\omega) = \lambda_{max}^{-1} \tag{4.9}$$

with λ_{max}^{-1} the maximum eigenvalue of:

$$\Lambda_{mn} = \sum_l \hat{\Phi}_{nl}(\omega)^{-1} \cdot T_{lm} \tag{4.10}$$

$$\text{and} \quad T_{lm} = |\overrightarrow{k_0}| \int_{\theta_0-\frac{\Delta}{2}}^{\theta_0+\frac{\Delta}{2}} e^{i\overrightarrow{k}\left(\overrightarrow{A_l}-\overrightarrow{A_m}\right)} \cdot d\theta \tag{4.11}$$

The parameter Δ as to be adjusted depending on the settings of the analysis.

Davis & Regier compare both estimators, estimating that the DASE is better adapted to the continuous nature of $S(\overrightarrow{k},\omega)$. However, in the case deterministic waves generated from a discrete spectrum, the MLE estimator should be the method of choice. The MLM uses directly the MLE, and this will be the method benchmark for the rest of this thesis.

4.2.3.3 Modification done by the MMLM to the MLM

? consider the case of a wave field affected by the presence of a reflector made of an infinite rectilinear wall of reflective coefficient $R_{coeff}(\overrightarrow{k},\omega)$. The authors propose to treat the problem of phase locking due to the reflected wave components by considering the observed wave field as the sum of an incident *wavenumber-frequency* spectrum $S^I(\overrightarrow{k},\omega)$ and a reflected *wavenumber-frequency* spectrum $S^R(\overrightarrow{k},\omega)$ linked by the relation:

$$S^R(\overrightarrow{k},\omega) = R_{coeff}(\overrightarrow{k},\omega)^2 \cdot S^I(\overrightarrow{k},\omega) \tag{4.12}$$

For the rest of this section, the notation $R_{coeff}(\overrightarrow{k},\omega)$ is simplified to $r(\overrightarrow{k},\omega)$ to clarify the equations.

This results in a modified formulation of the relation between the total directional spectrum $S(\overrightarrow{k},\omega) = S^I(\overrightarrow{k},\omega) + S^R(\overrightarrow{k},\omega)$ and the observed cross spectrum $\Phi_{nm}(\omega)$ between two points A and B presented in Eq. 4.13.

$$\begin{aligned}\Phi_{AB}(\omega) = \int_{\overrightarrow{k}} &\left[e^{i\overrightarrow{k}\cdot\overrightarrow{A}} + r(\overrightarrow{k},\omega)e^{ik\cdot\overrightarrow{A^R}}\right] \\ &\qquad\qquad \left[e^{-i\overrightarrow{k}\cdot\overrightarrow{B}} + r(\overrightarrow{k},\omega)e^{-ik\cdot\overrightarrow{B^R}}\right] \cdot S(\overrightarrow{k},\omega)\cdot d\overrightarrow{k}\end{aligned} \tag{4.13}$$

A^R and B^R are the reflected point of A and B relative to the reflector. It is interesting to rewrite Eq. 4.13 in the discrete case. The links between the cross-spectra as a function of the frequency f and the discrete *frequency-direction* energy spectrum is presented in Eq. 4.14:

$$\boxed{\underline{\Phi}_{AB,f_p} = \sum_{q=1}^{N} \frac{\Delta\theta}{2} \cdot S^I_{f_p,\theta_q} \cdot \left(e^{-i\overrightarrow{k_{pq}}\cdot\overrightarrow{A}} + r_{pq}e^{-i\overrightarrow{k_{pq}}\cdot\overrightarrow{A^R}}\right)\left(e^{i\overrightarrow{k_{pq}}\cdot\overrightarrow{B}} + r_{pq}e^{i\overrightarrow{k_{pq}}\cdot\overrightarrow{B^R}}\right)} \tag{4.14}$$

The complete derivation of Eq. 4.14 is presented in Appendix B on page 204.

? presented a derivation similar to the one used for the DASE to estimate the reflection coefficient $\hat{r}(\overrightarrow{k},\omega)$. However, the presented estimators for $\hat{S}(\overrightarrow{k},\omega)$ are derived for the MLE estimator. For the pairs $(\overrightarrow{k},\omega)$ such as $\hat{r}(\overrightarrow{k},\omega) \leq 0$ the normal MLE estimator is used to get $\hat{S}(\overrightarrow{k},\omega)$, and a correction term is added for the cases where $\hat{r}(\overrightarrow{k},\omega) > 0$.

4.2.3.4 Spectrum estimate normalisation

With the MLM, a normalisation of the discrete estimated spectra $\hat{S}_{\overrightarrow{k},\omega}$ is necessary. This is done by insuring that, at each w, $\hat{S}_{\omega}$ is equal to the mean of the auto-spectra observed at each from for this frequency. Through this thesis, it is implemented as shown in Eq. 4.15:

$$normed\, \hat{S}_{\overrightarrow{k},\omega} = \hat{S}_{\overrightarrow{k},\omega} \cdot \frac{\overline{\hat{\Phi}_{nm}(\omega)}}{\sum_{\overrightarrow{k}} \hat{S}_{\overrightarrow{k},\omega} \cdot \Delta\theta} \tag{4.15}$$

The normalisation method was modified specifically for the MMLM by **?**. While it was used successfully during previous study such as Davidson *et al.* (1998), the method presented did not yield satisfactory results during the course of the project. It is thought that it is due to the low level of reflection present in the virtual data and in the tank, and also due to the discrete nature of the directional spectra used to generate the wave elevation. Consequently, Eq. 4.15 as been used for both the MLM and the MMLM results exhibited in this study.

4.2.4 Adaptation to wave characteristics

4.2.4.1 discrete frequency spectrum

There are fundamental differences between working in a controlled environment such as the Edinburgh Curved Wave Tank and working with ocean data. Specifically, when using pseudo-deterministic wave generation methods (see Section 3.2.2 on page 22), the wave elevation time series at a wave probe is periodic (excluding noise), whereas wave elevation records from ocean waves are stochastic. Hence, it is possible to use discrete Fourier transform on the wave elevation records without pre-processing the wave elevation records (windowing, added zeros) and get exact values for each bin instead of an estimation.

Two directional spectra can be defined following the generation technique described in Section 3.2.2: the general discrete spectrum (frequency resolution ΔF) for which the variance of each set (ω_p, θ_q) is noted $S_{\overrightarrow{k},\theta}$, and an expended spectrum, with a frequency resolution Δf, for which the variance of each set $(\omega_{p'}, \theta_q)$ is noted $s_{\overrightarrow{k'},\theta}$.

The method used to estimate the general spectrum from wave records taking into account the nature of the wave generated is:

- Compute the relevant cross spectra from the wave elevation records at the Δf frequency resolution.
- Using this cross-spectra, derive the spectral estimates $\hat{s}_{\overrightarrow{k'},\theta}$, either from the MLM or the MMLM.
- Normalize the spectrum as described in Section 4.2.3.4
- Compute the measured the $\hat{S}_{\overrightarrow{k},\theta}$ for each frequency band and direction of propagation from the spectral estimate $\hat{s}_{\overrightarrow{k'},\theta}$ of the expanded spectrum as:

$$\hat{S}_{\overrightarrow{k},\theta} = \sum_{f'=u}^{u+32} \hat{s}_{\overrightarrow{k'},\theta}, \qquad \text{with } u = f * 32 \tag{4.16}$$

4.2.4.2 discrete angular spectrum

In the case of the MLM and its derivatives, the spectral estimator $\hat{S}(\overrightarrow{k},\omega)$ is computed by minimising the convolution between a window function $W(\overrightarrow{k},\overrightarrow{k}')$ and $S(\overrightarrow{k},\omega)$, leading to a narrow window function around $\overrightarrow{k}$. For waves generated from a discrete spectrum, this is most effective if the wavenumbers at which the spectrum is estimated corresponds to wavenumbers used to generate the waves. As the spectrum is already estimated at frequencies matching the one used for the spectrum generation, this is enforced by using the same angular discretization for the wave generation and the spectral analysis.
However, this prior knowledge of the generated wave is only applicable if the wave direction of propagation generated are precise and accurate. In the present case, the angle between each wave component is $\approx 3°$, implying that any error in the direction of propagation $> 1°$ is significant. The results presented in Section 3.3.2 on page 28 show that the tank only comply with this requirement in the $[-20°; +20°]$ range. The spectra used for this thesis are generated in the $[-40°; +40°]$ range. This means that one cannot assumes that the recommendation given above can be enforced over the full spectra, but it can be noted that the most energetic wave components of the spectra are comprised in the $[-20°; +20°]$ range (77% in the worst case of this thesis, see Section 3.3.2 on page 28).

Finally, the same angular discretization are used both for wave generation and spectral estimation, acknowledging its limitation. As a consequence, a random error is introduced in the

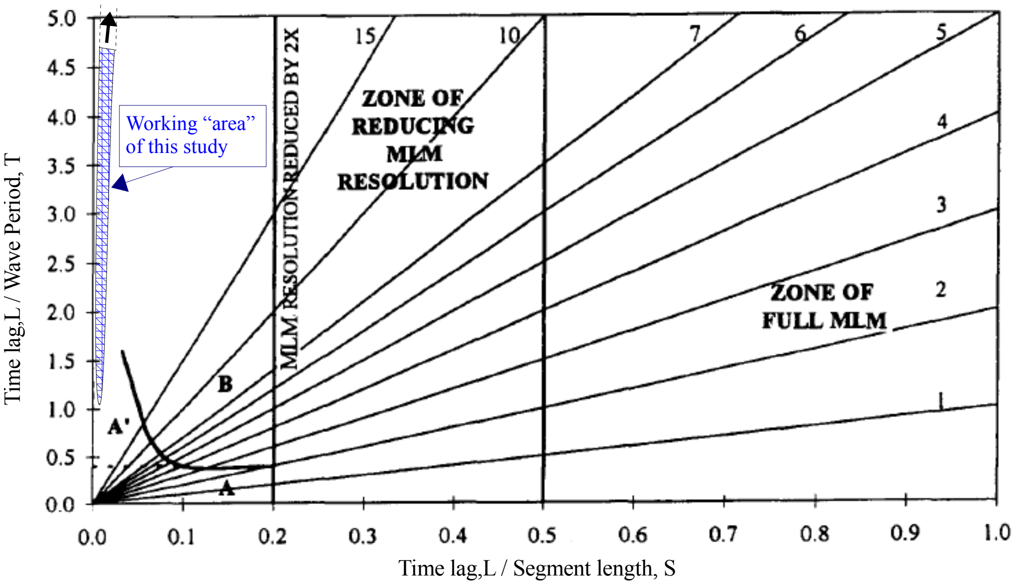

Figure 4.1: *Graphs from Huntley & Davidson (1998) representing the zone in which phase locked or non phase locked method should be applied. The hatched zone shows the working zone of this study.*

simulated data used to evaluate the method performance in order to take into account the possible deterioration of the method performances due to this imprecision in the physical wave generation (see Section 4.3.2.2).

4.2.5 Adaptation of the spectral estimation method to the tank geometry

Huntley & Davidson (1998) studied the conditions requiring the use of a method taking into account phase locked waves close to a reflector. These conditions include the probes' distance to the reflector, the wave length and the length of the recorded time series. The authors' conclusions are summarized in Fig. 4.1. In some cases (zone *A* and B), methods taking into account phase locking are required as others are loosing accuracy due to the reflection, but they will produce spurious peaks (zone *B*). Those spurious peaks are the consequences of emphasised uncorrelated noise close to theoretical nodes between incident and reflected waves. Their location in the directional spectrum plan (f, θ) depends upon probe position. Estimating the spectrum from several elevation gauges leads to several spurious peak patterns. This can be seen as an advantage as they are averaging themselves out but they are also more difficult to filter!

Fig. 4.1 superimposes the working zone of this study and the zones presented by Huntley & Davidson (1998). It shows that, considering the tank geometry and the spectrum character-

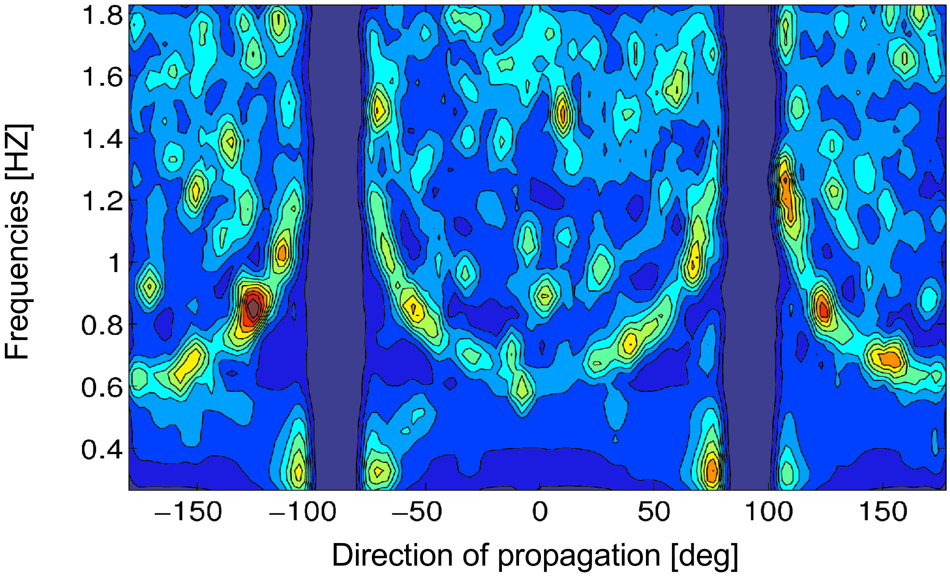

Figure 4.2: *Estimated spectrum from virtual data made of random noise. A pattern of spurious peaks can be clearly seen. It corresponds to the pattern shape described by Huntley & Davidson (1998). By generating a large number of those spectrum and averaging them, a mask can be constructed to help filter those peaks in the estimated spectrum*

istics, experiments will be done exactly in the zone where phase locked methods such as the MMLM are theoretically required but with the generation of spurious peaks.

4.2.5.1 Creating a mask to selectively remove unwanted spurious peaks

It is necessary to remove those artefacts from the estimated spectrum (see Fig. 4.2) prior to computing any spectral statistics. This is done by applying a mask to the estimated spectrum, preserving the real estimates but selectively erasing the spurious peaks where no energy should be found. As the spurious peaks are linked to the probe positions, a specific mask has to be created for every probe array considered. A theoretical approach has been first intended to generate a suitable mask. The position of the spurious peaks can be predicted by searching the pairs (f,θ) that corresponds to destructive interactions as a function of each probe position. The results from each probes are them summed up together and normalized to form the mask. However, this approach prove to be unsuccessful. Instead, an empirical method is used, based on the observed spurious peak generated while measuring virtual data made only of uncorrelated noise (see Fig. 4.2)

An appropriate mask for each array is constructed by running the method several times with virtual data made only of uncorrelated noise, then averaging and normalising (value in $[0;1]$)

the estimated spectra. Fig. 4.3 shows that 30 iteration is a reasonable number as the difference between the mask after 30 and 200 iterations is $< 3\%$ and only marginal gains can be expected. The estimated spectrum used during these runs are previously corrected by forcing the energy in the $\pm[85\,^{\circ}, 95\,^{\circ}]$ to 0, as very high level of spurious peaks are constantly observed in those direction and that no energy is expected in the virtual or tank data for those direction of propagation.

A mask with clear zones where spurious peaks should occur is obtained, but the main part of the mask shows values around 0.5. If applied directly, this mask will erase half of the energy in large parts of the estimated spectrum. Hence, the mask median value is then computed, all the values inferior to it are set as equal to the median, the median value is subtracted to the new mask and finally the mask is re-normalised.

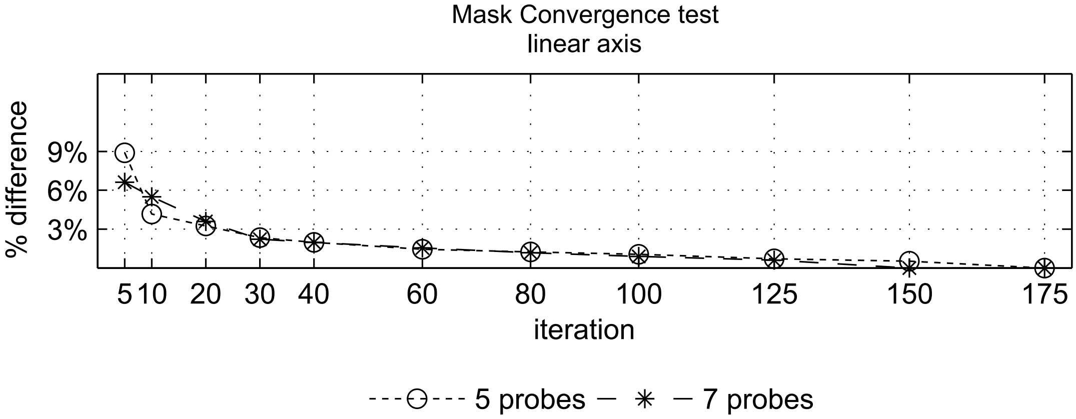

Figure 4.3: *Convergence study of the mask building process.*

Fortunately, the zones with the highest values are located in the $\pm[35°, 85°]$ range of direction of propagation, which means that the centre zones $[-35°, +35°]$, where most of the energy is generated, should be unaffected. This is further insured by not applying the mask in this central range.

The mask is then inverted so that the value at the predicted peaks is 0. The spurious peaks in an estimated spectrum are then filtered by multiplying, value by value, the spectrum and the mask. The corrected spectrum is then normalised to ensure that m_0 remains constant. An example of the final mask is shown in Fig. 4.4.

Fig. 4.5 demonstrates the need of filtering the MMLM estimates. In Fig. 4.5a, zones with unexpected level of energy are presents at $\theta \approx \pm 110\,^{\circ}$ and a peak of energy is visible at $\theta \approx -60\,^{\circ}$. The mask as efficiently reduced them in Fig. 4.5b.

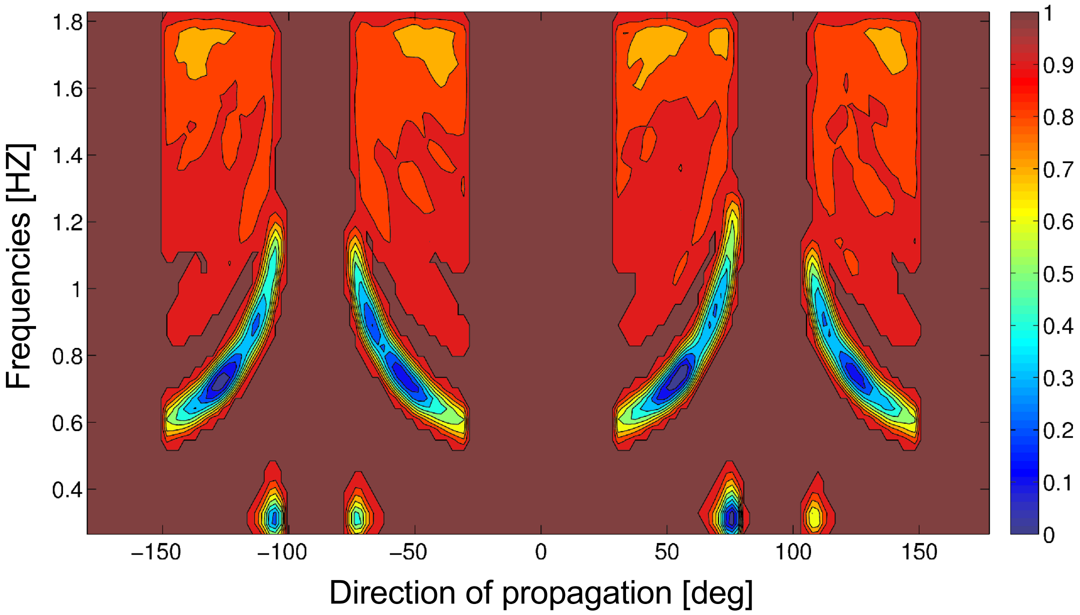

Figure 4.4: *example of masks used to insure that spurious peaks due to the tank geometry and the MMLM method are filtered before isolating the wave systems.*

This masking technique proved to be efficient in filtering the spurious peaks. However, it introduces directional sensitivity to the estimation method. The filtered MMLM can only be used for incident wave spectra which mean direction is close to $0\,^{\circ}$. While this is not a constraint in the Edinburgh Curved Wave tank, it represents a limitation.

After generating the mask and realising that most of the peaks are located in the $\pm[40\,^{\circ};80\,^{\circ}]$ and that very little energy energy would be located in those zones, it was arguable to limit the spectral estimate to the center of the plan (f,θ) and discard the estimate with direction of propagation above $\pm 40\,^{\circ}$. However, it was decided otherwise as this would have prevented any chances of observing the reflected spectrum and it might have affected the estimates with the broadest spectra used.

4.3 Virtual Data Characteristics

Virtual data are generated to explore the performance of the implemented MLM and MMLM. The virtual wave elevation are based on Eq. 3.1 on page 22 and extra terms are added to simulate the condition in a real wave tank. The following subsections describe and discuss those added components components.

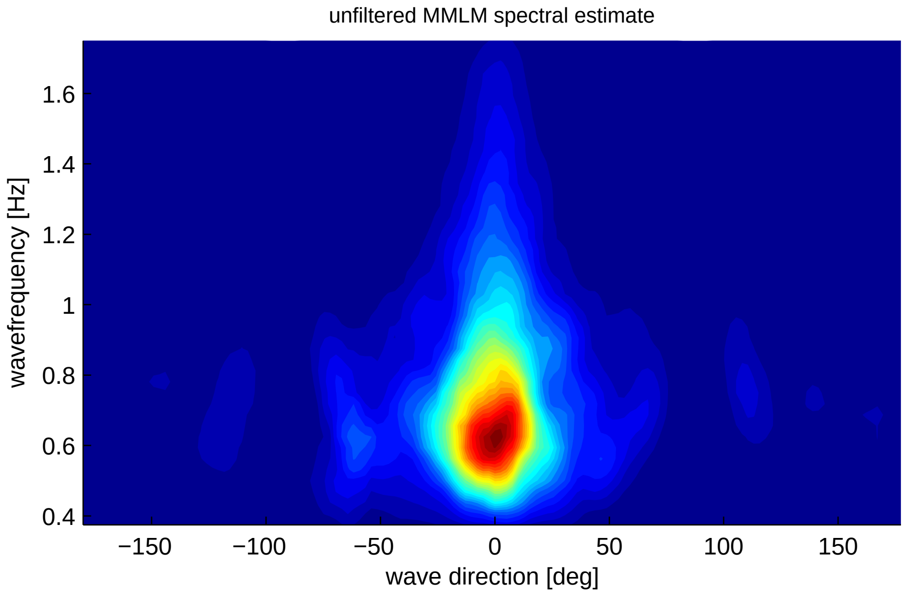

(a) unfiltered MMLM estimate

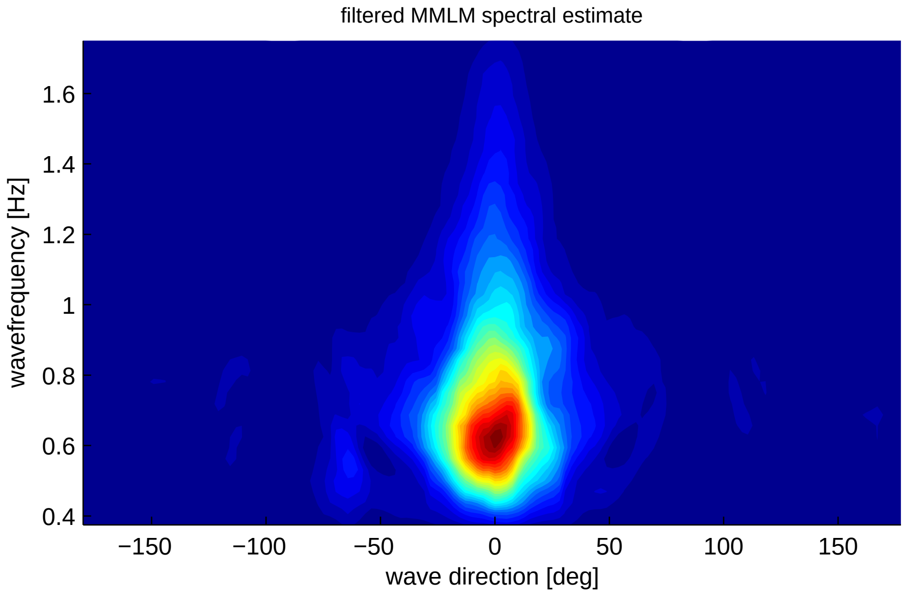

(b) filtered MMLM estimate

Figure 4.5: *Visualisation of the mask's effect on a estimated spectrum by the MMLM. a) the mask was not applied. b) the mask was applied to the estimated spectrum*

4.3.1 Wave Complexity

While the generation of waves in the tank assumes linear theory, the real waves propagating in it are cnoidal (Korteweg & De Vries, 1895). For the virtual wave elevation to be a step closer to the real waves, second order Stokes waves are considered (Stokes, 1847; Craik, 2005). The bound harmonic are added to the expression of the wave elevation at each frequency:

$$\frac{k_p \cdot a^2_{f_p,\theta_p}}{2} \cdot cos\left(2(-2\pi f_p t + \overrightarrow{k_p}' \cdot \overrightarrow{A}) + \varphi_p\right) \tag{4.17}$$

Adding the bound harmonic is a simple process. However, adding the ”free” harmonics generated at the paddle due to their shape is not trivial, and is out of scope of this study. The effect of evanescent waves created at the wave paddle is also neglected as the closet wave probes is located $> 2\,\mathrm{m}$ away from the paddle. According to Dean & Dalrymple (1991), 95% of these should have been dissipated.

4.3.2 Wave parameters precision

4.3.2.1 Frequency

The Edinburgh Curved Wave tank proved itself to be very accurate while generating waves at a specific frequency. A frequency analysis of regular wave demonstrate it as no spillage is observed if the adequate record duration is used.

In the case of mixed seas, errors in the wave component frequencies could also be the results of wave interactions. As shown in Section 3.3.1 on page 27, the phenomenon is limited and then can be neglected. Hence, no errors is introduced in the wave components nominal frequencies.

4.3.2.2 Direction of propagation

As specified in Section 4.2.4.2, errors in wave direction of propagation cannot be neglected while considering the waves in the tank. To simulate this inaccuracy in the virtual wave data, an uniformly distributed error of up to $1\,^\circ$ is introduced for each wave component of the spectrum.

4.3.3 Probe position error

The location of the wave elevation measurements is an input to the estimation methods. These positions are subject to two sources of error: the position of each probe relative to the others, and the precise point of measurement while knowing the probe position itself. The cumulated maximum error related to the gauge set up in the tank is estimated to $\pm 2.5\,\mathrm{mm}$. Hence, the virtual wave elevation at a point A is actually generated at a point $A'(x_{A'}, y_{A'})$ such as:

$$x_{A'} = x_A + \varepsilon_1 \tag{4.18}$$

$$y_{A'} = y_A + \varepsilon_2 \tag{4.19}$$

$$\text{with } (\varepsilon_1, \varepsilon_2) \in \pm \frac{10^{-3}}{\sqrt{2}} [-2.5; 2.5]^2 \tag{4.20}$$

4.3.4 Simulating reflections

The use of the MMLM is mainly motivated by the need of taking into account the unavoidable reflection in the tank. Including their effect into the virtual data is consequently necessary to evaluate the advantage of using the MMLM instead of the traditional MLM. For this, a constant reflection coefficient R_{coeff} for all wave components is assumed. The effect of wave reflection is then added to the virtual elevation at a point M by adding the contribution of each wave component at the point M_r symmetric of M relative to the reflector.

The effect of reflection on the glass in the tank is not taken into account as only waves with a direction of propagation $> 30\,°$ will affect the area of measurement. While generating mixed seas in the tank, those wave components are carrying low amount of energy (mean direction of $0\,°$) and so they can be neglected.

4.3.5 Probe and Uncorrelated noise

No measurement can be free of noise. To simulate the effect of noise due to probes, real signal from the probes at water at rest is added to the final virtual wave elevation to account for the inherent noise due to our measuring system. A different record is added to each wave elevation to avoid correlation between them.

Finally, random noise is added to the signal. Its level is assessed by comparing directly tank measurement data with virtual wave elevation with different level of noise. From Fig. 4.6, it can clearly be seen that the plots with $1\,\mathrm{mm}$ of added random noise is more irregular than the

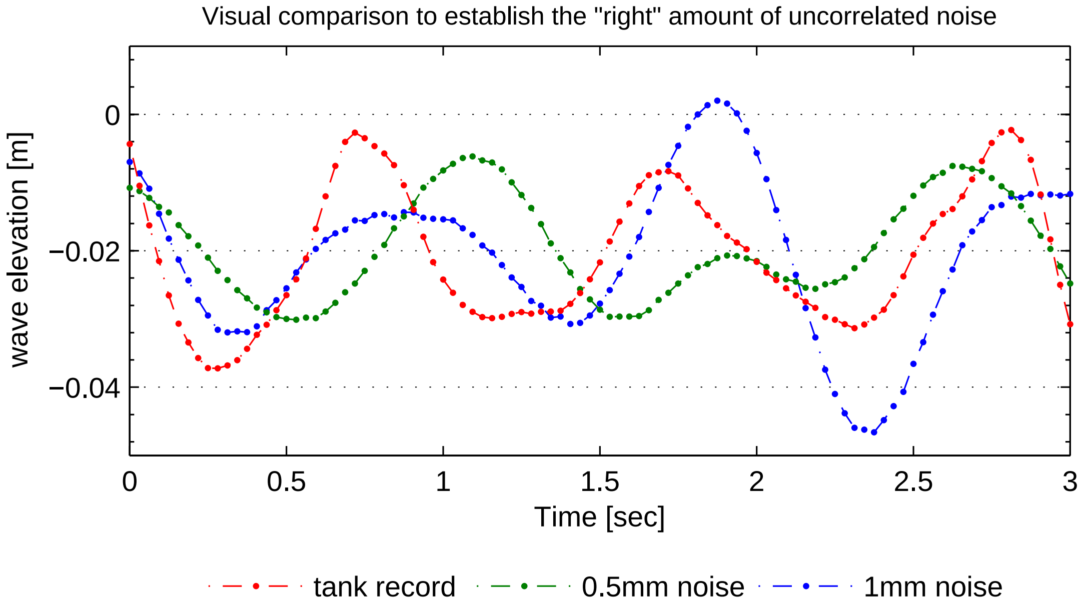

.

Figure 4.6: *This plots shows 2 virtual time series with respectively* $0.5\,\mathrm{mm}$ *and* $1\,\mathrm{mm}$ *of random noise added to the computed wave elevation and a real record from the Edinburgh Curved Wave Tank*

tank record (particularly obvious on the crest around $1\,\mathrm{s}$).

The plot of the signal with $0.5\,\mathrm{mm}$ of noise is more similar to the tank record. Hence, this is the level of noise selected to generate the virtual wave elevation.

4.3.6 Final expression

The final expression for the virtual wave elevation is:

$$\begin{aligned}\eta(A,t) = \sum_{p=1}^{M\cdot N} \Big[& a_{f_p,\theta_p} \cdot cos(-2\pi f_p t + \overrightarrow{k_p}' \cdot \overrightarrow{A'} + \varphi_p) \\ & + \frac{k_p \cdot a^2_{f_p,\theta_p}}{2} \cdot cos\left(2(-2\pi f_p t + \overrightarrow{k_p}' \cdot \overrightarrow{A'}) + \varphi_p\right) \\ & + R_{coeff} \cdot a_{f_p,\theta_p} \cdot cos(-2\pi f_p t + \overrightarrow{k_p}' \cdot \overrightarrow{A'_r} + \varphi_p)\Big] \\ & + P_n(t) + 2(rand - 0.5) \cdot 0.5 \cdot 10^{-3}\end{aligned} \tag{4.21}$$

with:

$$\overrightarrow{k_p}' = k_p \left(\cos\theta_p' \overrightarrow{x} + \sin\theta_p' \overrightarrow{x} \right)$$

$$\theta_p' = \theta_p + 2(rand_{pq} - 0.5)\frac{\pi}{180}, \quad rand_{pq} \in [0:1] \text{ randomly chosen}$$

$$P_n(t) = \text{measured probe noise at water at rest.}$$

4.4 Spectrum analysis method

4.4.1 on the smoothing of the spectral estimates

Despite the adaptation to the wave characteristics and tank geometry, the directional spectrum estimated by the MMLM is not usable as such. Instead of the expected smooth surface, the raw estimation is very irregular, with sharp energy peaks located in the high energy density portion of the spectrum as shown in Fig. 4.7.

Smoothing the obtained result is necessary, but does not come without issues! The principal of them is to "over-smooth" the estimated spectrum to the point that real features of the spectrum can be lost. This is especially visible in double peak spectra for which the "distance" in the

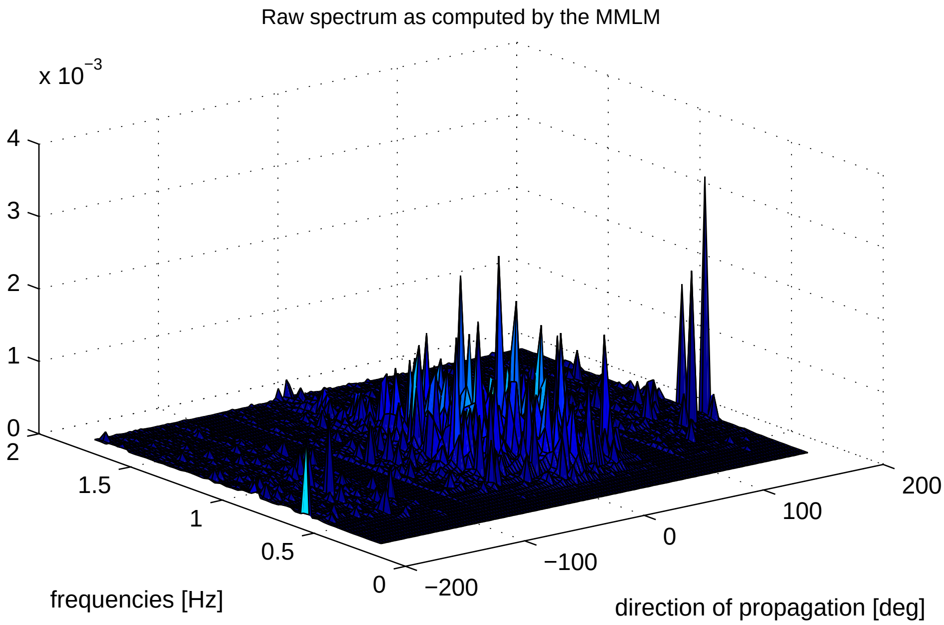

Figure 4.7: Directional spectrum as computed the MMLM before smoothing. Peaks of high energy are principally located in the high energy part of the spectrum

(f, θ) plan between each peak is small. Smoothing also tends to spread the estimated spectrum, which emphasises a problem seemingly inherent to the methods based on the Maximum Likelihood approach and reported by Ilic *et al.* (2000).

In this work, reasonably smoothed spectrum estimate are necessary, especially for the peak isolation technique (see Section 4.4.2). A weighted square window W_S was used, and was parametrised by the side length in cells l_s (an odd number) and a steepness coefficient C_s.

The smoothing window W_S was built as a $l_s * l_s$ matrix as shown in Eq. 4.22 to Eq. 4.24:

$$W_{S,ij} = \frac{C_s\left(\frac{l-1}{2} - d\right) + 1}{\sum\limits_{l_s}\sum\limits_{l_s} Wij} \tag{4.22}$$

$$\text{width} \quad d = \left|i - \frac{l_s - 1}{2}\right| + \left|j - \frac{l_s - 1}{2}\right|$$

Two constraints are imposed on W_S. They limit the range of values that C_s can take as a function of l_s. Eq. 4.24 shows the resulting limits:

$$\begin{cases} \forall (i,j) \in \left[\frac{-l_s}{2}, \frac{l_s}{2}\right]^2 & W_{S,ij} \geq 0 \\ \forall (i,j) \quad d = \frac{l_S}{2} & W_{S,ij} = 1 \end{cases} \tag{4.23}$$

$$\Rightarrow C_s \leq \frac{2}{l_s - 1} \tag{4.24}$$

Then, for each set (f, θ) of the discrete spectrum $S_{f,\theta}$, a sub-spectrum S_{sub} is extracted as a $l_s * l_s$ matrix with $S_{sub}(i,j) = S_{f_{p-l_s+i}, \theta_{q-l_s+j}}$ and the smooth spectral estimate $S_{smooth}(p,q)$ is computed as

$$S_{smooth}(p,q) = \sum_{i=1}^{l_s}\sum_{j=1}^{l_s} W_{S,ij} \cdot S_{sub}(i,j) \tag{4.25}$$

Increasing the value of l_s broadens the base of the smoothing window, while increasing C_s gives more emphasis to the centre of the window.

It is essential to select good values for l_s and C_s. In the case of double peak spectra, using a too broad window mixes the information relative to each peak. Excessive smoothing also tends to broaden the estimated spectrum. Fig. 4.8 presents the evolution of the angular spreading parameter Θ_S (see Section 2.3.3) computed from a directional spectrum estimate which has been smoothed using different value for l_s and C_s. It clearly shows that increasing smoothing (increasing l or decreasing C_s) leads to a larger estimate of Θ_S.

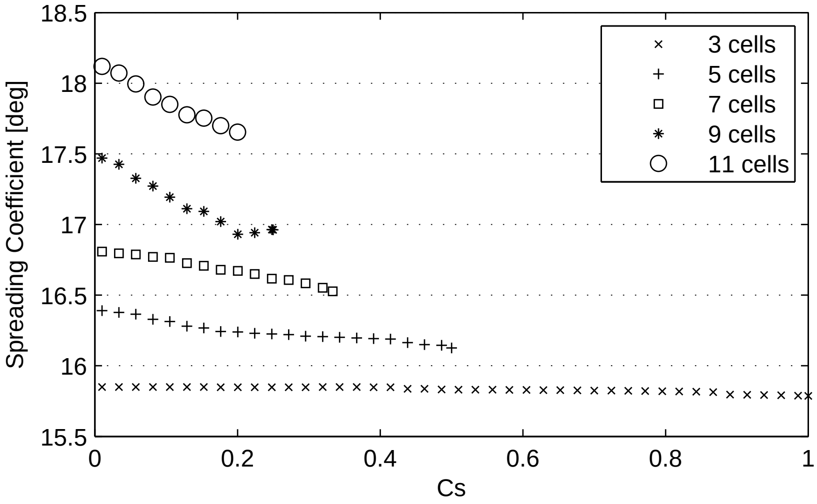

Figure 4.8: *Angular spreading parameter Θ_S as a function of C_s for different smoothing window bases l_s.*

In the presented results, $l_s = 7$ and C_s is set at its maximum possible, i.e $C_s = \frac{1}{3}$. This was observed visually to be the minimum smoothing possible in order to get regular enough spectral estimates.

4.4.2 Peak isolation

Some spectral parameters are more easily computed only for a wave system rather than for the whole spectrum. It can be of interest to compute parameters such as the energy period, and angular and frequency spreading characteristics for such segments of the spectrum.

A method to isolate wave systems in a directional wave spectrum has been developed. Its goal is mainly to isolate wave systems so that noise in the spectrum estimates does not affect the computation of the parameters associated to the wave system. This is different than the approach taken by Kerbiriou *et al.* (2007b), where the entire spectrum is partitioned into wave systems but the procedure used is also inspired by Hanson & Phillips (2001).

A general flow chart of the method is given in Fig. 4.9 for the bi-modal spectrum case. The following section describes the progression of the developed algorithm for bi-modal spectra. The algorithm is simplified as needed for uni-modal spectra. The maxima of the spectrum are first identified using a method fitting quadratic surfaces over portion of the spectrum. A maxima is detected where both square coefficient are negatives. The two significant maxima are then

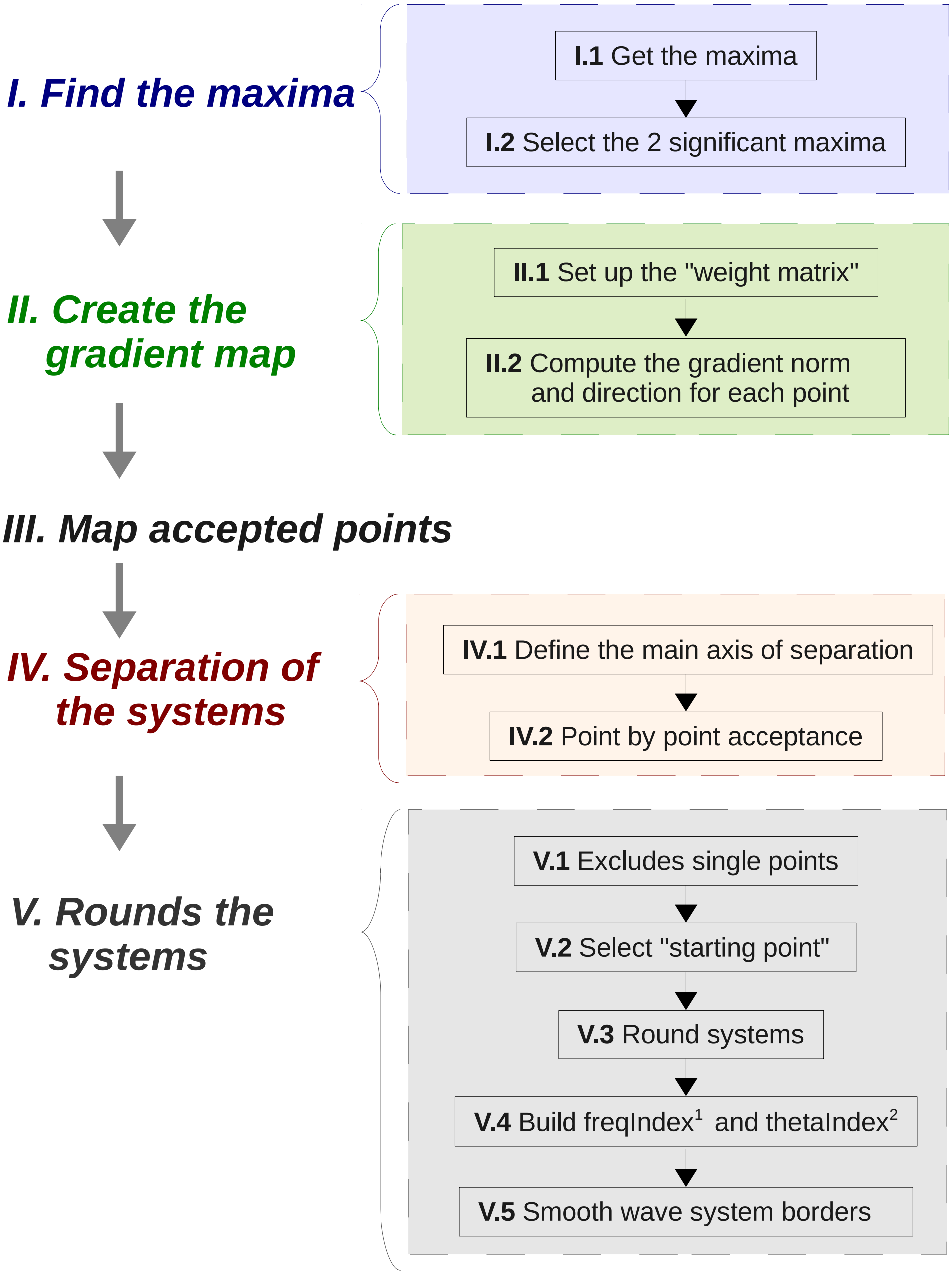

Figure 4.9: *General flow chart of the wave system isolation method.*

selected as the highest two with significant separation between: a 'distance' is defined between the position of the spectra as $dist = \sqrt{(x_2 - x_1)^2 + (y_2 - y_1)^2}$, with x and y the coordinate indices in the discrete (f, θ) plan. Two identified submit are considered significantly separated if $dist > 5$. This threshold is dependant on the angular and frequency resolution of the (f, θ) plan.

A gradient map is built. For each point, a weighted average gradient magnitude and direction is computed as described in Eq. 4.26 to Eq. 4.28. The weight matrix W gives more emphasis to the frequency dimension as most wave systems are more elongated along it.

$$W = \begin{pmatrix} 1 & 1 & 1 & 1 & 1 \\ 1 & 1 & 2 & 1 & 1 \\ 1 & 2 & 3 & 2 & 1 \\ 2 & 3 & 4 & 3 & 2 \\ 1 & 2 & 3 & 2 & 1 \\ 1 & 1 & 2 & 1 & 1 \\ 1 & 1 & 1 & 1 & 1 \end{pmatrix} \tag{4.26}$$

$$\begin{cases} L_{t,1} = W_{u+4,v+3} \cdot (S_{p+u,q+v} - S_{p,q}) \cdot u \\ L_{t,2} = W_{u+4,v+3} \cdot (S_{p+u,q+v} - S_{p,q}) \cdot v \\ L_{18,1} = L_{18,2} = 0 \end{cases} \tag{4.27}$$

$$with \quad t = 5(u+3) + (v+2) + 1 \quad u \in (-3, 3), \ v \in (-2, 2)$$

$$\begin{cases} ||\overrightarrow{grad_{p,q}}|| = \sqrt{\left(\sum_t L_{t,1}\right)^2 + \left(\sum_t L_{t,2}\right)^2} \\ \angle\overrightarrow{grad_{p,q}} = \arctan\left(\frac{\sum_t L_{t,2}}{\sum_t L_{t,2}}\right) \end{cases} \tag{4.28}$$

Each point of the spectrum is then tested for acceptance in the waves systems. The criterion is that its gradient magnitude should be at least 23% (25% in the case of uni-modal spectrum) of the highest observed magnitude or its spectral estimate should be at least 30% of the highest spectral estimate. As many of the thresholds in this thesis, they were set by trial and error.

The two wave systems are then separated. The main axis of separation is defined. If the separation along the frequency axis of the two identified maxima is higher than one and a half time the separation along the angular axis, the main axis is set along the angular dimension, otherwise it is set along the frequency dimension. Each of the accepted point is then attributed to a wave system. For the points in between the two maxima, the difference between the gradient direction and the direction from the point toward each maxima is used. This part results into two spectra which values are > 1 for the points attributed to the considered wave system and 0 for the others.

Each spectrum is filtered and any single point is discarded. The wave system associated to each spectrum is then rounded in order to identify the points forming its periphery. The developed algorithm builds step by step a list of the peripheral points starting from the outer point on the right of the identified wave system centre. The step by step procedure is described in Fig. 4.10 and Fig. 4.11.

The algorithm progresses along the periphery of the accepted points, storing each points into

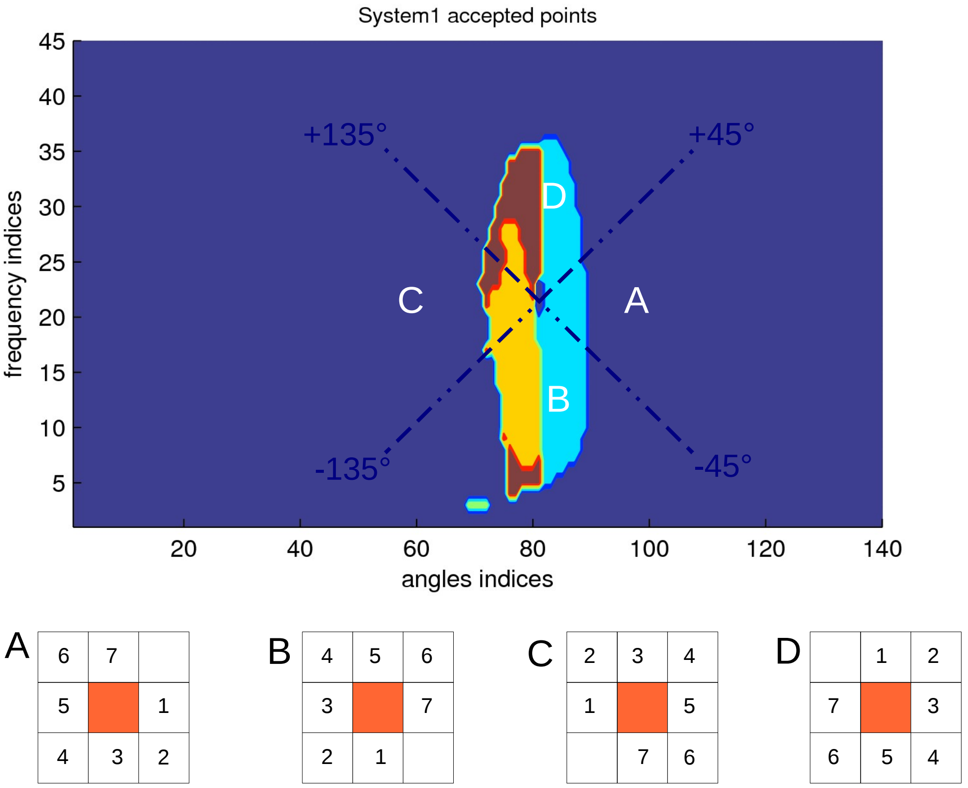

A

6	7	
5	🟧	1
4	3	2

B

4	5	6
3	🟧	7
2	1	

C

2	3	4
1	🟧	5
	7	6

D

	1	2
7	🟧	3
6	5	4

Figure 4.10: *Division of the spectrum of accepted point into four zones as a function of the direction between the wave system centre and the points. Depending on the zone, the order in which the points will be checked changes. The colored zones represents the accepted points as generated by point III and IV of Fig. 4.9*

a list. At each step, the next point must be the most distant point from the wave system centre. It is done by dividing the accepted points into four zones depending of the direction from the centre to the points as shown in Fig. 4.10. Depending of the zone, the algorithm checks the adjacent points clockwise starting from a different points and moves to the first of those points marked as accepted. Fig. 4.11 describes three steps of the methods, passing from zone A to zone B between step 2 and 3. The method goes backward in the list of point forming the boundary when encountering a dead end. The algorithm ends when the list encloses an area containing the wave system centre.

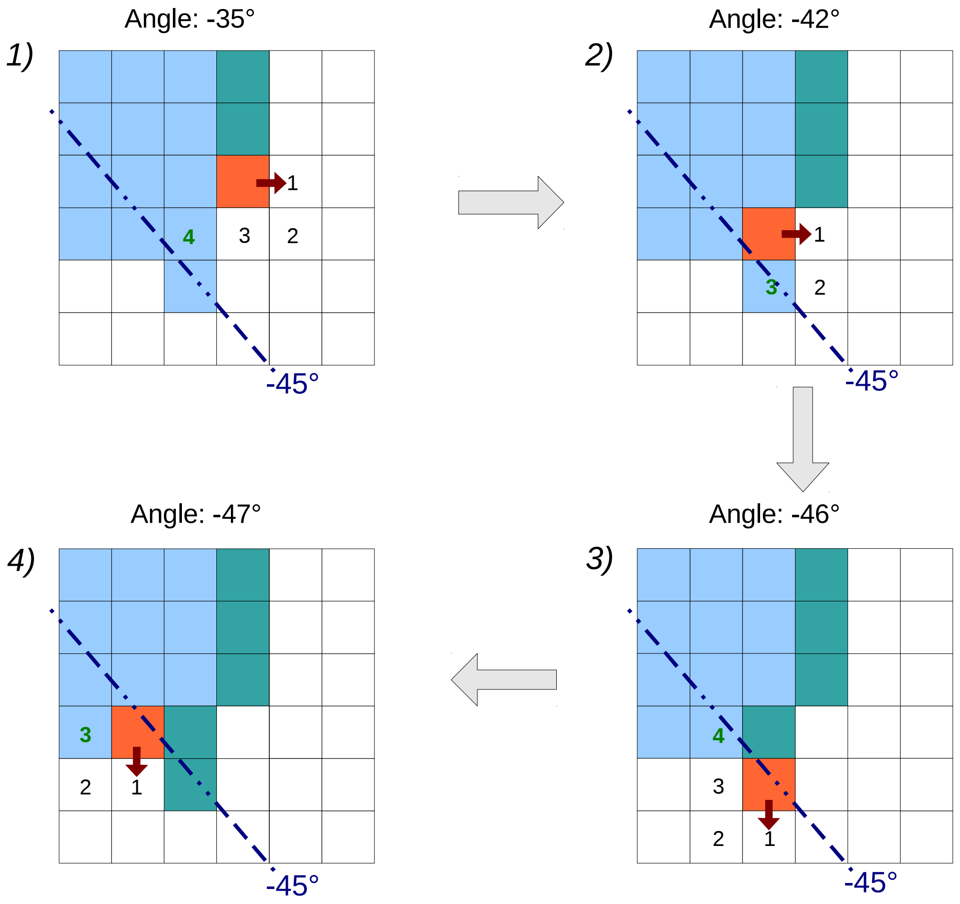

Figure 4.11: *Steps of the rounding method. Each matrix is a portion of the full spectrum. Given angles are speculative. Blue squares identify points that are part of the wave system. The orange square is the latest point included into the wave system boundary at each step and the darker blue squares identify the points that are already included in the system boundary. The numbers define in which order the method tries to move. The red arrow illustrates the direction outward the wave system depending on the angle from the wave system center to the current point (orange).*

Finally, for each wave system, a frequency vector stores all the frequency indices present in the list in an ascending order, and for each stored frequency the minimum and maximum angular indices are stored in an angular matrix. Fig. 4.12 gives an example of bi-modal spectra with the two wave systems isolated by the method described above.

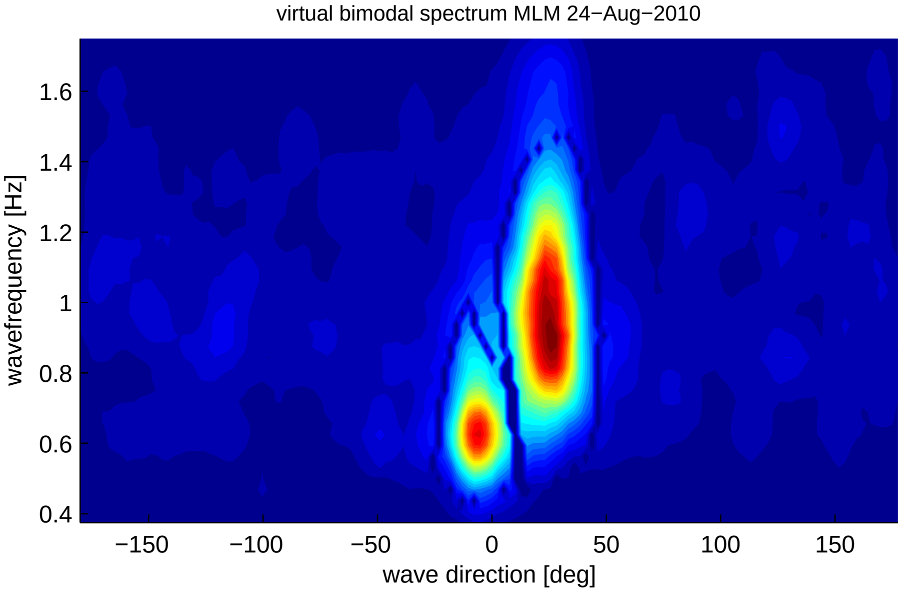

Figure 4.12: *Exemple of bi-modal spectrum with wave systems isolated. The point stored in the frequency vector and the angular matrix are set to 0 to visualise to wave system boundaries.*

4.5 Probe array design

4.5.1 Background

The results on wave measurement presented in this thesis were all obtained using an identical probe arrangement, both for virtual results and for measurements in the Edinburgh Curved Wave tank. However, as the probe positions represent an input to the method, the question of an optimal probe arrangement is automatically raised. Haubrich (1968) and Jefferys *et al.* (1981) discussed this issue early during the development of the directional spectrum measurement methods. Their main conclusion was that the final array should present a wide range of distance between probes in order to effectively separate waves with different wave lengths. It is also acknowledged that spatial aliasing, when some distances between probes are larger than the smallest wave length of the measured sea state, can reduce the accuracy of the method as energy in short wave lengths get allocated to their aliased long wave lengths. These conclusions should lead to the design of relatively small arrays to avoid aliasing, with non symmetrical probe positions to create a wide range of distances between probes.

Young (1994) extended those studies and quantified the errors on the measurement of $D_{f,\theta}$ as a function of the array geometry and the wave length. An error function is introduced as described in Eq. 4.29.

$$\epsilon_f = \sum_q |D_{f,\theta_q} - \hat{D}_{f,\theta_q}|\Delta\theta \tag{4.29}$$

The side length of the square enclosing each array under consideration is denoted R. Young (1994) demonstrated a strong dependency of ϵ_f to the non-dimensional parameter $\frac{\lambda}{R}$. In most cases, a abrupt decrease of ϵ_f is observed for $\frac{\lambda}{R} = 1$, and ϵ_f raises again for $\frac{\lambda}{R} > 10$. It is explained by the effect of aliasing at the lower end and the slow degradation of the cross-spectra matrix when λ increases. The benefit of arrays with a wide range of distances between probes is also demonstrated. They are shown to extend the $\frac{\lambda}{R}$ for which ϵ_f is optimal. Finally, the authors observed a general decrease of ϵ_f while increasing the number of probes from 4 to 10, but only marginal gains can be obtained with array made of 5 probes or more.

The sensitivity of the methods to errors in the position of the wave elevation measurements can also be a factor in array design. Young (1994) mentioned in their conclusion that their results were subject to changes due to the inaccuracy by which the array geometry is known. Using twin wires conductivity probes, there is an inherent difficulty to estimates where the wave elevation measurements are done. This adds to the difficulty to measure precisely the probe position on the supporting frame. In the course of this work, the error in measurement position is estimated to $\pm 5\,\mathrm{mm}$ in both x and y directions. It is not suspected that this error will vary significantly as a function of the array dimension. As the probe array gets larger, those errors are less significant, which supports the design of a large array.

Requirements to keep the array dimension small enough to avoid aliasing do not necessarily concur with the need of minimising the effect of the error in probe positioning. In the following sections, the influence of both requirements on the method accuracy to estimate the wave directional parameters is investigated.

4.5.2 Method

Contrary to the most common deterministic approach use to investigated array design (Haubrich, 1968; Davis & Regier, 1977; Young, 1994), the method used in this work is to investigate the probe layout properties by mean of statistical analysis of the results given from a large number of different arrays. While a deterministic method will provide some insight about the governing factors of the array performance, a statistical method allows to explore more configurations,

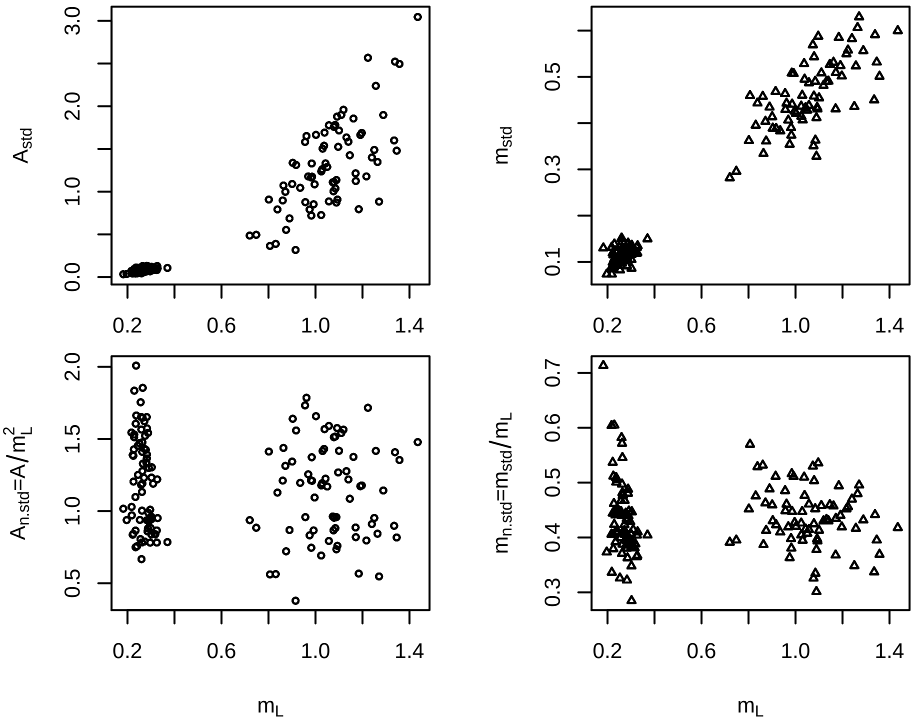

Figure 4.13: *Repartition of the parameter A, m_{std}, A_n and $m_{n,std}$ as a function of m_L.*

specially when considering bi-dimensional arrays. Additionally, the findings of the statistical approach can be compared and discussed afterwards against the deterministic approach results. Random arrays were created with 5 and 7 and 9 probes. For each probe number, 25 arrays without spatial aliasing and 25 arrays with spatial aliasing were created. Each array was then tested with virtual wave elevations generated from five uni-modal sea states based on a Bretschneider spectrum. For each test, differences between target and estimated spectrum parameters are recorded along with the array swept area A, the mean distance m_L between each pair of probes and the standard deviation m_{std} of the distance between each pair of probes were recorded. Normalised standard deviation $m_{n,std} = \frac{m_{std}}{m_L}$ and area $A_n = \frac{A}{m_L^2}$ are introduced to effectively decorrelate both parameters from m_L as shown in Fig. 4.13.

Two parameters are used to investigate array performances. The normalised difference $\epsilon_{n,\Theta}$ between the *estimated isolated* and the *target isolated* integrated angular spreading, the total difference ϵ_T and a weighted total difference $\epsilon_{w,T}$ between the estimated and the target spectra.

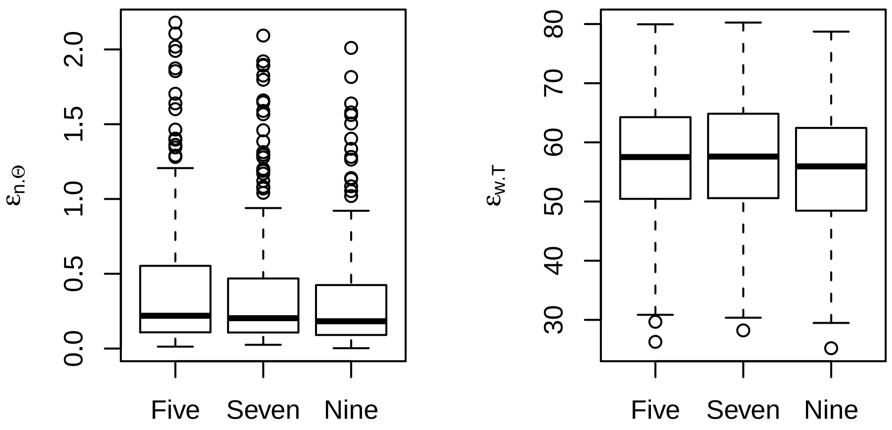

Figure 4.14: *Observation of $\epsilon_{n,\Theta}$ and $\epsilon_{w,T}$ as a function of the probe number.*

Their expression are given in Eq. 4.30 and Eq. 4.31.

$$\epsilon_{n,\Theta} = \frac{\hat{\Theta}_{S,1} - \Theta_{S,1}}{\Theta_{S,1}} \tag{4.30}$$

$$\epsilon_{w,T} = 100 \cdot \frac{\sum_{pq} |\hat{S}_{f_p,\theta_q} - S_{f_p,\theta_q}| \cdot S_{f_p,\theta_q}}{\sum_{pq} S^2_{f_p,\theta_q}} \tag{4.31}$$

$\epsilon_{n,\Theta}$ is used as the MLM based techniques have a tendency to over spread $\hat{S}_{p,q}$ which affects the estimation of the integrated angular spreading. In order to be able to quantify the effect of the integrated angular spreading on the scaled WECs, the method to estimate directional spectra must provide good estimation of this parameters. This justifies using $\epsilon_{n,\Theta}$ as a performance indicator of the method. $\epsilon_{w,T}$ provide a more global assessment of the method performances. It measures how much estimated spectra differ from target spectra. As it is weighted by S_{f_p,θ_q}, the noise outside of the target spectra (where $S_{f_p,\theta_q} = 0$) is discarded. A survey of different versions of $\epsilon_{w,T}$ is presented in Appendix D.1 on page 217.

4.5.3 Results

4.5.3.1 The probe number

The probe number is first investigated and its effect is thought to be independent from the other array parameters. Fig. 4.14 shows the observations of the two selected criteria in relation with the number of probes in each array generated. There is no clear effect of the probe number on those graphs. The difference between the means do not seem to be significant in any case.

Nonetheless, a trend to decrease $\epsilon_{n,\Theta}$ by increasing the number of probes is suggested, which agrees with the initial intuition.

4.5.3.2 Observation using $\epsilon_{n,\Theta}$

Fig. 4.15 presents a summary of the $\epsilon_{n,\Theta}$ observation as a function of $\hat{\Theta}_S$ and the three array parameters m_L, $m_{n,std}$ and A_n. Results from large and small array ($m_l < 0.4\,\mathrm{m}$) are differentiated.

The driving parameters is clearly $\hat{\Theta}_{S,1}$. As shown later in Section 4.6.1.1 in more details, there is a clear decrease of the overspread of the estimated spectra by the MLM when $\hat{\Theta}_{S,1}$ increases. The differentiation between small and large arrays also put in evidence the difference between the two types of arrays. For large values of $\hat{\Theta}_{S,1}$ ($\hat{\Theta}_{S,1} \gtrsim 12\,°$), no large difference between small and large array can be expected. However, large arrays handle narrow spectra much better than small arrays. This is a significant argument in favour of large arrays. Finally, there is little evidence of the influence of either the normalised standard deviation $m_{n,std}$ and normalised area A_n of the arrays. A regression differentiating between large and small arrays provide a

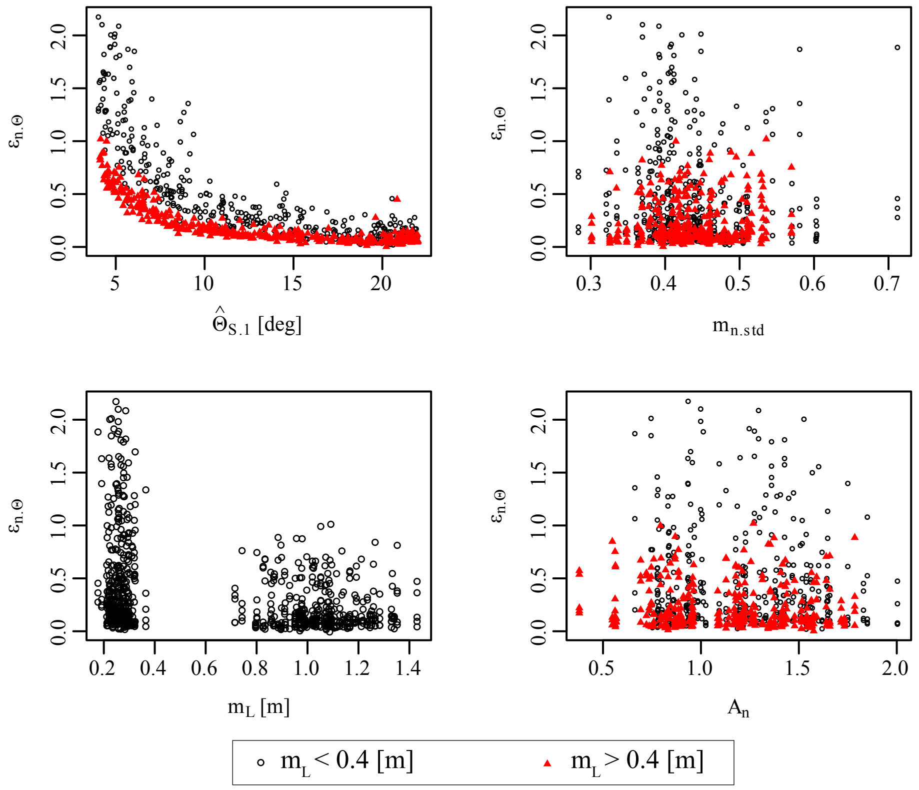

Figure 4.15: *Observation of* $\epsilon_{n,\Theta}$ *as a function of* A_n, m_L *and* $m_{n,std}$.

good model for the observed $\epsilon_{n,\Theta}$. Equations related to this model are given in Eq. 4.32 and a representation is displayed in Fig. 4.16. Details are available in Appendix D.1.2 on page 219.

$$\begin{cases} \epsilon_{n,\Theta} = e^{1.647-0.316\cdot\hat{\Theta}_{S,1}+0.006\cdot\hat{\Theta}^2_{S,1}} & m_L < 0.4\,\mathrm{m} \\ \epsilon_{n,\Theta} = e^{1.150-0.386\cdot\hat{\Theta}_{S,1}+0.010\cdot\hat{\Theta}^2_{S,1}} & m_L > 0.4\,\mathrm{m} \end{cases} \tag{4.32}$$

The model is not entirely satisfactory as it tend to infinity for $\hat{\Theta}_{S,1} \to \infty$. A piecewise model based on the observations of Section 4.6.1.1 might be more appropriate but it was not thought necessary to implement it here.

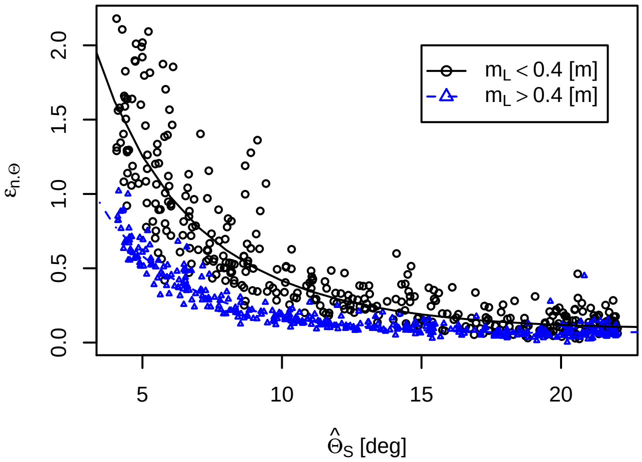

***Figure 4.16:** Models fitted to $\epsilon_{n,\Theta}$.*

The main conclusion from these observations of $\epsilon_{n,\Theta}$ and model is that *large* arrays ($m_L > 0.4\,\mathrm{m}$ provide a significant improvement on the handling of narrow spectra over *small* arrays.

4.5.3.3 Observation using $\epsilon_{w,T}$

Fig. 4.17 presents a summary of $\epsilon_{w,T}$ observations. As for Fig. 4.15, results from large and small array ($m_l < 0.4\,\mathrm{m}$) are differentiated.

Again, the principal parameters controlling $\epsilon_{w,T}$ observations is $\hat{\Theta}_{S,1}$, and a different behaviour between *large* and *small* array is evident. No influence of A_n or $m_{n,std}$ can be detected.

As expected, $\epsilon_{w,T}$ decreases when $\hat{\Theta}_{S,1}$ increases, confirming that the MLM does not evaluate correctly narrow spectra. For narrow spectra, *large* array seems to be better than *small* ones. However, the slope of the decrease is more marked for *small* arrays, which mean that for $\hat{\Theta}_{S,1} \gtrsim 12\,°$, *small* arrays do perform better than *large* ones according to $\epsilon_{w,T}$ criterion.

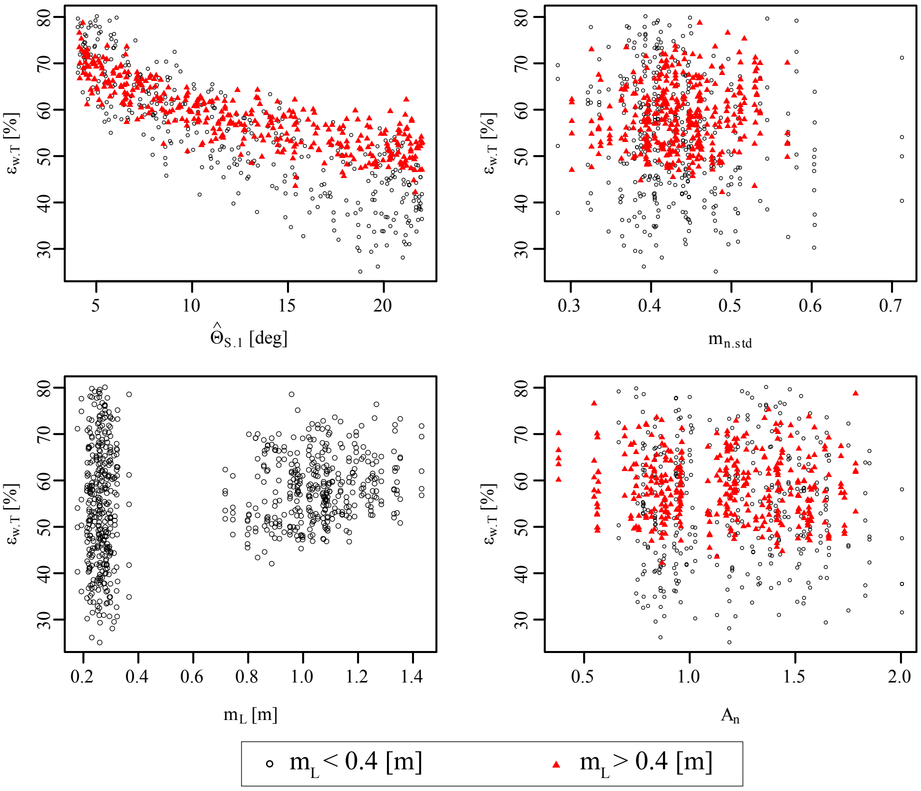

Figure 4.17: *Observation of* $\epsilon_{w,T}$ *as a function of* A_n, m_L *and* $m_{n,std}$.

Those results probably show that *small* arrays spectral estimation are not as affected by noise as *large* arrays. Source of this noise could be aliasing, particularly in the tail of spectra (components with the shortest wave lengths).

4.5.3.4 Array performances conclusions

First, minor improvements were correlated with an increase in the number of probes, specially by looking at $\epsilon_{n,\Theta}$. However, the size of the arrays (m_L) and the integrated angular spreading have a much stronger influence on the observed results. The two other array geometry parameters, the normalised area A_n and the normalised standard deviation $m_{n,std}$ do not have any visible influence on the two performance criteria utilised.

The previous results show that in the worse conditions for the MLM (narrow spectra), *large* array perform better. In those condition. it is likely that both $\epsilon_{w,T}$ and $\epsilon_{n,\Theta}$ were dominated by spectra overspread.

However, using a criterion robust but still sensitive to noise, it is shown that the spectra from *small* improves more than results from *large* array when analysing broader spectra. As all source of noise where identical for all arrays, this seems to show that *small* arrays are jointly more impacted by the error in probe positions but less sensitive to aliasing.

Assuming that hypotheses made on the errors on probe positioning are realistic, it appears that spatial aliasing is not critical while designing the array. It seems a better compromise to use *large* arrays to obtain more consistent performances aver the full range of spectra and allow some level of aliasing affecting the performance of the estimation over all type of spectra. In case only broad spectra were to be utilised, a *small* array might be preferred, but it is not the case in this work, specially for the purpose of separating bi-modal spectra.

Young (1994) mentioned the accuracy at which the array geometry is known as a source of errors for the estimation of $D_{f,\theta}$. However, they did not quantify this errors and did not reckon that it might have a stronger negative effect than spatial aliasing. The presented results in this section proved that the array geometry accuracy must be taken into account at the same level as aliasing as a source of errors.

4.5.4 The final array

During the thesis, timing constraints forced the probe layout to be fixed before the finalisation of results presented above. Fortunately, a rather large array was chosen only on suspicion

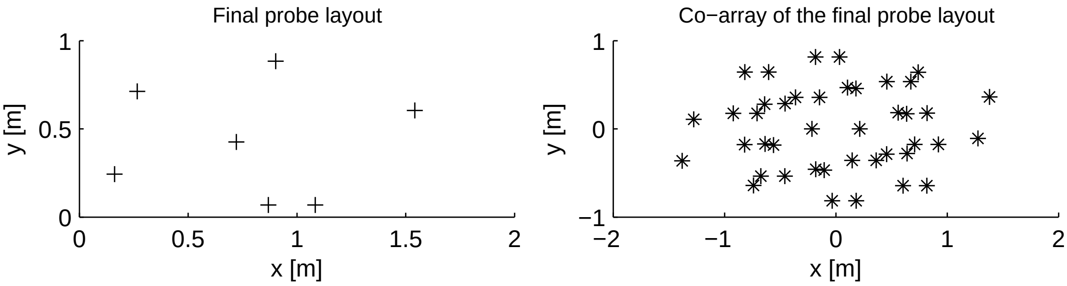

(a) probe layout ***(b)*** associated co-array

Figure 4.18: *Final probe layout used to measure directional spectra and its co-array (Haubrich, 1968).*

that probe positioning error will be the driving constraint. 7 probes were used as this was the maximum number of probes available. A schematic of the array is presented in Fig. 4.18 with its co-array and the array parameters are given in Table 4.1. The co-array is defined by the points formed by the vectorial difference between each pairs of points of the array. It can be linked directly to the spectral estimates as in Eq. 4.4. A full description of the co-array is presented in Haubrich (1968). The values in Table 4.1 define the used array as average in regards of the parameters range as seen in Fig. 4.13. As it is, it should have performance in line with the results presented in Section 4.5.3.

Parameter	Value
m_L	$0.76\,\mathrm{m}$
A	$0.76\,\mathrm{m}^2$
m_{std}	$0.29\,\mathrm{m}$
a_n	1.32
$m_{n,std}$	0.38

Table 4.1: *Parameters of the probe layout used to measure directional spectra.*

Compared to the type of array presented by Young (1994), this probe layout without symmetry exhibits an interesting co-array, with a large number of spatial lag evenly distributed across the plan. This should normally be the sign of good performances for a wide range of wave direction.

4.6 Results with virtual data

4.6.1 Method choice and performance characterisation

This initial test using virtual data is primarily intended to aid the selection of which version of the method (MLM or MMLM) is the most appropriate for the type of wave encountered in the Edinburgh Curved wave tank. While the MMLM is potentially the best suited method, the low level of reflection (less than 10% of the wave amplitude) and the presence of spurious peaks may make the MLM the best method for estimating directional spectra.

Initial observations of both uni-modal and bi-modal spectra do not allow a clear distinction between the two methods (see Fig. 4.19 and Fig. 4.20). Both methods captured relatively well the two spectra, and both methods are able to separate the two wave systems in the bi-modal case.

A formal study is performed on uni-modal and bi-modal spectra with random spectral parameters. The results are analysed following the method described in Appendix C on page 211. For uni-modal spectra, the method's performance is evaluated by investigating the value of the spectral parameters computed from their spectral estimates. For bi-modal spectra, the ability to separate the wave systems is selected as the performance indicator.

4.6.1.1 The uni-modal case

The spectra used are Bretschneider and JONSWAP (with $\gamma = 3.3$), $T_z \in [0.63\,\mathrm{s}\;\; 0.96\,\mathrm{s}]$, $H_{m0} \in [0.05\,\mathrm{m}\; 0.075\,\mathrm{m}]$ and $s \in [1\;100]$ (see Fig. 3.15 on page 40).

The main interest of the uni-modal tests is to get awareness of the method's capability to estimate the integrated spreading parameters (frequency and angular) of the spectra.

the integrated angular spreading For both methods separately, Fig. 4.21 shows the *estimated isolated* integrated angular spreading $\hat{\Theta}_{S,1}$ as a function of the integrated angular spreading of the corresponding target spectra Θ_S.

An analysis of covariance (ANCOVA) is done. The linear model includes the two levels factors *method* ('MLM' and 'MMLM') and *type1* (JONSWAP and Bretschneider), the continuous explanatory variables Θ_S and Θ_S^2 and all the 2-way interactions. The summary of the associated minimal adequate model is presented in Appendix D.2.1 on page 222. The results of the model are presented in Fig. 4.21, omitting to differentiate between the treatment associated to the two

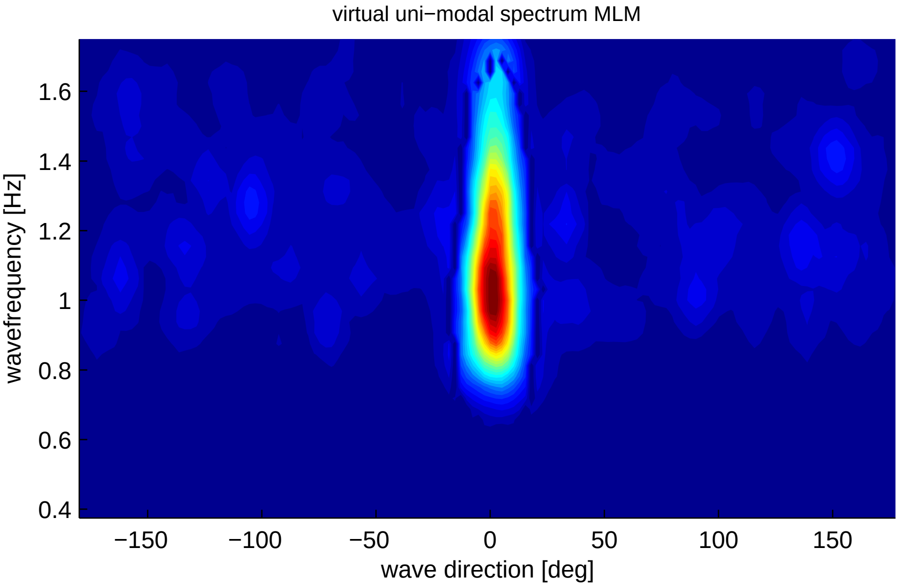

(a) Uni-modal spectrum estimated by the MLM.

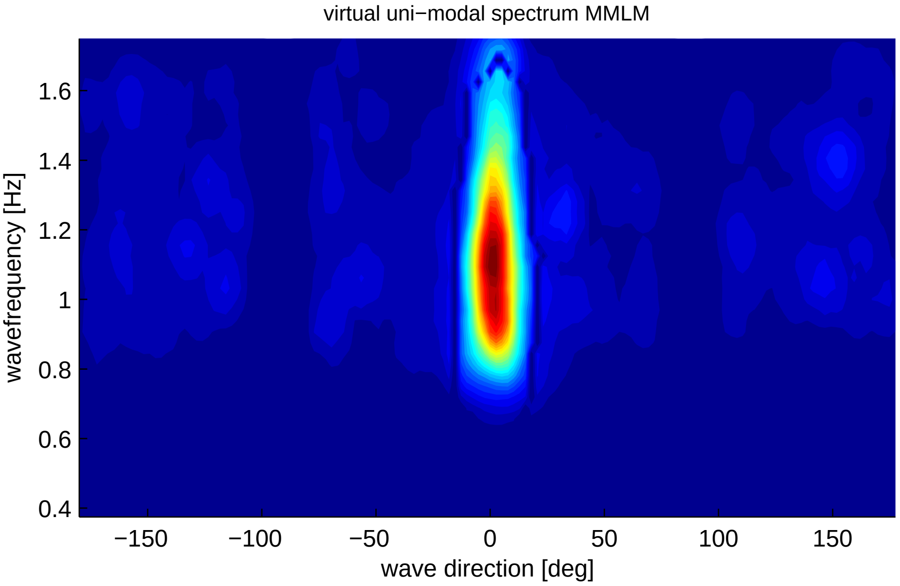

(b) Uni-modal spectrum estimated by the MMLM..

Figure 4.19: *Identical uni-modal spectrum from virtual waves estimated by the adapted MLM and the adapted MMLM. The estimated spectrum is slightly wider in the MMLM case, suggesting that the MLM gave a better estimation as both methods have a tendency to overspread the spectral estimates.*

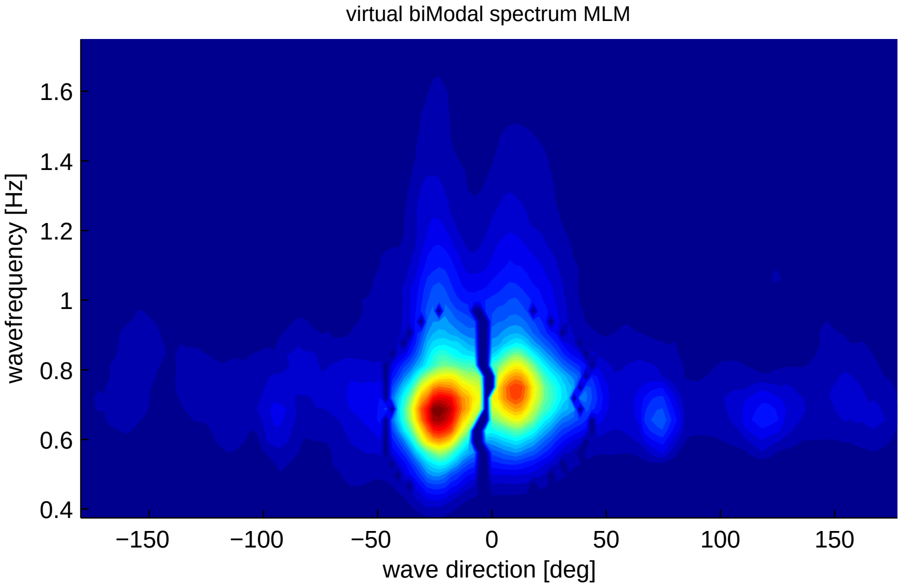

(a) Bi-modal spectrum estimated by the MLM.

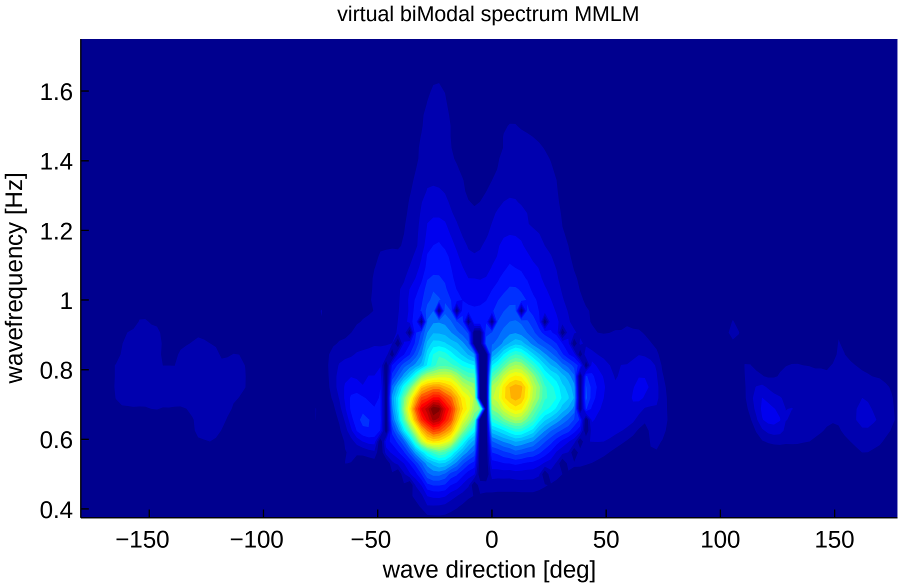

(b) Bi-modal spectrum estimated by the MMLM..

Figure 4.20: *Identical bi-modal spectrum from virtual waves estimated by the adapted MLM and the adapted MMLM.*

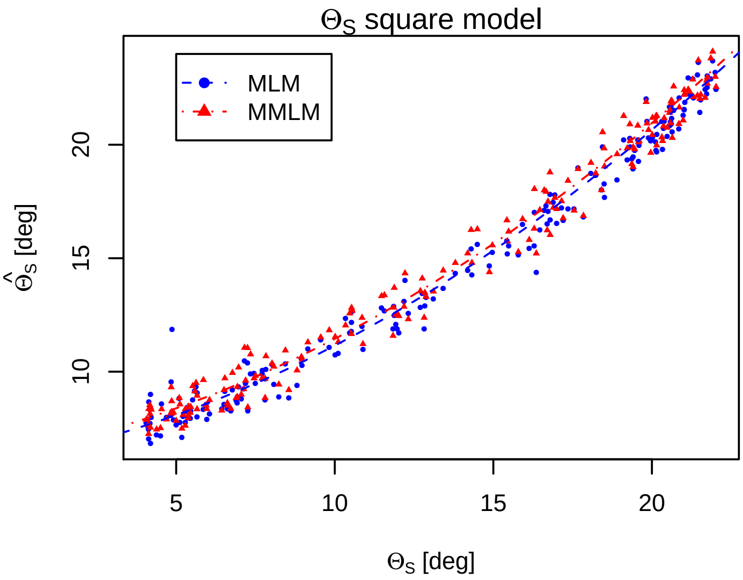

Figure 4.21: *Observation of the isolated estimated angular spreading $\hat{\Theta}_{S,1}$ with respect to the target angular spreading Θ_S. A linear model including the square term Θ_S^2 to account for the curvature in the data is fitted to the observations.*

types of spectra (JONSWAP and Bretschneider). The lines for each method are parallel as the minimal adequate model do not retain any interactions between the method and any other variable. This is an important observation as it means that differences in using the MLM or the MMLM are not dependant on the other considered factors. Any conclusion over the methods is valid independently of Θ_S or the type of frequency spectrum.

The second conclusion of this *ancova* test is that the relation between the measured angular spreading and the theoretical one is not linear: the square term, while having a small coefficient, is highly significant ($Pr(>|t|) < 2e-16$). However, a square model for these data with a positive coefficient is not realistic, as it will lead to an ever increasing difference between the target and the measured values.

A second model is fitted to the data using the information on the first model. The curvature in the data is modelled by a piecewise linear model and do not include Θ_S^2. Fig. 4.22a shows the representation of this model, omitting to differentiate between the treatment associated to the two types of spectra (JONSWAP and PM). The breaking point is estimated by looking at the evolution of the *residual standard error* of the model as a function of the breaking point value and choosing the minimum as the optimum (Fig. 4.22b). The minimum *residual standard error* is observed for a breakpoint located at $12.8\,^\circ$.

A series of standard test plots does not reveal any particular issue about the fit of the linear piecewise model. Finally, an *anova* test between the two models does not show significant differences between their respective explanatory power. The details of the model and the check plots are available in Appendix D.2 on page 222 (see Fig. D.4). All the terms are marked as significant. This evidence leads to the acceptance of the fitted linear piecewise model as appropriate.

The first conclusion is that the MMLM tends to predict angular spreading coefficient $0.30 \pm 0.7\,^{\circ}$ higher than the MLM. While this value is not large, it is still statistically significant. As both methods are known to overspread the estimated spectra, this leads to the use of the MLM instead of the MMLM for the estimation of uni-modal spectra.

The angular spreading of broad spectra (spreading $> 12.8\,^{\circ}$) is well estimated by both methods. The coefficient of the slope is 1.09 ± 0.02. From all practical matter, Θ_S is considered to be correctly estimated for broad spectra as the errors are contained under 10% (see Fig. 4.36). For the narrow spectra, there is no constant offset (slope is $\simeq 0.65$). It is more likely that the method cannot predict narrow enough spectra and this effect is more pronounced the narrower the target spectra. The intercept of the model with the y-axis in the MLM case is $4.74 \pm 0.76\,^{\circ}$, which can be considered as the maximum error due to the measurement method itself.

The integrated frequency spreading The integrated frequency spreading parameter f_s is more straight forward. An *ancova* model is fitted to the observed $\hat{f}_{s,1}$. The factors used are the target values f_s and T_Z of the target spectrum and the methods. T_Z is used instead of T_E as it is the one used directly into the formulas of the spectral shape. The associated minimal adequate model retains f_s, T_Z and the *intercept* as significant factors. The average difference observed between the MLM and the MMLM is not recognised as significant, hence each method can be use indifferently to estimate the frequency spreading. The summary of the model and the tests plots are available in Appendix D.2 on page 222. The fit of the model is not entirely satisfactory as the residuals show some sign of heteroscedasticity. However, standard transformation of the response variable or the use of *generalised linear model* did not yield significant improvements. It is likely that the repartition of $\hat{f}_{s,1}$ in two clusters is an obstacle to achieve a more satisfactory model. Indeed, it do not seems natural to fit a line trough two clusters of point. Further work could focus on using several $gamma$ values to better monitor the performances of the method relative to the estimation of the integrated frequency spreading.

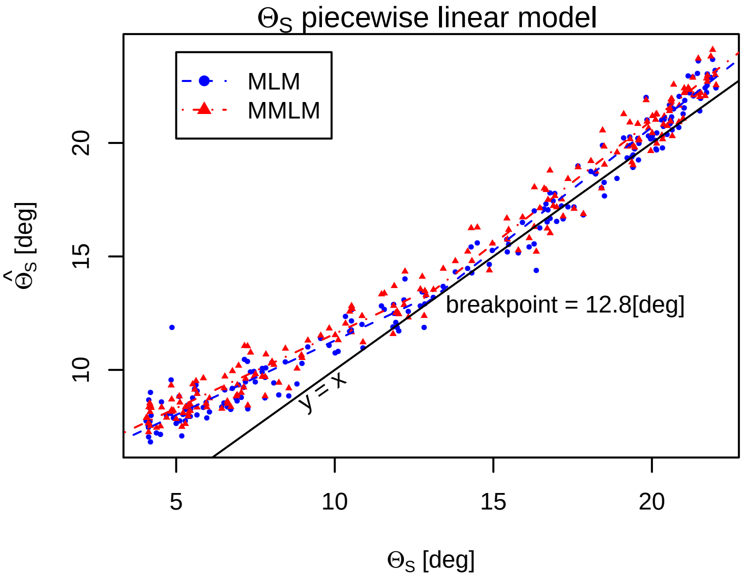

(a) Linear piecewise model fitted to the observed data. The lines for each method are parallel as the model do not include any interactions between the *method* and any other variables.

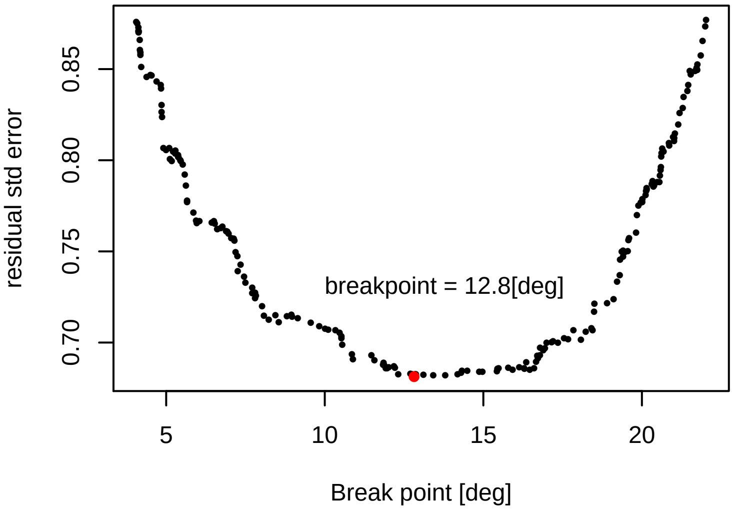

(b) *Residual standard error* of the linear piecewise model as a function of the breaking point.

Figure 4.22: *Characteristics of the piecewise linear model fitted to the observed* $\hat{\Theta}_S$.

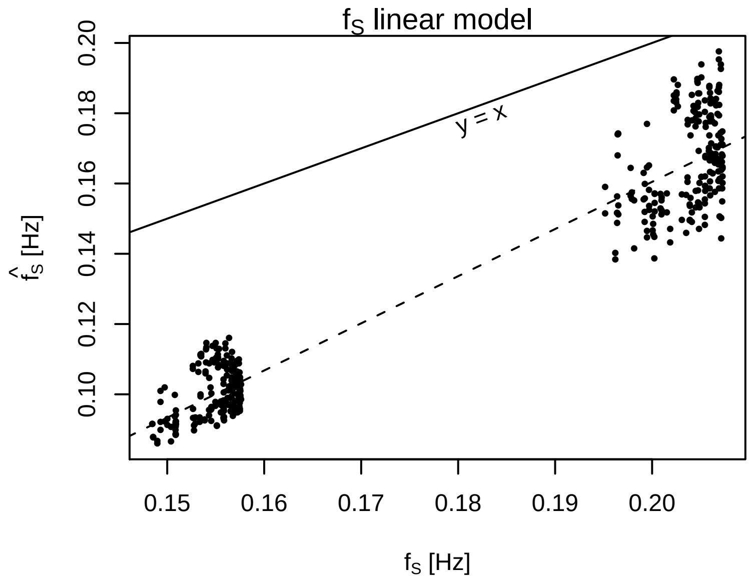

Figure 4.23: *Graphical representation of the linear model fitted to the estimated isolated* $\hat{f}_{s,1}$. *The model line is drawn using the mean value of* T_Z. *No distinction is made between MLM and MMLM results as the two treatments are not found to be significantly different.*

The mathematical expression is presented in Eq. 4.33 and graphical representation of the model using the mean value of T_Z is shown in Fig. 4.23.

$$\hat{f}_{s,1} = (-0.060 \pm 0.005) + (1.34 \pm 0.02) \cdot f_s + (-0.060 \pm 0.004) \cdot T_Z \tag{4.33}$$

From this graph, it is clear that the integrated frequency spreading is underestimated by the process of directional spectrum estimation followed by the isolation method. The isolation method is probably the main reason for it: the tail of the wave spectrum presents normally rather low gradients, so they can be easily discarded by the isolation routine, which in turn reduce the estimated frequency spreading.

Mean wave period and significant wave height Both methods tend to underestimate the significant wave height. An initial investigation of the variation of *estimated isolated* significant wave height $\hat{H}_{m0,1}$ with respect to the parameters of the target spectra suggests a dependency with H_{m0}, f_s and Θ_S. A linear model including H_{m0}, f_s and Θ_S, the *method* factor and a term to test a curvature in the data related to ${H_{m0}}^2$, is fitted to the observed data. The summary of the associated minimal adequate model is presented presented in Appendix D.2.1 on page 222 with the test plots provided by the R language. The resulting model is given in Eq. 4.34 and

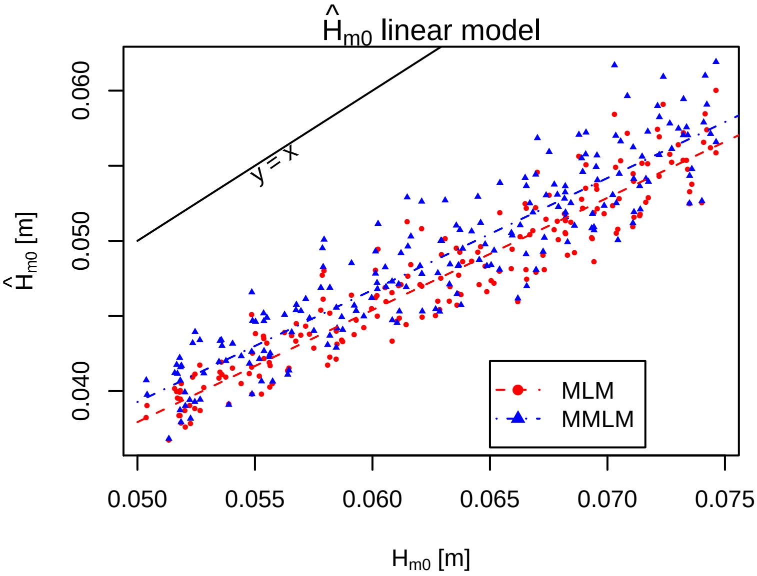

Figure 4.24: *$\hat{H}_{m0,1}$ as observed during the virtual data test with uni-modal spectra. The linear regression represents Eq. 4.34 taking the mean value of f_s and Θ_S. The black line represents the ideal case when estimated and target values match.*

a graphic representation is provided in Fig. 4.24. A linear relation is observed between $\hat{H}_{m0,1}$ and H_{m0} (the ${H_{m0}}^2$ is not retained in the minimal adequate model).

$$\begin{cases} \text{MLM:} & \hat{H}_{m0,1} = -1.2 \cdot 10^{-2} + 1.9 \cdot 10^{-4} \cdot \Theta_S + 4.6 \cdot 10^{-2} \cdot f_s + 7.7 \cdot 10^{-1} \cdot H_{m0} \\ \text{MMLM:} & \hat{H}_{m0,1} = -1.1 \cdot 10^{-2} + 1.9 \cdot 10^{-4} \cdot \Theta_S + 4.6 \cdot 10^{-2} \cdot f_s + 7.7 \cdot 10^{-1} \cdot H_{m0} \end{cases} \tag{4.34}$$

Focusing on the *method*, higher values of $\hat{H}_{m0,1}$ are found on spectral estimates from the MMLM after isolating the spectra. As the significant wave height is always underestimated, it suggests that using the MMLM might be a better choice to estimate this parameters.

These observations are surprising as one would expect the MMLM coupled with the isolation routine to produce lower *estimated isolated* significant wave height $\hat{H}_{m0,1}$ than the MLM coupled with the isolation routine. As the MMLM has been shown to produce broader spectra than the MLM, it is indeed expected that less energy would be present inside the isolated wave system. This could hint that there is more to explore than what was done in Section 4.6.1.1 as they might be interaction between the estimates and the isolation routine.

However, a possible explanation is that the MMLM benefit from masking the noise in some part of the spectrum (see Section 4.2.5), thus inducing higher values everywhere else as the spectra is re-normalised after the mask is applied. Finally, as the significant wave height is not one of the parameter which effect will be investigated (see Chapter 6 on page 122), those results do

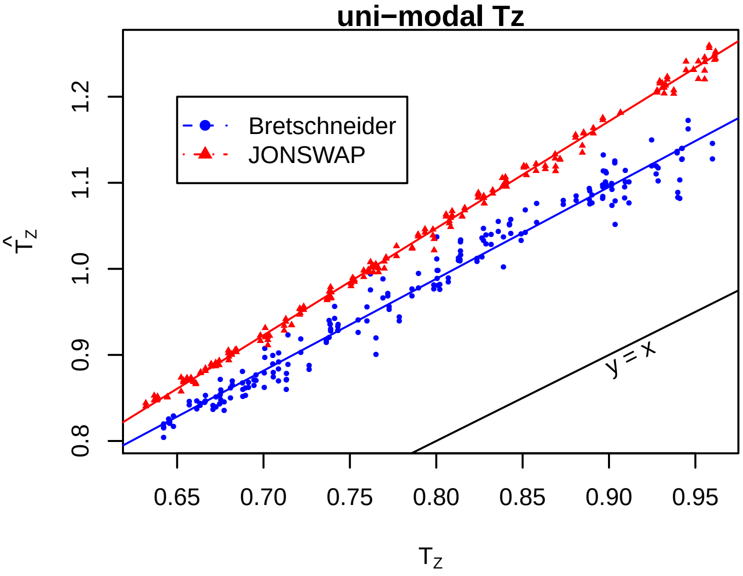

Figure 4.25: *$\hat{T}_{Z,1}$ as observed during the virtual data test with uni-modal spectra. The black line represents the ideal case when estimated and target values match.*

not questioned the choice of the MLM instead of the MMLM.

The residuals observed from linear model fitted to $\hat{T}_{Z,1}$ are not following any common distribution, and consequently it is difficult to conclude on the significance of any of the factors or to comment on the error margin of the parameter estimates. In particular, no observations can be done on the effect of the method as their magnitude is easily masked by the correlation between $\hat{T}_{Z,1}$ and T_Z. A simple regression gives nevertheless acceptable results, fitting a different slope for each type of spectrum. The results are presented in Eq. 4.35 and the regression are presented in Fig. 4.25.

$$\begin{cases} \text{JONSWAP:} & \hat{T}_{Z,1} = 0.05 + 1.24 \cdot T_Z \\ \text{Bretschneider:} & \hat{T}_{Z,1} = 0.13 + 1.07 \cdot T_Z \end{cases} \tag{4.35}$$

The zero-crossing period is clearly overestimated in both cases. However, a distinction can be made between JONSWAP or Bretschneider spectra. $\hat{T}_{Z,1}$ from Bretschneider spectra is consistently less overestimated. The estimated slope is only 1.07 against 1.24 for the JONSWAP spectra. As the wave elevation are generated considering specifying the zero-crossing frequency f_z, it is easier to formulate explanations based on frequency rather than period. Fig. 4.26 is the frequency version of the previous graphic.

Basically, the underestimation of $\hat{f}_{Z,1}$ increases with f_Z. This is explained by the genera-

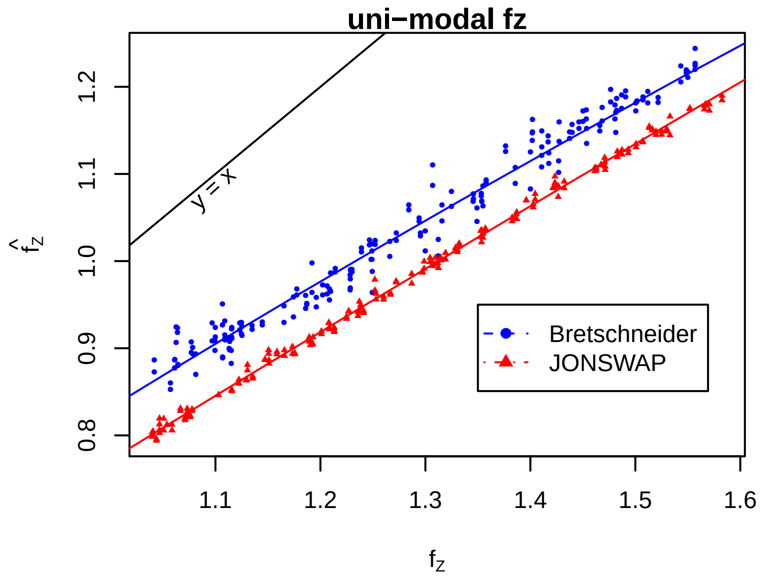

Figure 4.26: *$\hat{f}_{Z,1}$ as observed during the virtual data test with uni-modal spectra. The black line represents the ideal case when estimated and target values match.*

tion method. Any energy specified in the spectrum formulation above $1.75\,\mathrm{Hz}$ is discarded, which induces a decrease of the frequency parameters. The discrepancy between JONSWAP and Bretschneider spectra is explained by the isolation routine. This is based on the ratio between the highest gradient observed and the gradient of each point (see Section 4.4.2). The JONSWAP spectra are sharper, so the gradient ratio in the tail of the spectra decreases faster than for Bretschneider spectra. All the more, adding second order wave components tends to create a small plateau in spectra's tail, which in turn decreases even more the ratio of gradient. As the JONSWAP spectra present a higher variation of energy between the peak and the tail of the spectra, the spectral shape is more sensitive to this *plateau effect*. Those two observations combined are probably a good interpretation for the difference observed between the two types of spectra.

Overall, it has been decided to use the MLM instead of the MMLM to analyse uni-modal spectra as the MLM does estimate narrower spectra. The 10% reflection included in the virtual data seems to affect it less than the damage created by the spurious peaks inherent to the MMLM.

4.6.1.2 The bi-modal case

The results presented in this section are built over the analysis of 100 different bi-modal spectra. They were generated as described in Section 4.3, and the characteristics of the 2 wave systems composing each spectrum were randomly chosen. The range of each characteristics is presented in Table 4.2. Those ranges intend to cover the type of spectra that are both interesting for the work conducted in this thesis and practical in the Edinburgh Curved tank.

For bi-modal cases, the critical aspect of the wave measurement method is the ability to separate the wave systems. The MLM and the MMLM are consequently tested to evaluate if one method is more suitable than the other on this specific issue. It is important to note that $\delta\theta_M = |\Theta_{M1} - \Theta_{M2}|$ is higher than $10\,^\circ$ for all the generated spectra. These results might consequently not be relevant for spectra with two wave systems of identical mean direction of propagation. At the time of this part of the work, it was not planned to test the WECs with sea states 1,2, 5 and 6 of Table 6.3 on page 137.

Parameter	Range
Type	Bretschneider or JONSWAP($\gamma = 3.3$)
T_Z	$[0.75 : 1.25]\,\mathrm{s}$
H_{m0}	$[0.050 : 0.075]\,\mathrm{m}$
Θ_M	first wave system: $[-25 : -5]\,^\circ$, second wave system: $[5 : 25]\,^\circ$
spread s	$[1 : 100]$

Table 4.2: *Range of parameters used to generate the virtual bi-modal spectra.*

The *estimated isolated* parameters $\hat{\Theta}_{M,n}$, $\hat{T}_{Z,n}$, $\hat{H}_{m0,n}$, $\hat{s}_n$, $\hat{f}_{s,n}$ and the peak of energy max_n are recorded for both wave systems. The wave system with the highest maximum is considered predominant. For each sea state, the parameters are then arranged into primary and secondary wave systems parameters (the primary *estimated isolated* main direction of propagation $\hat{\Theta}_{M,p}$ equals $\hat{\Theta}_{M,1}$ or $\hat{\Theta}_{M,2}$ depending of which system is predominant). An extra set of induced parameters is then introduced. They are presented in Table 4.3.

Nine parameters characterising each sea state are retained as variables to explain the observed success and failure of the process. The method, MLM or MMLM, is added as a tenth variable. The response variable is binary, 0 for failure to isolate the wave systems, 1 for success. The presented data analysis is following the method presented in Crawley (2007) for Binary Response Variables.

An early examination of the data is done with boxplots (see Appendix C.1 on page 211). The plots are presented in Fig. 4.27.

Parameter	Definition
$\delta\Theta_M$	$\|\Theta_{M,p} - \Theta_{M,s}\|$
δT_Z	$T_{Z,p} - T_{Z,s}$
$H_{m0,r}$	$\frac{H_{m0,p}}{H_{m0,s}}$
max_r	$\frac{max_s}{max_p}$
interference	measure of the system overlap. See Appendix D.2.2 on page 227

Table 4.3: *Induced parameters introduced to explain the observed success rate of the wave system isolation method.*

From these plots, max_r, $f_{s,p}$ and $\delta\Theta_M$ seems to be the most important factors. The case of $interference$ is more difficult to interpret due to the many outliers. However, interaction and correlation between the variables may change the interpretation.

The *method* variable is categorical, so a table is used to summarised its effect:

```
table(method,Success)
      Success
method  0  1
  MLM  35 65
  MMLM 30 70
```

At first view, the MMLM succeded more often than the MLM.

A *tree model* (Crawley, 2007) is built to examine the interaction structures between the 10 variables together. Such *tree models* are intended as a pre analysis of the data to sort out the most influential parameters and are excellent to give an overview of the interactions between variables. The tree is read from top to bottom. At each step, the variables that explain the most variance of the observations is selected, and the observations are divided into two subsets. The value given at each node is the threshold of the variable used to split the observations. At the end of the branches, the mean value of the subset of observation is given. The first variables to appear in the tree are likely to be the most important variables to explain the variance of the observations. A complex tree, where variables appear at more than one node is the sign that complex interactions between variables are at play.

The resulting tree is presented in Fig. 4.28. The indications from this *tree model* partially confirms the early observation. max_r and $\delta\Theta_M$ are the most important parameters. For $\delta\Theta_M < 21.1\,^\circ$ or $max_r < 0.4$, the method will probably not identify the two wave systems: the mean Success is < 0.065. On the other side of the tree, a complex interaction patterns between the variables can be expected. Interestingly, the variable $f_{s,p}$ is not given any significant role with this model. Its apparent significance in Fig. 4.27 may have been due to some

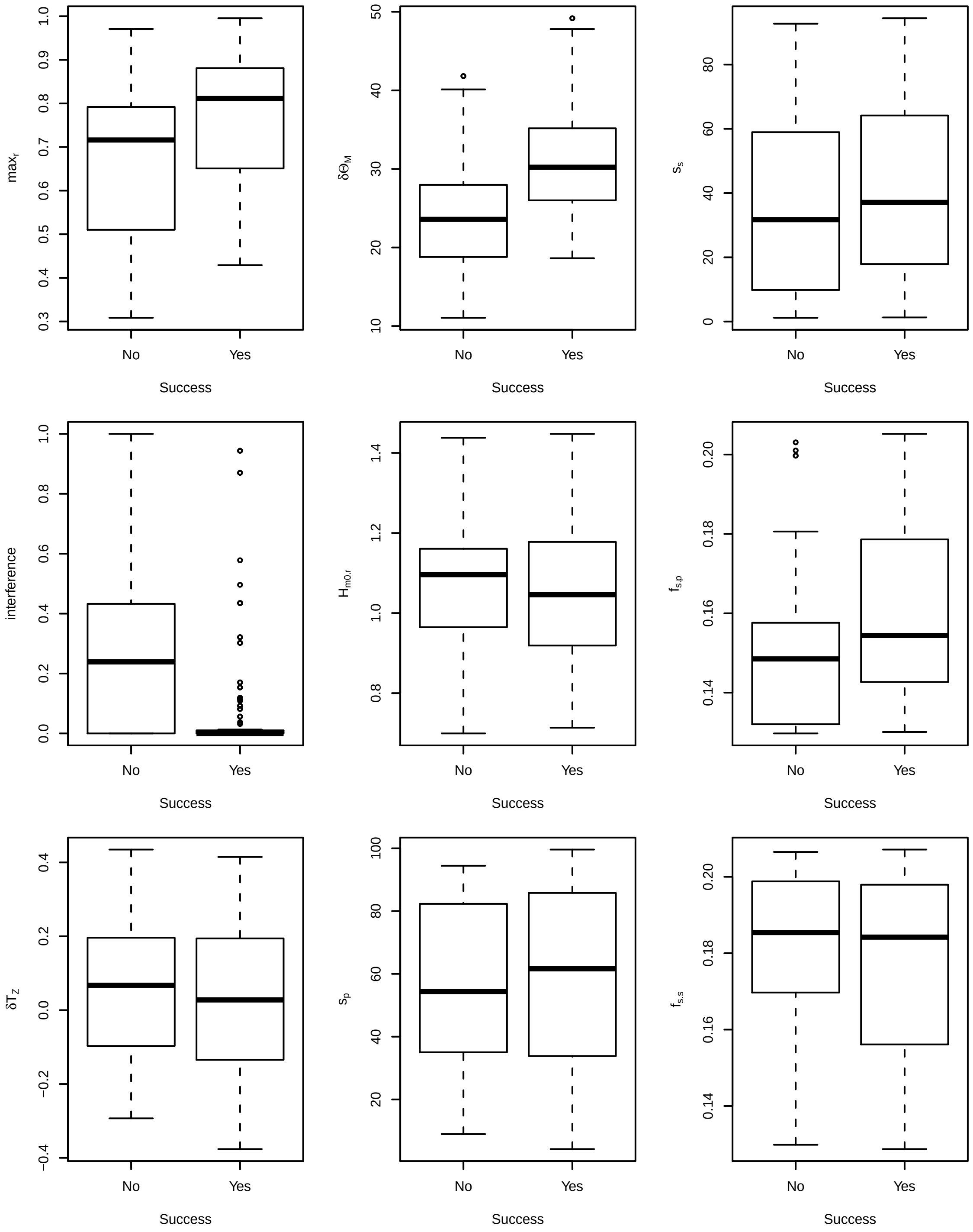

Figure 4.27: *Examination of the results of the bimodaltests with virtual data.*

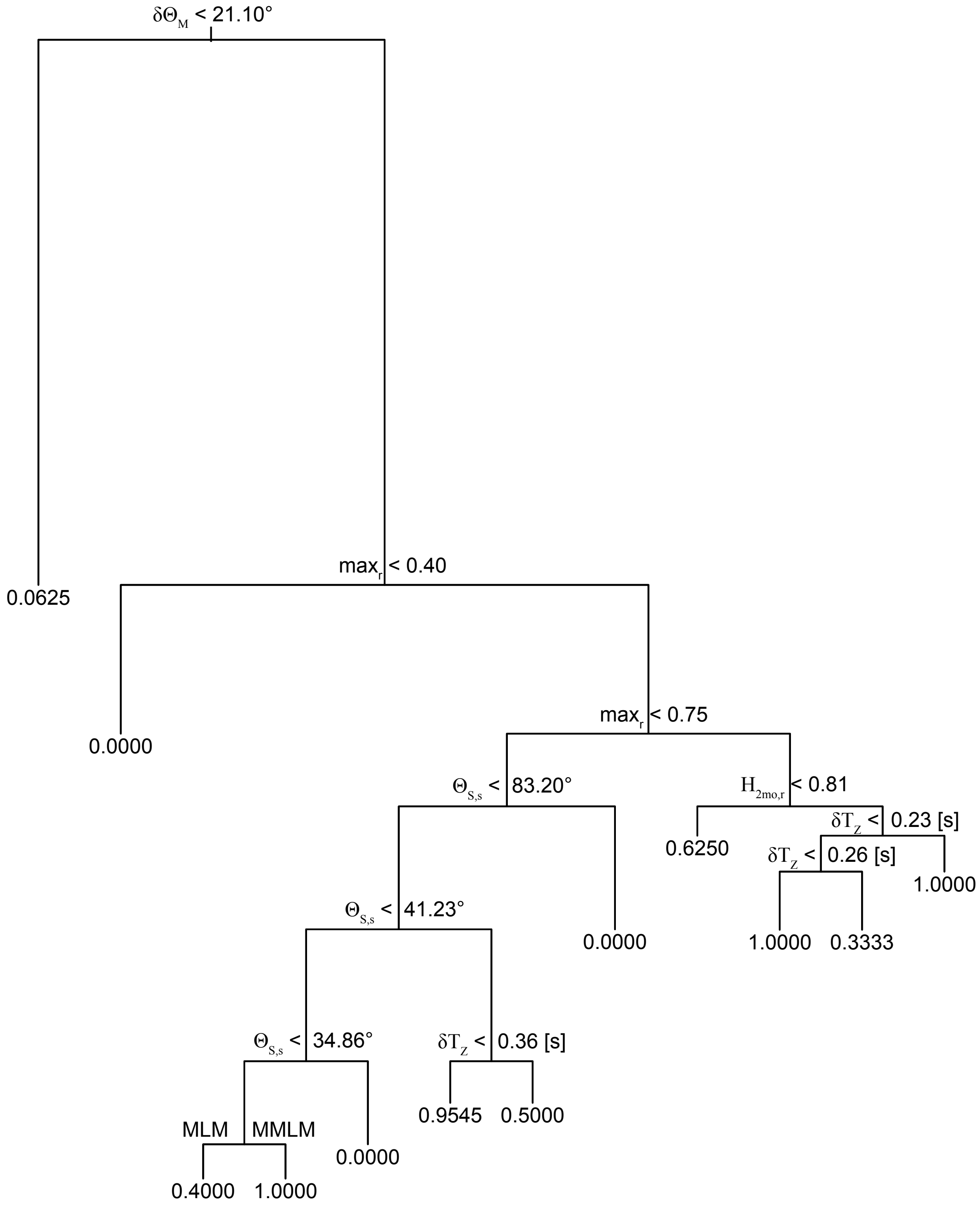

Figure 4.28: *Tree model of the results of the bimodal tests with virtual data.*

correlation with max_r (see Fig. D.7 on page 230). The *method* variable does not appear before the very end of a branch of the tree. This suggests that it may not have any significant effect over the observed results. Finally, the *interference* factor is not present in the three. Again, this is probably that it is not significant.

Based on the previous observation, a statistical model is built including all the variable minus $f_{s,p}$ and $f_{s,2}$ as they are not present in the *tree model* and without $H_{m0,r}$ (including two parameters related to the energy in the wave systems seems unnecessary). All the interactions up to the third level are included in the model. The minimal adequate model associated is presented below:

Initial model:

$$model \leftarrow glm(Success \sim (method + \delta\Theta_M + \delta T_Z + max_r + s_p + s_s)^3, family = binomial)$$

minimal adequate model summary:

Call:

$$\begin{aligned} glm(formula =& Success \sim \delta\Theta_M + \delta T_Z + max_r + s_p + s_s + \delta\Theta_M : \delta T_Z + \\ & \delta\Theta_M : max_r + \delta\Theta_M : s_p + \delta\Theta_M : s_s + \delta T_Z : max_r + \\ & \delta T_Z : s_s + max_r : s_p + s_p : s_s + \delta\Theta_M : \delta T_Z : max_r + \delta\Theta_M : max_r : s_p, \\ & family = binomial) \end{aligned}$$

Deviance Residuals:

```
  Min        1Q        Median    3Q        Max
 -2.2210    -0.5617    0.1270    0.6683    1.9910
```

Coefficients:

	Estimate	Std. Error	z value	Pr(> $\|z\|$)	
(Intercept)	3.463e+01	1.463e+01	2.366	0.017960	*
$\delta\Theta_M$	-1.734e+00	5.591e-01	-3.101	0.001931	**
δT_Z	-6.046e+01	2.858e+01	-2.115	0.034398	*
max_r	-6.074e+01	1.998e+01	-3.040	0.002365	**
s_p	-5.374e-01	2.247e-01	-2.391	0.016788	*
s_s	1.619e-01	4.458e-02	3.631	0.000282	***
$\delta\Theta_M : \delta T_Z$	2.506e+00	1.091e+00	2.296	0.021656	*
$\delta\Theta_M : max_r$	2.786e+00	7.658e-01	3.638	0.000275	***
$\delta\Theta_M : s_p$	2.579e-02	8.762e-03	2.944	0.003240	**
$\delta\Theta_M : s_s$	-5.148e-03	1.593e-03	-3.231	0.001234	**
$\delta T_Z : max_r$	1.025e+02	4.116e+01	2.490	0.012787	*
$\delta T_Z : s_s$	-1.302e-01	4.713e-02	-2.761	0.005756	**
$max_r : s_p$	7.294e-01	2.935e-01	2.485	0.012955	*
$s_p : s_s$	-6.748e-04	2.922e-04	-2.310	0.020911	*
$\delta\Theta_M : \delta T_Z : max_r$	-3.938e+00	1.530e+00	-2.574	0.010060	*
$\delta\Theta_M : max_r : s_p$	-3.228e-02	1.107e-02	-2.916	0.003544	**

```
---
Signif. codes:  0    ***    0.001    **    0.01    *    0.05    .    0.1
    ⤳     1


(Dispersion parameter for binomial family taken to be 1)

    Null deviance: 252.23  on 199  degrees of freedom
Residual deviance: 149.27  on 184  degrees of freedom
AIC: 181.27

Number of Fisher Scoring iterations: 7
```

The model confirms the previous observations. First, the *method* variable is not retained in the minimal adequate model. This means that the MMLM and the MLM cannot be separated based on this test. As it is now, the MLM version will be used in future measures as it is less computationally intensive.

The complex interaction structure is confirmed, and it is difficult to interpret it clearly. There is no clear range of the parameters were the two wave systems are always identified.

The range of the investigated parameters must be acknowledged. $\delta\Theta_M$ was always $> 10^\circ$ and

δT_Z could only vary between 0 and $0.5\,\mathrm{s}$ (equivalent to $5\,\mathrm{s}$ at full scale). It is expected that with wider ranges, δT_Z influence would have been stronger. As explained in Section 3.2.3 on page 26, the generation techniques may also mask the effect of δT_Z by limiting the wave system separation for bi-modal spectra exhibiting small $\delta\Theta_M$.

In term of accuracy and precision of the method, it is assumed that the results obtained for uni-modal spectra can be applied to each wave system of a bi-modal spectrum when the isolation method is successful.

4.6.2 Importance of adaptation to the wave characteristics

The sensitivity of the method (MLM plus isolation) to the error sources was analysed. The level of reflection r, the uncertainty in the wave angle of propagation ϵ_d and the error in probe position ϵ_p are considered. Due to the way the method is implemented, it is not possible to test the effect of the use of an inadequate frequency discretisation (see Section 4.2.4.1 on page 54). The method would simply not yield significant results.

Due to the complexity of the method, an analytical approach is not suitable. Instead, the sensitivity is estimated by running a large number of tests (600) with different level of the three considered factors. Tests were done using the final probe layout (see Section 4.5.4) and the wave elevations were generated from a Bretschneider spectra characterised by $H_{m0} = 0.05\,\mathrm{m}$, $T_Z = 0.75\,\mathrm{s}$ and $s = 15$ corresponding to $\Theta_S \simeq 10.3\,°$. For each iteration, a random level of error for each source was applied. The reflection coefficient range is $[0, 0.1]$, the uncertainty in wave direction range is $[0\,°, 1\,°]$ and the range of the error in probe position is $[0\,\mathrm{mm}, 2.5\,\mathrm{mm}]$. Details about how those errors are introduced into the virtual wave elevations are described in Section 4.3.

Three parameters were used to evaluate the method performances: the total difference ϵ_T as defined in Eq. D.1 on page 217, the normalised error over the integrated spreading parameter $\epsilon_{n,\Theta}$ defined in Eq. 4.30 on page 74, and the normalised error $\epsilon_{n,Hm0}$ over H_{m0}. ϵ_T relates only to the MLM whereas $\epsilon_{n,\Theta}$ and $\epsilon_{n,Hm0}$ relate to the MLM combined with wave system isolation.

4.6.2.1 Analysis of ϵ_T

Fig. 4.29 gives an overview of the sensitivity of ϵ_T to the 3 considered sources of error. Fig. 4.29a shows clearly that there is no influence of the error in probe position over the weighted difference. This is reassuring as a large array was specifically chosen to avoid issues related to this. Fig. 4.29b do not show any strong correlation between ϵ_T and ϵ_d but it is not possible to rule out completely the influence of ϵ_d: the minimum ϵ_T observed do seems to increase with ϵ_d. Finally Fig. 4.29c shows a strong correlation and curvature between ϵ_T and R_{coeff}.

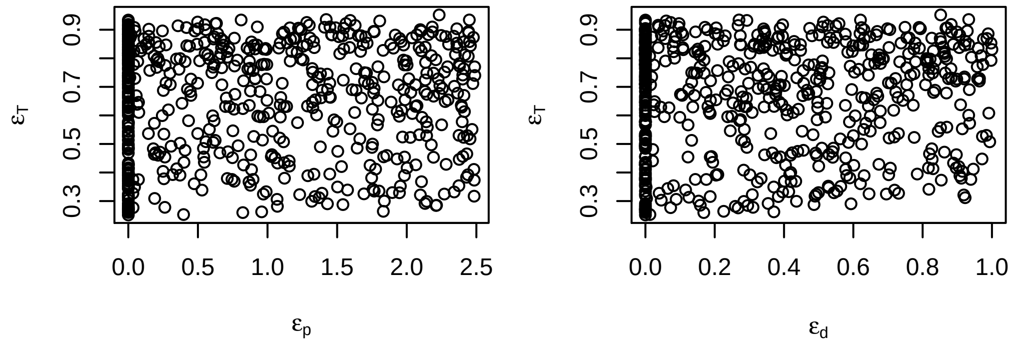

(a) ϵ_T as a function of ϵ_p *(b)* ϵ_T as a function of ϵ_d

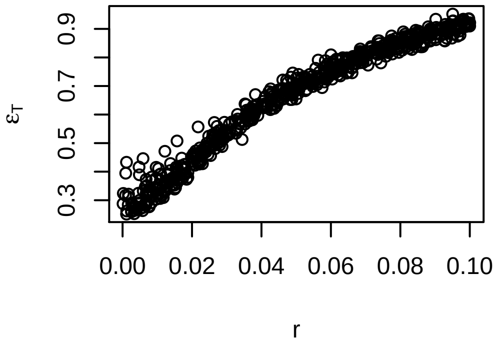

(c) ϵ_T as a function of R_{coeff}

Figure 4.29: *Observation of ϵ_T as a function of the 3 considered sources of error.*

None of the common transformation of ϵ_T (square, root or logarithmic) yield reasonable linear relation between ϵ_T and R_{coeff}. Hence, a piecewise multi-linear regression model is fitted to the data to take into account the observed the curvature. ϵ_d is introduced in the model as well as its interaction with R_{coeff}. The break point in the model is estimated by minimising the residual standard error with respect to R_{coeff} as shown in Fig. 4.30a. The linear model results in two different formulation depending on the breaking point. Eq. 4.36 shows the explicit formulation.

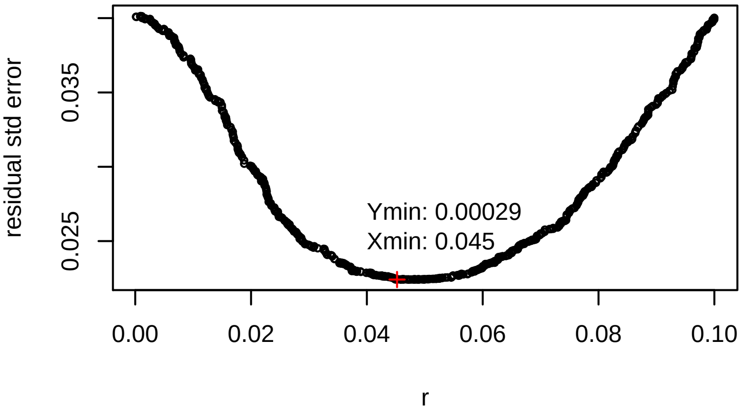

(a) residual standard error of the model fitted to ϵ_T as a function of the breaking point.

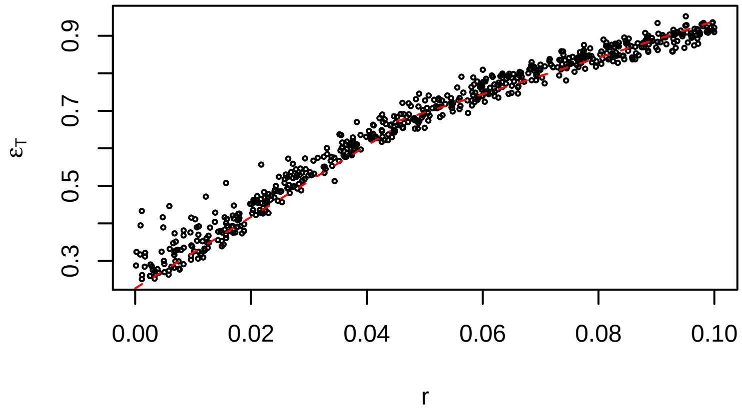

(b) multi-linear piecewise model fit the the observed ϵ_T as a function of R_{coeff}. Terms involving ϵ_d are neglected for the representation.

Figure 4.30: *graphic representation of the piecewise multi-linear regression model fitted to the observed* ϵ_T *.*

A graphic representation of Eq. 4.36 is given in Fig. 4.30b neglecting the terms involving ϵ_d.

$$\begin{cases} \epsilon_T = 0.227 + 0.0876 \cdot \epsilon_d + 9.51 \cdot R_{coeff} - 0.881 \cdot R_{coeff} \cdot \epsilon_d \ , \\ \qquad\qquad\qquad\qquad R_{coeff} \in [0; 0.045], \ \epsilon_d \in [0,1] \\ \epsilon_T = 0.452 + 0.0733 \cdot \epsilon_d + 4.87 \cdot R_{coeff} - 0.881 \cdot R_{coeff} \cdot \epsilon_d \ , \\ \qquad\qquad\qquad\qquad R_{coeff} \in [0.045; 0.1], \ \epsilon_d \in [0,1] \end{cases} \tag{4.36}$$

The summary of the model provided by *R* is available in Appendix D.2.4 on page 229. It shows that the difference of coefficient for ϵ_d is not statistically significant. However, the negative coefficient given to the interaction term leads to the conclusion that the influence of ϵ_d over

ϵ_T decreases as R_{coeff} increases. This test shows that wave reflection is the main parameter inducing a resolution degradation of the MLM.

4.6.2.2 Analysis of $\epsilon_{n,Hm0}$

Fig. 4.31 gives an overview of the sensitivity of $\epsilon_{n,Hm0}$ to the 3 considered sources of error. Concordant with the observation on ϵ_T, Fig. 4.31a shows clearly that there is no influence of the error in probe position over $\epsilon_{n,Hm0}$. No strong correlation between $\epsilon_{n,Hm0}$ and ϵ_d is exhibited in Fig. 4.31b, but again it is not possible to rule out completely the influence of ϵ_d: the maximum $\epsilon_{n,Hm0}$ observed decreases with ϵ_d. Finally, Fig. 4.31c shows a strong correlation and curvature between $\epsilon_{n,Hm0}$ and R_{coeff}.

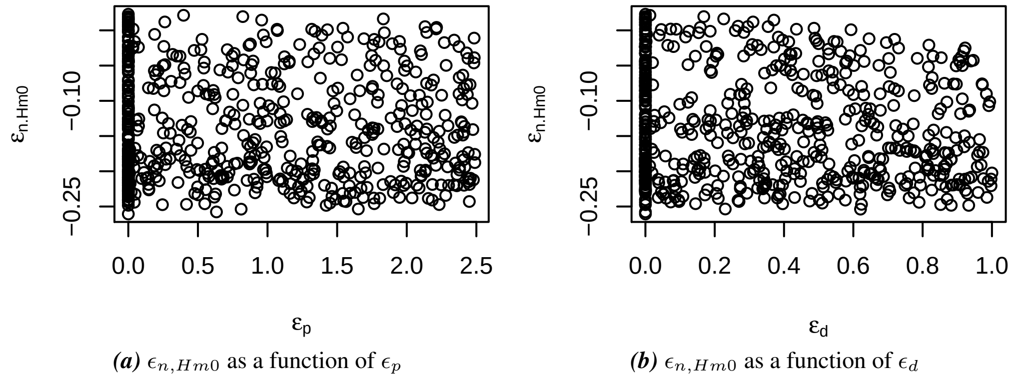

(a) $\epsilon_{n,Hm0}$ as a function of ϵ_p

(b) $\epsilon_{n,Hm0}$ as a function of ϵ_d

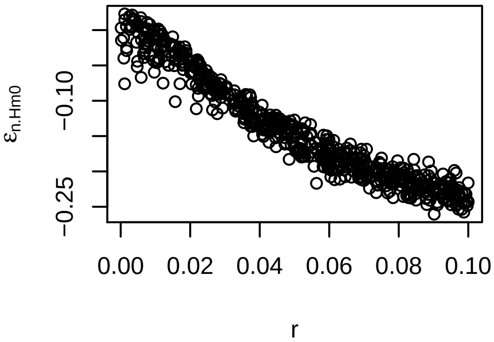

(c) $\epsilon_{n,Hm0}$ as a function of R_{coeff}

Figure 4.31: *Observation of* $\epsilon_{n,Hm0}$ *as a function of the 3 considered sources of error.*

As for ϵ_T, a piecewise multi-linear regression model is fitted to the data to take into account the observed the curvature. ϵ_d is introduced in the model as well as its interaction with R_{coeff}. The break point in the model is estimated by minimising the residual standard error with respect to R_{coeff} as shown in Fig. 4.32a. The linear model results in two different formulation depending

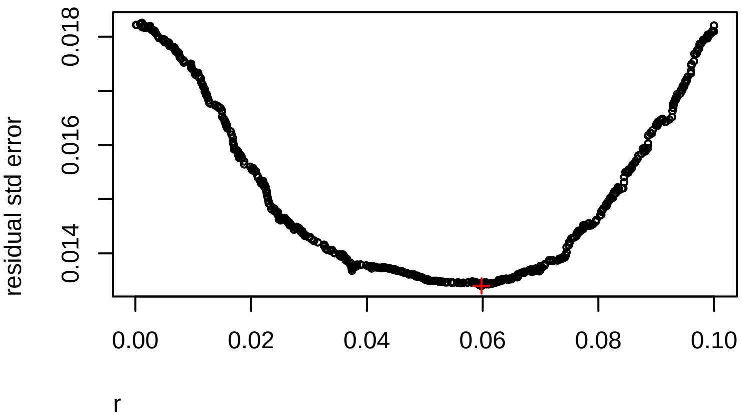

(a) residual standard error of the model fitted to $\epsilon_{n,Hm0}$ as a function of the breaking point.

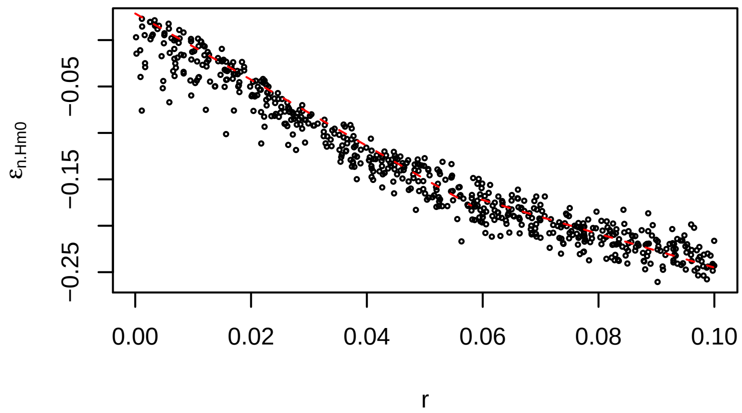

(b) multi-linear piecewise model fit the the observed $\epsilon_{n,Hm0}$ as a function of R_{coeff}. Terms involving ϵ_d are neglected for the representation.

Figure 4.32: *graphic representation of the piecewise multi-linear regression model fitted to the observed* $\epsilon_{n,Hm0}$.

on the breaking point. Eq. 4.36 shows the explicit formulation. A graphic representation of Eq. 4.37 is given in Fig. 4.32b neglecting the terms involving ϵ_d.

$$\begin{cases} \epsilon_{n,Hm0} = 0.0286 - 0.0542 \cdot \epsilon_d - 3.57 \cdot R_{coeff} + 0.910 \cdot R_{coeff} \cdot \epsilon_d \ , \\ \qquad\qquad\qquad\qquad\qquad R_{coeff} \in [0; 0.0598], \ \epsilon_d \in [0,1] \\ \epsilon_{n,Hm0} = -0.0629 - 0.0761 \cdot \epsilon_d - 1.82 \cdot R_{coeff} + 0.910 \cdot R_{coeff} \cdot \epsilon_d \ , \\ \qquad\qquad\qquad\qquad\qquad R_{coeff} \in [0.0598; 0.1], \ \epsilon_d \in [0,1] \end{cases} \tag{4.37}$$

The summary of the model provided by *R* is available in Appendix D.2.4 on page 229. Conclusions are similar to the ϵ_T, although the difference of coefficient of ϵ_d is marked as significant.

4.6.2.3 Analysis of $\epsilon_{n,\Theta}$

Fig. 4.33 gives an overview of the sensitivity of $\epsilon_{n,\Theta}$ to the 3 considered sources of error. There is a strong correlation between $\epsilon_{n,\Theta}$ and R_{coeff}, and ϵ_p and ϵ_d do not seem to have any influence. It must be noticed that the scatter in the observed data increases with R_{coeff} contrary to what could be observed in Fig. 4.29c and Fig. 4.31c. This means that a simple linear model as in the previous cases cannot be used (see Crawley (2007) on chapter 13) as the variance is not constant with the mean. A clearer view of the evolution of the variance is shown in Fig. 4.34a. It can be seen that there is a fairly linear relation between $var(\epsilon_{n,\Theta})$ and R_{coeff}. This is leading to fit a *generalised linear model* with *poisson* distributed error to the observed data. The summary of the model is available in Appendix D.2.4 on page 229 with the plots confirming the good fit between the model and the observed data. Fig. 4.34b gives a visual representation of the model.

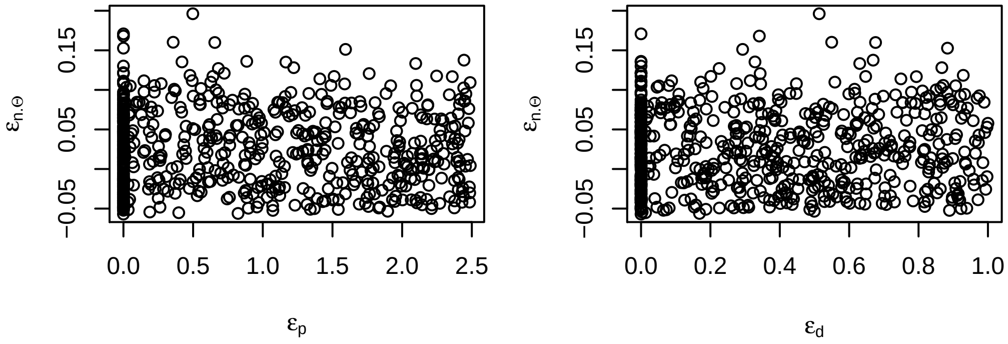

(a) $\epsilon_{n,\Theta}$ as a function of ϵ_p

(b) $\epsilon_{n,\Theta}$ as a function of ϵ_d

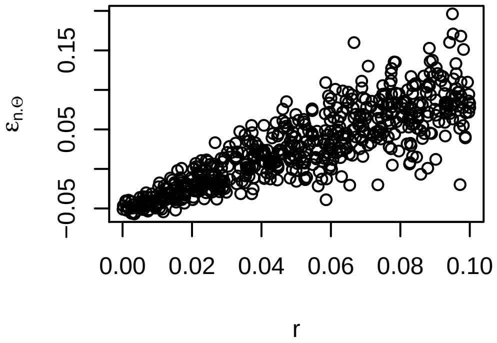

(c) $\epsilon_{n,\Theta}$ as a function of R_{coeff}

Figure 4.33: *Observation of* $\epsilon_{n,\Theta}$ *as a function of the 3 considered sources of error.*

The resulting model for $\epsilon_{n,\Theta}$ is presented in Eq. 4.38.

$$\log(\epsilon_{n,\Theta}) = -4.60 + 24.0 \cdot R_{coeff} \ , \quad R_{coeff} \in [0; 0.1] \tag{4.38}$$

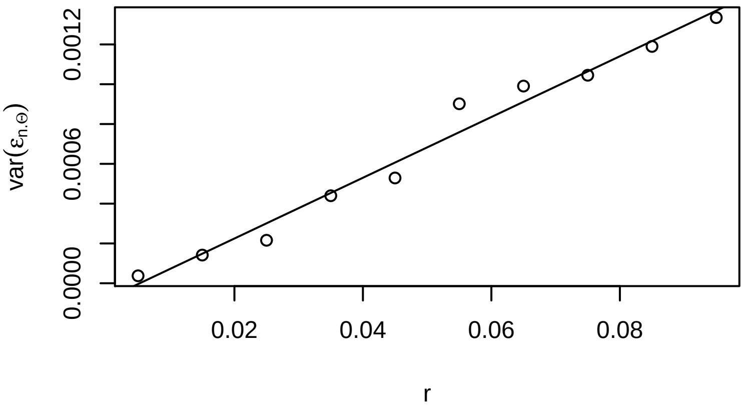

(a) evolution of $var(\epsilon_{n,\Theta})$ as a function of R_{coeff}.

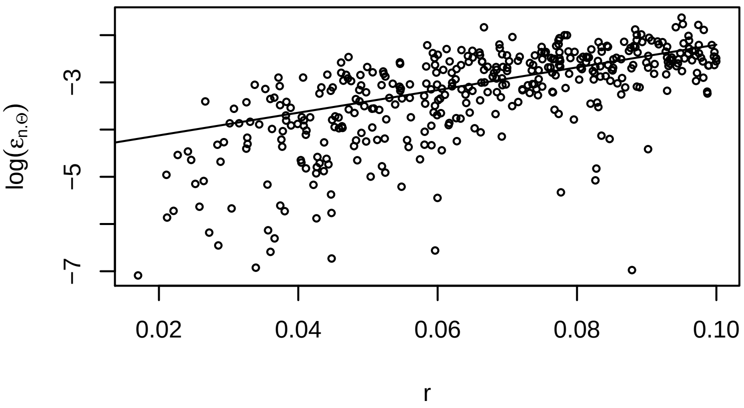

(b) Graphic representation of the model fit to the observed $log(\epsilon_{n,\Theta})$ as a function of R_{coeff}.

Figure 4.34: *Generalised linear model with Poisson distributed errors fit to the observed* $log(\epsilon_{n,\Theta})$ *as a function of* R_{coeff}.

The minimal adequate model for $\epsilon_{n,\Theta}$ does not retain any term involving ϵ_d or ϵ_p. It is probable that the higher scatter in the data is masking the more subtle effect of ϵ_d shown with the previous parameters.

Overall, it is demonstrated that the expected level of wave reflections in the tank have a much stronger effect when looking at the degradation of the estimates from the MLM combined with the wave system isolation. The rate of degradation of the estimates as a function of R_{coeff} was also shown to decrease while R_{coeff} increases, either trough piecewise linear relationship or by identifying a linear relation between $log(\epsilon_{n,\Theta})$ and R_{coeff}. The uncertainty in the wave front direction of propagations also have a statistically significant effect over $\epsilon_{n,Hm0}$ and ϵ_T but none has been identified over $\epsilon_{n,\Theta}$. When identified, this effect is also shown to decrease for higher value of R_{coeff}. Fig. 4.35 shows the effect on the spectral estimate of $\epsilon_{n,\Theta}$. Only the corrective term on wave angle uncertainty was added to the virtual wave elevation used to generate those graphs. They represent the spectral estimate before any smoothing is applied. There is clearly more noise in the estimate with error in angle direction of propagation than without.

It is also interesting to replace this sensitivity analysis in the context of the method precision study of Section 4.6.1.1. Fig. 4.36 shows in the same graph the observed $\epsilon_{n,\Theta}$ obtained during the unimodal virtual wave analysis, the maximum $\epsilon_{n,\Theta}$ observed in the sensitivity analysis and the predicted value by the model fitted to the observed $\epsilon_{n,\Theta}$ for $R_{coeff} = 0.1, \ \epsilon_d = 0$ and $\epsilon_p = 0$.

It can be seen that the predicted value (blue cross) lies very close to the lines resulting from the gam model. Its value represent 87.7% of it. The missing 12% are statistically not significant, but it is expected that the extra amount of errors included in the data would slightly increase $\epsilon_{n,\Theta}$. The conclusion of those combined study is that the level of reflection is by far the predominant factor driving the errors in all the studied parameters. Reducing the reflections in the tank is consequently seen as the best way to improve the directional wave measurement and should be the focus of any newly built directional wave tank.

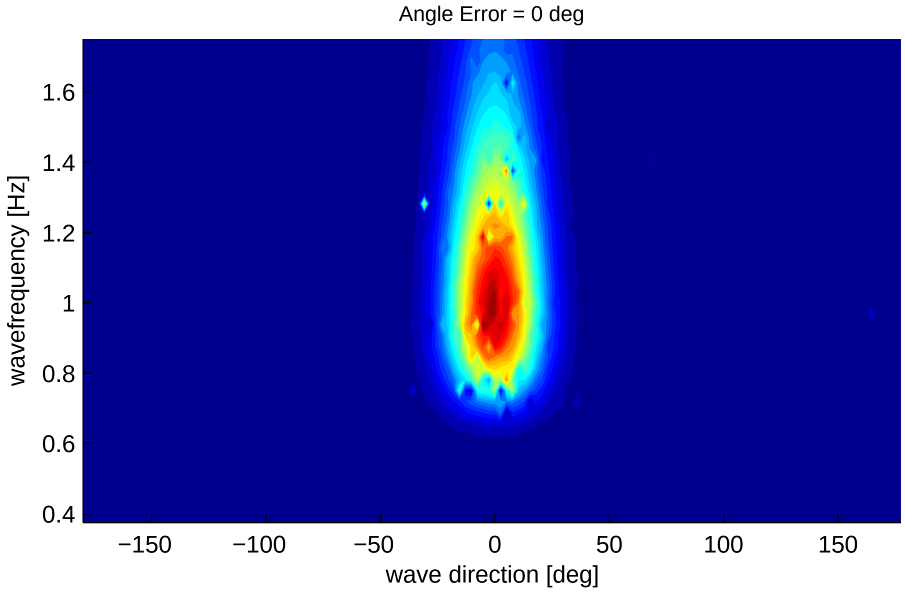

(a) Spectral estimate from the MLM without any error introduced in the virtual wave elevation

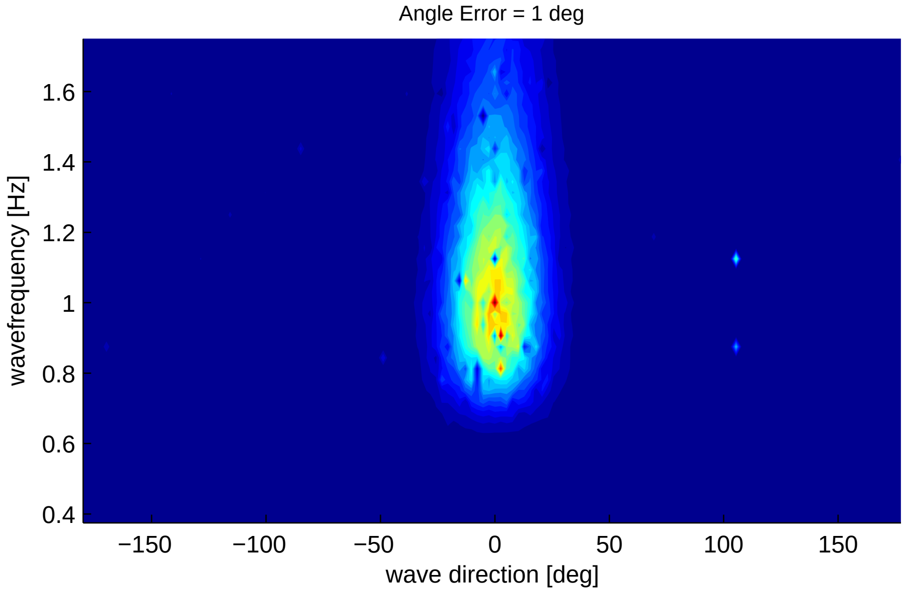

(b) Spectral estimate from the MLM with only error on the wave front direction of propagation introduced in the virtual wave elevation

Figure 4.35: *Comparison of the spectral estimate before smoothing with and without uncertainty in wave front direction of propagation.*

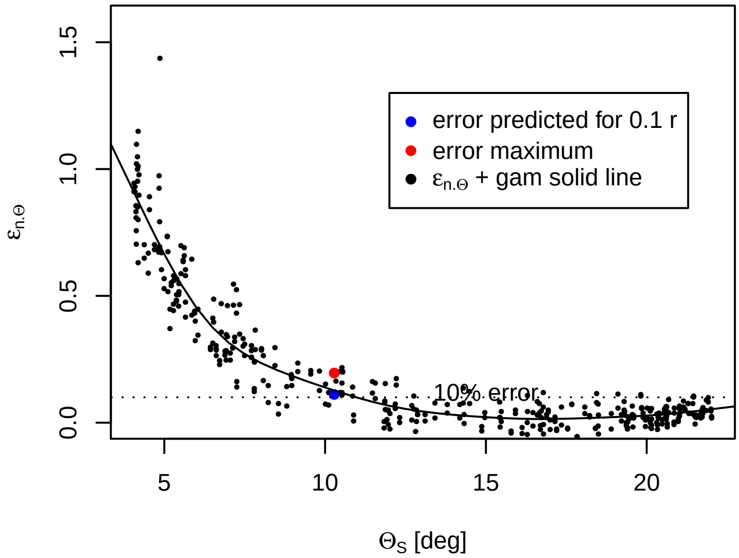

Figure 4.36: *Results of the sensitivity analysis over $\epsilon_{n,\Theta}$ placed in the context of the precision study. The black dots represent the observed value during the precision study, and the black line results from a gam model fitted to them. The blue cross results from the prediction of the model fitted to the observed $\epsilon_{n,\Theta}$ during the sensitivity analysis with $R_{coeff} = 0.1$, $\epsilon_d = 0$ and $\epsilon_p = 0$. The red cross is the maximum of $\epsilon_{n,\Theta}$ observed during the sensitivty analysis*

4.7 Comparison with *Wavelab™*

A short comparison with the industry standard, *Wavelab™(v3.34)*, has been done in order to evaluate the benefit of the method. *Wavelab™* allows the use of both the traditional MLM and the Bayesian Directional Method (BDM) (Benoit *et al.*, 1997). The BDM normally estimates narrower spectra and it is generally considered as the best performing method. The comparison is done using measured wave elevation in the tank. The spectrum used was the 3^{rd} run of wave 13 (see Table 6.2 on page 127). The BDM parameters are set in order to adapt the method as much as possible to the generated wave: 140 angles are used and no windowing is done for the cross-spectra computation. The first element of comparison is the running time. The Matlab built adapted MLM produced its spectrum estimate much faster (ten times) than the BDM implementation in *Wavelab™*. This is probably due to the fact that the cross-spectra calculations are limited to the range of interest during the MLM. Therefore, treating a large number of sea states will be much more practical with the method developed during this work.

The mean direction results are presented in Fig. 4.37 and the angular spreading in Fig. 4.38. The results are only valid in the $[0.4 \ 1.5]$ Hz range where the wave system as been isolated. The first impression is that the results from the BDM are less stable than the results from the MLM. This is caused by not using a frequency resolution matching the resolution of the generated

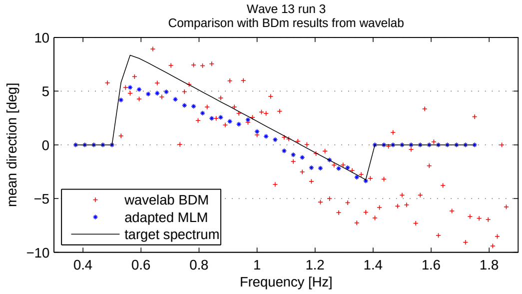

Figure 4.37: *$\hat{\theta}_{m,p}$ estimated by the BDM and the adapted MLM. The black line represents the target value.*

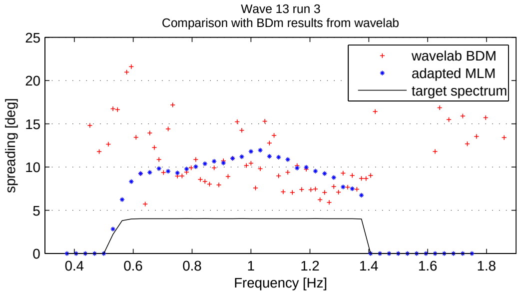

Figure 4.38: *$\hat{\theta}_{s,p}$ estimated by the BDM and the adapted MLM. The black line represents the target value.*

waves. The BDM tries to estimate the mean direction at frequencies where little energy has been produced, propagating at direction far off the target mean direction of propagation. As the MLM uses the same frequency resolution ΔF to compute $\hat{\theta}_{m,p}$ over a larger number of significant $S_{p,q}$, it can produce a smoother estimate.

The same type of observation is true for the angular spreading graphs. However, it can be seen that the BDM do produce a slightly narrower estimate while still being less stable over the range of interest. This really shows the advantage of the BDM over the MLM as the spreading estimates from the BDM were made over the full spectrum and not the wave system only. Knowing the MLM characteristics, the more stable $\hat{\theta}_{s,p}$ estimates of the adapted MLM across the frequency range might make it easier to get a real estimates of the wave system spreading. The BDM performance was good compared to the adapted MLM and it is suspected that much of the instability observed in the predicted $\hat{\theta}_{sp}$ and $\hat{\theta}_{m,p}$ will disappear if the same adaptation was done. As it is now, these results demonstrate the benefit of the adaptation of the MLM to the generated waves and the system isolation for the computation of the spectral estimates. The adapted MLM, with very short computational times, provided overall better results than their *Wavelab*^{TM} counterpart.

4.8 Discussion and summary

A novel implementation of the MLM and one of its derivative, the MMLM, has been done. Common measurements methods such as the MLM actually estimate directional spectra at specific points of the (f, θ) plan, effectively discretising the frequency spectrum. The contribution of this work is to ensure that the discretization of the (f, θ) plan is matching the discretization used for the wave generation.

The MMLM was considered as it takes into account reflection which are always present in the testing environment. However, a masking method had to be developed to minimize the effect of spurious peaks generated by the method due to the geometric constraint of the tank. Those peaks are extremely concentrated at angles of propagation equal to $\pm 90\,^{\circ}$. This is limiting the use of the MMLM to spectra with the energy restricted in the centre, away from the peak concentration. No specific study was conducted on this aspect to this date, hence it is not possible to issue recommendation about the maximum angular range that can be handled by the MMLM

The aim of these measurement was to consistently and precisely evaluate a list of sea state parameters. Some of these parameters, such as the angular spreading, must be defined relative to a wave system in case of multi-modal spectra. Hence, a wave system isolation method had to be used. The previous methods were more precisely dedicated to partitioning the spectra into wave system, instead of identifying the systems and isolating from each other and from the noise in the rest of the spectrum. This lead to the development of a novel method. It is based on the same idea as the previous one, i.e on the gradient at each point of the spectra, to attribute a point to a wave system.

In this chapter, this new method was tested with simulated time series. Chapter 6 on page 122 provides examples of the isolation method used with directional spectra estimated from tank measurements. The method was successful, both with uni-modal and bi-modal spectra, as long as the separation between wave systems in the estimated spectra was clearly visible. Visual evaluation shows that the wave systems are well tracked around the peaks. However, the method shows significant weakness in the tracking of spectra tails. This do not damage significantly the estimation of most parameters as spectra tails do not contain a significant part of the energy and the method was safely be used for the remaining of this work. However, spectral parameters such as the crest period T_c or even the zero-crossing period T_z based on the higher moments of the spectra could be affected.

The probe layout is always an issue in such study. Contrary to previous published research, the effect of uncertainty on the array geometry was incorporated in this work along errors due to noise or wave reflection. Using random generated arrays, the effect of the average distance between probes, the standard deviation of the distance between probes and the area covered by the arrays were studied using a large number of uni-modal spectra.
Compared to previous studies, it was shown that spatial aliasing is not the main factor to constrain the size of arrays. Small arrays not subjected to aliasing have proved to be more likely to overspread narrow spectra. This work shows that when the probe layout geometry is not perfectly controlled, it is better to accept some level of spatial aliasing to minimize the effect of error in the probe position. Spatial aliasing is also affecting primarily high frequency components of the spectra where there is less energy.

Overall, based on the simulated wave elevation used in this chapter, the MLM offered better performances than the MMLM. The MMLM did not show any significant resolution advantage estimating either uni-modal or bi-modal spectra.
In uni-modal tests, the MMLM consistently estimated broader spectra than the MLM. As it is also more computationally intensive than the MLM, it was decided to use the MLM for the rest of this work. A possible explanation is that the low level of reflection (10% in amplitude translating into 1.5% of the energy) do not deteriorate the MLM results as much as the MMLM results are affected by the presence of spurious peaks in the spectral estimate. However, these conclusions have to be taken with care as the spectral estimation methods were evaluated jointly with the wave system isolation techniques. There is maybe some interactions at play between the two stages of the sea state parameter estimation (1^{st}-estimation of the spectra, 2^{nd}-isolation of the wave system) that were not explored in details.
In bi-modal spectra tests, a statistical analysis of the success rate of the isolation technique to effectively separate both wave systems did not show any significant advantage of the MLM or the MMLM. This do not mean that they are equivalent, but only that if a difference exists it could not be identified with the currents tests.

The MLM abilities with the final probe layout to estimate key spectra parameters were characterised with simulated waves. A linear piecewise relation was established between the estimated spreading parameter $\hat{\theta}_S$ and the spreading parameter θ_S of the target spectra. It shows that θ_S is well estimated with an offset around $+4\,^\circ$ for $\theta_S > 10\,^\circ$. For narrower spectra ($\theta_S < 10\,^\circ$), the method cannot properly estimate the spreading parameter and the difference can be measured up to $+6.5\,^{\circ}$. f_s and T_z are well estimated by the method and no noticeable care is needed to interpret the method results. Finally, H_{m0} estimates shows a linear relationship between estimate and target values, but with a coefficient significantly lower than 1.

The sensibility of the method to the error in probe position, uncertainty in wave angle of propagation and wave reflection was also tested. The reflection results to be by far the dominant factor to explained the observed deviation between target and estimated parameters, The effect of probe position error is negligible. The uncertainty in wave angle of propagation has a faint effect that was identified in some cases, and its importances decreases as the reflection coefficient increases (negative interaction). The results of the sensitivity analysis are well matched with the results from the method accuracy exploration. It appears that the reflection alone are probably the cause of nearly 90% of the observed error on the integrated spreading parameter. Those results have to be considered with the test conditions in mind. The probe layout that was used was rather large, so it is not unexpected that the sensitivity to probe position is low. It would be interesting to repeat this part of the work using a smaller array and also to compare the results from both the MLM and the MMLM. Altogether, there is a lot of parameters that are involved to produce those results. This make any observations specific to the current setting. Such study should be repeated with the value of each parameters chosen in accordance to the experimental environment in which directional spectra measurement method will be used.

Finally, the MLM was compared to the BDM implemented in the industry standard *Wavelab™* using real wave elevation from the Edinburgh curved tank. The newly implemented MLM show as accurate and more stable spectral estimate across the considered frequency range, while the BDM is normally reckoned as a better performer. It shows that the adaptation to the deterministic waves characteristics was successful and generally improved the MLM performances. However, it is expected that similar adaptation to the BDM could be done, improving further more the BDM for the purpose of estimating directional spectra of deterministically generated waves. The MLM should retain a computing time advantages over the BDM and it is already showing good performances for all spectra but the narrowest ($\Theta_S \lesssim 12.8\,^{\circ}$).

Overall, the combination of the newly implemented MLM and wave system isolation method was judged precise and stable enough to use it for the estimation of directional spectra parameters required for this work. Detail results of the spectral analysis of the sea states used in this work are presented in the second part of this work.

Chapter 5
Wave Energy Converters description and characteristics

This chapter describes the WEC models utilised during the course of this work. The design and instrumentation of the scaled down WECs is detailed and the choice of damping for the OWC is presented. Some considerations on the repeatability of the power measurements are provided. The scaled oscilating water column are presented first, then the Duck is introduced.

5.1 The OWC models

5.1.1 Design

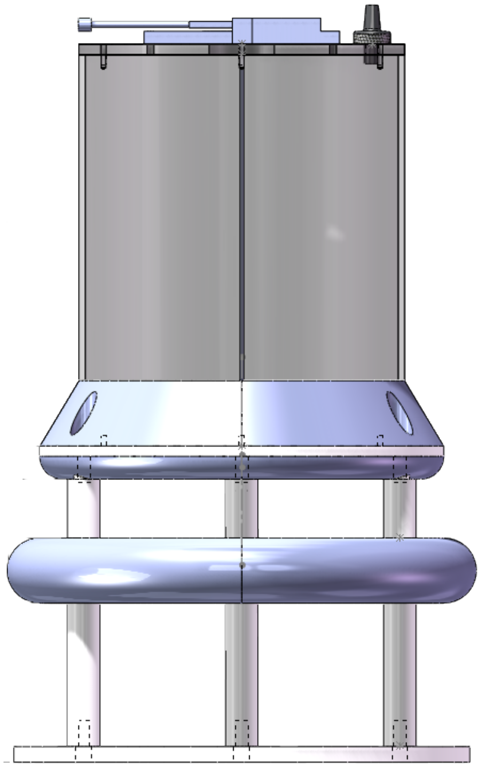

Figure 5.1: *SolidWorks model of the OWC provided by Queen's University Belfast.*

The main body is constituted of a $300\,\mathrm{mm}$ high column Perspex tube of $240\,\mathrm{mm}$ inner diameter. The designed immersion from the bottom of the column is $110\,\mathrm{mm}$, giving a theoretical resonating frequency of $1\,\mathrm{Hz}$.

The water entrance is set between the bottom of the column and a plate located $62.5\,\mathrm{mm}$ under it. The edges of the entrance are rounded as shown in Fig. 5.1 in order to reduce turbulences in the flow.

The power take-off is simulated by an orifice at the top of the column. The pneumatic power dissipated trough the orifice is estimated by measuring the volume of air flowing through the orifice and the pressure differential accross it.

For the first phase of tests, the devices are provided by Queen's University Belfast. They had to be replicated for the second phase. However, some change had to be made during the manufacturing process, which may induce some inconsistency in the results between the two phases. Differences between OWCs are described in more details in Section 5.1.4.1.

5.1.2 Instrumentation

The sensors consist of two wave gauges and a low pressure transducer.

The wave gauges are conductivity wave gauges and they require calibration on a daily basis (Pascal, 2006). Using a pair of wave gauges allows to reduce the error due to sloshing inside the water column. Some errors can be expected, particularly with high amplitude waves inside the column. In such cases, miniscus effects between the walls of the column and the rods can be visually observed. However, the measurement where satisfactory in much cases, and there is no particular source of concern. The volume of air flowing deducted from the wave elevation measures by numerical derivation.

The low pressure sensors are PX277-05D5V from *Omega*[1]. Sensors are pre-calibrated at the factory and do not need further calibration. The *high* pressure entry is link to the air chamber. The *low* pressure entry is open to the atmospheric pressure surrounding the experiment. The pressure sensors are set to deliver $\pm 10\,\mathrm{V}$ output for a $\pm 625\,\mathrm{Pa}$ pressure differential.

5.1.3 Power estimation

The average pneumatic power $\overline{P}$ dissipated through the orifice during each sea state is computed from the volume flow rate Q through the orifice and the pressure differential $P_{d,o}$ as shown in

---

[1] http://www.omega.com/pptst/PX277.html

Eq. 5.3:

$$\eta_o = \frac{1}{2} \cdot (\eta_{o,1} + \eta_{o,2}) \quad [m] \tag{5.1}$$

$$Q = \frac{\pi \cdot {D_{o,I}}^2}{4} \cdot \frac{d\eta_o}{dt} \quad [m^3 \cdot s^{-1}] \tag{5.2}$$

$$\overline{P} = \frac{1}{T} \cdot \int_0^T P_{d,o} \cdot Q \cdot dt \quad [W] \tag{5.3}$$

5.1.4 Performance characteristics

An initial investigation of the orifice characteristics is done in order to define a suitable setting for the rest of the experiments. This setting is kept for all the following tests.

As the OWCs are designed to be resonating at 1 Hz, the orifice characteristics is explored by measuring the energy produced by the column during 16 s with a incident 1 Hz regular wave. Three measures for each damper setting are taken. Fig. 5.2 shows the variation of the pneumatic energy as a function of the damper setting. From this test, the damper is set to 5 as this is the setting delivering the highest energy with very controlled errors.

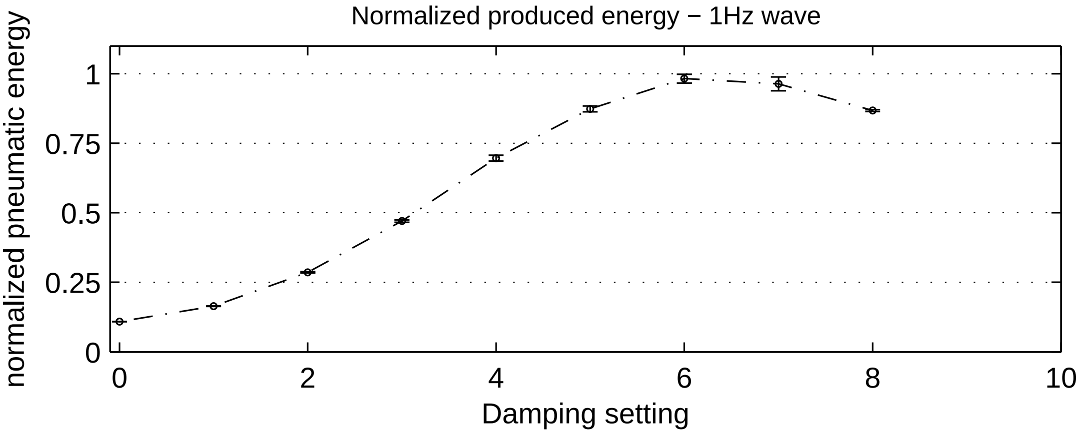

Figure 5.2: *Normalized energy produced as a function of the damper setting for* 1 Hz *regular waves. 0 is the highest damping possible (closed orifice). The larger error bars for damper setting of 6, 7 and 8 are due to measure uncertainty of the air flow associated with large amplitude of the water column. This was obtained with the first generation of OWC.*

It is important to acknowledge that the sensitivity of the OWCs to sea state parameters is a function of the damping level. The results related to the OWCs presented in this work are then only valid for the selected damping level. It is not expected that the structure of the device responses presented in Eq. 7.6 on page 150 and Eq. 7.10 on page 155 would be entirely different by changing the damping by a reasonable amount (10% - 20%), but the value of the coefficients would vary.

5.1.4.1 Difference between first and second set of OWC

As stated above, the OWCs had to be replicated for the second phase of tests. While most of the pieces were just copies of the initial ones, some parts had to be redesigned. A particularly important piece is the damper, which had to be made new. Fig. 5.3 provides a detailed view of the new orifice. However, the dimension of the *new* damper where slightly different, and it appears that the setting corresponding to position 6 and 7 on Fig. 5.2 could not be reach. Consequently, the plot cannot be reproduced for the second set of OWC. As a similar level of damping was necessary to allow comparison between the results of both phase, replication of

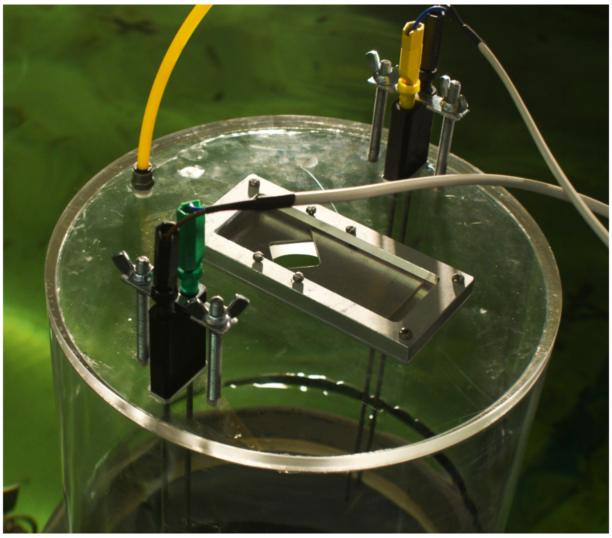

Figure 5.3: *Detailed view of the new orifice.*

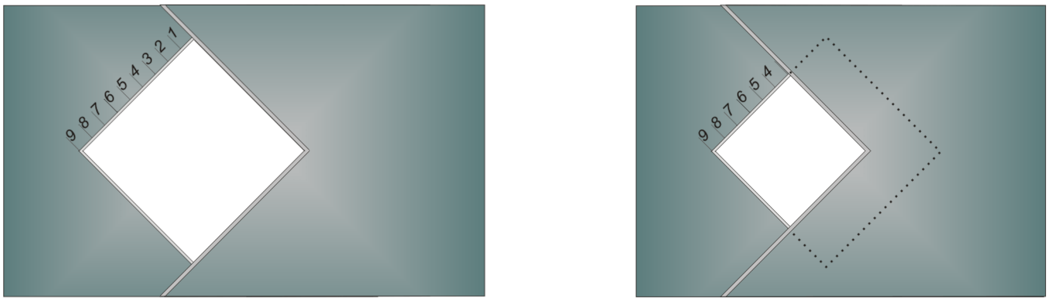

Figure 5.4: *Schematic of the new orifice and damper settings. The numbers represent the damper setting used in Table 5.1.*

OWC	Damper setting	energy produced [W]
First Phase		29.98
Second Phase	1	31.88
Second Phase	2	30.54
Second Phase	3	26.58

Table 5.1: *Results of the tests for the second set of OWC. The damper setting do not correspond to the damper setting of Fig. 5.2*

tests of the first phase were done to choose the good setting for the new damper. Sea state 13 was used (see Table 6.2 on page 127) and the results are presented in Table 5.1. From those results, a damping between 2 and 3 (see Fig. 5.4) was selected.

5.1.5 A double OWC: a weakly directional attenuator

The double OWC consists of two identical OWCs. The axis formed by the centre of each columns is aligned with the $0\,^\circ$ wave of the tank. The column centres are separated by $660\,\mathrm{mm}$. The disposition can be seen in Fig. 5.5.

Using a tandem of devices is the simplest possible model of an array. It is expected that the results could provide an insight into the influence of sea state parameters over array of devices.

5.2 The Desalination Duck model

As mentioned previously, the Duck model used during this work has been extensively tested at the University of Edinburgh during the last 4 years. While the intended testing ground always was the Edinburgh Curved Tank, the model was designed with a rather low resonant frequency. Depending of the configuration, it varies between 0.5 and $0.75\,\mathrm{Hz}$, which puts it definitely in the low range of the tank. The test planned for this work will be centred around $1\,\mathrm{Hz}$, so the duck will not be exploited at the maximum of its possibilities. This should not be a problem for the planned tests are there is no interest in the absolute value of the devices performances.

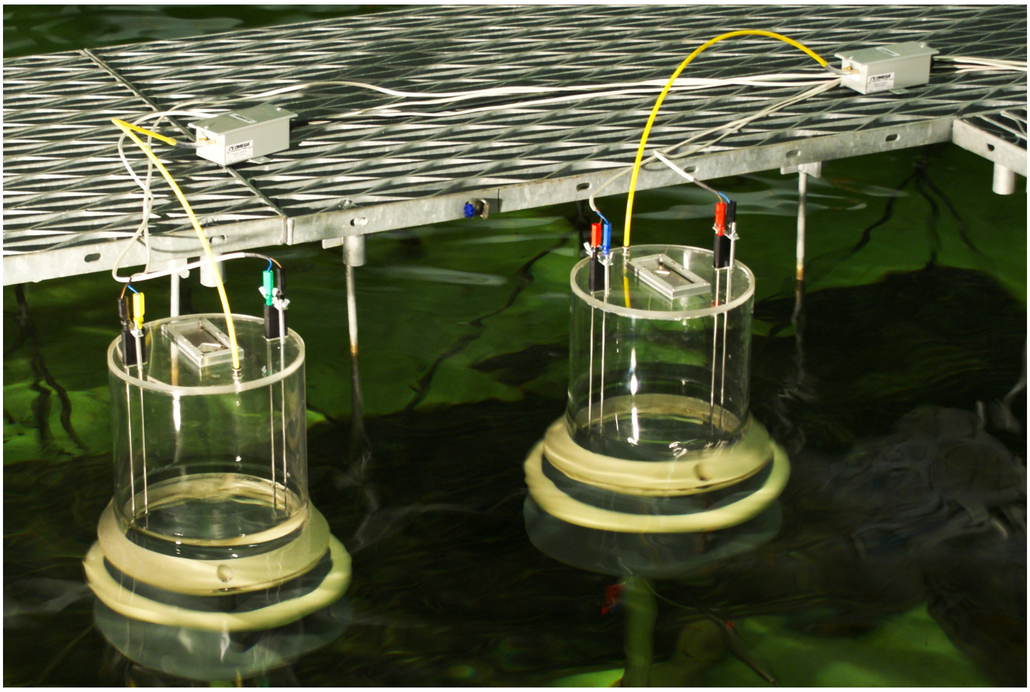

Figure 5.5: *Photo of the double OWC during the second phase of measurements. These are the second version of the OWCs.*

5.2.1 Design

5.2.1.1 main body and working principle

The desalination duck model is an evolution of the Edinburgh Duck design presented by Salter (1974). The came shape of the initial device was approximated by a cylinder pitching around an off-centre axis. The point here is to use a much simpler shape, a cylinder, to approximate the ideal device at a much lower cost. Most of the testing of the model at the University of Edinburgh was focused on assessing the performance lost due to the shape approximation. It should now be assessed relative to the cost saving associated if this device was to be developed for full scale operation.

The power take off of system is unusual: it is primary designed for water desalination instead of electricity generation. It is based on the action of a water pendulum occupying a bit more than half the volume inside the cylinder. The upper part of the cylinder is divided longitudinally into two separate chambers. While the cylinder is pitching, the water pendulum is compressing and decompressing successively each chamber and the pressure differential can be used to run a vapour compression desalination process. Salter *et al.* (2007) and Lucas *et al.* (2008) describe in more details the principle of ”pumping with waves”. Fig. 5.7 shows a schematic cut of the

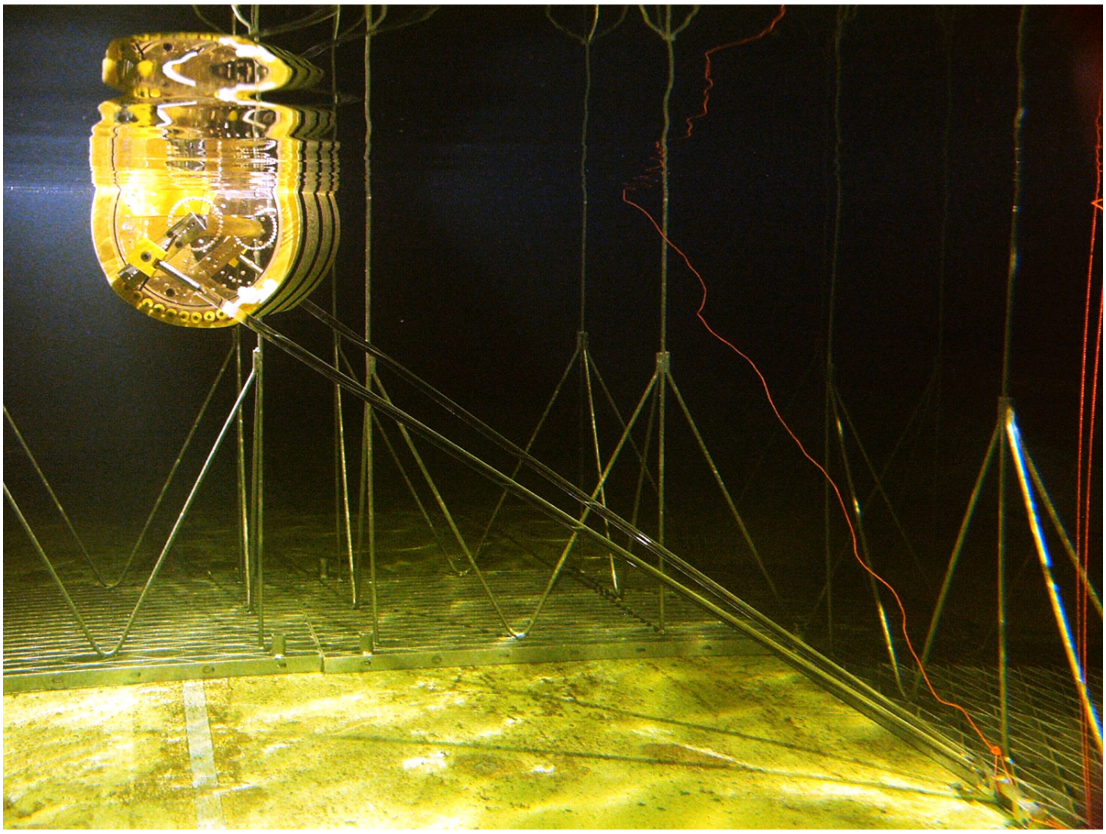

Figure 5.6: *Underwater photo of the desalination duck model moored in the Edinburgh Curved Wave tank.*

desalination duck.

In the model, the pressure differential between the two chamber is used to let an air flow passing trough orifices from a chamber to the other. The damping coefficient K_d of the orifices has been measured by Lucas *et al.* (2008). It allows to measure the power dissipated trough the orifices by knowing only the pressure differential across the chambers (see Eq. 5.4).

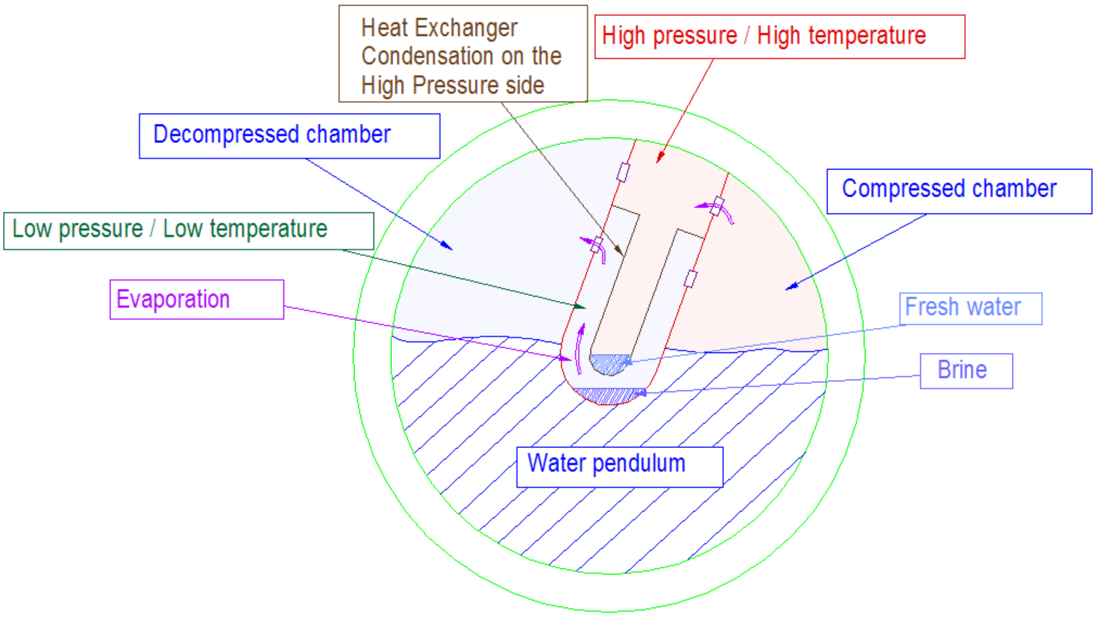

Figure 5.7: *Schematic cut of the desalination duck.*

5.2.1.2 mooring arrangement

The Duck model is moored to the bottom of the tank trough two rigid legs forming a triangle as seen on Fig. 5.6. The legs are made of a neutrally buoyant material so the mooring arrangement should be dynamically neutral.

At the bottom, the head of the triangle is linked to the foundation trough a joint allowing free rotation in pitch and yaw. When built initially, it was not though necessary to remove any constraint in roll, but later observation have shown that any imbalance of the duck body create a torque at the bottom which is transferred into a rotation along the yaw axis. This is slightly limiting the ability of the duck to align with the waves and could have generated unwanted effect, specially with bi-modal spectra.

On the Duck body, a systems allows to vary to attachment point of the legs, in order to effectively vary the position of the off-centre axis. The chosen combination (hole number 10, slider plate angle $15\,°$) is issued from work conducted by Lucas (2011). It is the combination for which the resonant frequency is the closest to 1 Hz, the centre of the range explored during this work.

5.2.2 Instrumentation

- The air pressure sensor: is is the most important instrument for the experiment of these study. The air pressure sensor allows the record of the pressure differential between the chambers during the experiments.
- The force sensor: for a more general assessment of the device and survivability tests, a force sensor is mounted on the fixation points of the moorings.
- The *Qualysis*® motion tracking system: an optical motion tracking is installed in the Edinburgh curved wave tank. It enables contact-less motion monitoring of a model in all the 6 axes of freedom. This will enable the evaluation of the duck model alignment with the wave direction of propagation. The pitch records can also be used as a proxy to the power trough the relation described in the following section. Fig. 5.9 shows the Duck model in still water with 5 markers used by the *Qualysis*® system.

5.2.3 Power estimation

The average pneumatic power $\overline{P}$ dissipated through the duck partition during each sea state is computed from the pressure differential as shown in Eq. 5.4:

$$\overline{P} = \frac{1}{T} \cdot \int_0^T \frac{{P_{d,d}}^2}{K_d} \cdot dt \quad [W] \tag{5.4}$$

with: $K_d = 29953.7 \quad [s \cdot m^{-5}]$ (Lucas *et al.*, 2008).

5.2.4 Relation between angular velocity and pressure

From the working principle of the Duck, a direct relationship between the angular velocity of the main body and the pressure differential across the partition is predicted. This relation was established for the configuration of the duck used during this work using the records of the second phase of tests (see Section 6.2 on page 126). The pressure records from the first phase turn out to be unusable due to problem with water getting inside the pressure sensor box. Fig. 5.8a show the established relation between the average pressure $\overline{P}$ and the average angular velocity $\overline{A_v}$. The markers of different colours and shape show the records from different runs. The black point is the only record of a sea state from the first phase. The test was repeated at the end of the second phase and was added to the curve to verify that the relation could be utilised to infer the power from the pitch records of the first phase of test.

A simple linear regression do not fit the observed data properly. Specifically, a linear regression between the average pressure and the average angular velocity requires an non-zero intercept, which is not possible. The square relationship presented offers a better fit, and crucially, the intercept is non-significant (the origin point is inside the confidence interval). During the pressure sensor calibration exercise, Lucas (2011) demonstrates that the damper itself was linear but some leakage were measurable. Those leakage are small orifices and the damping is quadratic is relation to the air flow in such cases. It is believed that the quadratic law observed in Fig. 5.8a is due to the contribution of the damper and the leakages.

Fig. 5.8bshows the actual relation used to derive the power from the angular velocity records. The square relation between the average power and the average angular velocity models the observed data very satisfactorily. It is presented in Eq. 5.5. The intercept is close to insignificant as it fell just outside the 95% confidence interval (dashed grey lines) of the model. The model provides good confidence in estimating the power from angular velocity records in the 0 to 50 °/s range. Where needed, the power will be estimated from the angular velocity records with :

$$\overline{P} = 4.093 \cdot 10^{-3} + 2.444 \cdot 10^{-4} \cdot \overline{A_v}^2 \tag{5.5}$$

Whenever needed, the angular velocity is computed as the absolute value of the derivative of the pitch records from the *Qualysis*® system.

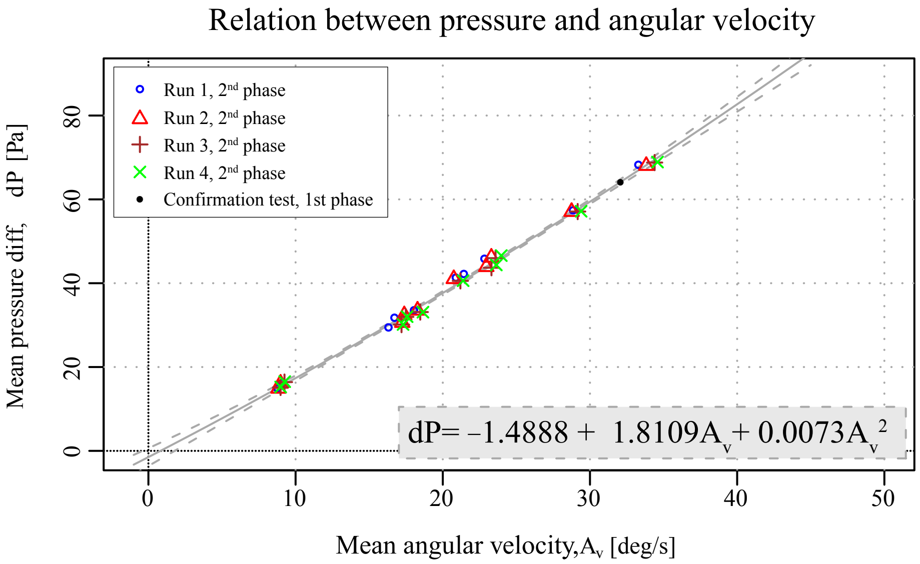

(a) Relation between the average angular velocity of the average pressure differential.

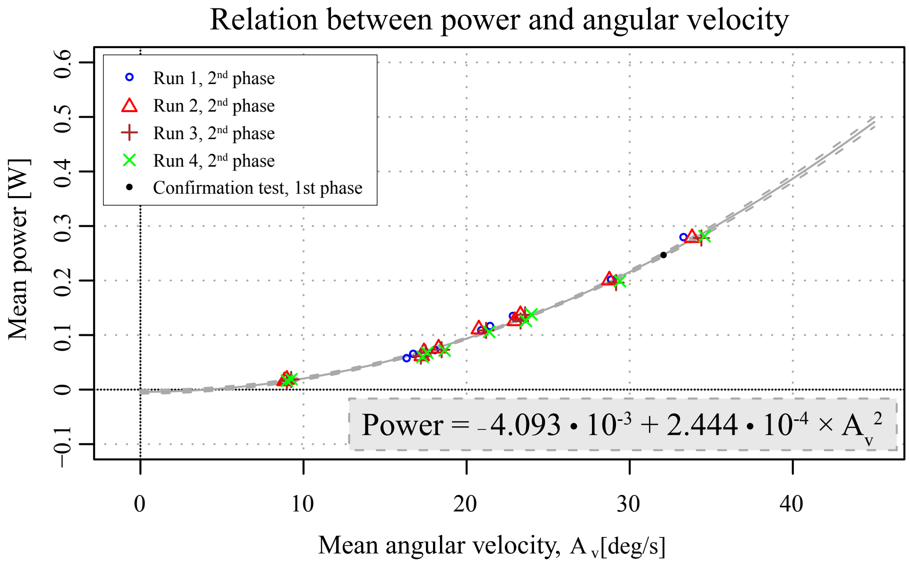

(b) Relation between the average angular velocity of the average power dissipated by the damper.

Figure 5.8: *Relations between the average angular velocity of the Duck and a) the average pressure differential across its chambers and b) the average pneumatic power dissipated in the damper.*

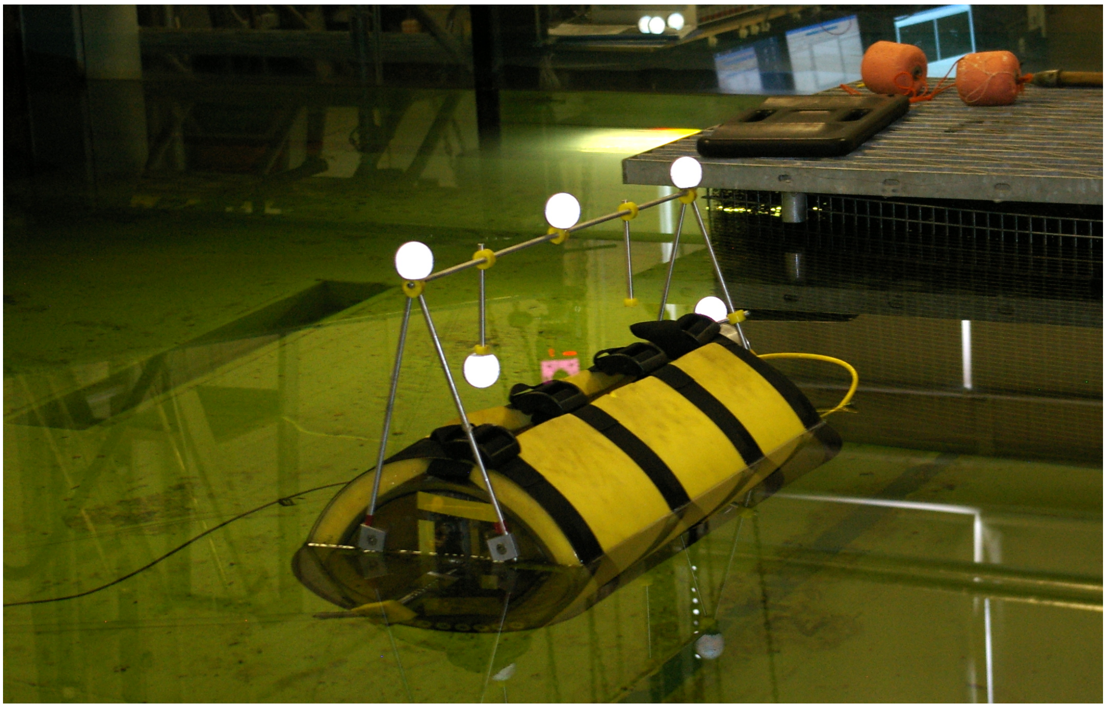

Figure 5.9: *The desalination duck model waiting for the waves to come. The model is equipped with 5 markers for the Qualysis® system.*

Chapter 6
Experimental plan

This chapter discusses the selection of sea state parameters included in the test plan. Justifications for including or discarding each parameters are provided.
From the selected parameters, an experimental plan is derived. Its main target is to allow the quantification of the influence of each selected parameters over the set of Wave Energy Converter models (see Chapter 5 on page 110) while keeping in mind the practical aspect of the testing environment.
Finally, the estimation of those parameters from tank measurements are presented. Comments are done about their consequences on methods used to analyse the device performances.

6.1 Sea state parameters list and discussion

As stated in Section 1.1 on page 1, the principal aim of this work is to question and maybe evolve the common approach to estimate power production from WECs. This common approach is based on the use of two wave parameters computed over the entire directional spectra: T_E and H_{m0}. Those parameters were initialy chosen as their knowledge is enough to estimate the energy in the sea state. However, they do not convey any information about the energy repartition across the (f, Θ) plan. An infinite number of sea states with the same T_E and H_{m0} can be observed.

In this work, the sensitivity of wave energy converters to other parameters is investigated. Those parameters are either taken from the literature or newly devised. They are separated into two groups. The parameters related to the shape of a wave system are considered first. Then a second set of parameters describing multi-modal sea states is introduced.

An upper limit in the number of considered parameters is required to keep the amount of hours of tank tests needed under a practical limit. It is inevitable that some simplification about energy repartition must be done. With this consideration, this work is limited to uni-modal and bi-modal sea states. Together they represents a large portion of the commonly observed sea states ($\approx 70\%$) as shown by Kerbiriou *et al.* (2007b).

6.1.1 Constrain on the parameters

In order to use a parameter for the performance estimation of wave energy converters, it must satisfies two constraints: 1) it must be possible to infer it from the directional spectrum $S(f, \theta)$ characteristic of a sea state, and 2) it must be possible to turn it into a statistical quantity describing the wave climate of a location by repeated sea states measurements over a long time period.

Individual directional spectra observed normally do not exhibit the standard spectral shape commonly used for modelling and testing WECs. Hence, it must be possible to compute the selected parameters from any spectral shape.

6.1.2 The selected parameters

The selected parameters included in the test plan can be classified into three categories. They are listed in Table 6.1. Their definition and mathematics formula has been presented in Table 2.1 on page 18 and Table 2.2 on page 18.

- omnidirectional parameters

  The first category includes parameters that are not linked to any wave system, such has the energy period T_E. Those parameters are the ones traditionally used in scatter diagrams. Only T_E is kept for the purpose of benchmarking the influence of other parameters. Its influence over different WECs can vary, and it could be interesting to see this variation in relation with the influence of other parameters. The energy period was preferred over other period period parameter as it is directly linked to the wave energy in deep water and most previous works investigating the estimation of performances recommend the use of the energy period.

- Spectral shape parameters

  The second category includes parameters that are linked to a wave system. The angular and frequency spreading parameters intent to measure and quantify wave system shapes.

Parameter	Symbol	Unit	Physical Meaning
omnidirectional parameters			
energy period	T_E	second	linked to the energy in deep water P_T $P_T = \frac{\rho g^2}{64\pi} T_E H_{m0}^2$
wave system specific parameters			
Local energy period	$T_{E,n}$	second	energy period of a wave system
Mean Direction Variability	$\delta\theta_{m,n}$	deg($^\circ$)	the coefficient of the linear regression fitted to the values $\theta_{mean,p}$ of the considered wave system
Local integrated angular spread factor	$\Theta_{s,n}$	deg($^\circ$)	wave spreading factor of the wave system.
Local integrated frequency spread factor	$f_{s,n}$	hertz	frequency spreading factor of the wave system.
relational parameters between wave systems			
uni-modality index	μ	-	$\mu = \frac{T_{E,1} \cdot H_{m0,1}^2}{\sum_i T_{E,i} \cdot H_{m0,i}^2}$
Period Difference	δT_E	second	$\delta T_E = T_{E,1} - T_{E,2}$
Mean direction difference	$\delta\theta_M$	deg($^\circ$)	$\delta\theta_M = \lvert\theta_{M,1} - \theta_{M,2}\rvert$

Table 6.1: *List of the parameters which influence over WECs is evaluated.*

As soon as two wave systems are present, those parameters have to be estimated separately for each system. A general spreading parameter for a multi-modal sea state is unlikely to be meaningful.

The variability of the mean direction of propagation as a function of the frequency is included to simulate the effect of waves created by a fast moving weather system. As long and short wave do not travel at the same speed, a variation in their main direction of propagation can be expected.

In the case of uni-modal sea states, the influence of omnidirectional energy period T_E and of the *isolated* energy period $T_{E,1}$ should be similar. They indeed represents the same physical phenomenon, but as stated in Section 2.3.4 their values may differ due to the isolation method. Only one of those two parameters is used in such case.

- Parameters linked to the relation between wave systems

  Finally, the third category groups parameters that describe relations between wave systems. Those parameters can only be defined for multi-modal sea states. Specifically, the index of uni-modality μ is introduced to quantify to which level a sea state can be considered multi-modal. For multi-modal sea states, the wave system noted 1 is the wave system conveying the most energy.

6.1.3 The discarded parameters

- The significant wave height

  In order to reduce the number of parameters to explore, the significant wave height is left out of this work. Only the energy period will be used for comparison with the other parameters. This choice was motivated by the hypothesis that all wave energy converters will be sensitive to the significant wave height H_{m0} while some non-resonant devices such as the wave dragon may show a limited sensitivity to period related parameters.

- The frequency dependant parameters

  For this part of the work, it is important to be select parameters which can be expressed as a single number for each sea state. The frequency dependant parameters do no comply with this requirement, therefore the level of details they provide on the spectral shape cannot be used at this level.

- The mean direction of propagation

  The initial plan of this work was to study the reaction of single wave energy converters to several sea state parameters. One of the main hypothesis was that deep water WECs are either omnidirectional or able to align themselves with the wave main direction of propagation. Consequently, the main direction of propagation of wave systems is only relevant to compute $\delta\theta_M$ for bi-modal sea states. The effect of the main direction in uni-modal cases was not to be tested and understanding the effect of the shape of the wave system was prioritized. It is acknowledged that the main direction of propagation would have its importance with deep water devices when array would be considered.

  With the introduction of the double OWC (see Section 5.1.5 on page 114), the hypothesis is no longer valid. However, the emphasis was kept as intended on the effect of the spectral shape of uni-modal spectra. Later work could explore the influence of the main direction of propagation, specially if arrays of wave energy converters are formally considered.

- Time series parameters

  Parameters related to time series had to be neglected. The waves generated in the Edinburgh Curved tank are deterministic, and it induces an error on the parameters statistics linked to time series and extreme values distribution. A detailed explanation is available in Tucker *et al.* (1984). This prevents a systematic study of the effect of those parameters.

Five realisations of each sea states with different phase spectra will be utilised to average out the effects of such parameters.

6.2 The tests: Method and Plan

A large number of sea state parameter are considered in this study. It is impossible to consider a full factorial design including all the parameters in one extensive experimental plan. It would require to much experimental time, and the subsequent data analysis will be extremely complex. Such a experimental plan might even be counter-productive if no significant results arises from it: confidence on the results and measurements is key, and complexity is not the easiest way to generated it.

The experimental plan is separated in two phases. The first phase is aimed at testing the influence of the parameters related to the shape of wave systems (group 2). The second phase is focused on the parameters helping to position wave systems relatively to each other (group 3).

6.2.1 First phase: uni-modal sea states

The four parameters relevant to this phase are: T_E, $f_{s,1}$, $\Theta_{S,1}$ and $\delta\theta_{m,1}$.

It is largely know that a linear relationship between T_E and resonating wave energy converters cannot be expected, so three levels are used for it. For the other three parameters, only 2 levels are used in order to minimize the number of combinations. The two levels of $f_{s,1}$ are generated by utilising two different *Types* of spectral shape: JONSWAP and Bretschneider. The angular spreading values are modelled with a $\cos^{2s}$ spreading function. s values of 5 and 100 are used. The two levels of $\delta\theta_{m,1}$ are achieved by varying $\tau_n = |\theta_{mean,max} - \theta_{mean,min}|$, expressed in degrees. The mean directions $\theta_{mean,p}$ of each frequency bands p (see Section 3.2.2 on page 22) are linearly set between the values taken by $\theta_{mean,max}$ and $\theta_{mean,max}$. The parameter τ_n is thus directly linked to $\delta\theta_{m,n}$.

Altogether, this leads to 24 combinations, and accounting for 5 runs of each, 120 different sea states. As three models are considered and adding the dry runs needed to measure the waves, a full factorial design needs 480 individuals measurements of $1024\,\mathrm{s}$, roughly accounting to $150\,\mathrm{h}$ of tests. This is considered to be to upper limit of what is manageable in the scope of this study. The list of sea states is described in Table 6.2.

Sea State	T_E	corresponding T_z	τ_n	Θ_S	Spectral shape
seaState 1	0.83	0.635	0	small	Bretschneider
seaState 2	0.83	0.665	0	small	JONSWAP
seaState 3	0.83	0.635	0	large	Bretschneider
seaState 4	0.83	0.665	0	large	JONSWAP
seaState 5	0.83	0.635	20	small	Bretschneider
seaState 6	0.83	0.665	20	small	JONSWAP
seaState 7	0.83	0.635	20	large	Bretschneider
seaState 8	0.83	0.665	20	large	JONSWAP
seaState 9	1	0.800	0	small	Bretschneider
seaState 10	1	0.830	0	small	JONSWAP
seaState 11	1	0.800	0	large	Bretschneider
seaState 12	1	0.830	0	large	JONSWAP
seaState 13	1	0.800	20	small	Bretschneider
seaState 14	1	0.830	20	small	JONSWAP
seaState 15	1	0.800	20	large	Bretschneider
seaState 16	1	0.830	20	large	JONSWAP
seaState 17	1.14	0.920	0	small	Bretschneider
seaState 18	1.14	0.960	0	small	JONSWAP
seaState 19	1.14	0.920	0	large	Bretschneider
seaState 20	1.14	0.960	0	large	JONSWAP
seaState 21	1.14	0.920	20	small	Bretschneider
seaState 22	1.14	0.960	20	small	JONSWAP
seaState 23	1.14	0.920	20	large	Bretschneider
seaState 24	1.14	0.960	20	large	JONSWAP

Table 6.2: *List of sea state used during the first phase of tests. The T_z is indicated as it is used to build up the spectra. The two levels of frequency spreading are generated using Bretschneider and JONSWAP spectra ($\gamma = 3.3$). The two levels of angular spreading are generated applying a $\cos^{2s}$ function, with $s = 5$ and $s = 100$ for the "large" and "small" values respectively. For all the sea states, the target H_{m0} = $60\,\mathrm{mm}$.*

It is important to note the *small* angular spreading corresponds to $\Theta_S \approx 4\,^\circ$. Due to time constraints, this value had to be chosen before the performance characterisation of the wave measurement method was completed. $4\,^\circ$ is unfortunately in the zone where the MLM cannot produce narrow enough spectra to yield satisfactory angular spreading estimates. Large scatter in $\hat{\Theta}_{S,1}$ for *small* values of Θ_S is therefore expected.

6.2.1.1 sea state measures

Measuring the actual values of those sea states is essential. The calibration of the Edinburgh Curved Tank is not fully established as no practical mean of refining it is available. Hence, differences between target and estimated values can find their cause either in the method inaccuracy or in the waves actually generated by the tank. Each of the 120 runs were recorded with the probe of arrays presented in Section 4.5.4 on page 78. The relevant parameters are estimated for each run using the MLM and the wave system isolation method where required. A summary the observations for each parameter is given in the following sections.
All the presented plots includes the parameters estimated after isolation (*estimated isolated*), as well as the parameters computed from the target spectra but using the boundaries of the system defined by the isolation routines (*target isolated*). The latest set of measures informs over the performances of the isolation routine.

$\hat{\Theta}_S$ Fig. 6.1 relates the observed $\hat{\Theta}_{S,1}$ in the tank to Θ_S. The values are slightly larger than expected from the virtual tests, with more scatter. As the only differences between those measures and the virtual test are the provenance of the wave elevation records (same generation method, same estimation routines and identical array), the differences have to be explained either by the inadequacy of the virtual wave elevation, or by extra variations present in the spectra. Given that the results are mainly sensitive to the level of reflection (see Section 4.6.2 on page 96) and that the 10% included in the virtual data is on the safe side (see Section 3.3.3 on page 40), it is believed that the differences observed reflects real variations of the generated spectra. The tank calibration used during those tests is the first possibility as described in Section 3.3.4. As the level of angular spreading is shown to vary more than expected, it is difficult to treat $\hat{\Theta}_{S,1}$ as a bi-level factor in the subsequent analysis. It will be introduced into the model as a continuous variable.

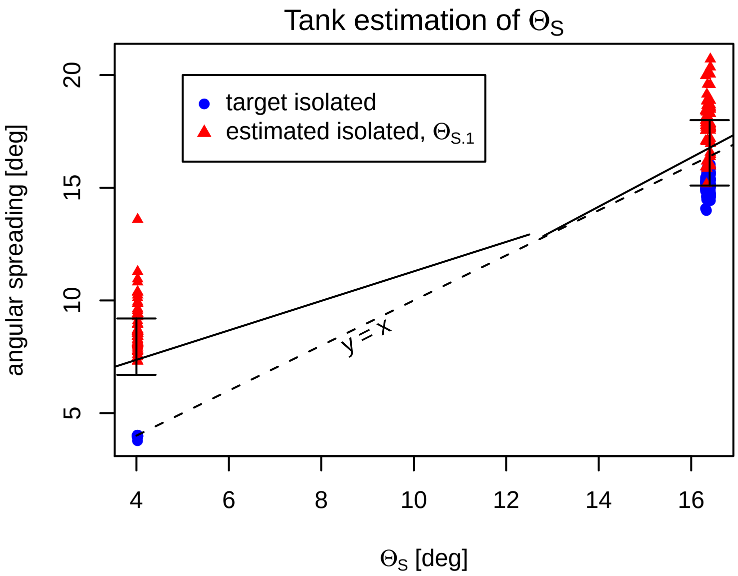

Figure 6.1: *Graphic relating the observed $\hat{\Theta}_S$ in the tank and Θ_S. The solid line is a reminder of the model estimated from the virtual data. The bars represent the scatter observed in the virtual data test. The dash lines represent the ideal case where observed and target values match entirely.*

$\hat{H}_{m0}$ While the initial test plan did not include any variation of H_{m0}, clipping of the high frequencies at 1.75 Hz, inaccuracies of the tank calibration and influence of the isolation routine introduce H_{m0} variations with respect to the spectra type, T_E and the angular spreading. H_{m0} is not specifically a directional parameter, so for uni-modal spectra one should be able to use an estimate of either H_{m0} or $H_{m0,1}$. However, selecting the right estimator for the significant wave height is problematic. The summary of the observed values in the tank given on Fig. 6.2 shows that none of the two estimates is entirely satisfying. Correlations between estimates of H_{m0} and other values can be observed:

- A negative correlation is observed between $\hat{H}_{m0}$ and T_E while there is a positive relation between the *target isolated* values of H_{m0} and T_E. The same trends can be observed with respect to $\hat{T}_E$. In both cases, $\hat{H}_{m0,1}$ appears to be decoupled from the energy period estimates. This suggests that $\hat{H}_{m0,1}$ should be the most relevant estimator for the significant wave height.
- The correlation between the significant wave height estimators and $\hat{\Theta}_S$ expected from the test with virtual waves is also present. $\hat{H}_{m0}$ and $\hat{H}_{m0,1}$ exhibit similar trends pointing towards higher significant wave height for broader spectra. This is thought to be the results of both the influence of the isolation routine and of the tank calibration.

The examination of the correlation defines $\hat{H}_{m0,1}$ as the most appropriate form. Also, $\hat{H}_{m0}$ does not separate incident and reflected spectra, which might be an issue while analysing the results from a directional sensitive device. However, $\hat{H}_{m0,1}$ values are low compared to $\hat{H}_{m0}$ ($\sim 60\%$), which would leads to higher than expected estimations of capture width in comparison with previous published studies. Finally, and for a consistency point of view, the *estimated simulated* significant wave height $\hat{H}_{m0,1}$ will be used for the performance analysis of the devices. $\hat{H}_{m0,1}$ and $\hat{H}_{m0,2}$ will have to be used with bi-modal sea sates to compute μ. However, the capture width of the devices will be estimated using $\hat{H}_{m0}$. It will make the numbers presented in this study comparable with other works.

$\hat{T}_E$ As $\hat{H}_{m0,1}$ is selected over $\hat{H}_{m0}$, $\hat{T}_{E,1}$ is preferred over $\hat{T}_E$ for consistency. Fig. 6.3 summarises the observations of the different energy period parameters relatively to the energy period of the specified spectra.

First, the *target isolated* and the *estimated isolated* observations are matching very well. It shows that the isolation routine is the driving force influencing the results. When the wave system is isolated, the target spectra and the estimated spectra have very similar energy period. $\hat{T}_{E,1}$ are consistently between 2% and 9% higher than $\hat{T}_E$ and this error do not vary significantly with T_E. This is probably explained by the isolation routine that is cutting the tail of the spectra, thus shifting the frequency parameters toward lower values.

In comparison, the omnidirectional parameter $\hat{T}_E$ estimated from the full spectra shows very different results. $\hat{T}_E$ values are consistently lower than expected, and the difference between $\hat{T}_E$ and T_E increases with T_E. The values of $\hat{T}_E$ do not show any scatter, indicating the the actual energy period of the omnidirectional spectrum in the tank (including incident and reflected spectra) is very well defined and results entirely from the specified spectra, the tank calibration and the reflection characteristics. A possible explanation for the lower than expected values of $\hat{T}_E$ is, as shown by Fig. 3.19 on page 44, the variability of the reflection with respect to the frequency. It is expected to be higher for low frequency waves, thus shifting the period parameters to larger values than the one specified.

The observed $\hat{T}_{E,1}$ are also not matching with the prediction for the virtual data tests. They are lower than expected, which reinforce the observation that energy periods of spectra generated in the tank are actually lower than specified. As $T_{E,1}$ should not be affected by the reflected spectra, this is an indication that the calibration of the tank itself could be adjusted.

Overall, the $\hat{T}_{E,1}$ are still very progressive, and there is not enough scatter in the data to bring

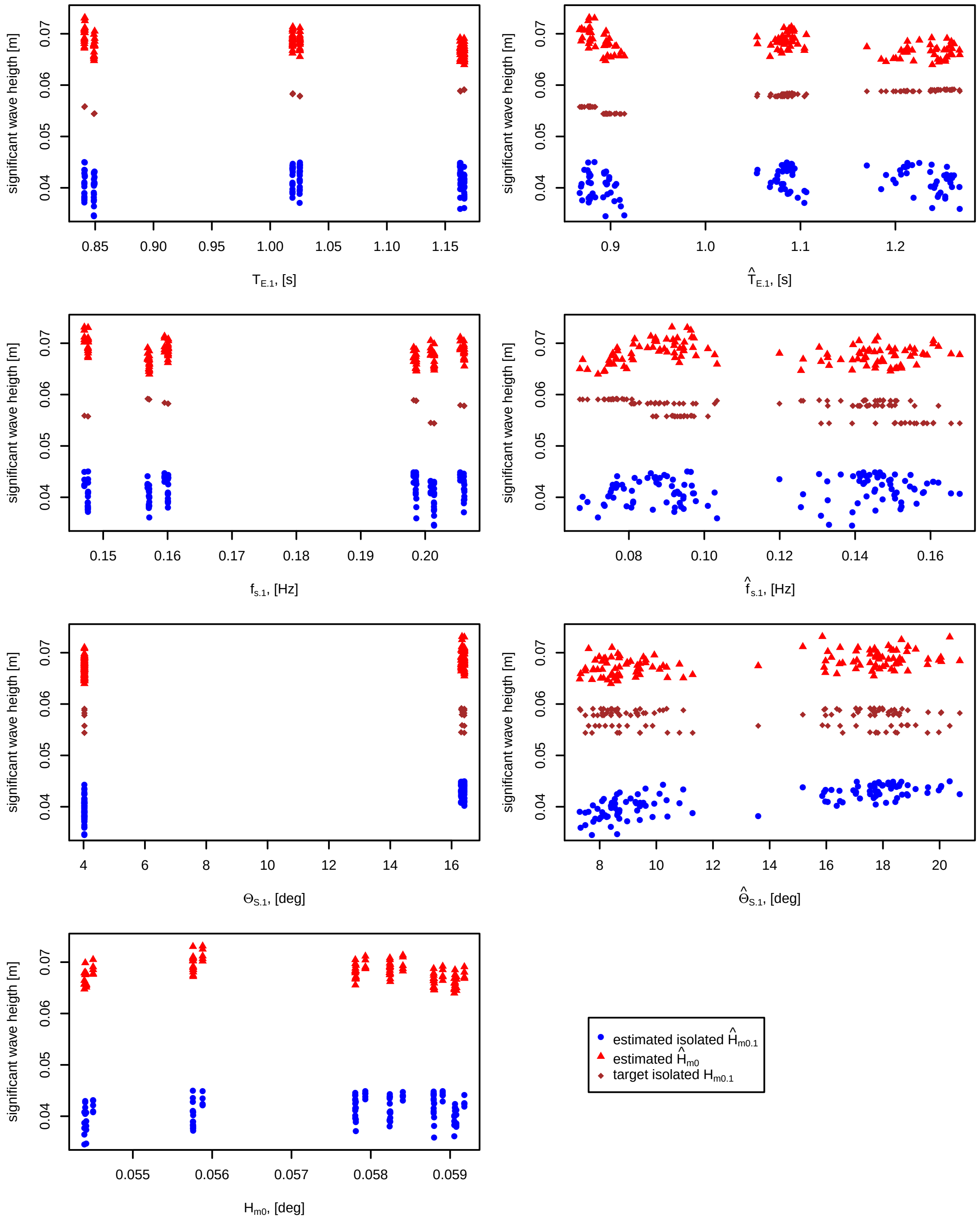

Figure 6.2: *Various significant wave height indicators of the first phase of tests presented with respect to the relevant spectrum parameters.*

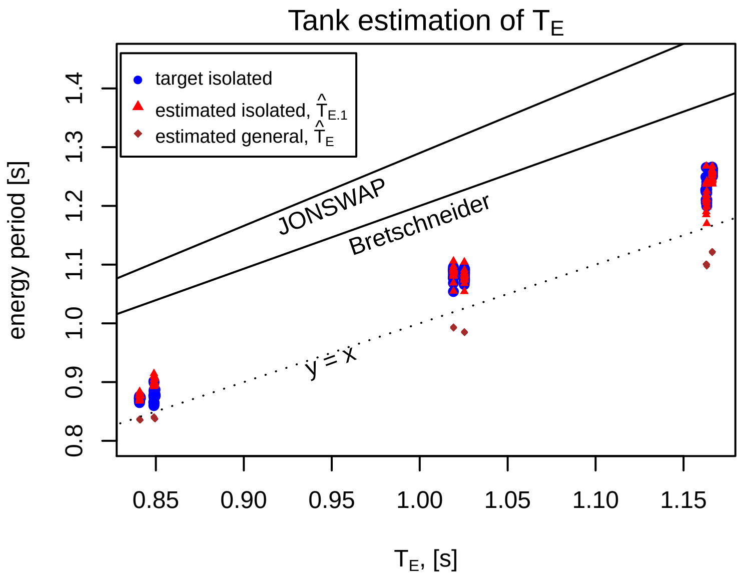

Figure 6.3: *Graphic relating the observed energy period parameters in the tank and T_E. The solid line is a reminder of the model estimated from the virtual data. The dash lines represent the ideal case where observed and target values match entirely.*

confusion between the three different level of T_E as specified in the plan. Nonetheless, $\hat{T}_{E,1}$ will be introduced as a continuous variable in the analysis of the device performances.

$\hat{f}_s$ Fig. 6.4 shows $\hat{f}_{s,1}$ as a function of f_s. The values are fitting relatively well with the model from the virtual wave testing, so there is no particular concern here. The same explanation given in Section 4.6.1.1 on page 84 applies. Despite the scatter in the data, it is possible to make a clear distinction between the two types of spectra, JONSWAP and Bretschneider. At this stage, it is not clear if the scatter in the data really represents variation of f_s for the same type of spectra or if its only an artefact of the measurement method. Alternative model using either the continuous variable $\hat{f}_{s,1}$ or the bi-level factor *Type* will be used in the subsequent device performance analysis, and the final decision will be made on comparing which model fit best the data.

Focusing on sea states 13 and 15 While it is not possible to give a detailed account of all measures, it is informative to presents the frequency dependant parameters ($\theta_{mean,p,1}$ and $\theta_{sp,1}$ introduced in Table 2.1 on page 18) for at least two different sea states presented in Table 6.2. Wave 13 and 15 are particularly interesting: they are both Bretschneider type so they cover a wide range of frequencies, the mean direction of propagation is varying with the frequency and

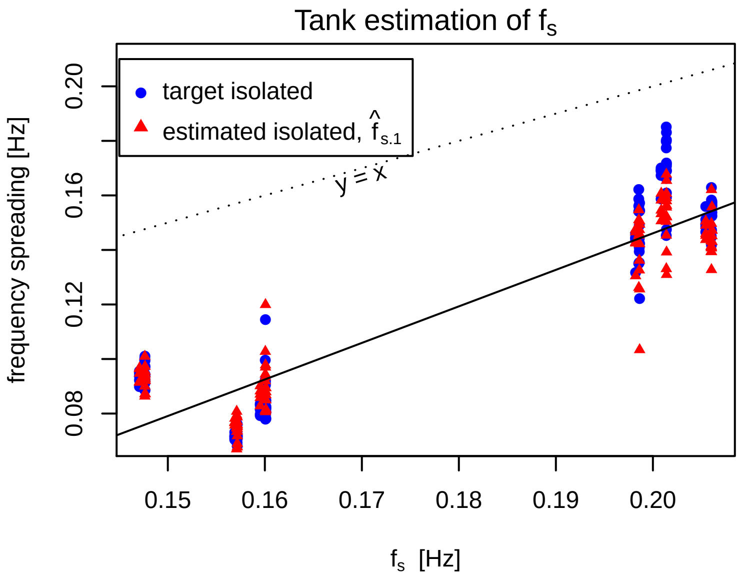

Figure 6.4: *Graphic relating the observed $\hat{f}_{s,1}$ in the tank and f_s. The solid line is a representation of Eq. 4.33 using the mean value of $\hat{T}_{Z,1}$. The dash line represents the ideal case where observed and target values match.*

the effect of angular spreading can be studied.

Fig. 6.5 and Fig. 6.6 show $\theta_{sp,1}$ and $\theta_{mean,p,1}$ for Wave 13 and 15 respectively. The mean direction and the angular spreading are estimated for each frequency. Two estimates are provided, one computed from the average spectrum estimated over the 5 runs of each sea states, and one computed as the average of the parameters computed for each run. *target isolated* values of those parameters are also presented. Finally, the omnidirectional energy spectrum is overlaid on the background of each graph to give an information about the relative importance of each frequency.

The first observation is that results are very consistent. Parameters estimated from the average spectrum and the average of the parameters over the runs concord very well. The error bars are showing that the scatter in the results is limited to a few degree in each case. It shows the repeatability of the tanks and any errors between estimated and target parameters can probably be interpreted as real characteristics of the generated incident spectra.

In the core of the spectra, where most of the energy is present, a close to perfect agreement between the target values and values obtained from the isolated wave system in the target spectra shows that the isolation routine is performing in a very satisfactory way. Only in the estimation of $\theta_{sp,1}$ of wave 15 (broad angular spectrum) the method can be shown to discard significant amount of the wave system as the observed values are considerably lower than the specified

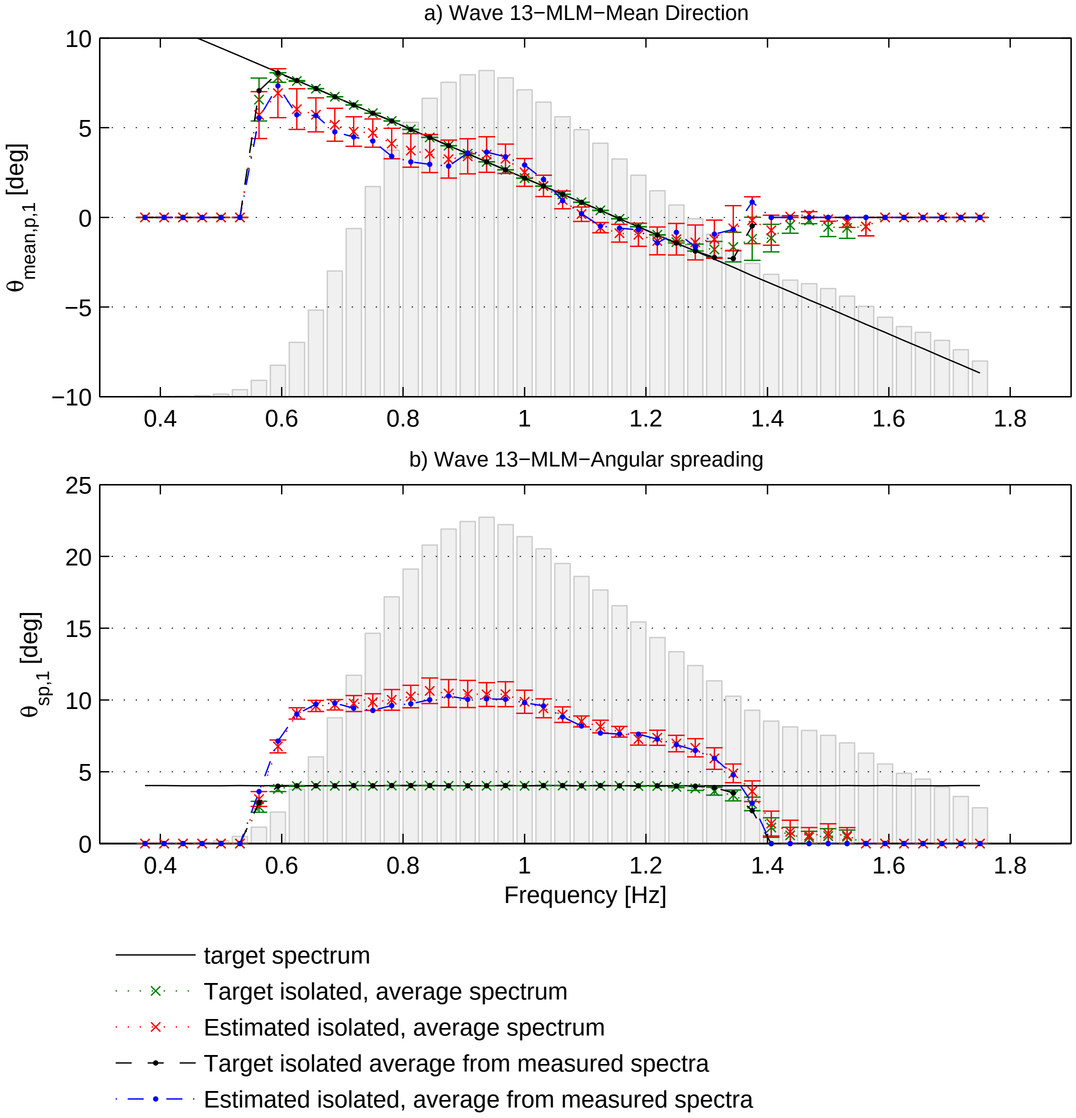

Figure 6.5: *Detail of $\theta_{mean,p,1}$ and $\theta_{sp,1}$ for wave 13 of the first test phase.*

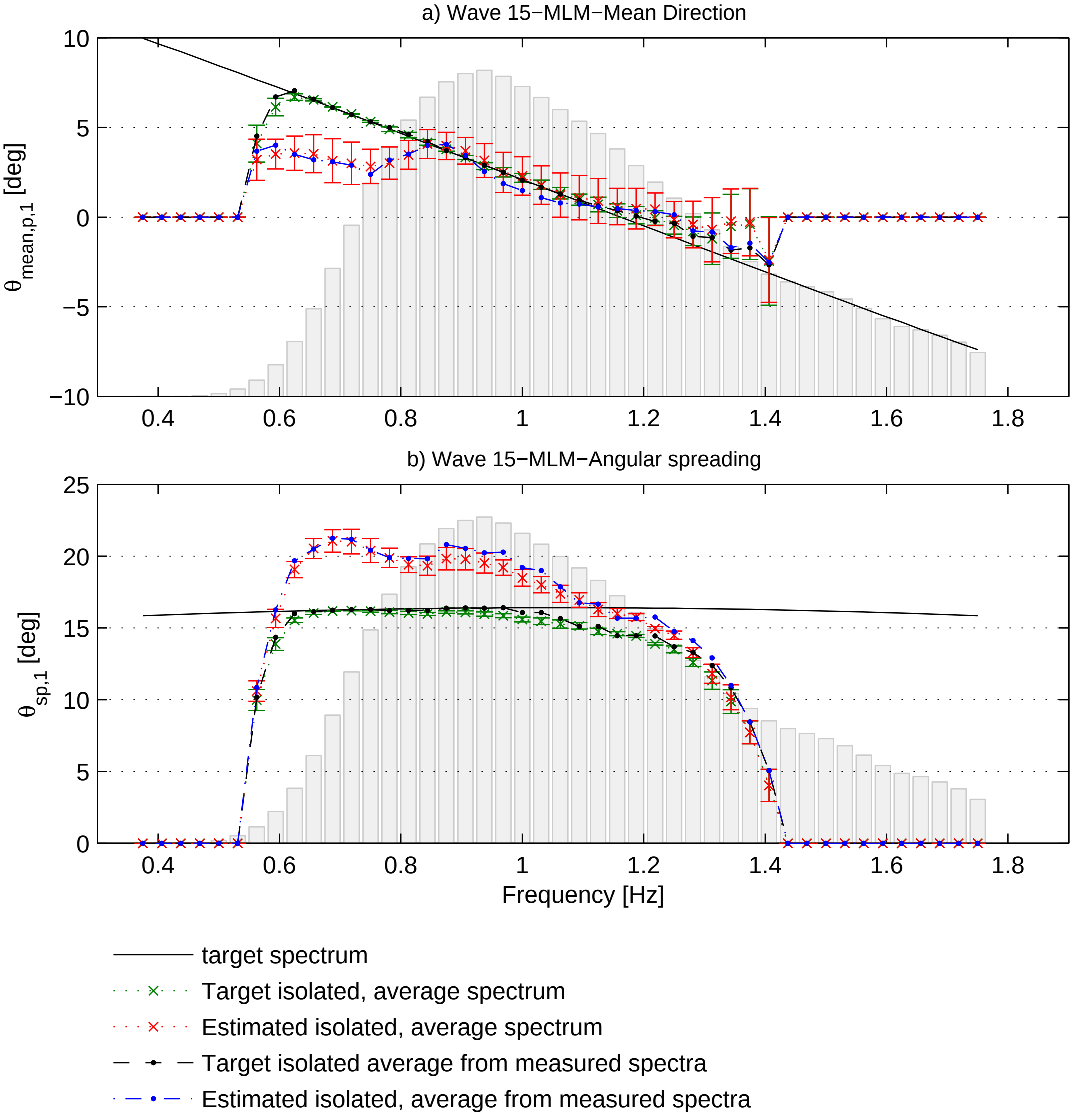

Figure 6.6: *Detail of $\theta_{mean,p,1}$ and $\theta_{sp,1}$ for wave 15 of the first test phase.*

angular parameter. This effect is specially visible for frequencies between $1\,\mathrm{Hz}$ and $1.4\,\mathrm{Hz}$.
For both sea states, it can be seen that the isolation routine clips the wave systems around $1.4\,\mathrm{Hz}$. Part of the spectra tails are clearly discarded. Some future evolution of the routine should focus on improving tracking of spectra tail.
From the mean direction graphs, it can be seen that estimating $\delta\theta_{m,1}$ is not very meaningful. The mean direction of propagation do not follow a linear evolution relative to the frequency as specified in the target sea states. It is believed that most of the difference observed between estimated and target values can be explained by the tank calibration. A decreasing trend can be identified, consistent with the target values, but it is expected that the effect of the variation of the mean direction over the performance of the devices will be difficult to identify.

Overall, the measures of waves 13 and 15 are in good agreement with the results on virtual waves, specially regarding estimates of $\theta_{sp,1}$. The details of the mean direction of propagation shows that the method can follow a slow variation of $\theta_{mean,p,1}$ as the scatter between measurements is contained to $\simeq 1\,°$. However, the observed pattern of variation of $\theta_{mean,p,1}$ show that the tank calibration as a significant effect over the spectral shapes and leads to the decision described in Section 3.3.4 on page 46.

6.2.1.2 Conclusion on uni-modal sea states

Measures confirmed that the waves generated by the tank are globally adequate for the tests. The *levels* of each parameters in the initial test plan can be identified at the exception of $\delta\theta_{m,1}$ which was the least relevant parameter.
The scatter observed in $\Theta_{S,1}$ measurements is higher than expected from the virtual wave data analysis. It is thought that the extra scatter is representing real variations of the sea states angular spreading and it might be important for the subsequent performance analysis of the devices. The measured values will consequently be used as a continuous variable instead of using the target values as a bi-level categorical factor.
The clipping of the spectra above $1.75\,\mathrm{Hz}$ also induces variation of $H_{m0,1}$ between the sea states. The variations might be amplified by the tank calibration which may not affect all generated sea states uniformly. A measure of the significant wave height must consequently be used in the analysis of the device measurements. The observations show that there is no ideal estimator. $\hat{H}_{m0,1}$ will be used for consistency as parameters specific to wave system will have

to be used in the case of bi-modal spectra and to avoid correlation with the energy period measurements. However, a positive correlation with the angular spreading might be a problem to isolate the effect of each parameter.

6.2.2 Second phase: bi-modal sea states

The second phase of the experiments is focused on exposing bi-modal spectra effects on devices. Due to the available frequency range, the maximum difference between the energy periods of the wave systems is set at $0.42\,\text{Hz}$ (see Section 1.5 on page 5). $\delta\Theta_M$, the difference between the mean direction of propagation of the systems is set to $30\,^\circ$. It is a compromise between the need to clearly separate the wave systems and the tank possibilities.

From the first phase results, the slope and the angular spreading of each wave system are discarded as shown in Section 7.2.2 on page 161. $f_{s,n}$ are also kept constant in most cases, mainly to reduce the number of test due to time constraints on the project and it is also expected that introducing a δT_E will have a stronger effect.

From the test with virtual data, it was clear that the most difficult type of bi-modal spectra to analyse for the method are the spectra with small $\delta\Theta_M$. In order to get a clear separation between the wave system for the case with $\delta\Theta_M = 0\,^\circ$, rather "steep" frequency spectral shape must be used and JONSWAP spectra were selected. After some early trial, it was found that the "peakedness" factor γ of the JONSWAP spectra shape had to be increased from the standard value 3.3 to 5 in order to insure that both wave system could be identified in the worth case scenario (wave 2 in Table 6.3). The standard $\gamma = 3.3$ was used in the cases were $\delta\Theta_M = 30\,^\circ$.

Sea State	$T_{E,1}$ [sec]	$H_{m0,1}$ [m]	$\Theta_{M,1}$ [deg]	$T_{E,2}$ [sec]	$H_{m0,2}$ [m]	$\Theta_{M,2}$ [deg]	γ
seaState 1	1.21	0.05	0	0.79	0.05	0	5
seaState 2	1.21	0.06	0	0.79	0.04	0	5
seaState 3	1.2	0.05	-15	1.2	0.05	15	3.3
seaState 4	1.2	0.06	-15	1.2	0.04	15	3.3
seaState 5	1.21	0.05	-15	0.79	0.05	15	3.3
seaState 6	1.21	0.06	-15	0.79	0.04	15	3.3
seaState 7	1	0.05	-15	1	0.05	15	3.3
seaState 8	1	0.06	-15	1	0.04	15	3.3
seaState 9	0.83	0.05	-15	0.83	0.05	15	3.3
seaState 10	0.83	0.06	-15	0.83	0.04	15	3.3

Table 6.3: *list of sea state used during the second phase of tests. The angular spreading are generated applying a $\cos^{2n}$ function with $n = 50$.*

A total of 10 sea states are defined. They corresponds to 5 relative positions of the wave systems. For each configuration, H_{m0} ratio of 1 and $\frac{2}{3}$ were used. With the range of frequency and wave direction available in the tank, other configurations cannot be configured. The variation of T_E for the sea states with $\delta T_E = 0\,\mathrm{s}$ will be used to evaluate the effect of δT_E, $\delta\Theta_M$ and μ in regards to the effect of $T_{E,1}$ evaluated during the uni-modal tests.

6.2.2.1 Calibration issues

An error in the way the wave gauge calibrated gains were used affected all wave measurements during the 2^{nd} phase of tests. The error was only uncovered in March 2011, much after all the testing for this work was finished. Fortunately, the data could be recovered so the presented measurements are as accurate as the 1^{st} measurements. However, 2^{nd} phase sea states were calibrated to have the same level of H_{m0} as 1^{st} sea states using the wrong set-up, which resulted in a $\sim 40\%$ overestimation of H_{m0}. The final situation is that 2^{nd} phase measures are accurate, but real H_{m0} levels are lower than 1^{st} phase H_{m0} levels.

6.2.2.2 sea state measures

Tests with virtual data (see Section 4.6.1.2 on page 90) did not allow to conclude on the superiority of either the MLM or the MMLM for analysing bi-modal spectra. The MLM was thus chosen as it is less computationally intensive. However, analysing wave records from the tank proved that the MMLM had a slightly better resolution than the MLM. Wave systems are more clearly separated. The difference between the method can be seen in Fig. 6.7a and Fig. 6.7b. The MMLM clearly distinguished the two peaks of sea state 3 of the second phase (see Table 6.3) while the MLM produce a directional spectra with only one peak.

It is not clear why the MMLM did not prove its superiority in the tests with virtual data. It could be either from differences between virtual data and real real that affect both method differently or the test was not well designed. Further investigation might be able to show the extend of the superiority of the MMLM over the MLM.

The sea states of phase 2 are analysed with the MMLM. Only two runs did not yield good separation between the wave systems or consistent estimation and are consequently ignored. The results of the other 38 runs are presented with satisfactory results. Fig. 6.8 shows a summary of sea state parameters estimations. The differentiation between the wave systems is clear as shown by the graphs b), d) and f). The estimation of $T_{E,n}$ are higher than the target values (see

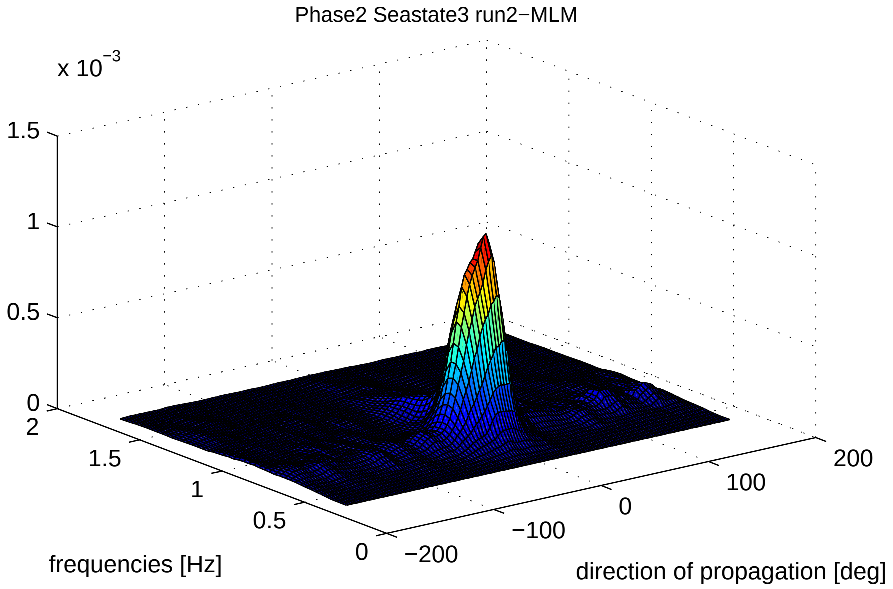

(a) Spectral estimate from the MLM of sea state 3 of the second phase.

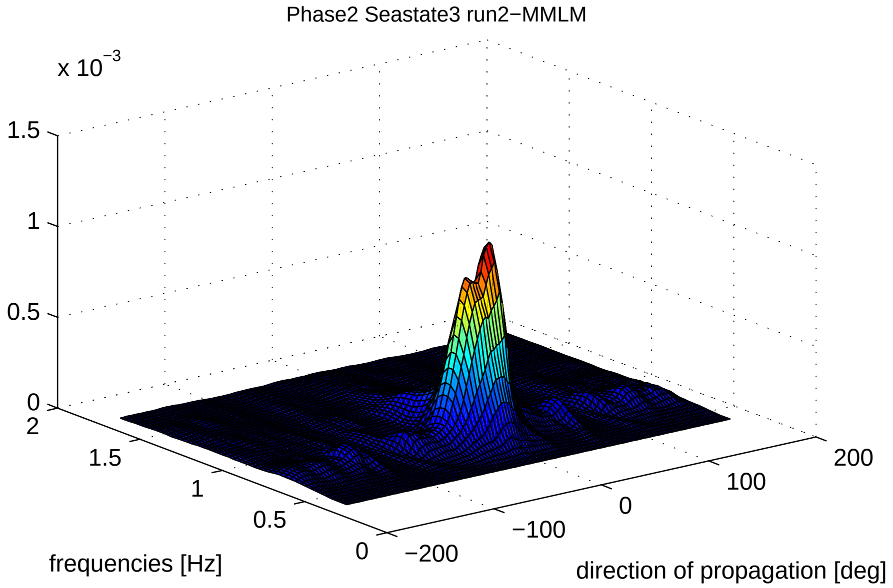

(b) Spectral estimate from the MMLM of sea state 3 of the second phase.

Figure 6.7: *Comparison of the spectral estimate of sea state 3 of the second phase by the MLM and the MMLM.*

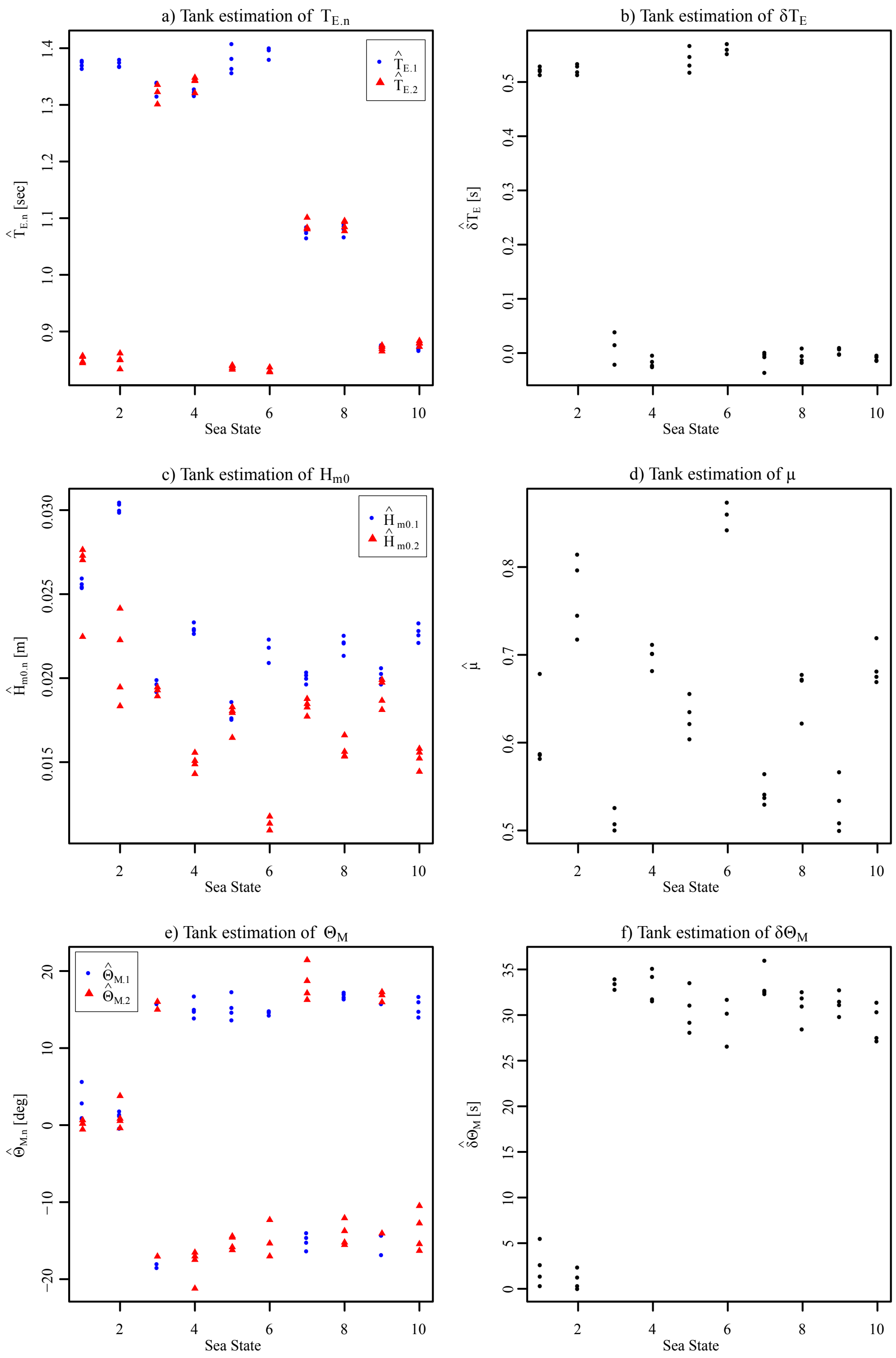

Figure 6.8: *Second phase, summary of the sea state analysis.*

Table 6.3) as expected from the uni-modal results. They are nonetheless very regular, and are perfectly usable for testing the devices.

$\hat{H}_{m0}$ is not as good. Sea states 1 and 2 exhibits higher values than expected compared to the sea states 3 to 10. It will introduce a bias into the sea states comparison. However, it is not possible to introduce $\hat{H}_{m0}$ into the models, as its variation will be entirely correlated with the variation introduced by $\delta\theta_M$, as shown by Fig. 6.9. Focusing the data analysis on the relative capture width may help to mask the effect of the variation of $\hat{H}_{m0}$.

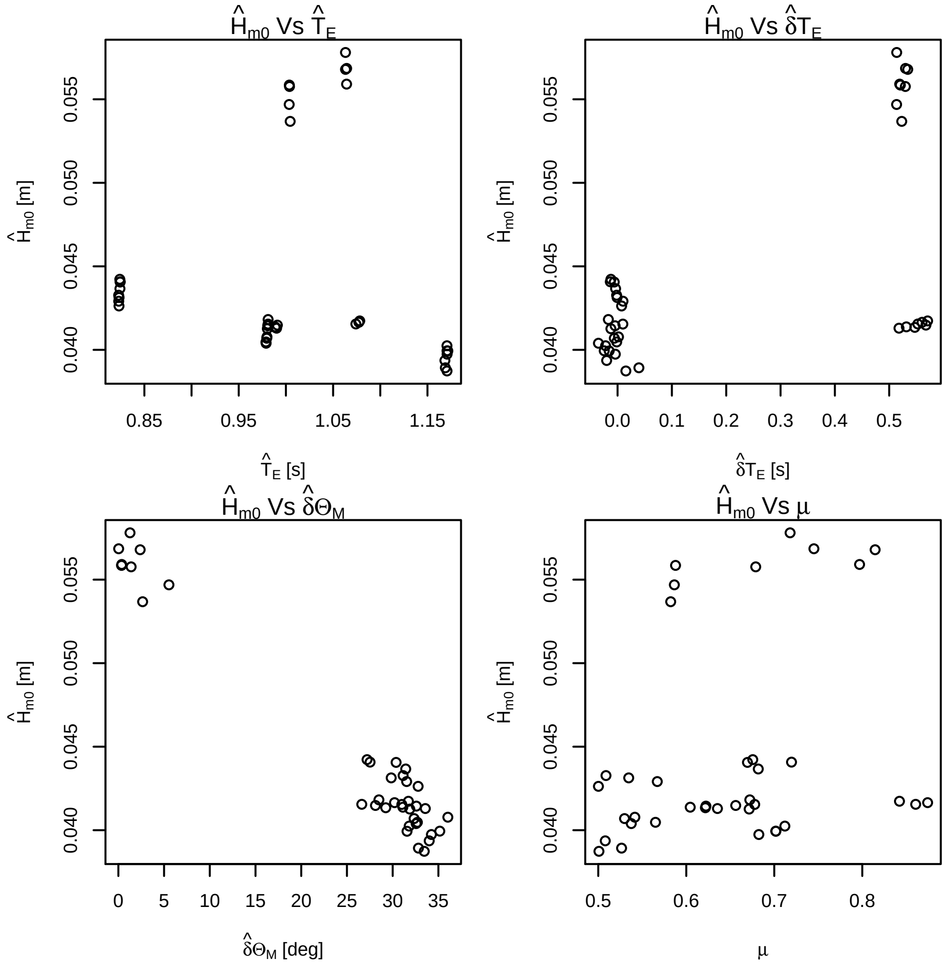

Figure 6.9: *Second phase, $\hat{H}_{m0}$ variation as a function of the other parameters.*

$\hat{\mu}$, the measure of bi-modality shows clear distinction between the pairs of sea states. The effect of bi-modality should be shown with its variation. Finally, the estimations of mean direction do not appeal for any special commentaries.

Overall, the tank and the MMLM have shown that bi-modal spectra with difference of 30 °

could be resolved. The MMLM and the estimation of the cross-spectra at wave-numbers matching the wave-numbers at which waves are generated proved to be a successful combination to estimate directional spectra in the tank. Those results also demonstrates the good control of the generated sea states provided by the Edinburgh Curved tank, with some exception for the significant wave height.

6.2.3 Chronology

The chronology of the measurements may help the reader to get a better appreciation of the results.

For each phase, the waves were measured first, then each device separately. The ideal setting would have been to measure everything in a randomised order, but this is not practical. However, for each item (waves, duck, single OWC and double OWC), the order of the measurements was randomised to average out external effect. The first runs of each sea states were measured first in a randomised order, then the second runs, up to the last. Table 6.4 gives chronological information about the tests.

Measures	Date	Observations
Waves 1^{st} phase	Mars-April 2010	5 runs
single OWC 1^{st} phase	April-May 2010	Queen's University Belfast OWCs. 5 runs
double OWC 1^{st} phase	June 2010	Queen's University Belfast OWCs. 4 runs
Duck 1^{st} phase	November 2010	Pressure sensor deficient. Power inferred from pitch records. 4 runs
Waves 2^{nd} phase	December 2010	4 runs
Duck 2^{nd} phase	December 2010	4 runs
double OWC 2^{nd} phase	January 2011	Edinburgh University OWCs. 4 runs

Table 6.4: *Chronological order of the measurements.*

6.2.4 Test phase: conclusion

Measurements in the tank confirmed the good quality of the wave generated. However, the default of calibration have been highlighted by the measurements. Those calibration errors are making it difficult to keep H_{m0} constant trough the tests. While the variation are kept under control for uni-modal spectra, bi-modal spectra have shown clear variation that will have to be addressed in the result analysis. Focusing on the capture width of the devices instead of the average power should help to hide the difference of H_{m0} between the sea states. With more time, a careful calibration of each sea states could decrease the variation of H_{m0}.

There is also some scatter observed in the parameter estimations. It marks a clear distinction from the experimental plan which was considering factors instead of continuous variables. In most case, the scatter is believed to be true features of the generated waves but for $f_{s,n}$ were no clear clue of the scatter origin is identified. Consequently, the statistical models of the device performances will use the parameters as continuous variables. Only the effect of $f_{s,n}$ will be modelled alternatively by a bi-level factor or by a continuous variable.

Chapter 7
Results

This chapter describes and interpret the results from the WECs models tested in the tank during the first and second phase of test. For the first phase (uni-modal spectra), an analysis of the results of each devices is provided separately and the possibility of defining parametric models for the power output of the devices is investigated. Some remarks about interactions between the 2 OWCs are also provided. For the second phase (bi-modal spectra), an attempt to characterise the data is done and a discussion about the relevant parameters for this type of sea states is started.

7.1 The retained performance indicators

The purpose of this study is to establish and compare the impact on the WECs' performance of several sea state parameters. It is therefore thought useful to utilise a performance indicator that will allow a direct comparison between the three selected devices. A normalised version of $\overline{P}$ would satisfy this criterion and if emphasis is put on the power estimation directly, the statistical models could easily be converted into models for $\overline{P}$.

A normalised power P^n is used. First, for each sea state the average mean power output over the runs is computed. P^n is then defined as the ratio of $\overline{P}$ to the maximum of the average mean power output. Due to its formulation, the normalised power P^n can actually take values above 1 as it is not normalised by the maximum mean power output produced by the device.

The relative capture width Cw is used as well (in %) as it is a commonly used performance indicators for wave energy converters. It follows the usual formulation as in Eq. 7.1:

$$Cw = 100 \cdot \frac{\overline{P}}{\dfrac{\rho g^2}{64\pi} \cdot \hat{T}_E \cdot \hat{H}_{m0}^2 \cdot C_l} \tag{7.1}$$

with: C_l device characteristic length

The characteristic length of the OWCs is their outer diameter, $C_l = D_{o,O}$, while the length of the Duck model is utilised, $C_l = L_D$. The values are given in Chapter 5 on page 110.

7.2 First phase results: uni-modal sea states

7.2.1 Individual device results

This section presents the observed results for the three devices separately. Comments and interpretation will be done in Section 7.2.3.

7.2.1.1 The single OWC

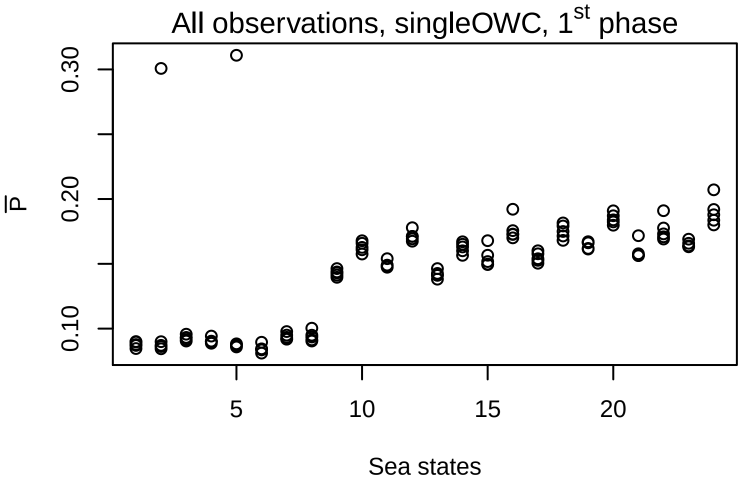

Figure 7.1: Observations of $\overline{P}$ for the single OWC with respect to the 24 sea states.

Single OWC observations Fig. 7.1 shows all the measurement of $\overline{P}$ from the single OWC during the first phase. Two runs out of the 120 recorded presented measurements with clear signs of instrumentation malfunction and were therefore discarded. The following results are consequently built over 118 measures. Also, the low variability observed for each sea states implies that the phase spectra do not have a strong influence on the average power produced by the devices.

Fig. 7.2 shows the variation observed between each of the 5 runs. Outputs for each run are very similar, and there is little concern about the repeatability of the measurements. This observation is creditable to the quality of the wave generated into the curved tank.

Fig. 7.3 and Fig. 7.4 show the variation of P^n and Cw with respect to the main sea state parameters. Additionally to the 4 selected parameters for this phase, the *estimated isolated* significant wave height $\hat{H}_{m0,1}$ is included as wave measurements (see Section 6.2.1 on page 126) show that it is not constant trough all sea states.

Results from JONSWAP sea states are marked by red triangles, and results from Bretschneider

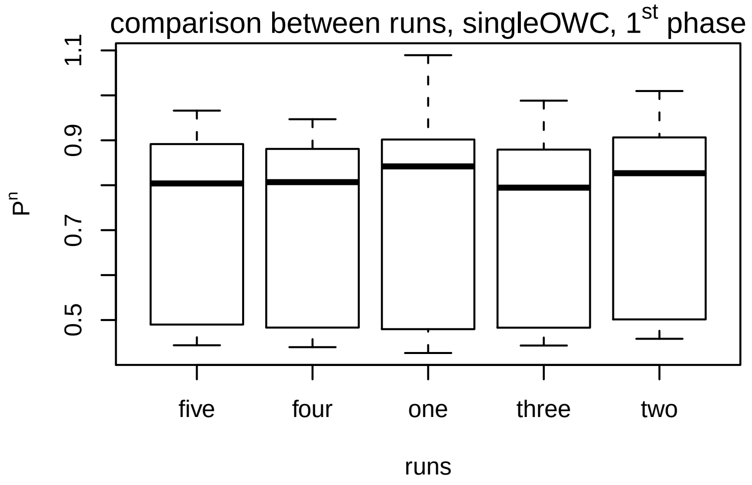

Figure 7.2: *variation of P^n as a function of each run.*

are marked in blue circles. They were differentiated in order to get a better view of the interaction between the bandwidth of the sea states[1] and the other parameters.

For both the normalised power P^n and the relative capture width Cw, Fig. 7.3a and Fig. 7.4a show strong correlation with $\hat{T}_{E,1}$ with some degree of non-linearity.
On Fig. 7.3c, the results can be separated between points with $P^n > 0.6$ and points with $P^n < 0.6$. The points in the second group correspond to the values of the *estimated isolated* energy period $\hat{T}_{E,1} \approx 0.9\,\mathrm{s}$. It can be seen that the *estimated isolated* frequency spreading $\hat{f}_{s,1}$ does not have the same influence on both group of points. On the top group of points, a negative correlation appears, while no evidence of correlation can be observed on the bottom group of points. This is a strong suggestion that there is a significant interaction between the *estimated isolated* energy period $\hat{T}_{E,1}$ and the *estimated isolated* frequency spreading $\hat{f}_{s,1}$. On Fig. 7.4c, these observations are even more marked as a negative correlation can be observed between the relative capture width Cw and $\hat{f}_{s,1}$ for points with $Cw > 23\%$ (corresponding to $\hat{T}_{E,1} > 1\,\mathrm{s}$), and a positive correlations for points with $Cw < 23\%$.

Positive trends relative to $\hat{H}_{m0,1}$ and $\hat{\Theta}_{S,1}$ can be observed on graphs b) and e) of Fig. 7.3. It is particularly visible for the group formed by the lower values of P^n. However, as some positive correlation was identified between $\hat{H}_{m0,1}$ and $\hat{\Theta}_{S,1}$ on Fig. 6.2 on page 131, it is difficult to give a definitive interpretation.

---

[1] At this stage, it is not known which bandwidth indicator is the most relevant between the *estimated isolated* frequency spreading $\hat{f}_{s,1}$ or a two-level categorical factor taking the two values *Bretschneider* and *JONSWAP*

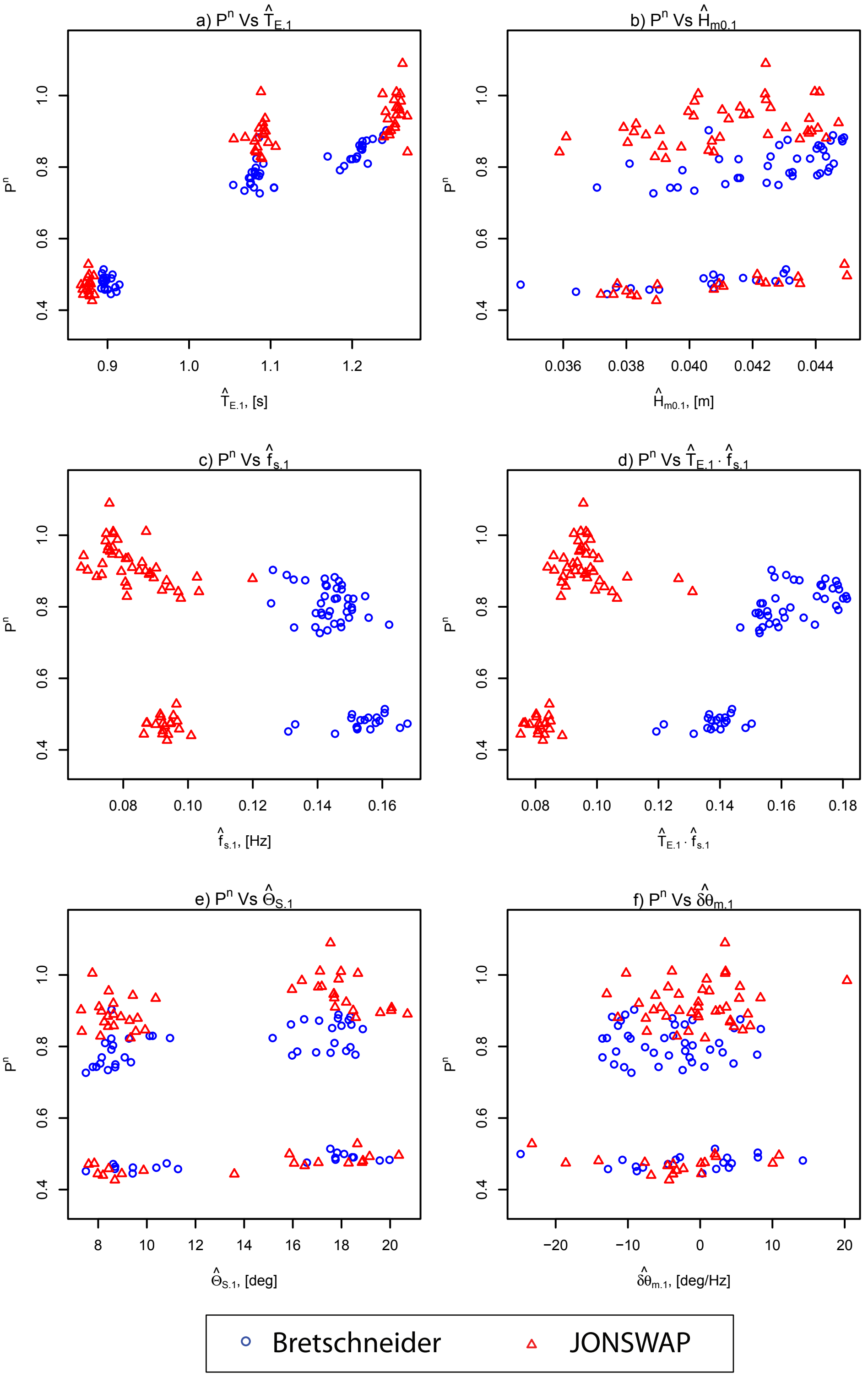

Figure 7.3: *variation of P^n as a function of the sea state parameters for the single OWC*

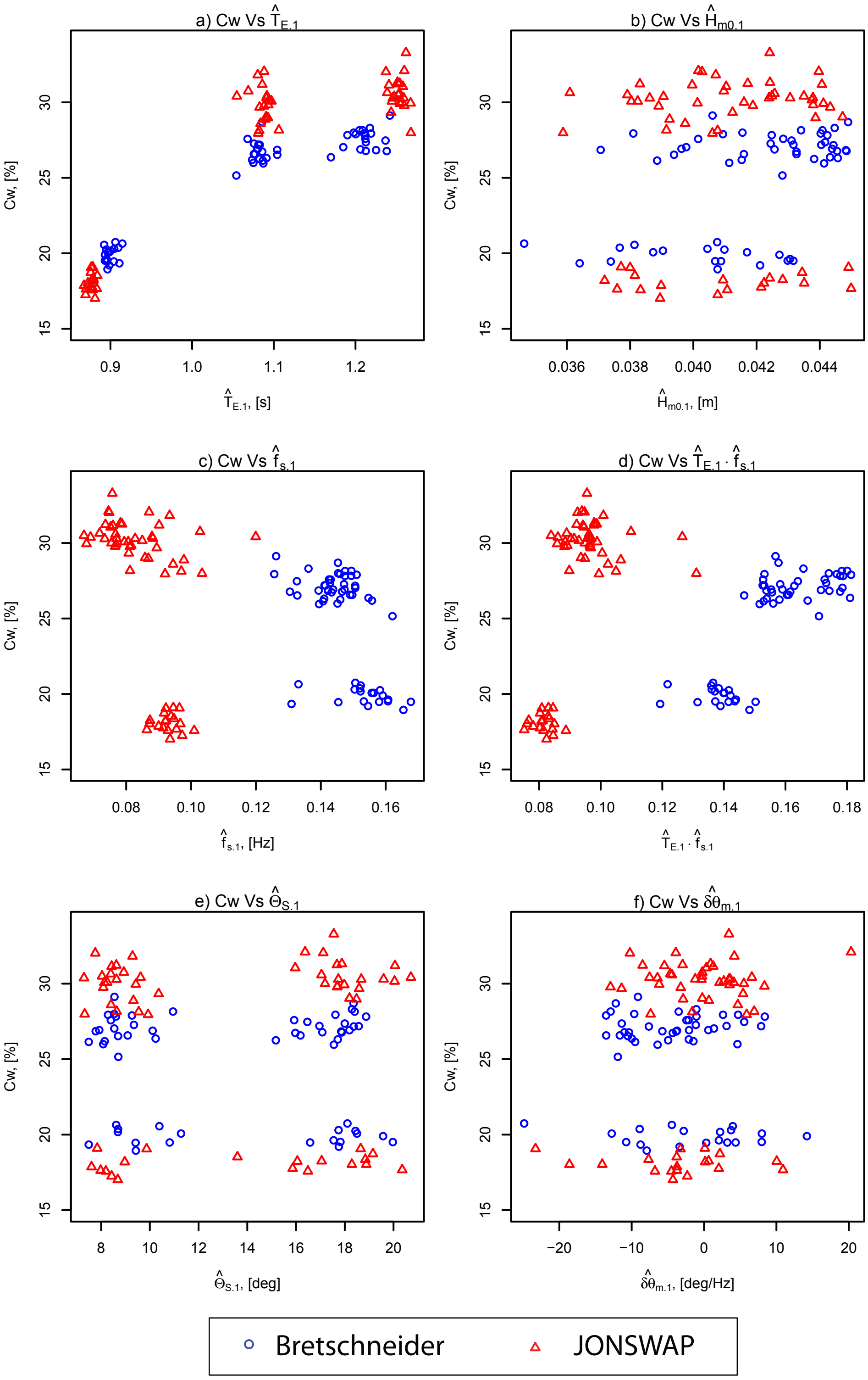

Figure 7.4: *variation of Cw as a function of the sea state parameters for the single OWC*

The variations of P^n with $\hat{H}_{m0,1}$ appear small but on the other hand, $\hat{H}_{m0,1}$ only varies by 20% throughout the tests. This range of variation for $\hat{H}_{m0,1}$ is limited but it should be bore in mind that those variations were not expected in the experimental plan and are only due to experimental variation and the $\hat{H}_{m0,1}$ estimation method.
As is could be expected, the small level of positive correlation with $\hat{H}_{m0,1}$ is gone when considering C_w. The correlation with $\hat{\Theta}_{S,1}$ has also disappeared, which illustrates well the relation between $\hat{\Theta}_{S,1}$ and $\hat{H}_{m0,1}$.
Finally, $\hat{\beta}_{\theta,1}$ does not seems to have a strong influence on the results as it was expected from Section 6.2.1.1 on page 132.

statistical modelling of the single OWC performances The statistical modelling of the device performances is interesting as it allows to evaluate the influence of each parameters. The choice of parameters to include in the model is important as well as their form. The statistical language *R* is used to perform either multi-linear regression or ANCOVA tests in order to help the selection. It is also important to remember that these models are only valid for the range of variation of the parameters explored in this study. For example, it is acknowledged that a quadratic relation between the average power of a WEC and the energy period cannot be established for the full range of energy period experienced by a device at sea. However, this more simplistic model might be enough if considering only a portion of this range.

From the wave measurement (see Section 6.2.1.1 on page 128), it is not possible to say in which form the spectral bandwidth should be included. It can be either as continuous variable using the the *estimated isolated* frequency spreading $\hat{f}_{s,1}$, or a bi-modal factor *Shape* taking the two values *Bretschneider* and *JONSWAP*.

Multiple linear regression models are fitted to the reduced dataset using either $\hat{f}_{s,1}$ or the two-level categorical factor *Shape* to include the spectral bandwidth and all the other main parameters. A quadratic term in $\hat{T}_{E,1}$ is introduced to take into account the observed curvature along the energy period axis. The second-order interactions between the main parameters are also included.The fit of the models is utilised to choose between the two forms.

The initial formulation in *R* of model are presented in Eq. 7.2 to Eq. 7.5. Their detailed meaning is presented in Appendix C on page 211.

$$PnModel1 \leftarrow lm\left(P^n \sim \hat{T}_{E,1}^{\;2} + \hat{H}_{m0,1} + (\hat{T}_{E,1} + \hat{f}_{s,1} + \hat{\Theta}_{S,1} + \hat{\beta}_{\theta,1})^2\right) \tag{7.2}$$

$$PnModel2 \leftarrow lm\left(P^n \sim \hat{T}_{E,1}^{\;2} + \hat{H}_{m0,1} + (\hat{T}_{E,1} + Type + \hat{\Theta}_{S,1} + \hat{\beta}_{\theta,1})^2\right) \tag{7.3}$$

$$CwModel1 \leftarrow lm\left(Cw \sim \hat{T}_{E,1}^{\;2} + \hat{H}_{m0,1} + (\hat{T}_{E,1} + \hat{f}_{s,1} + \hat{\Theta}_{S,1} + \hat{\beta}_{\theta,1})^2\right) \tag{7.4}$$

$$CwModel2 \leftarrow lm\left(Cw \sim \hat{T}_{E,1}^{\;2} + \hat{H}_{m0,1} + (\hat{T}_{E,1} + Type + \hat{\Theta}_{S,1} + \hat{\beta}_{\theta,1})^2\right) \tag{7.5}$$

Minimal adequate models are derived from which all non-significant parameters have been removed by first using the *R step* function (see Appendix C.5 on page 216) and then deleting any non-significant parameters (Venables & Ripley, 2002; Crawley, 2007). The fit of the models is evaluated with the standard set of plots provided by *R* and described in Appendix C.4 on page 214. For the P^n models, those plots are presented together in Fig. 7.5. The plots related to Cw models are presented in Fig. 7.6

First, the four models offer a relatively good fit. (max residuals $\approx 10\%$ and most residuals$<$ 4% for P^n, similar for Cw). In all cases, the highest residual are too high to be properly normally distributed, but the majority of points are.

The normality plots of residuals are better in models using the continuous variable $\hat{f}_{s,1}$ rather than the bi-level factor $Shape$. It gives credit to the hypothesis that at least part of the variation of $\hat{f}_{s,1}$ is due to real features of the generated waves, and not only due to the isolation method. $\hat{f}_{s,1}$ will consequently be utilised for any further models. None of the points presenting larger errors was single out as highly influential in the *Residuals vs Leverage* plots. It means that while they are associated with larger residuals than expected, they are not identified as causing significant variation in the estimated coefficient of the statistical models. They are therefore not excluded from the analysis.

The *minimal adequate model* issued of $PnModel1$ is presented in Eq. 7.6. Its summary is presented in Appendix E.1 on page 235.

$$\begin{aligned} P^n = &-(5.39 \pm 0.22) + (9.35 \pm 0.40) \cdot \hat{T}_{E,1} - (3.70 \pm 0.18) \cdot \hat{T}_{E,1}^{\;2} \\ &+ (15.11 \pm 1.98) \cdot \hat{H}_{m0,1} + (3.50 \pm 0.63) \cdot \hat{f}_{s,1} - (0.014 \pm 0.004) \cdot \hat{\Theta}_{S,1} \\ &- (4.73 \pm 0.60) \cdot \hat{T}_{E,1} \cdot \hat{f}_{s,1} + (0.012 \pm 0.004) \cdot \hat{T}_{E,1} \cdot \hat{\Theta}_{S,1} \end{aligned} \tag{7.6}$$

The only parameter not retained as significant is $\hat{\beta}_{\Theta,1}$. The *estimated isolated* angular spreading $\hat{\Theta}_{S,1}$ is kept in the model and marked as significant. The patterns of the two spreading param-

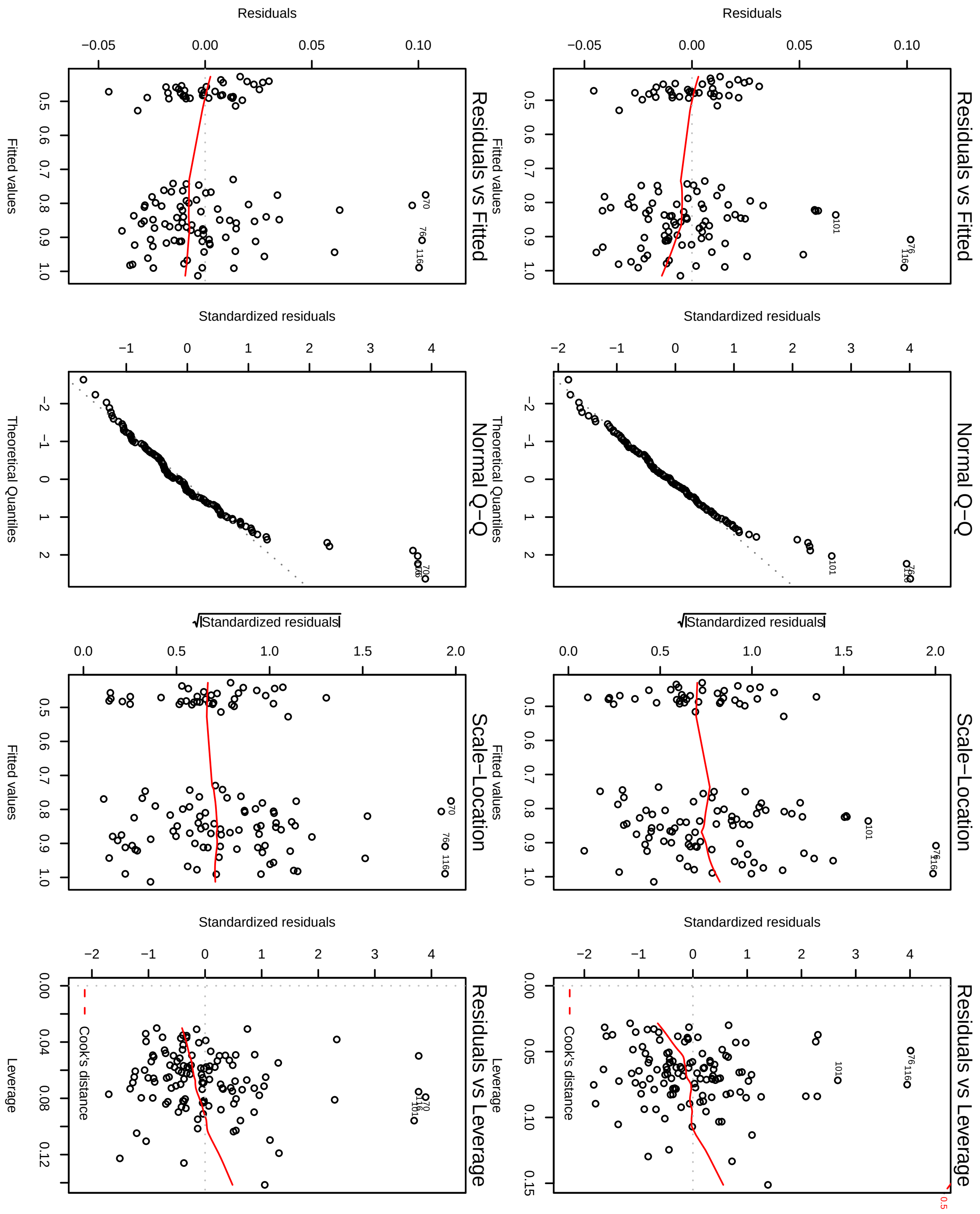

Figure 7.5: *Test plots for to evaluate the fit of the P^n models for the single OWC, 1^{st} phase. Plots related to $PnModel1$ are in the top row, plots related to $PnModel2$ are in the bottom row.*

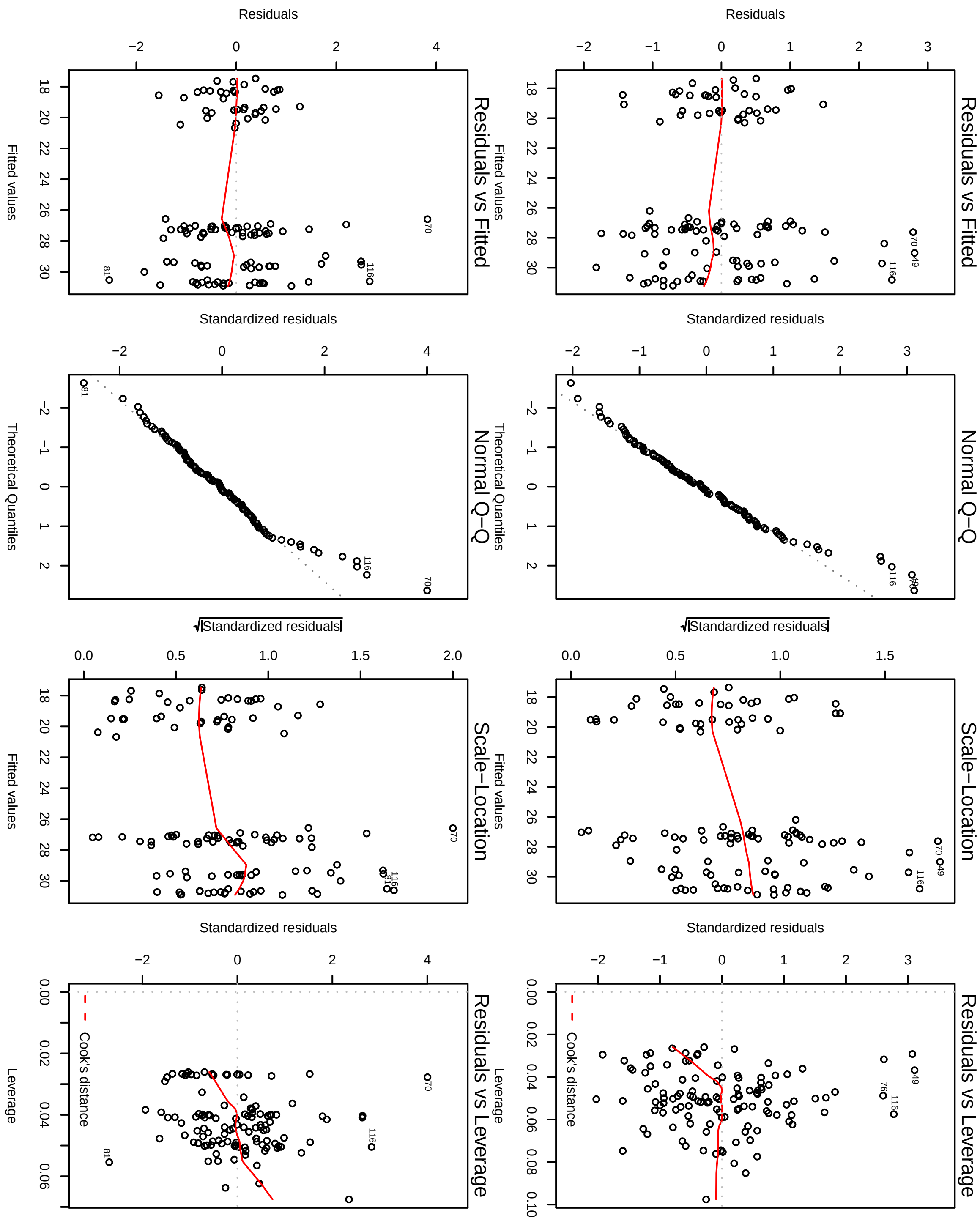

Figure 7.6: *Test plots to evaluate the fit of the* Cw *models for the single OWC,* 1^{st} *phase. Plots related to* $CwModel1$ *are in the top row, plots related to* $CwModel2$ *are in the bottom row.*

eters are similar: the coefficients attributed to their main effect and to their interaction with $\hat{\beta}_{\Theta,1}$ are of opposite signs. However, a negative coefficient is attributed to $\hat{\Theta}_{S,1}$ but a positive coefficient is attributed to $\hat{f}_{s,1}$. Section 7.2.2 compares the magnitude of each effect over P^n for all the devices.

The *minimal adequate model* issued of $CwModel1$ is presented in Eq. 7.7. The summary is presented in Appendix E.1 on page 235.

$$\begin{aligned} Cw = &-(170.69 \pm 7.62) + (326.86 \pm 13.75) \cdot \hat{T}_{E,1} - (131.31 \pm 6.21) \cdot \hat{T}_{E,1}^{\ 2} \\ &+ (80.57 \pm 37.91) \cdot \hat{H}_{m0,1} + (159.55 \pm 21.24) \cdot \hat{f}_{s,1} - (181.80 \pm 19.81) \cdot \hat{T}_{E,1} \cdot \hat{f}_{s,1} \end{aligned} \tag{7.7}$$

In Cw case, the *minimal adequate model* is simpler. No directional parameter is retained as expected for an omnidirectional device. Using the relative capture width did not mask completely the effect of $\hat{H}_{m0,1}$. This could be either due to measurement variations not linked to real features of the waves, or a real characteristics of the device.

Once again, the interaction between $\hat{T}_{E,1}$ and $\hat{f}_{s,1}$ is retained, as suggested by Fig. 7.4 d). It is interesting as it highlights the ambivalent effect of the spectral bandwith: close the the resonating frequency (larger values of energy period in this case), a large bandwith as a negative effect (more energy is spread away for the resonating frequency) while a large bandwith is positive if the energy period is away from the resonating frequency, (more energy is spread closer to the resonating frequency).

7.2.1.2 The Double OWC

Double OWC observations As the OWC had to be sent back to Queen's University Belfast at the end of June, only 4 runs for each sea state could be recorded for the double OWC. Additionally, during the data analysis some records exhibited clear sign of instrumentation problems and had to be discarded. This reduces the number of usable measures from 120 planned to only 84. While the number of test is still significant, it may lead to larger error on the estimation of the coefficient and the significance of parameter's effect may be more difficult to assess as the estimated standard deviation of the coefficient will increase..

Fig. 7.7 and Fig. 7.8 show the variation of P^n and C_w with respect to the same sea state parameters as for the Single OWC. Results from JONSWAP and Bretschneider spectra were differentiated in order to get a better view of the interaction between the spectral bandwidth and the other parameters. Fig. 7.8 shows the variation of Cw with respect to the main sea state

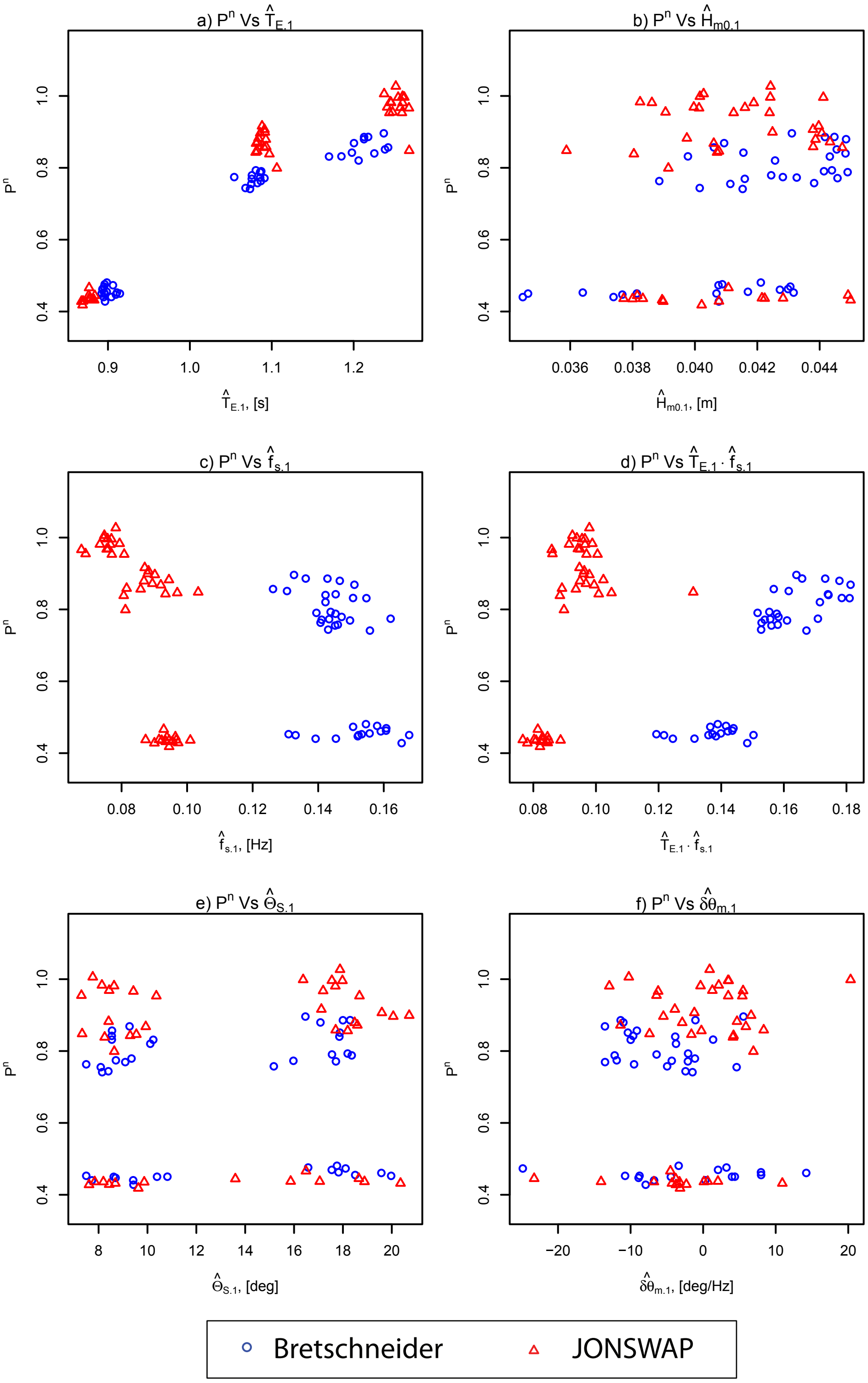

Figure 7.7: *Observations of P^n for the double OWC during the 1^st test phase.*

]

parameters. As for the Single OWC, a strong correlation with some curvature can be expected between the two performance indicators and $\hat{T}_{E,1}$. Again, $\hat{f}_{s,1}$ and its interaction with $\hat{T}_{E,1}$ seems to have the same type of influence over the observed results: broader spectra generate less variation of the power output of the Double OWC. From the plots f) of each figure, the influence of $\hat{\beta}_{\Theta,1}$ should be negligible.
The observation related to the influence of $\hat{H}_{m0,1}$ and $\hat{\Theta}_{S,1}$ are different. No influence over P^n can be suspected from the plots b) and e) of Fig. 7.7, whereas a negative trend for Cw can be identified on Fig. 7.8b) and e). The trend with respect to $\hat{H}_{m0,1}$ is more obvious, so it is expected that it is $\hat{H}_{m0,1}$ which drives those observations (there is a correlation between $\hat{H}_{m0,1}$ and $\hat{\Theta}_{S,1}$, see Fig. 6.2 on page 131). This could make physical sens as greater losses trough viscous effect can be expected in more energetic sea states.

statistical modelling of the double OWC performances From the Single OWC statistical models, it was concluded that $f_{s,1}$ should be included in the models as a continuous variable based on the estimated values $\hat{f}_{s,1}$. Initial calls in *R* for models of each indicator are presented in Eq. 7.8 to Eq. 7.9.

$$PnModel \leftarrow lm\left(P^n \sim {\hat{T}_{E,1}}^2 + \hat{H}_{m0,1} + (\hat{T}_{E,1} + \hat{f}_{s,1} + \hat{\Theta}_{S,1} + \hat{\beta}_{\Theta,1})^2\right) \tag{7.8}$$

$$CwModel \leftarrow lm\left(Cw \sim {\hat{T}_{E,1}}^2 + \hat{H}_{m0,1} + (\hat{T}_{E,1} + \hat{f}_{s,1} + \hat{\Theta}_{S,1} + \hat{\beta}_{\Theta,1})^2\right) \tag{7.9}$$

The models are then simplified until the *minimal adequate models* are obtained. The mathematical expression issued from *PnModel* is shown in Eq. 7.10. The model summary and test plots are available in Appendix E.1 on page 235.

$$\begin{aligned} P^n = &-(5.33 \pm 0.24) + (9.61 \pm 0.43) \cdot \hat{T}_{E,1} - (3.70 \pm 0.19) \cdot {\hat{T}_{E,1}}^2 \\ &+ (5.73 \pm 1.15) \cdot \hat{H}_{m0,1} + (3.14 \pm 0.66) \cdot \hat{f}_{s,1} - (4.17 \pm 0.62) \cdot \hat{T}_{E,1} \cdot \hat{f}_{s,1} \end{aligned} \tag{7.10}$$

This model is simpler than the one achieved for the single OWC. $\hat{\Theta}_{S,1}$ was not retained as a significant parameter. This is surprising, as the double OWC should have been more sensitive to wave directionality than the single OWC. It is possible that the reduced number of tests made it impossible to identify the effect of $\hat{\Theta}_{S,1}$. Most probably, the effect of $\hat{\Theta}_{S,1}$ in the single OWC case is resulting from its interaction with $\hat{H}_{m0,1}$. More tests, with a better controlled $\hat{H}_{m0,1}$ would be necessary to clearly separate both effects.

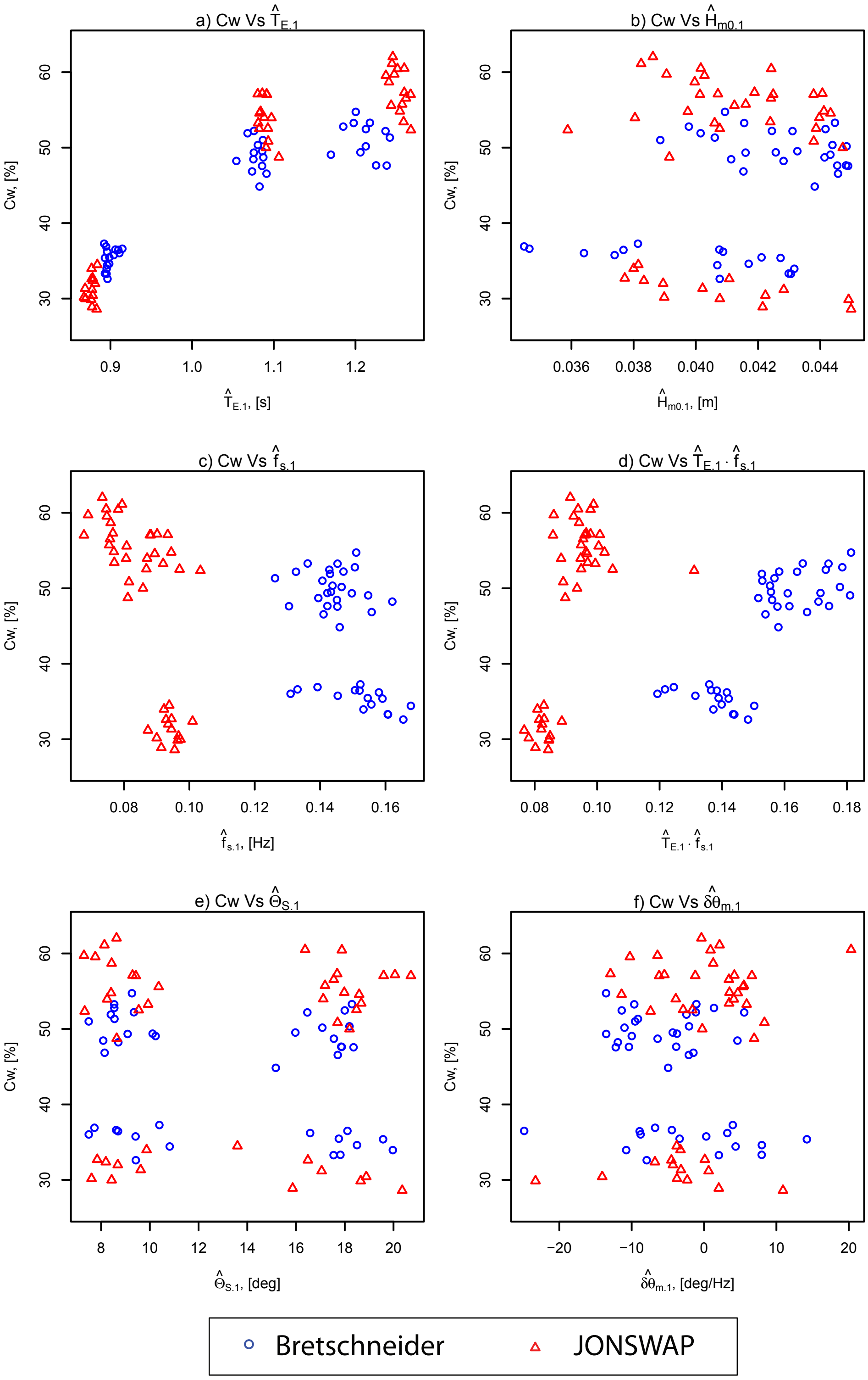

Figure 7.8: *Observations of Cw for the double OWC during the $1^{s}t$ test phase.*

The mathematical expression issued of *CwModel* is shown in Eq. 7.11. The model summary and test plots are available in Appendix E.1 on page 235.

$$\begin{aligned} Cw = &-(312.49 \pm 21.24) + (623.43 \pm 38.70) \cdot \hat{T}_{E,1} - (247.49 \pm 17.44) \cdot \hat{T}_{E,1}{}^{2} \\ &- (331.07 \pm 103.07) \cdot \hat{H}_{m0,1} + (305.13 \pm 59.01) \cdot \hat{f}_{s,1} - (336.15 \pm 55.43) \cdot \hat{T}_{E,1} \cdot \hat{f}_{s,1} \end{aligned} \tag{7.11}$$

In accordance with the observation of Fig. 7.8, the coefficient of $\hat{H}_{m0,1}$ is negative. This is the opposite findings of the single OWC. It could be a different level of interaction between the devices. The *masking* of the second device by the first could be positively correlated with $\hat{H}_{m0,1}$. From Fig. 6.2, $\hat{\Theta}_{S,1}$ is also increasing with $\hat{H}_{m0,1}$. It will be surprising is the higher level of masking were occurring in broader spectra, so this tends to confirm a sensitivity to $\hat{H}_{m0,1}$ instead of $\hat{\Theta}_{S,1}$. Again, further tests with variation of $\hat{H}_{m0,1}$ and $\hat{\Theta}_{S,1}$ clearly uncorrelated would be needed to gave a definitive answer. It is also important to notice the large error in the estimation of the coefficient of $\hat{H}_{m0,1}$, mos probably resulting from the uncontrolled and limited variation of this important parameter. This emphasize the need to repeat the experiment with a more controlled variation of $\hat{H}_{m0,1}$.

7.2.1.3 The solo Duck

At the end of the testing period of the duck during this phase, it appears that the pressure sensor had some issues with water getting in the sensor compartment. The records from run 3 and 4 are consequently not usable. Instead, pitch records are used as a proxy for the duck average power.e angular velocity of the Duck is derived and used in the relation established in Section 5.2.4 on page 118. 4 runs of each sea states were done in order the shorten the experimental time. After discarding some of the angular velocity records due to problems with the fixing of the Qualysis®reflectors, 90 measurements are available. None of the 24 sea states has less than 3 runs utilised in the analysis.

Duck observations Fig. 7.9 and Fig. 7.10 show the variation of P^n and Cw respectively with respect to the main sea state parameters. Results from JONSWAP and Bretschneider spectra were differentiated in order to get a better view of the interaction between $f_{s,1}$ and the other parameters.

Compared to the OWCs, a larger variation of P^n can be observed (from 0.2 to 1). This reflects

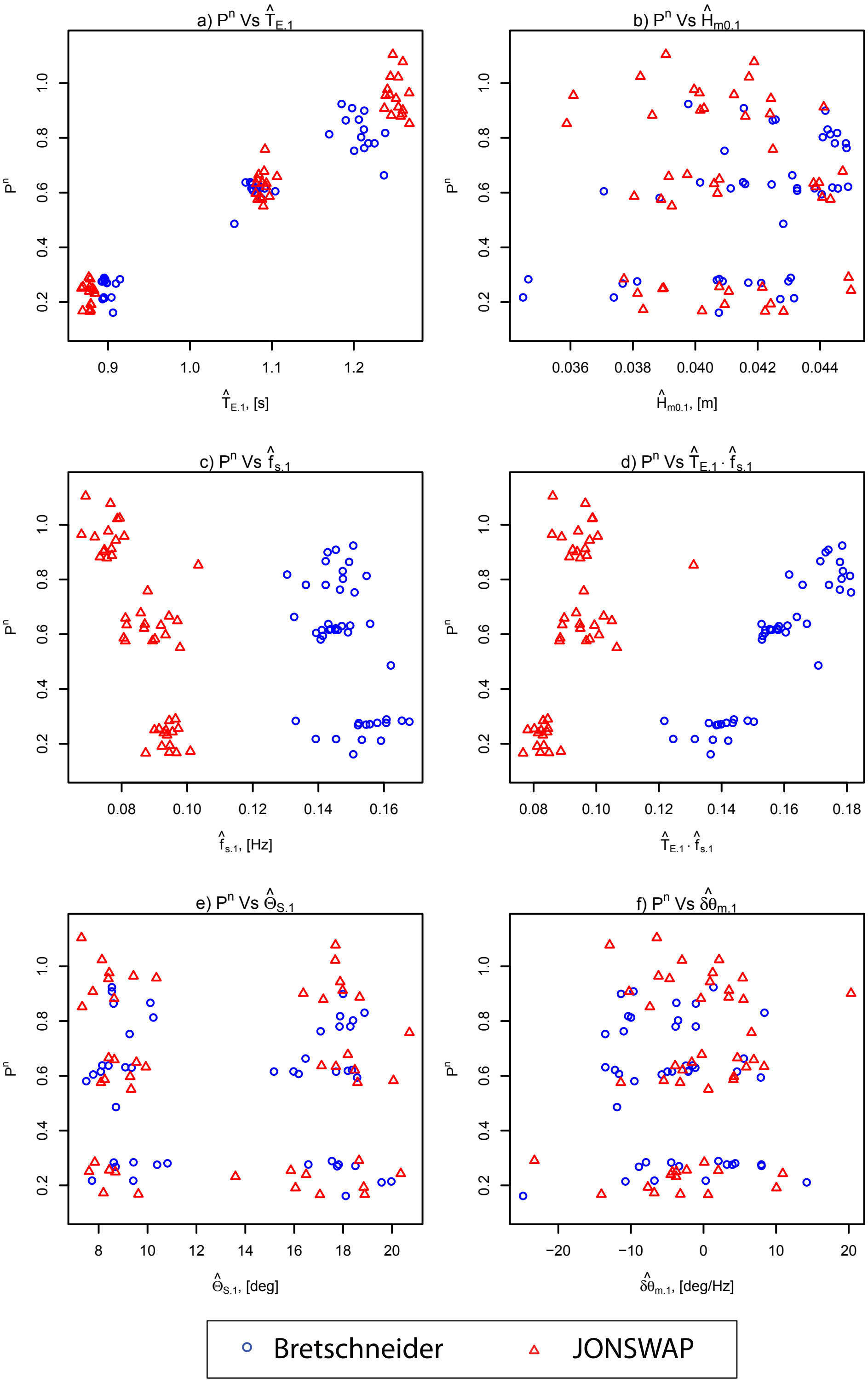

Figure 7.9: *variation of P^n as a function of the sea state parameters for the Duck.*

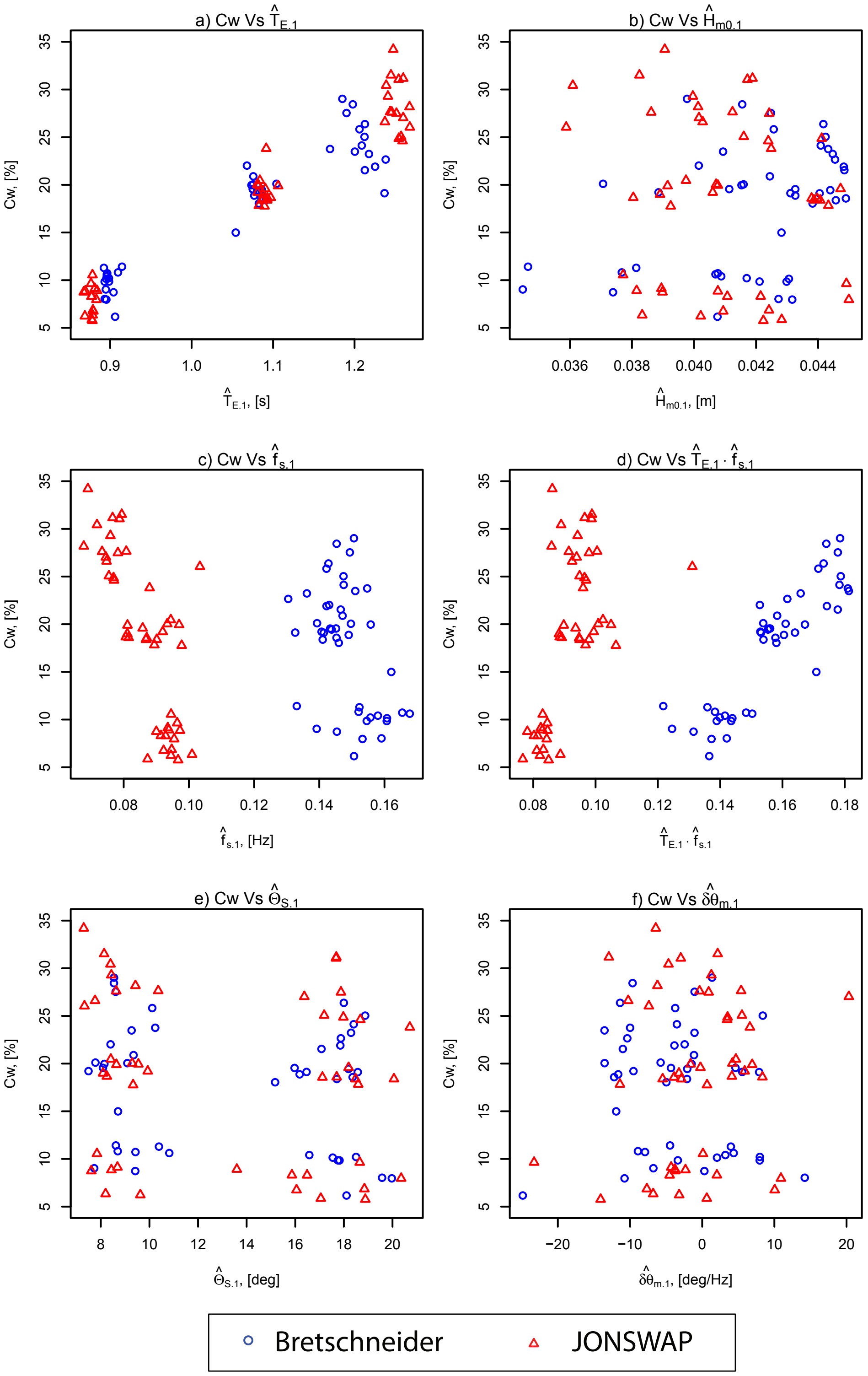

Figure 7.10: *variation of Cw as a function of the sea state parameters for the Duck.*

the fact that the Duck resonating frequency is lower than 1 Hz, so the investigated range is not located on the top of the performance curve of the duck, but on its steep side.

A strong correlation between $\hat{T}_{E,1}$ and P^n is shown on Fig. 7.9a), and Fig. 7.9c) suggests a sensitivity to the frequency spreading $\hat{f}_{s,1}$. There is distinguishable influence of the other parameters over P^n. As for the OWCs, there is signs of sensitivity of the Duck performances and interactions between $\hat{f}_{s,1}$ and $\hat{T}_{E,1}$. From the graphs b), e) and f) of Fig. 7.9, there is little evidence of influence of the other parameters.

The same observations can be done for Cw. The only difference is that Fig. 7.10b) and e) hint that Cw might be decreasing with increasing $\hat{H}_{m0,1}$ and/or $\hat{\Theta}_{S,1}$. It will make physical sense in each way, as the capture width of the Duck would be suspected to decrease with steeper waves and/or more spread spectra. Hydrodynamic losses are not linear and would be expected to decrease the efficiency in more energetic sea state. The Duck is also a directional device, so a decrease of performance when subjected to sea state with larger directional sea states would be expected.

statistical modelling of the Duck performances Initial calls in *R* for models of each indicator are presented in Eq. 7.12 to Eq. 7.13. Again, $\hat{f}_{s,1}$ is used following the single OWC results (see Section 7.2.1.1).

$$PnModel \leftarrow lm\left(P^n \sim \hat{T}_{E,1}{}^2 + \hat{H}_{m0,1} + (\hat{T}_{E,1} + \hat{f}_{s,1} + \hat{\Theta}_{S,1} + \hat{\beta}_{\Theta,1})^2\right) \quad (7.12)$$

$$CwModel \leftarrow lm\left(Cw \sim \hat{T}_{E,1}{}^2 + \hat{H}_{m0,1} + (\hat{T}_{E,1} + \hat{f}_{s,1} + \hat{\Theta}_{S,1} + \hat{\beta}_{\Theta,1})^2\right) \quad (7.13)$$

Models are then simplified until *minimal adequate models* are obtained. The mathematical expression from issued from *PnModel* is shown in Eq. 7.14. The model summary and test plots are available in Appendix E.3 on page 239.

$$\begin{aligned} P^n = &-(2.16 \pm 0.27) + (2.23 \pm 0.17) \cdot \hat{T}_{E,1} + (12.38 \pm 4.52) \cdot \hat{H}_{m0,1} \\ &+ (3.46 \pm 1.60) \cdot \hat{f}_{s,1} - (0.007 \pm 0.002) \cdot \hat{\Theta}_{S,1} - (3.69 \pm 1.50) \cdot \hat{T}_{E,1} \cdot \hat{f}_{s,1} \end{aligned} \quad (7.14)$$

$\hat{T}^2_{E,1}$ term is not retained in the minimal adequate model, showing that there is no evidence of curvature in the observation of P^n with respect to $\hat{T}_{E,1}$. The model retains a positive contribution of $\hat{H}_{m0,1}$, and a small negative contribution of $\hat{\Theta}_{S,1}$. This could be evidence that despite the degree of correlation observed between those last 2 parameters, the data allows the statistical modelling to differentiate their influence.

The mathematical expression of the minimal adequate model issued of *CwModel* is shown in Eq. 7.15. The model summary and test plots are available in Appendix E.3 on page 239.

$$Cw = -(312.49 \pm 21.24) + (51.21 \pm 1.55) \cdot \hat{T}_{E,1} - (0.18 \pm 0.05) \cdot \hat{\Theta}_{S,1} \tag{7.15}$$

This is the simplest model yet. Only the effect of $\hat{T}_{E,1}$ and $\hat{\Theta}_{S,1}$ were retained as significant. While it is surprising, not much difference can be seen between this model and the model retaining $\hat{f}_{s,1}$. Residuals are only increasing from 2.054 to 2.079, and the fit of the model do not deteriorate. The details of the model including $\hat{f}_{s,1}$ are also given in Appendix E.3 on page 239 for the reader to make its own judgement.

It is important to remember that this results do not mean that $\hat{f}_{s,1}$ has no influence on the relative capture width of the duck, but that these data do not allow the identification of a significant effect of $\hat{f}_{s,1}$. As it can be seen in Appendix E.3 on page 239, the fit of the model is also not as good as the fit of the model issued from the OWCs data.

The interaction term between $\hat{T}_{E,1}$ and $\hat{f}_{s,1}$ visible in all the other model can also suggests that the lower resonant frequency of the Duck do not allow $\hat{f}_{s,1}$ to have a significant effect.

7.2.2 Effect magnitude and relative influence

The main goal of this work is to establish a quantitative comparison of the effect on WEC performances of each sea state parameters with respect to each other.

The *effect magnitude* of a parameter is defined in this work as the variation of the normalised power or the relative capture width induced by the parameter. It is computed as the product of the coefficient attributed to the parameter in the mathematical models presented in the sections above with the observed range of variation of the parameters. In cases where models include square terms of parameters, both coefficients are used to estimate the effect magnitude.

Fig. 7.11a presents the effect magnitude upon P^n of each significant parameters for the three devices. Fig. 7.11b presents the normalised effect upon Cw. Normalising the effect over Cw makes the comparison easier as Cw range varies from device to device.

Looking at Fig. 7.11a, it appears that the effect of $\hat{T}_{E,1}$, $\hat{f}_{s,1}$ and their interaction are the largest. $\hat{H}_{m0,1}$ is associated with a rather small effect. However, sea states were not designed to quantify its influence, so no definitive conclusion should be drawn at this point. Rather surprisingly as

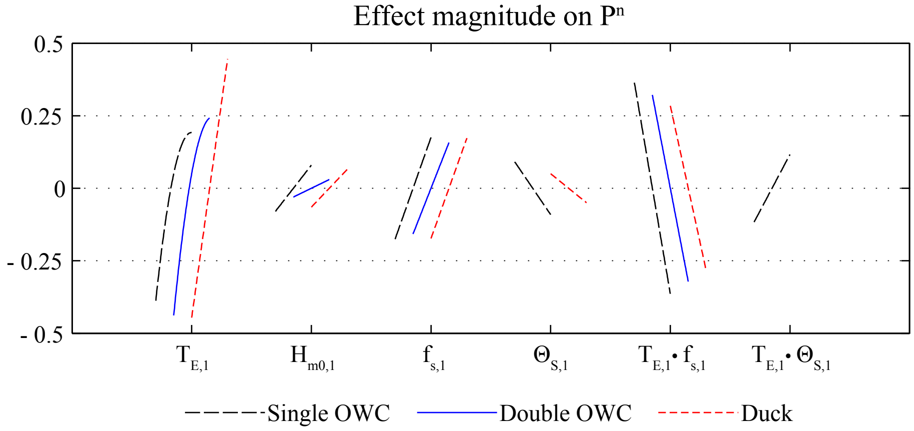

(a) effect over P^n

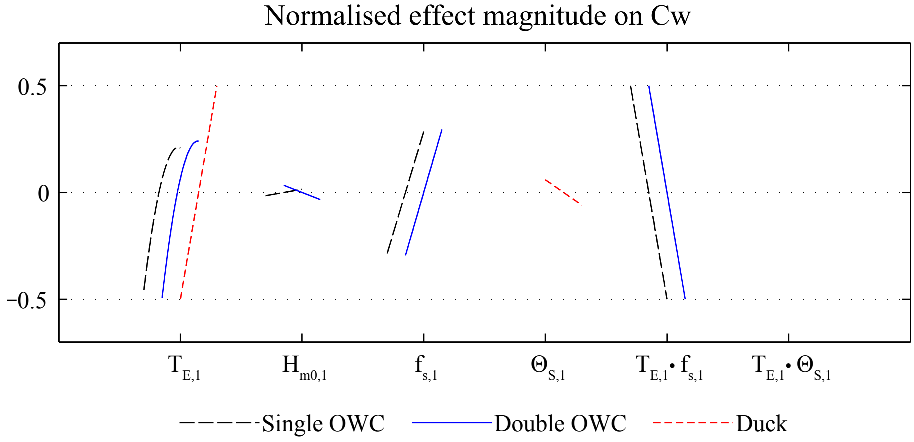

(b) normalised effect over Cw

Figure 7.11: 1^{st} *phase Effect magnitude of the investigated sea state parameters over the performances of the devices. For* Cw*, the effect have been normalised as the range of variation of* Cw *varies greatly from a device to another.*

the Duck is not an omnidirectional device, the estimated effect of $\hat{\Theta}_S$ for the Duck is not more significant than for the single OWC. A possible explanation is that the Duck model is extremely sensitive to $\hat{T}_{E,1}$ for the range of T_E explored, thus masking the effect of other parameters.
It is interesting to see a very similar pattern for these three devices. It gives hope that for resonant devices, a common set of parameters could be used for performance prediction in uni-modal sea states.

The picture for the effect of parameters upon Cw is rather different. Using the capture width instead of the power emphasis the importance of the frequency spreading upon the performance of the OWCs. However, $\hat{f}_{s,1}$ does not appear in the mathematical model for the Duck. There is no suggested explanation about why using the capture width has a different effect depending on the device.

From those two figures, it appears clearly that $\hat{T}_{E,1}$ and $\hat{f}_{s,1}$ are the dominant parameters. Within the limitations of this work (limited range of variation of the energy period and the angular spreading), there is no evidence that only the energy period and the significant wave height should be retained for the performance estimation of wave energy devices. A convincing way to present those conclusions is displayed in Fig. 7.12. The surface is a simplified version of the parametric model presented in Eq. 7.11. The model has been reduced to a function of only $\hat{T}_{E,1}$ and $\hat{f}_{s,1}$ by using the mean value of $\hat{H}_{m0,1}$. The strong interaction between the two variable can be seen by observing the change in curvature. The presented model is also very satisfying as the surface fits the measured points rather accurately, and the difference between the measured points and the surface do not follow any identifiable pattern.

7.2.3 Comparison between single and double OWCs

While this is not the main purpose of this thesis, it is interesting to compare the single and double OWC performances. It was originally thought that using two OWCs aligned along the main direction of propagation will induce different sensitivity to wave directionality. However, the results presented above do not confirm this hypothesis as effects of $\Theta_{S,1}$ or $\hat{\beta}_{\Theta,1}$ are not significant in the double OWC case.
A first element of comparison is obtained by looking at the performances on a sea state by sea state basis. The results are shown in Fig. 7.13.
Fig. 7.13 a) shows that both the pair of OWC and the single OWC have a very similar perfor-

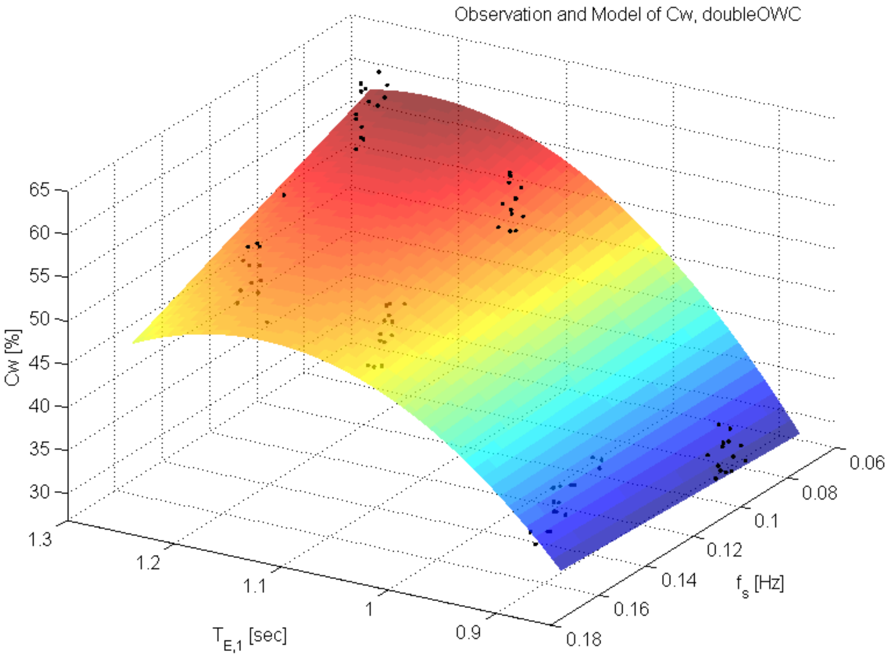

Figure 7.12: *Tank measurement of Cw for the double OWC overlayed upon a 3D representation of the R parametric model.*

mance variation in relation to the different sea states. For sea states 1 to 8, it can be observed that the double OWC produces systemically less than the single OWC. This observation cannot be made for sea states 9 to 24.

It indicates a higher sensitivity of the double OWC to the energy period which can also be observed in Fig. 7.11a. It might be the marks of different interactions between the OWCs depending of the energy period of the sea states.

Fig. 7.13 b) plots the power developed by each OWC with respect to the sea states. It highlights an important aspect of the double OWC. In average, the power output of each OWC do not match the power output of a single OWC. This observations is valid for all the sea states. It shows that the interaction between the devices are destructive overall.

The interaction factor q is defined in Eq. 7.16 in accordance with Folley (2009) and Child & Venugopal (2010). $q > 1$ means that there is positive interactions between the devices.

$$q = \frac{P_{2owc}}{2 \cdot P_{1owc}} \tag{7.16}$$

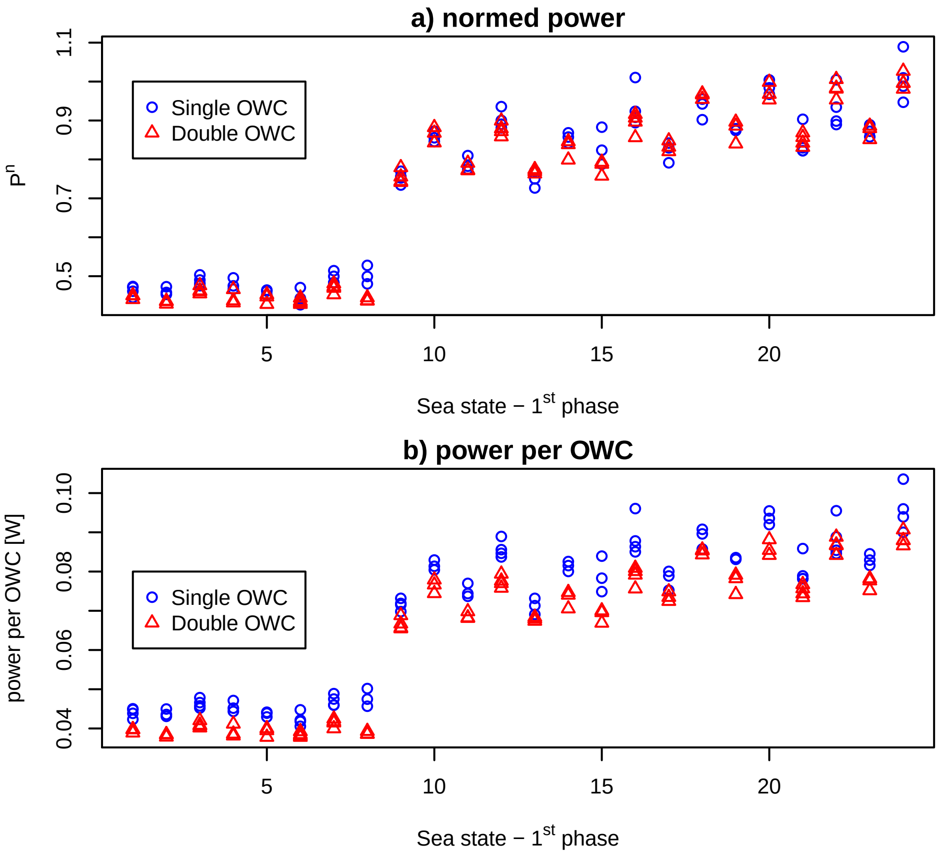

Figure 7.13: *Comparison of the single and double OWC performances during the first test phase.*

The interaction factor is related to the set of relevant parameters in Fig. 7.14. A positive correlation between q and $\hat{T}_{E,1}$ and with P_{2owc} can be observed, as well as a negative correlation between q and $\hat{H}_{mo,1}$ and $\hat{\Theta}_{S,1}$. No apparent effect of $\hat{f}_{s,1}$ or $\hat{P}_w$ can be suspected from those plots.

A direct correlation between $\hat{T}_{E,1}$ and P_{2owc} has been shown in Section 7.2.1.2, and a strong correlation between $\hat{H}_{mo,1}$ and $\hat{\Theta}_{S,1}$ is apparent on Fig. 6.9 on page 141. It is consequently difficult to untangle the effect of each parameters. It makes physical sense to relate a higher significant wave height with a higher level of interaction between the devices. This could be the source of the negative correlation. However, using linear theory, Child & Venugopal (2010) shoes that q is sensitive to variation of the wave angle of attack relative to the WEC array. Hence, broader spectra could indeed have an influence over q. Further work decoupling variations of $\hat{H}_{mo,1}$ and $\hat{\Theta}_{S,1}$ should clarify this issue.

Child & Venugopal (2010) also show a clear sensitivity of q with the wavenumber. This suggest a strong correlation of q with the spectra's energy period.

In order to look more closely at this interaction, Fig. 7.15 shows the average power output from each OWC for each sea states. The *single OWC* records corresponds to the tests with only one column in the tank. The *1st OWC* and *2nd OWC* correspond to the individual power output of each device during the double OWC tests. The records of the *single OWC* and *1st OWC* are issued from the same device. For the sea states 1 to 8, the results of both OWCs from the double OWC test are inferior to the output of the single OWC test. However, for the sea states 9 to 24, the power output levels from the *2nd OWC* are similar to the *single OWC*, while the power output from the *1st OWC* are lower. The destructive interaction seems to affect principally the power output of the *1st OWC*.

Much more work and data analysis could be done on the subject of interaction with the collected dataset. However, it is not the core of this work, so no attempt to develop this section beyond those observations is done.

7.2.4 Discussion: 1^{st} test phase

The observations have first confirmed once more the quality and the repeatability of the waves generated in the Edinburgh Curved tank. There is very little variation observed in the power of the devices from run to run. It also means that the power output of the devices is not influenced by the phase spectra.

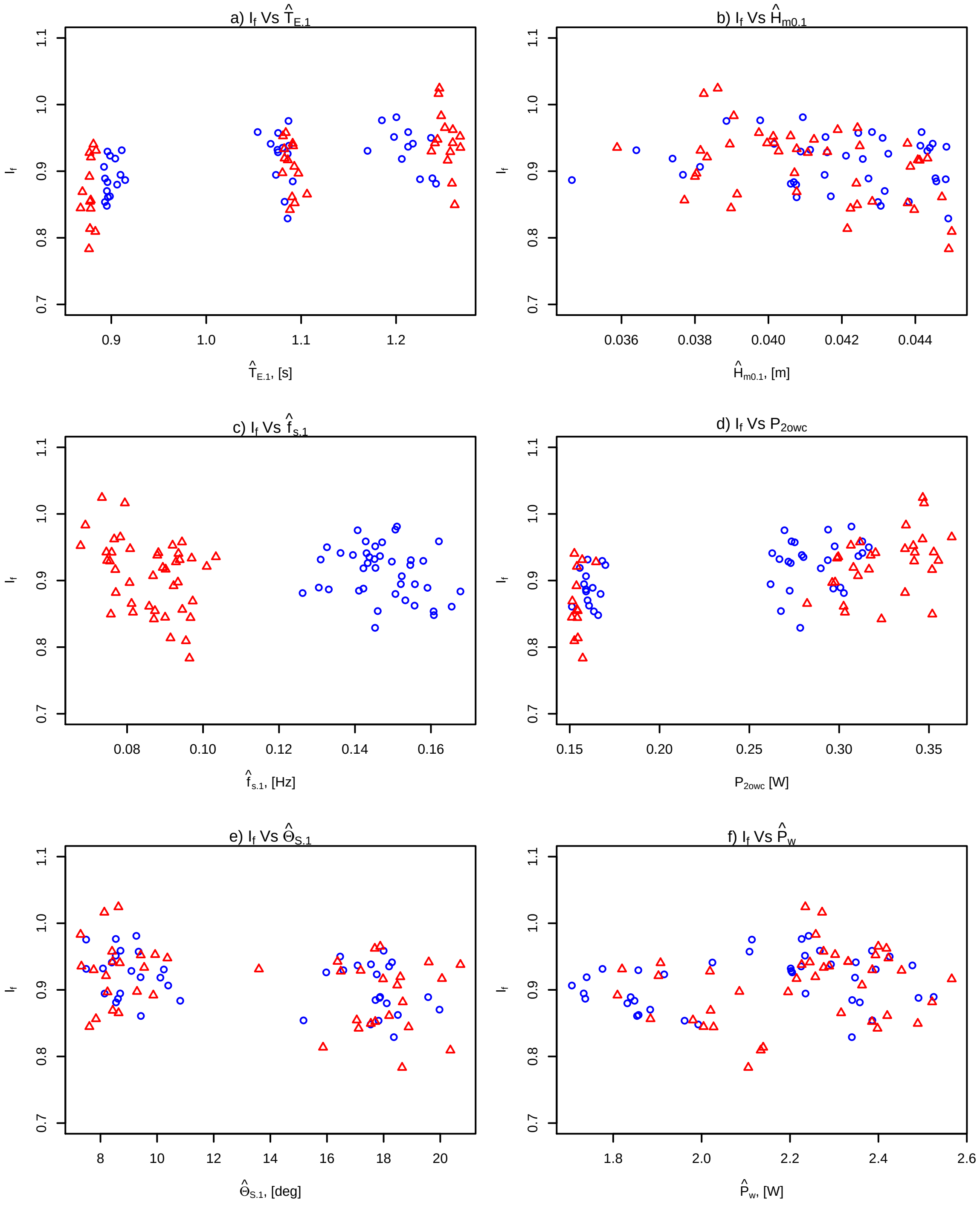

Figure 7.14: *Interaction factor q of the double OWC for the uni-modal sea states, related to a set of relevant parameters.*

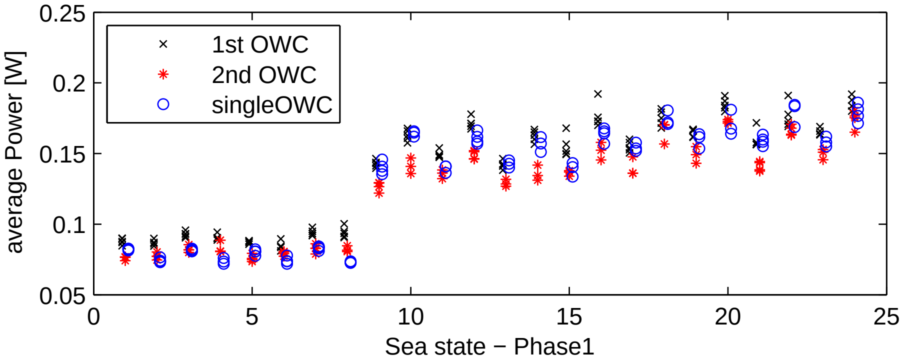

Figure 7.15: *Average power output for each OWC during the first phase tests. The results from the single OWC are presented alongside the results from each individual OWC during the double OWC tests. A small shift along the x axis between the three records is included for the clarity of the graphic.*

The number of observations on the duck model or the double OWC seems sufficient to isolate the effect of each sea states parameters, so only 4 runs instead of 5 of each sea state will be used during the 2^nd phase of tests.

The pattern of variation of the performance indicator of the double OWC and the single OWC proved to be very similar. Small level of interaction were witnessed between each individual OWC during the double OWC tests, and they did not vary by a large amount. The interaction factor q was < 1 for all sea states. For the second phase of test, only the double OWC will be used in order to reduce the experimental time.

The 1^st phase of tests has demonstrated that parametric models of wave energy converters performances are achievable in the case of uni-modal wave spectra. It appears that the effect of $f_{s,1}$ and its interaction with $T_{E,1}$ is as significant upon the power output of the three devices as the effect of $T_{E,1}$. The case to average the effect of $f_{s,1}$ and reduced the parameters taken into account to H_m0 and T_E to estimate the performance of WECs do not seems not justified.

The effect of wave directionality, measured by $\Theta_{S,1}$ and $\hat{\beta}_{\Theta,1}$, do not seems to be prominent. The effect of Θ_S was identified has significant over the relative capture width of the duck, but is magnitude is limited in comparison of the magnitude of the effect of $T_{E,1}$

Three factors limits the scope and validity of those results:

- Limited angular spreading available.

  As shown in Babarit *et al.* (2007), the effect of $\Theta_{S,1}$ over the SEAREV is marked for s values inferior to 5, which is the smallest s value used in this work. Using larger angular spreading might be necessary to demonstrate its effect, but it will need careful monitoring of the waves prior to any measurement to verify that the tank can produce such sea states.

- Limited number of devices.

  Only three devices were used. Prior to formulate recommendation about performance prediction of devices, more WEC models should be tested with the same sea states and Fig. 7.11 should be completed with their results. A device with compliant moorings would be particularly suitable, such as the sloped IPS buoy (Payne *et al.*, 2008) or a freely floating point absorber (Gilloteaux & Ringwood, 2009).

- Scale of the duck model.

  The duck model has a resonating frequency below any of the $T_{E,1}$ used during those tests. A new duck model, with a resonating frequency close to the resonating frequency of the OWCs will allow better comparison between those devices.

7.2.5 A better test plan for uni-modal sea states

Finally, it is thought important to formalise what will be an improved test plan with the gathered information from this part of the work. First, the number of repetitions for each test can be limited to four, as no large variation of power outputs between the runs of each sea states was witnessed. Second, at least 2 levels of H_{m0} must be introduced into the plan. This is absolutely needed to make sure inevitable variations of H_{m0} will not be correlated with other parameters. On the contrary, β_Θ should be dropped as its estimation is problematic, its effect at best minimal and its occurrence in realistic seas not clearly documented. Retrospectively, introducing it in the test plan was clearly an error, and the extra 12 sea states introduced to integrate it would have been better used for an other parameter such as the significant wave height.

Θ_S should be kept as a bi-level factor to limit the number of required tests, but broader spectra should be used. If the angular spreading is modelled through a cos^{2s} function, values of s around 1 and 20 should be utilised to make sure an impact of Θ_S could be monitored. This involves probably the generation of waves over a broader range of direction, probably between $[-60\,°; 60\,°]$.

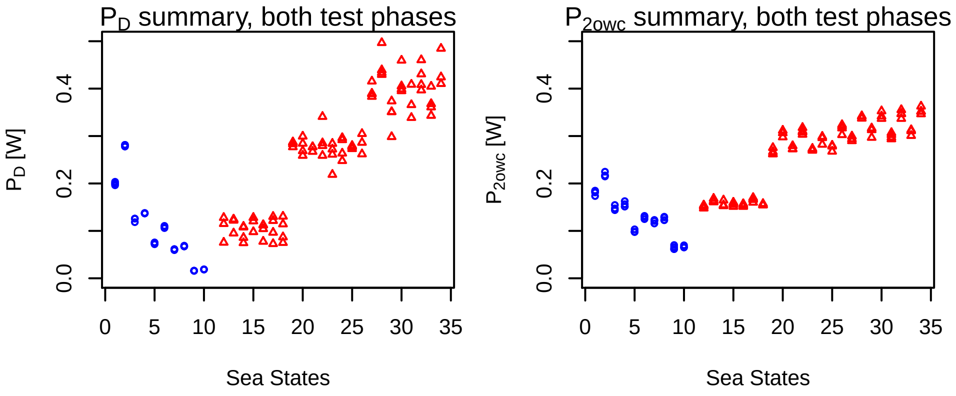

(a) Duck power output ***(b)*** Double OWC power output

Figure 7.16: *Power output of the duck and the double OWc for both phase. Unimodal sea states (1^{st} phase) are represented in red triangle, bi-modal sea states (2^{nd} phase) are represented in blue circles*

7.3 Second phase results: bi-modal sea states

7.3.1 Results coherence with the 1^{st} phase.

At the start of the second phase, tests were done to insure that the observations will be coherent with first phase observations. Particular concern was given to OWCs as different devices were used during each phase. A few runs from the first phase were repeated with the new devices to insure that power outputs were comparable.

Due to the issues with the calibration of the wave gauges (see Section 6.2.2.1 on page 138), power outputs from both Duck and OWCs during the 2^{nd} phase were as expected lower than during the 1^{st} phase. A summary of the power output for both devices and all tested sea states is presented in Fig. 7.16

Several step of verification were done to insure the quality of the results from the 2^{nd} phase before finding the problems in the wave measurements.

- The waves. As shown on Table 6.4 on page 142, waves for the 2^{nd} phase were measured in December 2010, and the double OWC measurements were done in January. In order to minimize any doubts on the waves themselves, sea state 3 was re-measured on the 2^{nd} of February. No significant changes were observed, so this seems to rule out any variations in the waves.

- Waves analysis method. Wave elevations from the 1^{st} phase were analysed using the MLM whereas wave elevations from the 2^{nd} phase were analysed with the MMLM. To ensure that this did not introduced an error, analysis of 2^{nd} phase wave elevations were repeated with the MLM. The results are presented in Fig. 7.17. There is no evidence of a difference between MMLM and MLM results. $\hat{H}_{m0,1}$ estimates are slightly higher with the MMLM, confirming that this method is probably producing *sharper* spectra.

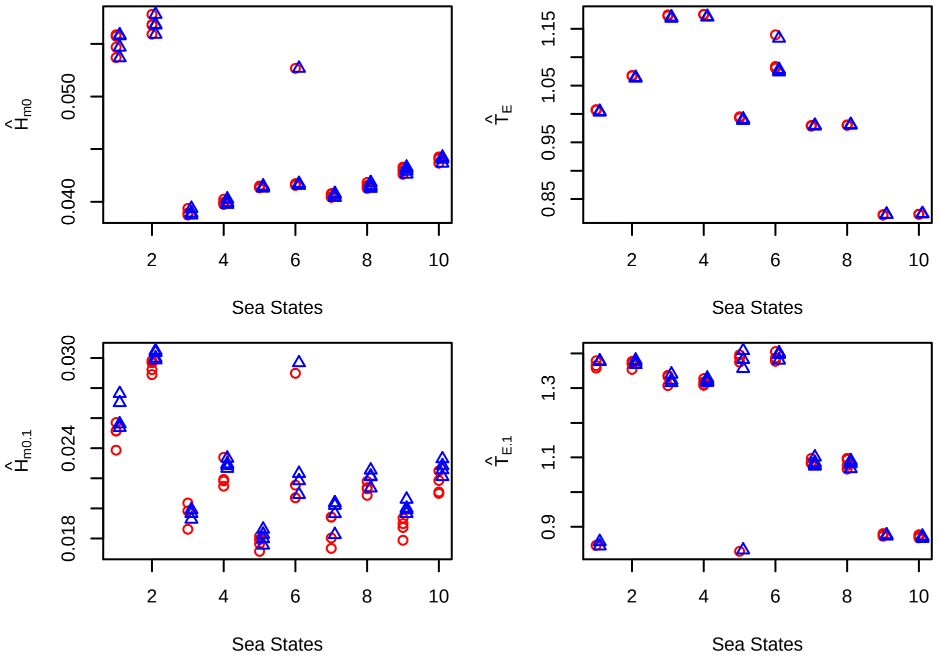

Figure 7.17: *Comparative analysis of* 2^{nd} *phase sea states parameters with the MLM and the MMLM. Red circles represent the MLM results and blue triangles represent the MMLM results.*

- Difference between the OWCs. As shown on Table 5.1 on page 114, power outputs from the new OWC are similar to Belfast OWCs used during the 1^{st} phase. While this does not insure that the devices are identical, large difference in power output seems unlikely to be the results of the change of devices. It also rules out differences in the acquisition system or the instrumentation of the OWCs.

- Difference on the analysis. All results presented in this work are issued from analysis done with the same routines after the last tests were done. Looking at each test separately, results are consistent and follow similar patterns for the three devices. Additionally, power outputs from the single and double OWCs are coherent, with the power output of the double OWC being roughly twice the power output of a single OWC.

- On the 2^nd of February, a test of a single OWC with second phase sea states showed similar power output to the power output from each OWC in the same conditions. Fig. 7.18 shows the power outputs from each OWC during the double OWC tests, and the outputs from a single OWC during the verification tests. The results from the double OWC tests appear to be very consistent, and match results from the single OWC(same OWC which test are also matching with the 1^{st} phase tests). This figure gives confidence in the measurements of the double OWC during the 2^nd phase of tests.

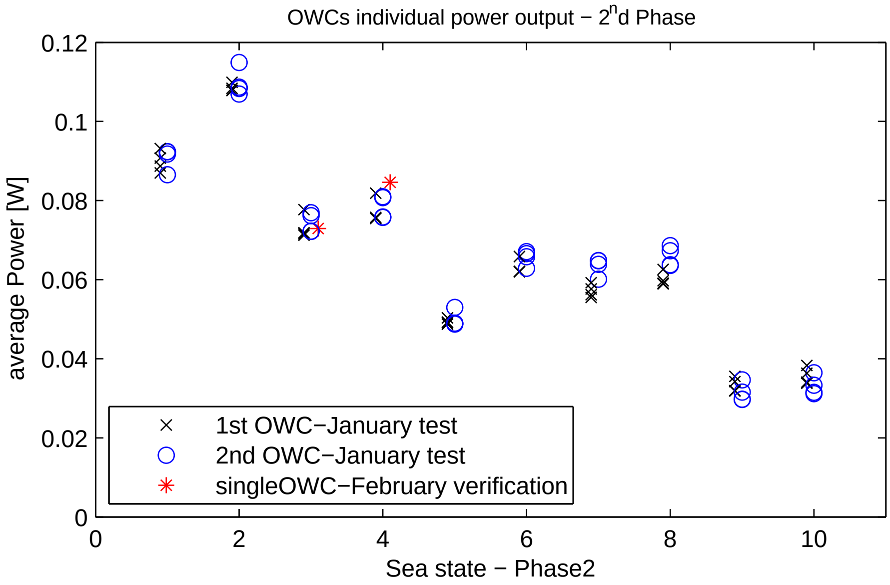

Figure 7.18: *Average power outputs from the OWCs,* 2^nd *phase. A small offset along the x-axis is introduced between each data series to ease the reading of the graph.*

7.3.2 General observation

As it happens, conditions of the second phase do not allow a rigorous analysis. The correlation between $\hat{H}_{m0}$ and $\hat{\delta\theta}_M$ do not allow to investigate the influence of each parameters. However, for both the double OWC and the Duck, observed power outputs and capture width are consistent and unsurprising.

The sea states can be classified into two categories: sea states with $\delta T_E << 1$ (sea states 1,2, 5 and 6 in Table 6.3 on page 137) and sea states with $\delta T_E > 0.12$. Due to the difference in H_{m0} levels between both phase of tests, only the capture width of the devices is used to compare the results from both phases.

7.3.3 Comments on first group of sea states

Concentrating on the first group, Fig. 7.19a shows the variability of Cw_D. In this figure, red triangles are the observation from the second phase and blue circles represents the observations from the first phase (only observations from JONSWAP spectra were used). A linear model using $\hat{T}_E$ and $\hat{H}_{m0}$ as variables is fitted to the first phase data, represented with a black line. The green points are the model prediction using $\hat{T}_E$ and $\hat{H}_{m0}$ values from the second phase observations. The green dashed line is a representation of the model using $\hat{T}_E$ and the mean value of $\hat{H}_{m0}$ values from the second phase observations.

The red triangles are significantly lower than the green points. It means that Cw_D for the bi-modal sea states is significantly lower than what would have been predicted based only on uni-modal sea states. Those results are outlying the effect of directionality on the duck performances, effects that were not shown by the uni-modal tests only. It reinforce the interpretation that generated uni-modal sea states were not broad enough to highlight directionality effects. An ANCOVA analysis applied to a linear model including $\hat{T}_E$, $\hat{H}_{m0}$ and $Type$ and all second order interactions suggests that it is mainly slopes in relation to $\hat{T}_E$ that are different from uni-modal to bi-modal spectra. The summary of the minimal adequate model is presented below:

minimal adequate model summary:

Call:

$$lm(formula = Cw_D \sim \hat{H}_{m0} + \hat{T}_E + Type + \hat{T}_E : Type)$$

Residuals:

Min	1Q	Median	3Q	Max
-3.35569	-0.80290	0.08714	0.74353	5.20454

Coefficients:

	Estimate	Std. Error	z value	Pr($>\lvert z\rvert$)	
(Intercept)	-26.49365	8.16845	-3.243	0.00189	**
$\hat{H}_{m0}$	-315.27708	148.51659	-2.123	0.03770	*
$\hat{T}_E$	53.15672	2.94449	18.053	¡ 2e-16	***
Unimodal	0.09211	5.43120	0.017	0.98652	
$\hat{T}_E$:Unimodal	14.53329	3.20774	4.531	2.68e-05	***

```
---
Signif. codes:  0    ***    0.001    **    0.01    *    0.05    .    0.1
    ⇝     1

Residual standard error: 1.621 on 63 degrees of freedom
Multiple R-squared: 0.9689,     Adjusted R-squared: 0.967
F-statistic: 491.2 on 4 and 63 DF,  p-value: < 2.2e-16
```

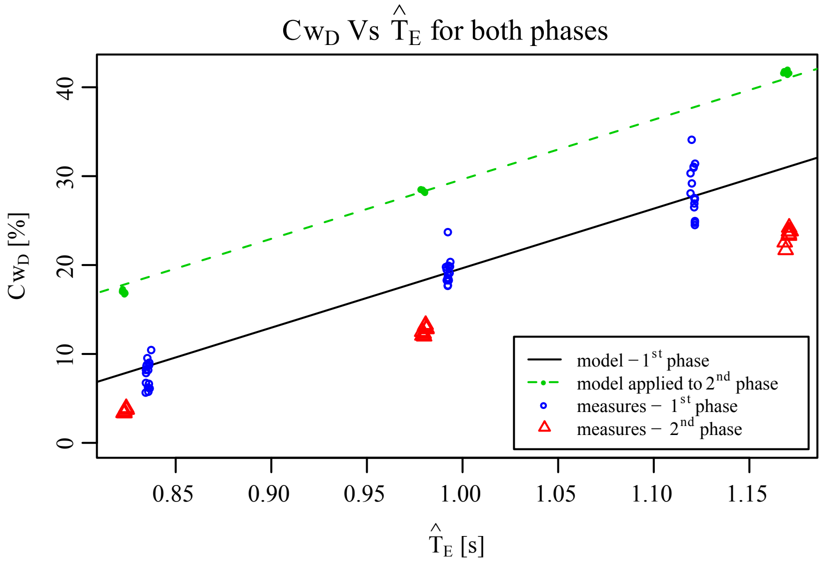

(a) Duck capture width

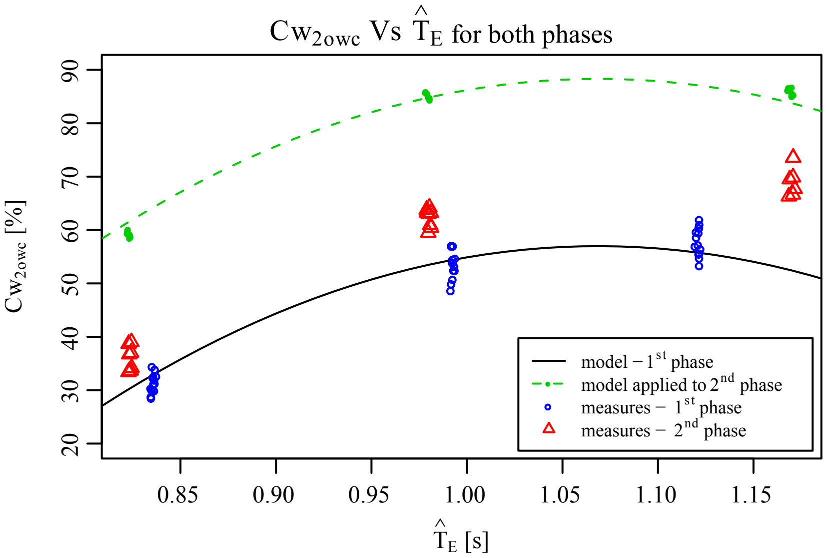

(b) Double OWC capture width

Figure 7.19: *Comparison of capture width from the Duck and the double OWC for 1^{st} phase results (JONSWAP spectra) and sea states 3,4,7,8,9,10 of the 2^{nd} phase.*

The same procedure is applied to the double OWC observations. Results are displayed in Fig. 7.19b. The figure shows that the double OWC performed well in the bi-modal sea states, with higher capture width than during the uni-modal sea states. The values observed are still lower that what could be expected from the model fitted to 1^{st} phase observations and applied to $\hat{T}_E$, $\hat{H}_{m0}$ from the 2^{nd} phase. However, the range of variation of $\hat{H}_{m0}$ in the 1^{st} phase is not sufficient to confidently characterise its influence, so applying this model to $\hat{H}_{m0}$ values from the 2^{nd} phase is a large extrapolation. Results from this operation are consequently only indicative.

Looking at Fig. 7.19a and Fig. 7.19b, it is clear that splitting the energy into two identical wave systems with 30° difference in mean direction of propagation affects the performances of the duck much more than it affects the performances of the double OWC.

Further tests are needed with comparable wave power level between uni-modal and bi-modal sea states to improve the quality of the conclusion. At the present stage, it is not possible to conclude confidently on the fact that OWCs performances are affected by this type of sea states.

Focusing on the bi-modal sea states of the first group, Fig. 7.20 provides an other point of view on the WECs different behaviours. It gives a more detailed examination of the variation of Cw as a function of $\hat{T}_E$ by differentiating the sea states with a large and small estimated uni-modality index $\hat{\mu}$. As a reminder from Section 6.1.2 on page 123, $\mu = 1$ describes uni-modal sea states, and μ decreases as the energy is spread into different wave systems.

It can be easily seen that $\hat{\mu}$ does not affect both device identically. The capture width of the Duck is visibly higher for sea states with a higher uni-modality index whereas the capture width of the double OWC do not seems to be influenced by it. This should be a good indication that the capture width of the double OWC is not sensitive to the bi-modal nature of the sea states.

7.3.4 Comments on second group of sea states

The second group of sea states ($\delta T_E > 0$) was intended to explore the influence of the $\delta\theta_M$ and μ. A strong correlation appeared between $\hat{\delta T}_E$ and $\hat{H}_{m0}$ which is probably due to the tank calibration (see Section 6.2.2.2 on page 138). This will not allow to evaluate the effect of $\delta\theta_M$ as H_{m0} effect will be predominant.

An other correlation is problematic: $\hat{\mu}$ and $\hat{T}_E$. By varying $\hat{\mu}$, the balance between the wave systems is shifted, resulting in a varying $\hat{T}_E$. It would have been very useful to be able to shift $T_{E,1}$ and $T_{E,2}$ jointly in order to decouple the effects of $\hat{\mu}$ and $\hat{T}_E$. A difficulty lies into

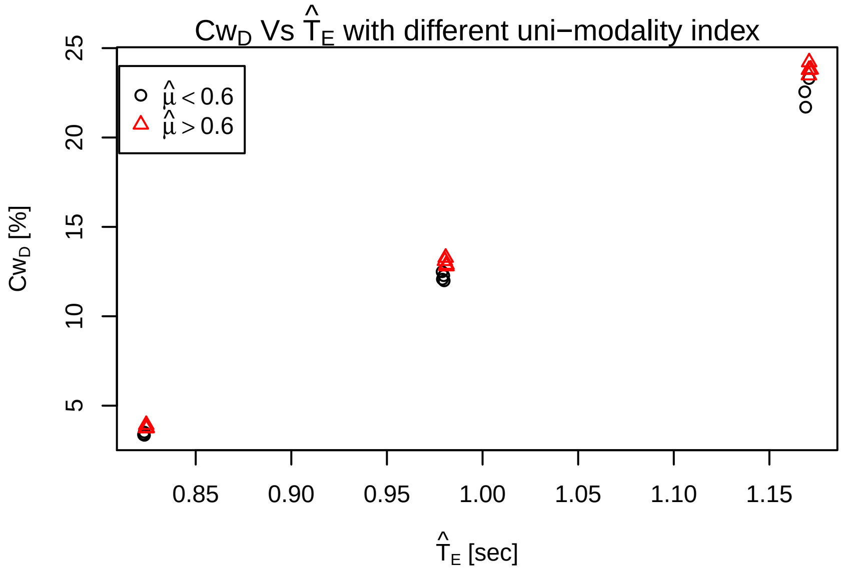

(a) Duck capture width

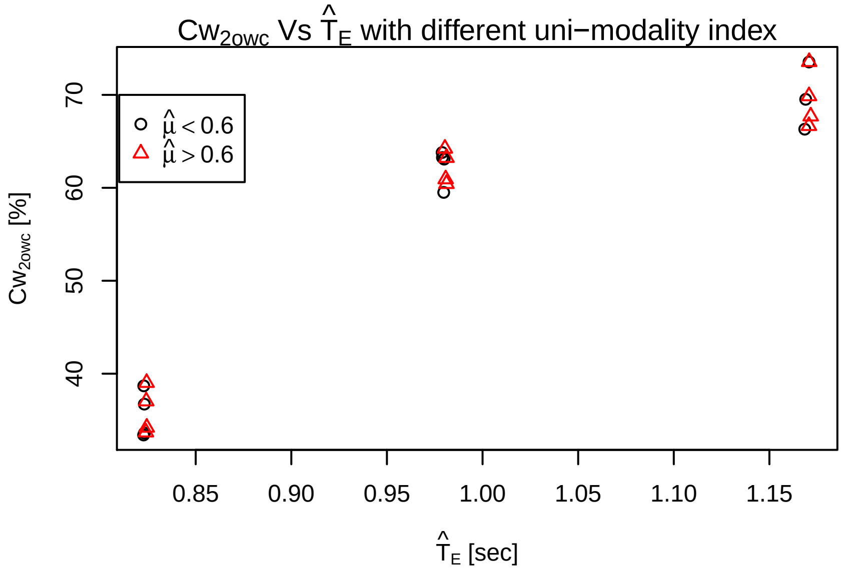

(b) Double OWC capture width

Figure 7.20: *Comparison of capture width from the Duck and the double OWC for sea states of* 2^{nd} *phase results with* $deltaT_E = 0$.

the range of frequencies available in wave tanks such as the Edinburgh Curved tank. By being constrained into $[0.4; 1.8]$ Hz, it is difficult to properly separate two wave systems with identical main direction of propagation and to be able to shift jointly the energy periods of the systems. All together, those tests are consistent: power outputs are increasing with the energy period and the significant wave height, but they do not provide new insight into the way to predict WEC performances in bi-modal sea states. It is interesting to see that $\hat{H}_{m0}$ and $\hat{T}_E$ are enough to give a good estimate of the observed power outputs of both devices: a multi-linear regression using those two parameters fitted to the data yield satisfactory models. Their mathematics expressions are presented in Eq. 7.17 and Eq. 7.18.

$$\overline{P}_D = -(0.95 \pm 0.10) + (10.24 \pm 0.52) \cdot \hat{H}_{m0} + (0.60 \pm 0.10) \cdot \hat{T}_E \text{ with } R^2 = 0.9714 \tag{7.17}$$

$$\overline{P}_{2owc} = -(0.51 \pm 0.04) + (5.89 \pm 0.19) \cdot \hat{H}_{m0} + (0.36 \pm 0.04) \cdot \hat{T}_E \text{ with } R^2 = 0.9878 \tag{7.18}$$

The limited number of tests does not allow to see any curvature in the data. The fact that only the two omnidirectional parameters are enough to model the data is satisfying. However, these findings are not confirmed by observations of resonant WEC at sea, which demonstrates the limit of the tests.

7.3.5 Discussion: 2^{nd} test phase

The second phase of test was not as successful as the first one. To the knowledge of the author, this was one of the first attempt to characterise the behaviour of wave energy converters in bi-modal sea states, and while the results are not as high as expected, many lessons can be learned from those tests.

The first lessons is that good control of bimodal sea states in wave tank is harder than uni-modal sea states. Inaccuracies on the tank calibration are emphasised as different part of the spectra are energised simultaneously. In the current absence of practical method for tank calibration, it means that every sea states generated should be carefully calibrated individually to match the requirements of the test plan. Time lacked at the end of this work, and the test results were consequently put in jeopardy.

The second lesson is that properly fixing the level of an important parameters such as H_{m0} is a wishful but impractical decision. It would have been better to force its variation in a controlled way instead of observing correlation between its unplanned variation and other parameters. With all the limitations previously mentioned, some observations are still valuable. There is strong evidences that the devices performed differently in bi-modal sea states. Using sea states for which each wave systems had an identical energy period but their mean direction of propagation was separated by $30\,^{\circ}$, it was shown that the capture width of the OWCs was not reduced while the capture width of the duck decreased significantly compared to uni-modal with similar energy period. This is unsurprising for a directional device compared to omnidirectional devices. The unimodality index μ introduced in Section 6 on page 122 proved to be a useful indicator of the differences between the two devices. Further tests with different level of $\delta\Theta_M$ are now needed to characterise this dependency of the duck towards this type of bi-modal sea states, and to explore how μ could be used to moderate the production estimation of WECs in multi-modal sea states.

Chapter 8
Conclusion

8.1 Main conclusions

As stated in the introduction, the main objective of this project was to quantify the influence of a set of key sea state parameters on the performances of wave energy converters. In essence, the content of this work responds to the initial problem, but under a set of limitations.
The approach taken was to use the influence of the energy period as a benchmark to evaluate other less used parameters. Three wave energy converter models were selected: a single omnidirectional OWC mounted rigidly on the bottom of the tank, a set of two of those OWCs to act both as a weakly directional device and as the simplest form of WEC array and a desalination duck model. Sea states were divided between uni-modal and bi-modal sea states. For the uni-modal sea states, parameters relative to the shape of the wave system were investigated. These include a frequency spreading parameter, an angular spreading parameter and a measure of the mean direction of propagation variation with respect to the frequency. For the bi-modal sea states, emphasis was given to the relative position of the wave systems in the frequency-direction (f, θ) plan. The effect of the separation along the frequency and along the direction axes was investigated. A uni-modality index was introduced in an attempt to evaluate the influence of bi-modality directly.

The results presented are all issued from measurements in the Edinburgh curved tank. The decision to use physical tests instead of numerical modelling results was driven by the necessity not to overlook any physical phenomenon that may affect the device performances, such as viscosity or the devices alignment with the waves. Also, long run times were required for each test ($1024\,\mathrm{s}$ at $16\,\mathrm{Hz}$) in order to get directional spectra with the required control and resolution. Generating large number of results with this run time with numerical model is still impractical today.

For uni-modal sea states, parametric models of the performances of the devices could be devised. The results presented show that the frequency spreading, and specially its interaction with the energy period, has an influence on the power output of the devices, which is as important as the influence of the energy period alone. This conclusion is valid for the three devices tested, which suggests that it might be the case for a large range of wave energy converters. The results were further contrasted while looking at the capture width ratio of the three devices. The influence of the frequency spreading could not be shown to be significant in the case of the duck. Surprisingly, the influence of wave directionality could not be shown to be significant during those test on any of the devices.

The validity of the parametric models is limited to the range of the parameters explored. For the energy period especially, only a portion of the range that a full scale device would experience in a real environment is covered in this work. Tests were not designed to evaluate the effect of the significant wave height. It is likely that a more complex relation between power output and the significant wave height could be observed than the linear relation exhibited by those tests.

Within the mentioned limitations, the fact that parametric models of WECs are strongly dependant on the frequency spreading calls into question the common choice of energy period and significant wave height as sole parameters for the electricity production estimation of wave energy converters. Specifically, it suggests that the combination of power matrices and scatter diagram might be an over simplistic method to estimate the power production of wave energy converters. A novel method, based on piecewise parametric models covering the full range of variation of the key parameters, may provide more reliable estimations for site with large proportion of uni-modal spectra.

The tests in bi-modal sea states were a first attempt to characterise WEC performances in such conditions. The observations reveal a drop of the duck performances for sea states with a mark difference between the mean direction of propagation of wave systems. On the contrary, the pair of OWCs do not seems sensitive to this parameter. During the course of this work, this was the only evidence of different behaviour between directional and omnidirectional devices.

Overall, the bi-modal sea states tests did not produced much useful knowledge toward more reliable production estimation in multi-modal conditions. However, taking an overview of the work presented, it appears that a method combining the wave system isolation inside sea states, the parametric models developed for uni-modal spectra and the uni-modality index could be considered. It might be possible to estimate the performances of wave energy converters in multi-modal sea states by summing the individual contribution of each isolated wave system. Each individual contribution would be estimated with the parametric models. The results of the summation could then be modulated by a parameter like the uni-modality index to accommodate possible destructive interactions between wave systems. If this method of performance estimation of wave energy converters proves to be practical, it will be entirely independent from the controversial concept of power matrices. It will use only records of the relevant sea states parameters and it would probably be easily transposable from one site to an other.

8.2 Reflection on the method

The initial experimental plan for the presented work was to treat the considered sea state parameters as categorical factors with two or three levels. Tests would then be conducted following full factorial plans (if practical) and the parameters' influence and interactions on the performances of the devices would be assessed using analysis of variance. This initial course of action had to be adapted after the results of the sea state tank estimations.

In the uni-modal case, the estimated values of each parameter varied around their target levels more than expected. It was thought that this reflects real variations of the sea states. From those observations, the parameters had to be considered as continuous variables and multi-regression was used. Beside those forced adjustments, the method proved adequate and it allowed separation and analysis of the influence of most parameters. However, as it appears that considering the parameters as categorical factors is not possible, it would have been more efficient to design the test plan accordingly.

In the bi-modal case, observed correlations between key parameters were such that the initial approach was abandoned altogether. The sea states had to be categorised and a mixed method was used. Some parameters could be evaluated jointly, while the influence of the uni-modality index was analysed separately and only with a subset of the sea states. This do not mean that the initial approach is not possible, but it will require a much more careful calibration of the sea states to avoid correlations between parameters.

For both uni-modal and bi-modal sea states, the initial plan was to fix the value of the significant wave height. This proved to be impractical and resulted in uncontrolled variation of a highly influential parameter. As it is now not believed that successful fixing of the level of energy in the sea states is not achievable, future test plans should include controlled variations of all the key parameters in order to ensure that no unwanted correlations appears.

This was not the only constraint associated with the use of physical model test. While providing a good level of control on the generated wave, wave tanks do not offer a very wide range of frequencies and directions.

For the frequency aspect, it is difficult with today experimental facilities to replicate real cases where the resonant frequency of a device is in a low energy area between the peak periods of a bi-modal spectra. The range of energy period available is also limited and the behaviour of resonant devices can only be evaluated around their natural frequencies. This clearly limit the scope of the parametric models that can be devised by testing one device in one tank. The problem could be overcome by using either different tanks to cover different part of the frequency range or by using several scales of model in one tank.

For the directional aspect, the range provided in the Edinburgh Curved tank limits the maximum broadness of uni-modal spectra as waves can only be safely generated in a $\pm 40^\circ$ range. This probably prevents the identification of thresholds from which the performances of directionally sensitive devices would start to be affected. For bi-modal spectra, the range of direction limits significantly the type of spectra that can be generated. However, the future generation of wave tanks should offer a much wider range of direction, which will enable efficient research into the influence of directionality.

8.3 Wave measurement conclusions

Wave tank tests required good directional spectral estimation of sea state generated with the capability to isolate wave systems in multi-modal sea states. This led to the adaptation of existing methods to the constraints of deterministically generated sea states in a reflective environment. The Maximum Likelihood Method (MLM) and one of its derivative, the Modified Maximum Likelihood Method (MMLM) were modified to ensure that the discretization of the (f, θ) utilised for spectral estimation was identical to the discretization employed by the deterministic wave generation method based on single summation. By ensuring that spectral estimates and wave generation were done for the same pairs of (f_p, θ_q), stable and accurate spectral estimate were obtained. Those estimates compared favourably with the industry standard, the BDM as implemented in *Wavelab*^{TM}.

A method to isolate wave systems was developed. It differs from previous spectrum partitioning tools as it does not aim to attribute every point of a spectrum to a wave system, but to isolate wave systems from noise in the spectra. This method proved useful to analyse bi-modal sea-states, but also uni-modal sea states as it allowed to compute accurate spectral parameters for the unique wave system. The isolation method has only been tested on tank data or simulated waves, but there is no reason why it could not be applied to ocean data.

Simulated data were used to characterise the spectral estimation methods coupled with the isolation routine and to gain understanding into the design of wave probe arrays. As for investigating the effect of sea state parameters, the approach taken was to generate a large number of simulated wave elevation from randomised sea states and to use statistical methods to analyse the results.

The principal findings are:

- Aliasing is not the most important phenomenon governing the design of probe arrays if there is uncertainty in the knowledge of the array geometry. In such case, using larger array subject to aliasing but less sensitive to the error in probe position reduces the risk of overspreading narrow spectra.
- For the angular spreading, a threshold value of $12.8\,^\circ$ was identified. For spectra narrower than this threshold, the angular spreading is overestimated whereas it is well estimated for broader spectra.
- Trying to choose the best method between the MLM and the MMLM, contrasting conclusions can be drawn from this work. Coupled with the isolation routine, the MLM did perform equally or better than the MMLM for tests with simulated data. However, bi-modal sea states measurements from the tank suggest that the MMLM may produce sharper estimates.

Altogether, the methods developed for this work proved to be accurate enough. Some limitation of the tank calibration could even be identified, which in itself demonstrates their good performances.

8.4 Further work

Additionally to what has been presented in the previous section, several short and well-defined projects could compliment the work done in this thesis and answer some specific questions:

- Further work should be conducted to investigated the link between individual wave amplitudes and the reflection coefficient for polychromatic waves. From the presented results, their influence could not be shown to be significant. This contrasts with previously published research in regular waves. It would be particularly interesting to be able to relate the reflection coefficient to other parameters such as the significant wave height. The work should also be extended to oblique waves.

- The PTPD method implemented to measure wave front directions of propagation could be used as a base to develop a routine to estimate directional spectra of deterministically generated waves. The methods utilised in this work would provide a good benchmark for a comparison.
- The adaptation for deterministic waves applied to the MLM and MMLM proved successful. It should consequently be experimented with the BDM which is accepted as more efficient.
- Experimenting on the nature of waves, it would be interesting to use wavelet analysis to monitor the evolution of the frequency spectrum of waves generated by deterministic routines. Such research would provide inside knowledge into the differences between deterministic and random waves.
- It is necessary to investigate if the MMLM is actually generating sharper spectral estimate even for uni-modal spectra, as suggested by the measures of bi-modal spectra in the tank. If it is the case, it would be necessary to explain why the tests with simulated data did not show this difference. The hypothesis that it is due to interaction with the isolation routine should be investigated.
- The shape and coefficients of the weighted window used to compute the gradient for the isolation routine could be modified as a function of the node position relatively to the wave system peak. An improvement in the tracking of wave system tails should be achievable.
- At the current stage, the separation of wave system is not very sophisticated. An improved version taking into account the *low point* between the two peaks could be implemented. The direction of the line of separation between the wave systems should also be made dependant to the relative position of the peaks.
- The first phase of test could be repeated with some modifications. $\delta\theta_M$ should be ignored and a controlled variation of H_{m0} should be introduced instead. A smaller version of the Duck with a resonant frequency closer to 1 Hz should be used to provide better comparison between the devices. The results of the single and double OWC were not different

enough to justify the use of both devices. Instead, a third WEC such as a point absorber with compliant moorings should be introduced.

- The current test plan should be put into context by scaling it to real seas. Beside using well-known spectral shapes, those sea states were selected based on the tank possibilities and were not scaled down version of realistic seas. It would be interesting to evaluate the reality level of the sea states generated into the tank.
- A validation must be applied to the parametric models devised for each devices in the case of uni-modal sea states. First, spectra with parameters inside the range of parameters used to define the parametric models and with random spectral shape should be used. If the parametric models are efficient to estimate the power absorbed by the devices in those sea states, a second group of sea states could be used to explore the extent into which the parametric models could be extrapolated to sea states with parameters outside the explored range of parameters.

Part I

Appendix

Appendix A
The wave generation and tank characteristics

A.1 *Ocean* code exemples used for generating the sea states

This is the code used to generate the uni-modal wave 13 described in Table 6.2 on page 127: (Note that a right arrow (↝) is used to indicate a line continuation.)

```
 experiment "phase1_wave13" with ("C:\0-jlucas_seas\ttf\30Jan2008.ttf")
#include <sea.inc>
#define PI 3.1415927
#define exp(num) (2.718282**num)

begin
/* Setting up the spectrum contants */
        print("setting up spectrum constants");
        real rate = 32.0;
        real freq = 1.0/32;
        int angles = 32;
        real tetaMin = D2R(-40);
        real tetaMax = D2R(40);
        int minCutOff = 12;             /* generated spectrum will start at
            ↝freq*minCutOff = 0.3750 Hz */
        int maxCutOff = 56;             /* generated spectrum will stop at
            ↝freq*maxCutOff = 1.75 Hz */
        int rNum = 15;                  /* rNum has to be changed according
            ↝to rate and angles. rNum = 14 for angles=16 and rate = 32;

/* setting freqBandVect */
        print("setting up freq vectors, freq = " ^ string(freq));
        real temp1 = minCutOff*freq+freq/2;
        real temp2 = maxCutOff*freq+freq/2;
        real freqBandVect[] = temp1 to temp2 step freq;
        real pulseVect[] = minCutOff*freq to  (maxCutOff+1)*freq-(freq/angles
            ↝) step freq/angles ;
```

```
        int lPulse = sizeof(pulseVect[]);
        int lBand = sizeof(freqBandVect[]);

/* Setting the angleVector*/
        real angleStep = (tetaMax - tetaMin) / (angles - 1);
        real tetaVect[] = tetaMin to tetaMax-angleStep step angleStep;
        print("angleStep = " ^ string(R2D(angleStep)));
        print("tetaVect(32) = " ^ string(R2D(tetaVect[32])));
        int lAngle = sizeof(tetaVect[]);

/* %%%%%%%%%%%%%%%%%%%%%%%%%%%%%%%%%%%%%%%%%%%%% */
/* Generating the ampVect*/

        real Tz = 0.80;        /*in [sec], peak period*/
        real Hm0 = 0.06;        /*im [m], significant wave height*/
        real limTheta = D2R(10);
        real stepTheta = 2*limTheta / (lBand-1);
        real tetaMean[] = -limTheta to limTheta step stepTheta;
        real spread = 100.0;    /* keeping constant spread trough the
            ⤳spectrum -> no need of "realisitic" seas. small = 100, large  =
            ⤳ 5*/
        real B = (Tz/0.751)**(-4);      /* Tucker book p101*/
        real A = B * Hm0**2 / 4;

        real spectrum[];
        for i = 1 to lBand do
                spectrum[i] = A * (freqBandVect[i]**(-5)) * 2.7183**( -B *
                    ⤳freqBandVect[i]**(-4) );
        end;

        /* now, defining the speading function */
        real normSpread = 0;
    real spreading[];
    spreading[lBand*lAngle] = 0;
    for i = 1 to lBand do
        for j = 1 to lAngle do
            spreading[(i-1)*lAngle+j] = cos(tetaVect[j]+tetaMean[i])**(2*
                ⤳spread);
            normSpread = normSpread + spreading[(i-1)*lAngle+j]*angleStep;
        end;
    end;
```

```
    for i = 1 to lBand*lAngle do
        spreading[i] = spreading[i] * lBand / normSpread;
    end;

        /* Computing the amp vector*/
        real ampVect[];
        ampVect[lPulse] = 0;

        for i = 1 to lBand do
                for j = 1 to lAngle do
                        ampVect[(i-1)*lAngle+j] = ((2*freq*spectrum[i])
                            ↝**(0.5)) * ((spreading[(i-1)*lAngle+j]*
                            ↝angleStep)**(0.5));
                end;
        end;

        /* The wave itself*/
        wave longCrested;
        wave tempWave;
        for i = 1 to lBand do
                for j = 1 to lAngle do
                        tempWave = single(pulseVect[(i-1)*lAngle+j] ,
                            ↝ampVect[(i-1)*lAngle+j] , tetaVect[j]);
                        longCrested = tempWave + longCrested;
                end;
        end;
        wave longCrested_1 = random(longCrested , 0);
        wave longCrested_2 = random(longCrested , 1);
        wave longCrested_3 = random(longCrested , 2);
        wave longCrested_4 = random(longCrested , 3);
        wave longCrested_5 = random(longCrested , 4);

/* %%%%%%%%%%%%%%%%%%%%%%%%%%%%%%%%%%%%%%%%%%% */
/* generating the << merged >> wave */
        run "phase1_wave13_run1" with (rNum,256,50)
                makewave longCrested_1 on 1;
        end;
        run "phase1_wave13_run2" with (rNum,256,50)
                makewave longCrested_2 on 1;
        end;
        run "phase1_wave13_run3" with (rNum,256,50)
```

```
                makewave longCrested_3 on 1;
        end;
        run "phase1_wave13_run4" with (rNum,256,50)
                makewave longCrested_4 on 1;
        end;
        run "phase1_wave13_run5" with (rNum,256,50)
                makewave longCrested_5 on 1;
        end;
end;
```

This is the code used to generate the bi-modal wave 1 described in Table 6.3 on page 137:

```
experiment "phase2_wave1" with ("C:\edesign\lib\edin_curve\default.ttf")

#include <sea.inc>

#define PI 3.1415927

#define exp(num) (2.718282**num)

begin

/* Setting up the spectrum contants */
        print("setting up spectrum constants");
        real rate = 32.0;
        real freq = 1.0/32;
        int angles = 32;
        real tetaMin = D2R(-40);
        real tetaMax = D2R(40);
        int minCutOff = 12;             /* generated spectrum will start at
            ↝freq*minCutOff = 0.3750 Hz */
        int maxCutOff = 60;             /* generated spectrum will stop at
            ↝freq*maxCutOff = 1.75 Hz */
        int rNum = 15;                  /* rNum has to be changed according
            ↝to rate and angles. rNum = 14 for angles=16 and rate = 32;

/* setting freqBandVect */
        print("setting up freq vectors, freq = " ^ string(freq));
        real temp1 = minCutOff*freq+freq/2;
        real temp2 = maxCutOff*freq+freq/2;
        real freqBandVect[] = temp1 to temp2 step freq;
```

```
        real pulseVect[] = minCutOff*freq to (maxCutOff+1)*freq-(freq/angles
            ↝) step freq/angles ;
        int lPulse = sizeof(pulseVect[]);
        int lBand = sizeof(freqBandVect[]);

/* Setting the angleVector*/
        real angleStep = (tetaMax - tetaMin) / (angles - 1);
        real tetaVect[] = tetaMin to tetaMax-angleStep step angleStep;
        print("angleStep = " ^ string(R2D(angleStep)));
        print("tetaVect(32) = " ^ string(R2D(tetaVect[32])));

        int lAngle = sizeof(tetaVect[]);

/*
    ↝%%%%%%%%%%%%%%%%%%%%%%%%%%%%%%%%%%%%%%%%%%%%%%%%%%%%%%%%%%%%%%%%%%%%%%%%%%%%%%%%%%%
    ↝ */
/* wave details    - - line 41 */

        real Tz1 = 1.05;                        /*in [sec], peak period*/
        real Hm01 = 0.061;                      /*im [m], significant wave
            ↝height*/
        real tetaMean1 = D2R(0);        /*in [deg], the mean wave direction
            ↝*/
        real spread1 = 50.0;            /* keeping constant spread trough
            ↝the spectrum -> no need of "realisitic" seas. small = 100,
            ↝large  = 5*/


        real Tz2 = 0.630;               /*in [sec], peak period*/
        real Hm02 = 0.041;                      /*im [m], significant wave
            ↝height*/
        real tetaMean2 = D2R(0);        /*in [deg], the mean wave direction
            ↝*/
        real spread2 = 50.0;            /* keeping constant spread trough
            ↝the spectrum -> no need of "realisitic" seas. small = 100,
            ↝large  = 5*/



/* Generating the ampVect1*/
        real B1 = ( Tz1 / 0.751 )**(-4);        /* Tucker book p101*/
        real A1 = B1 * Hm01**2 / 4;
```

```
    real spectrum1[];
    real gamma1 = 5;
  real sigma1 = 0.08;
    real G1;
    for i = 1 to lBand do
            G1 = gamma1 ** 2.718282**( -((1.286*Tz1*freqBandVect[i] - 1)
                ↪**2) / (2*sigma1**2) );
            print("G1 = " ^ string(G1));
            spectrum1[i] = G1*0.0749*Hm01**2*Tz1* (Tz1*freqBandVect[i])
                ↪**(-5) * 2.718282**(-0.4567/((Tz1*freqBandVect[i])**4))
                ↪;
    end;

    /* now, defining the spreading function */

    /* value was taken by looking at the spread value produced by
        ↪double_summation_RP.m */
    real normSpread1 = 0;
    real spreading1[];
    spreading1[lAngle] = 0;
    for i = 1 to lAngle do
            normSpread1 = normSpread1 + (cos(tetaVect[i]+tetaMean1)**(2*
                ↪spread1))*angleStep;
            spreading1[i] = cos(tetaVect[i]+tetaMean1)**(2*spread1);
    end;
    for i = 1 to lAngle do
            spreading1[i] = spreading1[i] / normSpread1;
    end;

    /* Computing the amp vector*/
    real ampVect1[];
    ampVect1[lPulse] = 0;

    for i = 1 to lBand do
            for j = 1 to lAngle do
                    ampVect1[(i-1)*lAngle+j] = ((2*freq*spectrum1[i])
                        ↪**(0.5)) * ((spreading1[j]*angleStep)**(0.5));
            end;
    end;
```

```
/* Generating the ampVect2*/

        real B2 = (Tz2/0.751)**(-4);    /* Tucker book p101*/
        real A2 = B2 * Hm02**2 / 4;

        real spectrum2[];
        real gamma2 = 5;
      real sigma2 = 0.08;
        real G2;
        for i = 1 to lBand do
                G2 = gamma2 ** 2.718282**( -((1.286*Tz2*freqBandVect[i] - 1)
                    ↝**2) / (2*sigma2**2) );
                print("G2 = " ^ string(G2));
                spectrum2[i] = G2*0.0749*Hm02**2*Tz2* (Tz2*freqBandVect[i])
                    ↝**(-5) * 2.718282**(-0.4567/((Tz2*freqBandVect[i])**4))
                    ↝;
        end;

        /* now, defining the speading function */


        /* value was taken by looking at the spread value produced by
            ↝double_summation_RP.m */
        real normSpread2 = 0;
        real spreading2[];
        spreading2[lAngle] = 0;
        for i = 1 to lAngle do
                normSpread2 = normSpread2 + (cos(tetaVect[i]+tetaMean2)**(2*
                    ↝spread2))*angleStep;
                spreading2[i] = cos(tetaVect[i]+tetaMean2)**(2*spread2);
        end;
        for i = 1 to lAngle do
                spreading2[i] = spreading2[i] / normSpread2;
        end;

        /* Computing the amp vector*/
        real ampVect2[];
        ampVect2[lPulse] = 0;

        for i = 1 to lBand do
                for j = 1 to lAngle do
```

```
                        ampVect2[(i-1)*lAngle+j] = ((2*freq*spectrum2[i])
                            ⤳**(0.5)) * ((spreading2[j]*angleStep)**(0.5));
                end;
        end;

/* The wave itself*/
        wave biModal;
        wave tempWave;

        for i = 1 to lBand do
                for j = 1 to lAngle do
                        tempWave = single(pulseVect[(i-1)*lAngle+j] ,
                            ⤳ampVect1[(i-1)*lAngle+j]+ampVect2[(i-1)*lAngle+
                            ⤳j]  , tetaVect[j]);
                        biModal = tempWave + biModal;
                end;
        end;
        wave biModal_1 = random(biModal , 1);
        wave biModal_2 = random(biModal , 2);
        wave biModal_3 = random(biModal , 3);
        wave biModal_4 = random(biModal , 4);

/*
    ⤳%%%%%%%%%%%%%%%%%%%%%%%%%%%%%%%%%%%%%%%%%%%%%%%%%%%%%%%%%%%%%%%%%%%%%%%%%%%%%%%%%%%%
    ⤳ */

/* generating the << merged>> wave */

        run "phase2_wave1_run1" with (rNum,256,50)
                makewave biModal_1 on 1;
        end;
        run "phase2_wave1_run2" with (rNum,256,50)
                makewave biModal_2 on 1;
        end;
        run "phase2_wave1_run3" with (rNum,256,50)
                makewave biModal_3 on 1;
        end;
        run "phase2_wave1_run4" with (rNum,256,50)
                makewave biModal_4 on 1;
        end;
```

```
end;
```

A.2 Precision of the angle estimation method

This document is used to explore the errors in the computation of θ associated to the error in the probe position and the phase mesurement.

Solving the sytem

In this part, the *a* and *b* represents the cosinus and the sinus of the wave direction of propagation.
The values in the form X21 are the distance between the probes along the x and y axis as variables
The ψ are the absolute phases at each probes

> *restart*

This system corresponds to the second stage

$$> \; syst := \{k\cdot(\mathrm{X21}\cdot\mathrm{a} + \mathrm{Y21}\cdot\mathrm{b}) = \psi 2 - \psi 1, k\cdot(\mathrm{X31}\cdot\mathrm{a} + \mathrm{Y31}\cdot\mathrm{b}) = \psi 3 - \psi 1\}$$

$$syst := \{k\,(X21\,a + Y21\,b) = \psi 2 - \psi 1,\; k\,(X31\,a + Y31\,b) = \psi 3 - \psi 1\}$$

$$> \; sol := solve(\mathrm{syst}, [\mathrm{a}, \mathrm{b}])$$

$$sol := \left[\left[a = \frac{-Y21\,\psi 3 + Y21\,\psi 1 + \psi 2\,Y31 - \psi 1\,Y31}{(X21\,Y31 - X31\,Y21)\,k}, b = -\frac{X31\,\psi 2 - X21\,\psi 3 + X21\,\psi 1 - X31\,\psi 1}{k\,(X21\,Y31 - X31\,Y21)}\right]\right]$$

$$> \; sol[1]$$

$$\left[a = \frac{-Y21\,\psi 3 + Y21\,\psi 1 + \psi 2\,Y31 - \psi 1\,Y31}{(X21\,Y31 - X31\,Y21)\,k}, b = -\frac{X31\,\psi 2 - X21\,\psi 3 + X21\,\psi 1 - X31\,\psi 1}{k\,(X21\,Y31 - X31\,Y21)}\right]$$

Calcul de Θ

Here, a and b are entered directly from the hand solving of the system. They are the expression that will be used for the rest of the computation.

In this part, a and b are defined from hand witten solving of the system:

$$> \; \mathrm{a} := (\varphi 1, \varphi 2, \varphi 3, \mathrm{X31}, \mathrm{X21}, \mathrm{Y31}, \mathrm{Y21}) \rightarrow \frac{-\mathrm{Y21}\,\varphi 3 + \mathrm{Y21}\,\varphi 1 + \varphi 2\,\mathrm{Y31} - \varphi 1\,\mathrm{Y31}}{\mathrm{k}\,(\mathrm{X21}\,\mathrm{Y31} - \mathrm{X31}\,\mathrm{Y21})}$$

$$a := (\varphi 1, \varphi 2, \varphi 3, X31, X21, Y31, Y21) \rightarrow \frac{-Y21\,\varphi 3 + Y21\,\varphi 1 + \varphi 2\,Y31 - \varphi 1\,Y31}{k\,(X21\,Y31 - X31\,Y21)}$$

$$> \; \mathrm{b} := (\varphi 1, \varphi 2, \varphi 3, \mathrm{X31}, \mathrm{X21}, \mathrm{Y31}, \mathrm{Y21}) \rightarrow -\frac{\mathrm{X31}\,\varphi 2 - \mathrm{X21}\,\varphi 3 + \mathrm{X21}\,\varphi 1 - \mathrm{X31}\,\varphi 1}{\mathrm{k}\,(\mathrm{X21}\,\mathrm{Y31} - \mathrm{X31}\,\mathrm{Y21})}$$

$$b := (\varphi 1, \varphi 2, \varphi 3, X31, X21, Y31, Y21) \rightarrow -\frac{X31\,\varphi 2 - X21\,\varphi 3 + X21\,\varphi 1 - X31\,\varphi 1}{k\,(X21\,Y31 - X31\,Y21)}$$

$$> \; \mathrm{sgn} := \mathrm{sign}(\mathrm{evalf}(\mathrm{eval}(\mathrm{arcsin}(\mathrm{b}(\varphi 1, \varphi 2, \varphi 3, \mathrm{X31}, \mathrm{X21}, \mathrm{Y31}, \mathrm{Y21})), \{\phi 1 = \varphi 1, \phi 2 = \varphi 2, \phi 3 = \varphi 3, \mathrm{X31} = \mathrm{x31}, \mathrm{X21} = \mathrm{x21}, \mathrm{Y31} = \mathrm{y31}, \mathrm{Y21} = \mathrm{y21}\}))) :$$

Θ can be computed by 3 different methods

$$> \; \Theta := (\varphi 1, \varphi 2, \varphi 3, \mathrm{X31}, \mathrm{X21}, \mathrm{Y31}, \mathrm{Y21}) \rightarrow \mathrm{sgn} \cdot \left(\frac{1}{2}\left(\arccos(\mathrm{a}(\varphi 1, \varphi 2, \varphi 3, \mathrm{X31}, \mathrm{X21}, \mathrm{Y31}, \mathrm{Y21})) + \mathrm{abs}(\arcsin(\mathrm{b}(\phi 1, \phi 2, \phi 3, \mathrm{X31}, \mathrm{X21}, \mathrm{Y31}, \mathrm{Y21})))\right)\right) :$$

$$> \; \Theta\mathrm{Sin} := (\phi 1, \phi 2, \phi 3, \mathrm{X31}, \mathrm{X21}, \mathrm{Y31}, \mathrm{Y21}) \rightarrow \arcsin(\mathrm{b}(\phi 1, \phi 2, \phi 3, \mathrm{X31}, \mathrm{X21}, \mathrm{Y31}, \mathrm{Y21})) :$$

$$> \; \Theta\mathrm{Cos} := (\phi 1, \phi 2, \phi 3, \mathrm{X31}, \mathrm{X21}, \mathrm{Y31}, \mathrm{Y21}) \rightarrow \mathrm{sgn} \cdot \arccos(\mathrm{a}(\varphi 1, \varphi 2, \varphi 3, \mathrm{X31}, \mathrm{X21}, \mathrm{Y31}, \mathrm{Y21})) :$$

Calcul de dΘ

dQ is the error in Θ due to the errors in the inputs. A different expression is associated to each expression of Θ.

dΘ from Θ as a sum of acos and asin

$$> \ d\Theta := (\phi1, \phi2, \phi3, X31, X21, Y31, Y21) \rightarrow \mathrm{abs}\left(\left(\frac{\partial}{\partial \phi1}\,\Theta(\phi1, \phi2, \phi3, X31, X21, Y31, Y21)\right)\right) \cdot d\phi + \mathrm{abs}\left(\left(\frac{\partial}{\partial \phi2}\,\Theta(\phi1, \phi2, \phi3, X31, X21, Y31, Y21)\right)\right) \cdot d\phi + \mathrm{abs}\left(\left(\frac{\partial}{\partial \phi3}\,\Theta(\phi1, \phi2, \phi3, X31, X21, Y31, Y21)\right)\right) \cdot d\phi + \mathrm{abs}\left(\left(\frac{\partial}{\partial X31}\,\Theta(\phi1, \phi2, \phi3, X31, X21, Y31, Y21)\right)\right) \cdot xd + \mathrm{abs}\left(\left(\frac{\partial}{\partial X21}\,\Theta(\phi1, \phi2, \phi3, X31, X21, Y31, Y21)\right)\right) \cdot xd + \mathrm{abs}\left(\frac{\partial}{\partial Y31}\,\Theta(\phi1, \phi2, \phi3, X31, X21, Y31, Y21)\right) \cdot xd + \mathrm{abs}\left(\frac{\partial}{\partial Y21}\,\Theta(\phi1, \phi2, \phi3, X31, X21, Y31, Y21)\right) \cdot xd :$$

dΘ from Θ computed as arcsin(b)

$$> \ d\Theta Sin := (\phi1, \phi2, \phi3, X31, X21, Y31, Y21) \rightarrow \mathrm{abs}\left(\left(\frac{\partial}{\partial \phi1}\,\Theta Sin(\phi1, \phi2, \phi3, X31, X21, Y31, Y21)\right)\right) \cdot d\phi + \mathrm{abs}\left(\left(\frac{\partial}{\partial \phi2}\,\Theta Sin(\phi1, \phi2, \phi3, X31, X21, Y31, Y21)\right)\right) \cdot d\phi + \mathrm{abs}\left(\left(\frac{\partial}{\partial \phi3}\,\Theta Sin(\phi1, \phi2, \phi3, X31, X21, Y31, Y21)\right)\right) \cdot d\phi + \mathrm{abs}\left(\left(\frac{\partial}{\partial X31}\,\Theta Sin(\phi1, \phi2, \phi3, X31, X21, Y31, Y21)\right)\right) \cdot xd + \mathrm{abs}\left(\left(\frac{\partial}{\partial X21}\,\Theta Sin(\phi1, \phi2, \phi3, X31, X21, Y31, Y21)\right)\right) \cdot xd + \mathrm{abs}\left(\frac{\partial}{\partial Y31}\,\Theta Sin(\phi1, \phi2, \phi3, X31, X21, Y31, Y21)\right) \cdot xd + \mathrm{abs}\left(\frac{\partial}{\partial Y21}\,\Theta Sin(\phi1, \phi2, \phi3, X31, X21, Y31, Y21)\right) \cdot xd :$$

dΘ from Θ computed as arccos(a).sgn(arcsin(b))

$$> \ d\Theta Cos := (\phi1, \phi2, \phi3, X31, X21, Y31, Y21) \rightarrow \mathrm{abs}\left(\left(\frac{\partial}{\partial \phi1}\,\Theta Cos(\phi1, \phi2, \phi3, X31, X21, Y31, Y21)\right)\right) \cdot d\phi + \mathrm{abs}\left(\left(\frac{\partial}{\partial \phi2}\,\Theta Cos(\phi1, \phi2, \phi3, X31, X21, Y31, Y21)\right)\right) \cdot d\phi + \mathrm{abs}\left(\left(\frac{\partial}{\partial \phi3}\,\Theta Cos(\phi1, \phi2, \phi3, X31, X21, Y31, Y21)\right)\right) \cdot d\phi + \mathrm{abs}\left(\left(\frac{\partial}{\partial X31}\,\Theta Cos(\phi1, \phi2, \phi3, X31, X21, Y31, Y21)\right)\right) \cdot xd + \mathrm{abs}\left(\left(\frac{\partial}{\partial X21}\,\Theta Cos(\phi1, \phi2, \phi3, X31, X21, Y31, Y21)\right)\right) \cdot xd + \mathrm{abs}\left(\frac{\partial}{\partial Y31}\,\Theta Cos(\phi1, \phi2, \phi3, X31, X21, Y31, Y21)\right) \cdot xd + \mathrm{abs}\left(\frac{\partial}{\partial Y21}\,\Theta Cos(\phi1, \phi2, \phi3, X31, X21, Y31, Y21)\right) \cdot xd :$$

Values

The values entered here correponds to the final probe layout. The distance x.. and y.. are in meters and correponds to the probe coordinates as measured on the final frame.
θ is the target angle in degree used to generate the virtual phases $\phi1, \phi2$ and $\phi3$.

Parameters

$$> \ x1 := 0.0 :$$

$$> \ y1 := 0.0 :$$

> $x2 := 0.8617$:

> $y2 := 0.7965$:

> $x3 := 0.8617$:

> $y3 := -0.7965$:

> $freq := 1.0$:

> $x21 := x2 - x1$:

> $x31 := x3 - x1$:

> $y21 := y2 - y1$:

> $y31 := y3 - y1$:

> $\theta := 1 \cdot \frac{-5 \cdot \pi}{180}$:

> $\Phi_0 := \frac{35 \cdot \pi}{180}$:

> $\varpi := 2 \cdot \pi \cdot freq$:

> $g := 9.81$:

> $k := \frac{\varpi^2}{g}$:

> $\phi 1 := k \cdot (x1 \cdot \cos(\theta) + y1 \cdot \sin(\theta)) + \Phi_0$:

> $\phi 2 := k \cdot (x2 \cdot \cos(\theta) + y2 \cdot \sin(\theta)) + \Phi_0$:

> $\phi 3 := k \cdot (x3 \cdot \cos(\theta) + y3 \cdot \sin(\theta)) + \Phi_0$:

For Control

Angle Computation:
Controloling that the expression for Θ are working

> $\mathrm{evalf}\left(\mathrm{eval}\left(\Theta(\varphi 1, \varphi 2, \varphi 3, X31, X21, Y31, Y21) \cdot \frac{180}{\pi}, \{\varphi 1 = \phi 1, \varphi 2 = \phi 2, \varphi 3 = \phi 3, X31 = x31, X21 = x21, Y31 = y31, Y21 = y21\}\right)\right)$;

$$-5.000000098$$

> $\mathrm{evalf}\left(\mathrm{eval}\left(\Theta Sin(\varphi 1, \varphi 2, \varphi 3, X31, X21, Y31, Y21) \cdot \frac{180}{\pi}, \{\varphi 1 = \phi 1, \varphi 2 = \phi 2, \varphi 3 = \phi 3, X31 = x31, X21 = x21, Y31 = y31, Y21 = y21\}\right)\right)$;

$$-5.000000000$$

uncertainty parameters

This is the estimated value of the errors in the phase measurement and in the probe position

> $d\phi := \frac{5 \cdot \pi}{180}$:

> $xd := 0.005$:

Error computed with the previous parameters:

values are in degree

```
> evalf(eval(dΘ(φ1, φ2, φ3, X31, X21, Y31, Y21)·180/π, {φ1 = ϕ1, φ2 = ϕ2, φ3 = ϕ3, X31 = x31, X21
      = x21, Y31 = y31, Y21 = y21}))
                                        18.60972592
> evalf(eval(dΘSin(φ1, φ2, φ3, X31, X21, Y31, Y21)·180/π, {φ1 = ϕ1, φ2 = ϕ2, φ3 = ϕ3, X31 = x31,
      X21 = x21, Y31 = y31, Y21 = y21}))
                                        1.956986226
> evalf(eval(dΘCos(φ1, φ2, φ3, X31, X21, Y31, Y21)·180/π, {φ1 = ϕ1, φ2 = ϕ2, φ3 = ϕ3, X31 = x31,
      X21 = x21, Y31 = y31, Y21 = y21}))
                                        37.21945181
```

For this angle, only the dΘSin expression gives a acceptable results

A bit of Programation

In this part of the code, the wave angle varies and the error contribution of each input is separated. The

```
> with(Statistics) :
> dSinA := Vector(25) :
> xAxis := Vector(25) :
> dCosA := Vector(25) :
> dSumA := Vector(25) :
> dFinal := Vector(25) :
> dFinalxd := Vector(25) :
> dFinaldφ := Vector(25) :
> for i from 1 by 1 while i < 26 do
    dϕ := 5·π/180 :
    xd := 0.005 :
    xAxis[i] := -65.1 + i·5 :
    θ := xAxis[i]·π/180 :
    ϕ1 := k·(x1·cos(θ) + y1·sin(θ)) + Φ_0 :
    ϕ2 := k·(x2·cos(θ) + y2·sin(θ)) + Φ_0 :
    ϕ3 := k·(x3·cos(θ) + y3·sin(θ)) + Φ_0 :
    dSinA[i] := evalf(eval(dΘSin(φ1, φ2, φ3, X31, X21, Y31, Y21)·180/π, {φ1 = ϕ1, φ2 = ϕ2, φ3
      = ϕ3, X31 = x31, X21 = x21, Y31 = y31, Y21 = y21})) :
    dCosA[i] := evalf(eval(dΘCos(φ1, φ2, φ3, X31, X21, Y31, Y21)·180/π, {φ1 = ϕ1, φ2 = ϕ2, φ3
```

$= \phi3, X31 = x31, X21 = x21, Y31 = y31, Y21 = y21\}\Big)\Big) :$

$dSumA[i] := evalf\Big(eval\Big(d\Theta(\varphi1, \varphi2, \varphi3, X31, X21, Y31, Y21)\cdot\frac{180}{\pi}, \{\varphi1 = \phi1, \varphi2 = \phi2, \varphi3 = \phi3, X31 = x31, X21 = x21, Y31 = y31, Y21 = y21\}\Big)\Big) :$

$dFinal[i] := min(dSinA[i], dCosA[i], dSumA[i]) :$

$d\phi := \frac{5\cdot\pi}{180} :$

$xd := 0 :$

$da := evalf\Big(eval\Big(d\Theta Sin(\varphi1, \varphi2, \varphi3, X31, X21, Y31, Y21)\cdot\frac{180}{\pi}, \{\varphi1 = \phi1, \varphi2 = \phi2, \varphi3 = \phi3, X31 = x31, X21 = x21, Y31 = y31, Y21 = y21\}\Big)\Big) :$

$db := evalf\Big(eval\Big(d\Theta Cos(\varphi1, \varphi2, \varphi3, X31, X21, Y31, Y21)\cdot\frac{180}{\pi}, \{\varphi1 = \phi1, \varphi2 = \phi2, \varphi3 = \phi3, X31 = x31, X21 = x21, Y31 = y31, Y21 = y21\}\Big)\Big) :$

$dc := evalf\Big(eval\Big(d\Theta(\varphi1, \varphi2, \varphi3, X31, X21, Y31, Y21)\cdot\frac{180}{\pi}, \{\varphi1 = \phi1, \varphi2 = \phi2, \varphi3 = \phi3, X31 = x31, X21 = x21, Y31 = y31, Y21 = y21\}\Big)\Big) :$

$dFinalxd[i] := min(da, db, dc) :$

$d\phi := 0 :$

$xd := 0.005 :$

$da := evalf\Big(eval\Big(d\Theta Sin(\varphi1, \varphi2, \varphi3, X31, X21, Y31, Y21)\cdot\frac{180}{\pi}, \{\varphi1 = \phi1, \varphi2 = \phi2, \varphi3 = \phi3, X31 = x31, X21 = x21, Y31 = y31, Y21 = y21\}\Big)\Big) :$

$db := evalf\Big(eval\Big(d\Theta Cos(\varphi1, \varphi2, \varphi3, X31, X21, Y31, Y21)\cdot\frac{180}{\pi}, \{\varphi1 = \phi1, \varphi2 = \phi2, \varphi3 = \phi3, X31 = x31, X21 = x21, Y31 = y31, Y21 = y21\}\Big)\Big) :$

$dc := evalf\Big(eval\Big(d\Theta(\varphi1, \varphi2, \varphi3, X31, X21, Y31, Y21)\cdot\frac{180}{\pi}, \{\varphi1 = \phi1, \varphi2 = \phi2, \varphi3 = \phi3, X31 = x31, X21 = x21, Y31 = y31, Y21 = y21\}\Big)\Big) :$

$dFinald\varphi[i] := min(da, db, dc) :$

end do:

```
> dcosPlot := ScatterPlot(xAxis, dCosA, color=red) :
> dsinPlot := ScatterPlot(xAxis, dSinA, color=green) :
> dsumPlot := ScatterPlot(xAxis, dSumA, ) :
> dFinalPlot := ScatterPlot(xAxis, dFinal, symbol=cross, color=black, symbolsize=15) :
> dFinalxdPlot := ScatterPlot(xAxis, dFinalxd, color=red, symbolsize=20) :
```

```
> dFinaldφPlot := ScatterPlot(xAxis, dFinaldφ, color = green, symbolsize = 20) :

> plots[display](dcosPlot, dsinPlot, dsumPlot, dFinalPlot, view = [-90 ..90, 0 ..10], gridlines
        = true);
> dFinalPlot := ScatterPlot(xAxis, dFinal, symbol = cross, color = black, symbolsize = 20) :
> plots[display](dFinalxdPlot, dFinaldφPlot, dFinalPlot, view = [-90 ..90, 0 ..3.5], gridlines = true);
> Mean(dFinal)
                                        2.233144671
> StandardDeviation(dFinal)

                                        0.2009701944
> dSinA[13]
                                        1.920190588
>
```

A.3 Statistical analysis for the reflection analysis

Results of the ANOVA test for the beach reflection analysis

```
g <- lm( R_Coeff ˜ Amplitude + Position + Line + Frequency,D)
```

The null hypothesis is:

H0: $\mu1 = \mu2 = \mu3 = ...$

The alternative hypothesis is:

H1: $\mu1 \neq \mu2 \neq \mu3 \neq ...$

for each factor.

```
Analysis of Variance Table
Response: R_Coeff
          Df   Sum Sq  Mean Sq F value    Pr(>F)
Amplitude  2 0.002279 0.001139  2.9515   0.05712 .
Position   2 0.001221 0.000611  1.5817   0.21104
Line       1 0.000233 0.000233  0.6029   0.43944
Frequency 10 0.025725 0.002573  6.6640 9.629e-08 ***
Residuals 94 0.036287 0.000386

---
Signif. codes:  0 *** 0.001 ** 0.01 * 0.05 . 0.1 ' ' 1
```

Results of the ANOVA test for the wave angle assessment

```
g <- lm(error ˜ Day + Triangle*Angle,D)
```

The null hypothesis is:

H0: $\mu1 = \mu2 = \mu3 = ...$

The alternative hypothesis is:

H1: $\mu1 \neq \mu2 \neq \mu3 \neq ...$

for each factor.

```
Analysis of Variance Table
```

```
Response: error
                Df    Sum Sq   Mean Sq  F value Pr(>F)
Day              1 0.0001606 0.0001606   0.0031 0.9559
Triangle         1    27.168    27.168 520.1794 <2e-16 ***
Angle            8    81.313    10.164 194.6113 <2e-16 ***
Triangle:Angle   8    19.240     2.405  46.0486 <2e-16 ***
Residuals      161     8.409     0.052
---
Signif. codes:  0 *** 0.001 ** 0.01 * 0.05 . 0.1 ’ ’ 1
```

Appendix B
Supporting derivation for the MMLM method

B.1 The wave surface elevation

In this section, the discrete finite directional variance spectrum $S_{f,\theta}$ is defined for M frequencies and N angles.

B.1.1 Elevation from the incident spectrum

Let's define the elevation due to the incident discrete and finite directional variance spectrum $S^I_{f,\theta}$ at a point $A(x, y)$ at any instant t:

$$\eta^I(A,t) = \sum_{p=0}^{M-1} \sum_{q=1}^{N} a^I_{f_p,\theta_q} \cdot cos(-2\pi f_p t + \overrightarrow{k_{pq}} \cdot \overrightarrow{A} + \varphi_{pq}) \tag{B.1}$$

with $\overrightarrow{k_{pq}}$ the wavenumber vector $\overrightarrow{k_{pq}} = k_p\,(\cos\theta_q\,\overrightarrow{x} + \sin\theta_q\,\overrightarrow{y})$.
Putting

$$a^I_{f_p,\theta_q} = \sqrt{2\,\Delta f\,\Delta\theta\,S^I_{f_p,\theta_q}} \qquad \text{and} \quad \omega_p = 2\pi f_p \tag{B.2}$$

we have, in complex notation:

$$\underline{\eta}^I(A,t) = \sum_{p=0}^{M-1} \sum_{q=1}^{N} c\,\sqrt{S^I_{f_p,\theta_q}}\,e^{i(\overrightarrow{k_{pq}}\cdot\overrightarrow{A} - \omega_p t + \varphi_{pq})} \tag{B.3}$$

$$\text{with: } c = \sqrt{2\,\Delta f\,\Delta\theta} \tag{B.4}$$

B.1.2 Elevation from the reflected spectrum

The reflected spectrum, $S^R_{f,\theta}$, and the reflection coefficient $r_{f,\theta}$ are defined as in **?**:

$$r_{f,\theta} = \frac{a^R_{f,\theta}}{a^I_{f,\theta}} \tag{B.5}$$

$S^R_{f,\theta}$ can be expressed as:

$$S^R_{f,\theta} = \frac{1}{c^2} \cdot (a^R_{f,\theta})^2 = \frac{r^2_{f,\theta}}{c^2} \cdot (a^I_{f,\theta})^2 = r^2_{f,\theta} \cdot S^I_{f,\theta} \tag{B.6}$$

Defining $A^R(x_r, y_r)$ the reflected point of A relative to the wave reflector, the wave elevation due to the reflected spectrum in A is:

$$\underline{\eta^R}(A,t) = \sum_{p=0}^{M-1} \sum_{q=1}^{N} r_{f_p,\theta_q} \cdot a^I_{f_p,\theta_q} \cdot e^{i(\overrightarrow{k_{pq}} \cdot \overrightarrow{A^R} - \omega_p t + \varphi_{pq})} \tag{B.7}$$

$$= \sum_{p=0}^{M-1} \sum_{q=1}^{N} r_{pq} \cdot c \cdot \sqrt{S^I_{f_p,\theta_q}} \cdot e^{i(\overrightarrow{k_{pq}} \cdot \overrightarrow{A_r} - \omega_p t + \varphi_{pq})} \tag{B.8}$$

with: $r_{pq} = r_{f_p,\theta_q}$

B.1.3 Total wave elevation

Finally, the total wave elevation at a point A can be written as the sum of η^I and η^R:

$$\underline{\eta}(A,t) = \sum_{p=0}^{M-1} \sum_{q=1}^{N} c \cdot \sqrt{S^I_{f_p,\theta_q}} \cdot e^{i(-\omega_p t + \varphi_{pq})} \cdot \left(e^{-i(\overrightarrow{k_{pq}} \cdot \overrightarrow{A}} + r_{pq} e^{-i(\overrightarrow{k_{pq}} \cdot \overrightarrow{A^R})} \right) \tag{B.9}$$

$$\underline{\eta}(A,t) = \sum_{p=0}^{M-1} e^{-i\omega_p t} \left[\sum_{q=1}^{N} c \cdot \sqrt{S^I_{f_p,\theta_q}} \cdot e^{i\varphi_{pq}} \cdot \left(e^{-i(\overrightarrow{k_{pq}} \cdot \overrightarrow{A}} + r_{pq} e^{-i(\overrightarrow{k_{pq}} \cdot \overrightarrow{A^R})} \right) \right] \tag{B.10}$$

A complex amplitude $\underline{G}(A, f)$ can be defined as

$$\underline{G}(A, f_p) = \sum_{q=1}^{N} c \cdot \sqrt{S^I_{f_p,\theta_q}} \cdot e^{i\varphi_{pq}} \cdot \left(e^{-i\overrightarrow{k_{pq}} \cdot \overrightarrow{A}} + r_{pq} e^{-i(\overrightarrow{k_{pq}} \cdot \overrightarrow{A^R})} \right) \tag{B.11}$$

giving a simplified expression for $\underline{\eta}$:

$$\underline{\eta}(A,t) = \sum_{p=0}^{M-1} e^{-i\omega_p t}\underline{G}(A, f_p) \tag{B.12}$$

B.2 Fourier Transform expression of the quantities

at a probe A, the recorded signal is called $\zeta_A(t)$. Discarding measurement noise, $\zeta_A(t)$ is a periodic signal, of period T as the waves are deterministic.
The Fourier Transform of it gives:

$$\zeta_A(t) = a_0 + 2\sum_{p=1}^{\infty} \left(a_p \cos\frac{2\pi pt}{T} + b_p \sin\frac{2\pi pt}{T} \right) \tag{B.13}$$

Using complex notation, you get:

$$\underline{X}_{p,A} = a_p - ib_p \tag{B.14}$$

$$\underline{X}_{p,A} = \frac{1}{T}\int_0^T \zeta_A(t)\cdot e^{-i2\pi pt/T}dt \tag{B.15}$$

Now, $\zeta_A(t)$ is considered as a discrete series $\zeta_{A,u}, u = 0, 1, .., (M-1)$ with $t = u\Delta$ and $\Delta = T/M$.
We have

$$\underline{X}_{p,A} = \frac{1}{T}\sum_{u=0}^{M-1} \zeta_{A,u}\cdot e^{-i(2\pi p/T)(u\Delta)}\Delta \tag{B.16}$$

$$= \frac{1}{M}\sum_{u=0}^{M-1} \zeta_{A,u}\cdot e^{-i(2\pi pu/M)} \tag{B.17}$$

$$\text{and } \zeta_{A,u} = \sum_{p=0}^{M-1} \underline{X}_{p,A}\cdot e^{-i(2\pi pu/M)} \tag{B.18}$$

note: the fft.m function in matlab return a set of coefficient $\underline{X'}_{p,A} \; = \; M \cdot \underline{X}_{p,A}$
using the same discrete notation to describe $\underline{\eta}$, we obtain:

$$\underline{\eta_{A,u}} = \sum_{p=0}^{M-1} e^{-i\omega_p u\Delta}\underline{G}(A, f_p) \tag{B.19}$$

$$\underline{\eta_{A,u}} = \sum_{p=0}^{M-1} \underline{G}(A, f_p) \cdot e^{-i(2\pi pu/M)} \tag{B.20}$$

$$\omega_p u\Delta = 2\pi f_p u\Delta = 2\pi p\,\delta f\; u\Delta = 2\pi p\frac{1}{T}u\Delta = \frac{2\pi pu}{M} \tag{B.21}$$

B.3 Spectral Estimate and Signal Spectrum

B.3.1 Reminders over the real value variance and its complex notation

Let's define:

$$x(t) = \sum_{p=0}^{M-1} a_p \cos(\omega_p t + \varphi_p) \tag{B.22}$$

$$\text{and} \quad \underline{x}(t) = \sum_{p=0}^{M-1} a_p e^{i(\omega_p t + \varphi_p)} \text{ it's complex notation.} \tag{B.23}$$

Now, computing the variance over time(t) of $x(t) = \overline{x(t)^2}$:

$$x(t)^2 = \sum_{p=0}^{M-1}\sum_{q=0}^{M-1} a_p a_q \cos(\omega_p t + \varphi_p)\cos(\omega_q t + \varphi_q) \tag{B.24}$$

$$= \sum_{p=0}^{M-1}\sum_{q=0}^{M-1} \frac{1}{2}a_p a_q \left(\cos(\omega_p t + \varphi_p - \omega_q t + \varphi_q) + \cos(\omega_p t + \varphi_p + \omega_q t + \varphi_q)\right) \tag{B.25}$$

$$= \sum_{p=0}^{M-1}\sum_{q=0}^{M-1} \frac{1}{2}a_p a_q \left(\cos\left[(\omega_p - \omega_q)t + \varphi_p - \varphi_q\right] + \cos\left[(\omega_p + \omega_q)t + \varphi_p + \varphi_q\right]\right) \tag{B.26}$$

over time, all the components for which $\omega_p \neq \omega_q$ are equal to 0 as they are purely oscillatory terms, so

$$\overline{x(t)^2} = \sum_{p=0}^{M-1} \frac{1}{2} a_p^2 \left(1 + \cos(2\omega_p t + 2\varphi_p)\right) \tag{B.27}$$

$$\overline{x(t)^2} = \frac{1}{2} \sum_{p=0}^{M-1} a_p^2 \tag{B.28}$$

now, comparing with the average over time of the product of $\underline{x(t)}$ and it's complex conjugate:

$$\underline{x}(t) \cdot \underline{x}^*(t) = \sum_{p=0}^{M-1} \sum_{q=0}^{M-1} a_p a_q e^{i(\omega_p t + \varphi_p)} e^{-i(\omega_q t + \varphi_q)} \tag{B.29}$$

$$= \sum_{p=0}^{M-1} \sum_{q=0}^{M-1} a_p a_q e^{i[(\omega_p - \omega_q)t + (\varphi_p - \varphi_q)]} \tag{B.30}$$

$$\Rightarrow \overline{\underline{x}(t) \cdot \underline{x}^*(t)} = \sum_{p=0}^{M-1} a_p^2 \tag{B.31}$$

so finally we're getting the relation:

$$\boxed{\overline{x(t)^2} = \frac{1}{2} \cdot \overline{\underline{x}(t) \cdot \underline{x}^*(t)}} \tag{B.32}$$

Similarly, considering a function:

$$y(t) = \sum_{p=1}^{M-1} a_p \cos\left(\frac{2\pi up}{M}\right) + b_p \sin\left(\frac{2\pi up}{M}\right) \tag{B.33}$$

it can also be written as:

$$y(t) = \sum_{p=1}^{M-1} \underline{X}_p e^{i\left(\frac{2\pi up}{M}\right)} \qquad \text{with } X_p = a_p - ib_p \tag{B.34}$$

and looking at it's discrete series y_u', it can be written that

$$\boxed{\overline{y_u^2} = 2 \sum_{p=1}^{M-1} \underline{X}_p \cdot \underline{X}_p^*} \tag{B.35}$$

Eq. B.32 and Eq. B.35 can be generalised to the product of the function at different points.

B.3.2 'cross-variance' of η_u in 2 points

we have:

$$\text{from Eq. B.32} \quad \overline{\eta_{A,u} \cdot \eta_{B,u}} = \frac{1}{2} \cdot \overline{\underline{\eta_{A,u}} \cdot \underline{\eta_{B,u}}^*} \tag{B.36}$$

$$\text{and Eq. B.35} \quad \underline{\eta_{A,u}} \cdot \underline{\eta_{B,u}}^* = \sum_{p=0}^{M-1} \sum_{s=0}^{M-1} \underline{G}(A, f_p) \cdot \underline{G}^*(B, f_s) \cdot e^{-i\frac{2\pi u}{M}(p-s)} \tag{B.37}$$

$$\text{so} \quad \overline{\underline{\eta_{A,u}} \cdot \underline{\eta_{B,u}}^*} = \sum_{p=0}^{M-1} \underline{G}(A, f_p) \cdot \underline{G}^*(B, f_p) \tag{B.38}$$

Expanding $\underline{G}(A, f_p)$ and $\underline{G}^*(B, f_p)$ leads to a rather long expression:

$$\begin{aligned} \overline{\underline{\eta_{A,u}} \cdot \underline{\eta_{B,u}}^*} = \sum_{p=0}^{M-1} \Bigg[& \sum_{q=1}^{N} c \cdot \sqrt{S^I_{f_p,\theta_q}} \cdot e^{i\varphi_{pq}} \cdot \left(e^{-i\overrightarrow{k_{pq}} \cdot \overrightarrow{A}} + r_{pq} e^{-i\overrightarrow{k_{pq}} \cdot \overrightarrow{A^R}} \right) \cdot \\ & \sum_{s=1}^{N} c \cdot \sqrt{S^I_{f_p,\theta_s}} \cdot e^{-i\varphi_{ps}} \cdot \left(e^{i\overrightarrow{k_{ps}} \cdot \overrightarrow{B}} + r_{ps} e^{i\overrightarrow{k_{ps}} \cdot \overrightarrow{B^R}} \right) \Bigg] \end{aligned} \tag{B.39}$$

$$\begin{aligned} \overline{\underline{\eta_{A,u}} \cdot \underline{\eta_{B,u}}^*} = \sum_{p=0}^{M-1} \sum_{q=1}^{N} \sum_{s=1}^{N} & c^2 \cdot (S^I_{f_p,\theta_q})^{1/2} \cdot (S^I_{f_p,\theta_s})^{1/2} \cdot e^{i(\varphi_{pq}-\varphi_{ps})} \cdot \\ & \left(e^{-i\overrightarrow{k_{pq}} \cdot \overrightarrow{A}} + r_{pq} e^{-i\overrightarrow{k_{pq}} \cdot \overrightarrow{A^R}} \right) \left(e^{i\overrightarrow{k_{ps}} \cdot \overrightarrow{B}} + r_{ps} e^{i\overrightarrow{k_{ps}} \cdot \overrightarrow{B^R}} \right) \end{aligned} \tag{B.40}$$

Considering averages over the previous equation, the random phase assumption implies that terms including $e^{i(\varphi_{pq}-\varphi_{ps})}$ are null ($= 0$). In that case, Eq. B.40 can be reduce to:

$$\overline{\underline{\eta_{A,u}} \cdot \underline{\eta_{B,u}}^*} = \sum_{p=0}^{M-1} \sum_{q=1}^{N} c^2 \cdot S^I_{f_p,\theta_q} \cdot \left(e^{-i\overrightarrow{k_{pq}} \cdot \overrightarrow{A}} + r_{pq} e^{-i\overrightarrow{k_{pq}} \cdot \overrightarrow{A^R}} \right) \left(e^{i\overrightarrow{k_{pq}} \cdot \overrightarrow{B}} + r_{pq} e^{i\overrightarrow{k_{pq}} \cdot \overrightarrow{B^R}} \right) \tag{B.41}$$

and finally, replacing c as in Eq. B.4 the 'cross-variance' of η_u became:

$$\overline{\eta_{A,u} \cdot \eta_{B,u}} = \sum_{p=0}^{M-1} \sum_{q=1}^{N} \Delta f \, \Delta\theta \cdot S^I_{f_p,\theta_q} \cdot \left(e^{-i\overrightarrow{k_{pq}} \cdot \overrightarrow{A}} + r_{pq} e^{-i\overrightarrow{k_{pq}} \cdot \overrightarrow{A^R}} \right) \left(e^{i\overrightarrow{k_{pq}} \cdot \overrightarrow{B}} + r_{pq} e^{i\overrightarrow{k_{pq}} \cdot \overrightarrow{B^R}} \right) \tag{B.42}$$

Similarly, using Eq. B.35, the measured 'cross-variance' elevation can be computed as:

$$\overline{\zeta_{A,u} \cdot \zeta_{B,u}} = \sum_{p=0}^{M-1} 2 \cdot \underline{X}_{p,A} \cdot \underline{X}^*_{p,B} \tag{B.43}$$

B.4 Link between cross-spectra and the directional variance spectrum

Finally, the measured and theoretical *cross-variance* of the surface elevation can be equalised:

$$\overline{\zeta_{A,u} \cdot \zeta_{B,u}} = \overline{\eta_{A,u} \cdot \eta_{B,u}}. \tag{B.44}$$

Term by term identification leads to:

$$\begin{aligned} 2 \cdot \underline{X}_{p,A} \cdot \underline{X}^*_{p,B} = \sum_{q=1}^{N} & \Delta f \, \Delta\theta \cdot S^I_{f_p,\theta_q} \cdot \\ & \left(e^{-i\overrightarrow{k_{pq}} \cdot \overrightarrow{A}} + r_{pq} e^{-i\overrightarrow{k_{pq}} \cdot \overrightarrow{A^R}} \right) \left(e^{i\overrightarrow{k_{pq}} \cdot \overrightarrow{B}} + r_{psq} e^{i\overrightarrow{k_{pq}} \cdot \overrightarrow{B^R}} \right) \end{aligned} \tag{B.45}$$

In the discrete case, the cross-spectra values between each probes is defined as:

$$\underline{\Phi}_{AB,f_p} = \frac{\underline{X}_{p,A} \cdot \underline{X}^*_{p,B}}{\Delta F} \tag{B.46}$$

Inserting Eq. B.46 into Eq. B.45, we obtain the formal formulation of the relation between the measured cross-spectra and the incident *frequency-direction* energy spectrum in Eq. B.47

$$\boxed{\underline{\Phi}_{AB,f_p} = \sum_{q=1}^{N} \frac{\Delta\theta}{2} \cdot S^I_{f_p,\theta_q} \cdot \left(e^{-i\overrightarrow{k_{pq}} \cdot \overrightarrow{A}} + r_{pq} e^{-i\overrightarrow{k_{pq}} \cdot \overrightarrow{A^R}} \right) \left(e^{i\overrightarrow{k_{pq}} \cdot \overrightarrow{B}} + r_{pq} e^{i\overrightarrow{k_{pq}} \cdot \overrightarrow{B^R}} \right)} \tag{B.47}$$

Appendix C
Data Analysis with R

Data analysis done during the course of this work were mostly performed using the statistical language *R* by R Development Core Team (2009). The method employed are principally described in Crawley (2007). In most cases, models were fitted to the data using varying *R* function depending on the nature of the data and the observed or anticipated structure of the variance associated to those data. In such cases, *R* provides a set of tools to interpret the validity of the model applied and a summary of the model. Without entering in the detail of each type of model used, the following sections describe the main elements extracted from *R*.

All the model presented are either *generalised linear models* , *anova* or *ancova*. The purpose of the models are to explain the observed data with a set of explanatory variables. The type of analysis used is dependant of the nature of the explanatory variables. *Generalised linear models* are used when only continuous explanatory variable are present, *anova* when all the variables are factors with a finite number of levels, and *ancova* are used with a mix of continuous and categorical explanatory variables.

The first objective of these analysis is to identify which of the explanatory variables are significant. Then, when a adequate model for the data with only significant variables and interactions is built (this defines the *minimal adequate model*), the coefficients attributed to each variables can be retrieved and interpreted.

C.1 Pre-analysis plots

Before fitting one of the model to the observed data, several plots can be used to visualise the data. For categorical explanatory variable (factors) with two or more levels, boxplots as in Fig. 7.2 on page 146 are commonly used in this work.

The horizontal bold line of a boxplot (named box-and-whisker plot) shows the median of the observations. The bottom and top of the box are located at the first and third quartiles. There is effectively 50% of the data contained *inside* the box. The dashed lines outside of the box, the whiskers, extend to the min and max of the data or to 1.5 times the interquartile range (roughly 2 standard deviation) if the later smaller. In the later case, observation falling outside the whiskers are called outliers. Boxplot in effect give good visual information about the data, its location and skewness. Outliers can be a sign of errors and should normally be investigated. Comparing boxplots from different levels of a factor gives information about the significance of the difference of mean between the levels. Principally, if the median value of a level falls outside the box of an other level, it is a good indication that the difference of mean is significant. An other useful plot is the so called *interaction.plot* (see Fig. 3.14 on page 39). They are used to visualise interaction between two categorical variables or one categorical and one continuous variable over the observed data. Interaction plots are 2D plots. The x-axis represent one of the variable, normally the one with the most numerous levels. The y-axis represents the observed quantity. A line is drawn for each level of the second variable. The values used to draw the lines are the mean of the observations for the level represented by the line and the value of the parameter in the x-axis. If the lines representing the different levels of the second parameter are pseudo-parallel, it is the sign that interaction between the two parameters are low.

C.2 The model formulation

```
model <- glm(Obs ˜ C1 + F1 + C2 + I(C1ˆ2) + C1:F1,family = normal)
```

The type of model is defined by the function used, here a *generalised linear model* (glm). The formula only includes the variable designation. In this case, the variable *Obs* is being described by the continuous variable *C1* and *C2*, the factor *F1*, the square of *C1* considered as a separate continuous variable *I(C1ˆ2)* and the interaction *C1:F1* between those two variables. Note the the *Intercept* is not mentioned in the formula. An optional *family* information is passed to the formula, informing *R* over the expected structure of the variance. Depending on it, transformation of the answer might be done, and different strategy such as the least square method are used to fit the model to the data.

With the provided variables, the algorithms implemented in *R* will fit a different linear relation between *Obs* and the continuous variable for each level of the discrete variables. In this case, assuming f_1 and f_2 the two possible level for *F1*, *R* will estimate 6 coefficients $(a_1, .., a_6)$ from the data to formulate the model as shown in Eq. C.2

$$Obs_{f1} = a_1 + a_2 \cdot C1 + a_3 \cdot C2 + a_4 \cdot C1^2 \quad \text{for } F1 = f_1 \tag{C.1}$$

$$Obs_{f2} = a_5 + a_6 \cdot C1 + a_3 \cdot C2 + a_4 \cdot C1^2 \quad \text{for } F1 = f_2 \tag{C.2}$$

A different intercept is evaluated for each value of the factor, as well as a different slope for *C1* as the interaction between *C1* and *F1* is included in the model. The slope coefficients for *C2* and *I(C1ˆ2)* are identical as no interaction between those variable and *F1* are added to the model.

An aletrnative formulation is presented below:

```
model <- glm(Obs ˜ (C1 + F1)ˆ2 + C2 + I(C1ˆ2),family = normal)
```

(C1 + F1)ˆ2 corresponds to *C1 + F1 + C1:F1*. Higher order interactions between variable can be formulated in this way.

It is also possible to introduce interaction between continuous variables. In this case, an extra coefficient is evaluated and the product of those two variables and the new coefficient are added to the model.

C.3 The model summary

Independent of the type of analysis, *R* provides a model summary based on the same template. This section describes the structure of this template and the meaning of its elements. A typical model summary is shown below:

```
 Call:
glm(formula = Obs ˜ C1 + F1 + C2 + I(C1ˆ2) + C1:F1,family = normal)

Residuals:
    Min      1Q  Median      3Q     Max
-2.0007 -0.4463 -0.0094  0.4201  3.8421

Coefficients:
                          Estimate Std. Error t value Pr(>|t|)
(Intercept)                6.16306    0.19355   31.84  < 2e-16 ***
C1                         0.27264    0.03443    7.92  2.5e-14 ***
F1f2                       0.29737    0.06625    4.49    0.065 .
C2                         0.16990    0.15682    1.08    0.279
I(C1ˆ2)                    0.02261    0.00131   17.22  < 2e-16 ***
C1:F1f2                   -0.02786    0.01083   -2.57    0.010 *
---
Signif. codes:  0    ***    0.001    **    0.01    *    0.05    .    0.1
    ⇝     1

Residual standard error: 0.663 on 394 degrees of freedom
```

```
Multiple R-squared: 0.985,     Adjusted R-squared: 0.984
F-statistic: 5.05e+03 on 5 and 394 DF,  p-value: <2e-16
```

The summary is divided into four parts: the *Call* which is a reminder of the model used, the *Residuals* quantile repartition, the *Coefficients* which gives the significance of each variable and the coefficient associated to it and a set of number describing the goodness of fit of the model.
The most important aspect of such a summary is the significance of the variables. For each variable, *R* is evaluating the probability that the data could have been observed if this variable was not significant. The probability is given in the $Pr(> |t|)$ column. A low probability signifies that this variable effect should be accepted as significant. In most cases and during all this work, a value of 0.05 is accepted as a threshold of significance (it corresponds to a 95% confidence). In the summary above, the probability attributed to *C2* equals 0.279. The parameters should consequently be discarded and the model re-evaluated without it.
The 6 lines of the coefficients do not corresponds exactly to the $(a_1, .., a_6)$ of Eq. C.2. Instead, *R* provides $(a_1, .., a_4)$ and the differences $a_5 - a_1$ and $a_6 - a_2$. Hence, the mathematical model associated to this summary is:

$$Obs_{f1} = 6.16 + 0.27 \cdot C1 + 0.17 \cdot C2 + 0.02 \cdot C1^2 \quad \text{for } F1 = f_1 \tag{C.3}$$

$$Obs_{f2} = (6.16 + 0.30) + (0.27 - 0.03) \cdot C1 + 0.17 \cdot C2 + 0.02 \cdot C1^2 \quad \text{for } F1 = f_2 \tag{C.4}$$

C.4 The diagnostic plots

It is nearly always possible to fit a model to the observed data. However, It is necessary to verify if it is adequate for those data. It is done by investigating the repartition and the structure of the resulting residuals. *R* provides a set of standard plots to help assessing the validity of the model. Fig. C.1 shows an example of those plots. A description of the information that can be retrieved from each plot is given below, and more details about their interpretation is available Chapter 9 of Crawley (2007).

Residual Vs fitted and Scale-Location plots Those two plots inform the user over the repartition of the residuals as a function of the fitted values of the model. The respect the common assumption of the normality of errors with constant variance, those two plots should exhibit a scatter of points without any recognizable pattern. A bend in the *Residual Vs fitted* plot can be

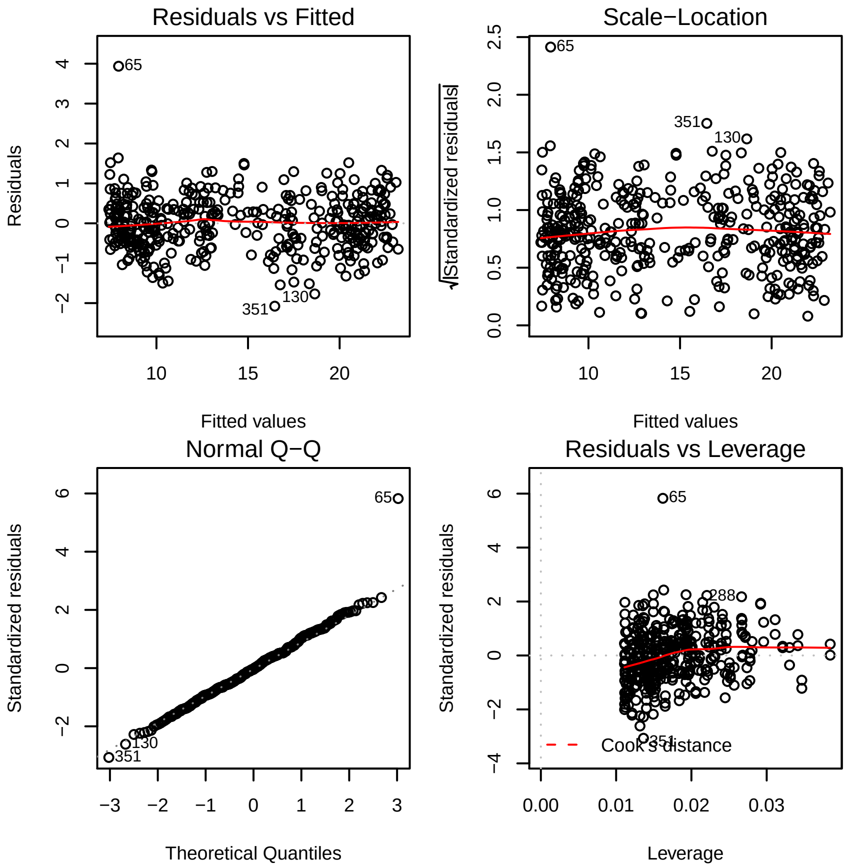

Figure C.1: *check plots provided by R to evaluate the validity of a model.*

the sign of curvature in the data that has not been taken into account in the fitted model, and increasing values on the *Scale-Location* plot is a sign of non-constance variance with the mean.

Normal Q-Q This plot gives a information about the structure of the residuals. Normal residuals should result in a plot where the point a aligned along the identity lines. When the points depart too much from the line, it is a sign of non-normality and a new model should be considered, either with a transformation of the response variable (log(), exp()) or by using a *generalised linear models* with a different error structure specified.

std residuals Vs leverage The is a plot showing the relative influence of each point over the coefficient of the model (the leverage). No points should be associated to a large leverage a large residual. In such case, the point should be removed from the dataset and the model refitted. In the case presented, the point 65 show a very large residual but it does not have a strong influence on the model. There is no need to remove it form the dataset.

C.5 The R step function and model simplification

The function *step* is used in the *R* language to simplify a statistical model. It is based on Akaike's Information Criterion (AIC). AIC is a measure of the *fit* of the model which penalises superfluous parameters in the model. The *step* function uses the AIC to test each parameter in the model, starting with the higher order interaction. The function compares the AIC of models with and without individual explanatory variables or interactions. If the AIC of the model without the parameter is lower, the simpler model is considered a better model for the data. The *step* function repeats this comparison until it cannot simplify the model any further.

As such, the *step* function is not based on the statistical significance of the parameters. However, Venables & Ripley (2002) reckon that *step* could be considered as providing a rather liberal test of significance. In this work, *step* has been used as a first method to simplify the models. It was followed by deletion of any remaining parameters that were not significant at the 5% level.

Appendix D
Additional material for the wave measurement estimation

D.1 Array design

D.1.1 Performance criteria

The selection of criteria to estimate the performances of the array is not straightforward. As mentioned in Section 4.5.2 on page 72, it is desirable that selected criteria offer a good sensitivity to the expected overspread of estimated spectra by the MLM, and a low sensitivity to noise in the low energy area of the spectrum.

$\epsilon_{n,\Theta}$ presented in Eq. 4.30 on page 74 is an obvious choice as it satisfies the two aspect mentioned above, but it was thought that a more generic criteria taking into account the full spectra would be a welcome addition. Three candidate criteria were studied to decide which one was the most relevant. They are defined in Eq. D.1 to Eq. D.2:

$$\epsilon_T = 100 \cdot \frac{\sum_{pq} |\hat{S}_{f_p,\theta_q} - S_{f_p,\theta_q}|}{\sum_{pq} S_{f_p,\theta_q}} \tag{D.1}$$

$$\epsilon_{w,T1} = 100 \cdot \frac{\sum_{pq} |\hat{S}_{f_p,\theta_q} - S_{f_p,\theta_q}| \cdot \hat{S}_{f_p,\theta_q}}{\sum_{pq} S^2_{f_p,\theta_q}} \tag{D.2}$$

$$\epsilon_{w,T2} = 100 \cdot \frac{\sum_{pq} |\hat{S}_{f_p,\theta_q} - S_{f_p,\theta_q}| \cdot S_{f_p,\theta_q}}{\sum_{pq} S^2_{f_p,\theta_q}} \tag{D.3}$$

ϵ_T is directly the mean of the difference between target and estimated spectra. It is expected to be quite sensitive to noise in the spectra. $\epsilon_{w,T1}$ and $\epsilon_{w,T2}$ are similar to ϵ_T but weighted either by $\hat{S}_{f_p,\theta_q}$ or S_{f_p,θ_q}. Weighting the difference by S_{f_p,θ_q} automatically discard discards part of the spectra where $S_{f_p,\theta_q} = 0$. It should however be robust to noise. $\epsilon_{w,T1}$, by using $\hat{S}_{f_p,\theta_q}$ should not discard any part of the spectra but should still be more robust to noise than ϵ_T.

Those three parameters are compared and studied on a particular case. A target spectra is defined with the following parameters: $Type = JONSWAP$, $T_z = 0.6730\,\mathrm{s}$, $H_{m0} = 0.0586\,\mathrm{m}$, $s = 9.8022$. Realistic noise and overspread are then added to this target spectra.

First, overspread is modelled by re-generating the spectra with 6 lower values of *s*. The noise is then added in two steps. A *noisy matrix* is generated as described in the code below.

```
noiseMat = smoothSpectrum(rand(m,n)  * (j*noiseLevel/jmax) * hmo1,
    ↝5, 'linear' ,3);
noiseMat = ones(m,n) + noiseMat - mean(mean(noiseMat));
```

noiseLevel is the maximum level of noise added, in this case it is set to 20. *jmax* is the number of steps used to reach *noiseLevel* starting from 0. This *noisy matrix* is then added to the overspread spectra (*spectraSpread* in the code below) by multiplying each spectral estimate by the corresponding value:

```
spectra = spectraSpread .* noiseMat
```

This noise affects only the shape of the wave system as every points out of it is still equal to 0. Realistic noise is then added to the rest of the spectra. It is done by analysing the simulated time series generated from the target spectra with the MLM, recording the noise outside of the wave system (into *noise1*), and adding this noise into the *noisy spectra*. Before adding it, the realistic noise is scaled according to the level of noise. Finally, the estimated spectra is scaled down to ensure that the energy into each generated spectra is constant and equal to the energy in the target spectra.

```
noise2 = noise1 * 1.7*j/jmax;
spectra = spectra + noise2;
spectra = spectra * energy / sum(sum(spectra));
```

$\hat{S}_{f_p,\theta_q}$ simulated with this method are realistics. The level of noise set at 20 and the 1.7 coefficient used to scale *noise1* allows $\hat{S}_{f_p,\theta_q}$ to reach slightly higher level of noise than what could be expected. Those values were set manually by visual examination of $\hat{S}_{f_p,\theta_q}$. The level of overspread for the lower value of s is also larger than the overspread expected from the MLM, so ranges utilised are suitable to explore the evolution of the three criteria.

Fig. D.1 shows the sensitivity of $\epsilon_{w,T1}$, $\epsilon_{w,T2}$ and ϵ_T to noise in the spectra and overspread. Each line corresponds to a different level of overspread. It is clear from this figure that $\epsilon_{w,T1}$ is not a suitable criteria: when the noise increases to realistic level ($\sim$ 12 to 16), there is very little distinction between the different level of spread. As expected, ϵ_T has a good sensitivity to overspread (the best of the 3 criteria for noise level =0) but it is sensitive to noise. $\epsilon_{w,T2}$ has still a good sensitivity to the overspread, and is not as sensitive to noise as ϵ_T. This should consequently be the criterion of choice. It will be named $\epsilon_{w,T}$ in any other section of this work.

D.1.2 $\epsilon_{n,\Theta}$ observations

A model is fitted to the observation of $\epsilon_{n,\Theta}$ using $\hat{\Theta}_S$ and m_L as a bi-level factor (*small* for $m_L < 0.4\,\mathrm{m}$, *large* for $m_L < 0.4\,\mathrm{m}$). As it can be seen in Fig. 4.16 on page 76 the variance of the observation is not constant with respect to $\hat{\Theta}_S$ so a direct regression is not valid. A log transformation of the results provides a accpetable solution to this problem, as presented in Fig. D.2: The model is consequently fiited to the log of $\epsilon_{n,\Theta}$. The summary is presented below:

```
Call:
lm(formula = log(firstSpreadDiff) ~ ThetaS + I(ThetaS^2) + mLFactor +
    ThetaS:mLFactor + I(ThetaS^2):mLFactor)

Residuals:
     Min       1Q   Median       3Q      Max
-3.36978 -0.21755 -0.02201  0.22716  1.91962

Coefficients:
                                 Estimate Std. Error t value Pr(>|t|)
(Intercept)                     1.6468714  0.1226488  13.428  < 2e-16 ***
ThetaS                         -0.3158122  0.0216674 -14.575  < 2e-16 ***
I(ThetaS^2)                     0.0063403  0.0008122   7.807 2.03e-14 ***
mLFactorlargeArray             -0.4969387  0.1736687  -2.861  0.00434 **
ThetaS:mLFactorlargeArray      -0.0706450  0.0304548  -2.320  0.02063 *
I(ThetaS^2):mLFactorlargeArray  0.0032951  0.0011447   2.879  0.00411 **
---
Signif. codes:  0    ***    0.001    **    0.01    *    0.05    .    0.1
    ⇝     1

Residual standard error: 0.4075 on 733 degrees of freedom
Multiple R-squared: 0.8415,     Adjusted R-squared: 0.8404
F-statistic: 778.2 on 5 and 733 DF,  p-value: < 2.2e-16
```

All the terms are marked as significant. The fit of the model is assessed by the usual plots provided in Fig. D.3. None of the plots show a significant problem. Point 693 is clearly departing from the model, but it is not marked as very influential on the coefficent of the model. There is no indication that the model should not be accepted.

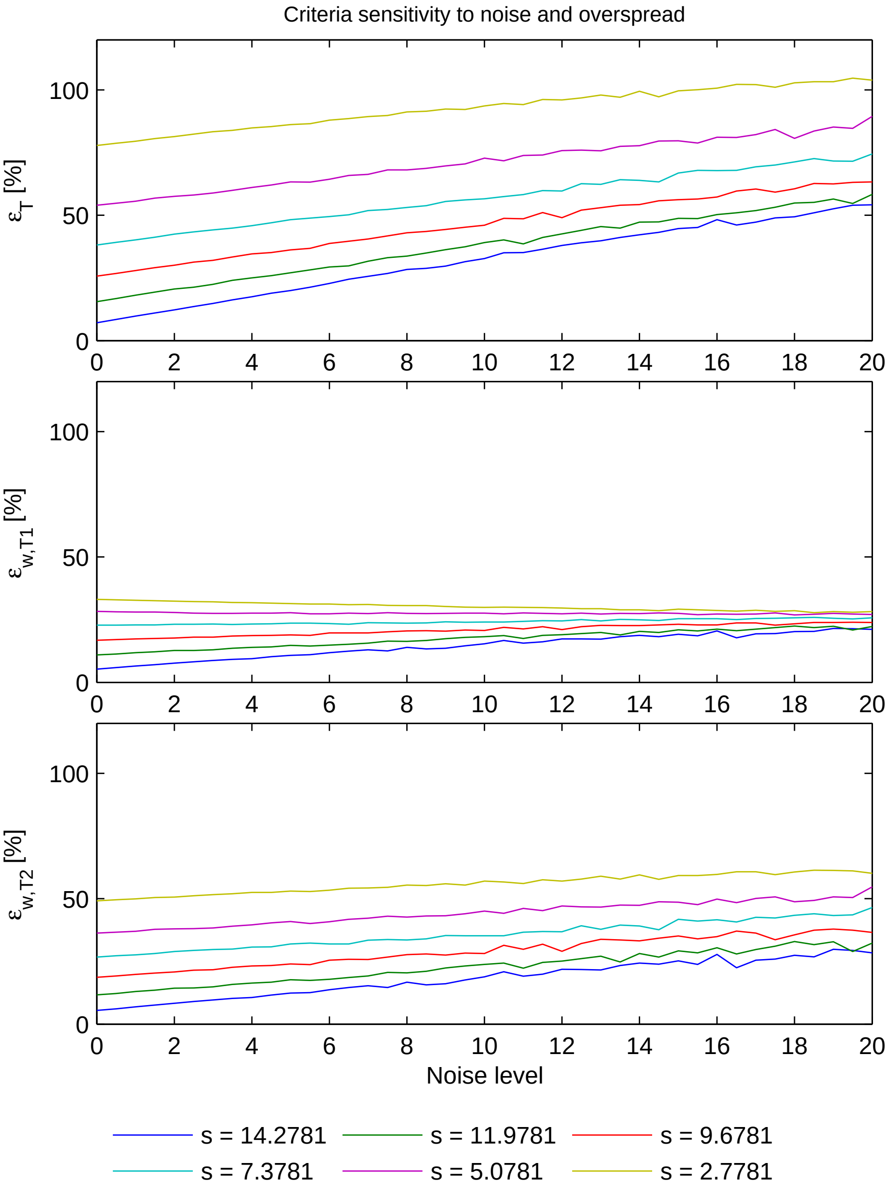

Figure D.1: *Compared sensitivity of* $\epsilon_{w,T1}$, $\epsilon_{w,T2}$ *and* ϵ_T *to noise in the spectra and overspread.*

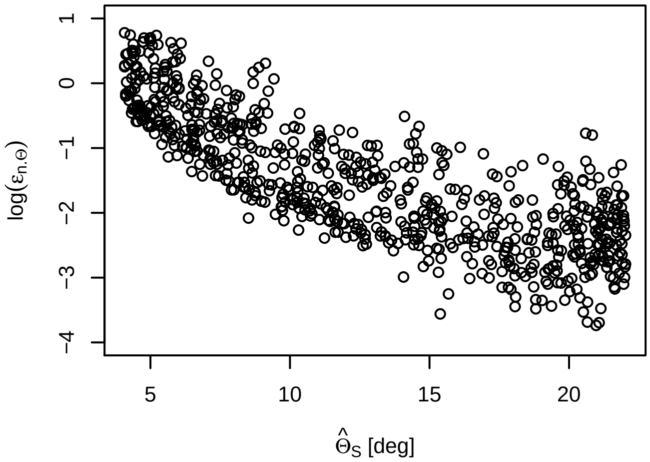

Figure D.2: *Log transformation of $\epsilon_{n,\Theta}$ with respect to $\hat{\Theta}_S$.*

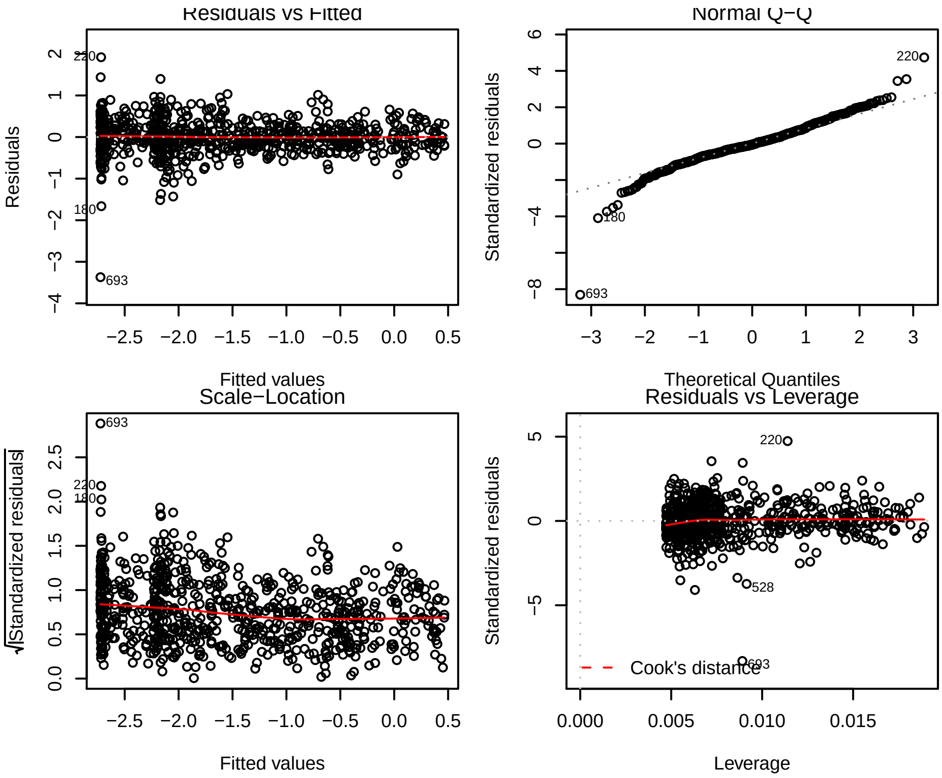

Figure D.3: *Test plot for the model fitted to the log of $\epsilon_{n,\Theta}$ obsevations.*

D.2 Results with virtual waves

D.2.1 Models summary for the uni-modal case

Summary of the model fitted to the observed $\hat{\Theta}_S$ as a function of Θ_S, including the square term Θ_S^2 to take into account the curvature in the data.

```
 Call:
lm(formula = spreadFactor1 ~ spreadFactor1Theo + method + type1 +
    I(spreadFactor1Theo^2) + spreadFactor1Theo:type1)

Residuals:
    Min      1Q  Median      3Q     Max
-2.0007 -0.4463 -0.0094  0.4201  3.8421

Coefficients:
                          Estimate Std. Error t value Pr(>|t|)
(Intercept)                6.16306    0.19355   31.84  < 2e-16 ***
spreadFactor1Theo          0.27264    0.03443    7.92  2.5e-14 ***
methodMMLM                 0.29737    0.06625    4.49  9.4e-06 ***
type1PM                    0.16990    0.15682    1.08    0.279
I(spreadFactor1Theo^2)     0.02261    0.00131   17.22  < 2e-16 ***
spreadFactor1Theo:type1PM -0.02786    0.01083   -2.57    0.010 *
---
Signif. codes:  0    ***    0.001    **    0.01    *    0.05    .    0.1
    ⇝     1

Residual standard error: 0.663 on 394 degrees of freedom
Multiple R-squared: 0.985,      Adjusted R-squared: 0.984
F-statistic: 5.05e+03 on 5 and 394 DF,  p-value: <2e-16
```

Summary of the linear piecewise model used to analyse the observed $\hat{\Theta}_S$ from virtual data as explained in Section 4.6.1.1 on page 80.

```
Call:
lm(formula = spreadFactor1 ~ (spreadFactor1Theo < breakPointPM1) *
    spreadFactor1Theo + (spreadFactor1Theo >= breakPointPM1) *
    spreadFactor1Theo + method + type1 + spreadFactor1Theo:type1)

Residuals:
    Min      1Q  Median      3Q     Max
-2.0765 -0.4449 -0.0240  0.3943  3.9367
```

```
Coefficients: (2 not defined because of singularities)
                                                        Estimate Std. Error
(Intercept)                                              -1.0842     0.3724
spreadFactor1Theo < breakPointPM1TRUE                     5.8278     0.3895
spreadFactor1Theo                                         1.0890     0.0199
spreadFactor1Theo >= breakPointPM1TRUE                        NA         NA
methodMMLM                                                0.2974     0.0681
type1PM                                                   0.1527     0.1613
spreadFactor1Theo < breakPointPM1TRUE:spreadFactor1Theo  -0.4342     0.0270
spreadFactor1Theo:spreadFactor1Theo >= breakPointPM1TRUE      NA         NA
spreadFactor1Theo:type1PM                                -0.0257     0.0111
                                                        t value Pr(>|t|)
(Intercept)                                               -2.91   0.0038 **
spreadFactor1Theo < breakPointPM1TRUE                     14.96  < 2e-16
   ↪***
spreadFactor1Theo                                         54.73  < 2e-16
   ↪***
spreadFactor1Theo >= breakPointPM1TRUE                       NA       NA
methodMMLM                                                 4.37  1.6e-05
   ↪***
type1PM                                                    0.95   0.3445
spreadFactor1Theo < breakPointPM1TRUE:spreadFactor1Theo  -16.10  < 2e-16
   ↪***
spreadFactor1Theo:spreadFactor1Theo >= breakPointPM1TRUE     NA       NA
spreadFactor1Theo:type1PM                                 -2.31   0.0214 *
---
Signif. codes:  0    ***    0.001    **    0.01    *    0.05    .    0.1
   ↪     1

Residual standard error: 0.681 on 393 degrees of freedom
Multiple R-squared: 0.984,      Adjusted R-squared: 0.984
F-statistic: 3.97e+03 on 6 and 393 DF,  p-value: <2e-16
```

The test plots provived by *R* in Fig. D.4 shows that the model is well adequate for the data.

Summary of the linear model used to analyse the observed $\hat{f}_s$ from virtual data as explained in Section 4.6.1.1 on page 80.

```
Call:
lm(formula = freqSpread1 ~ method + freqSpread1theo + Tz1theo,
    data = uniModal)
```

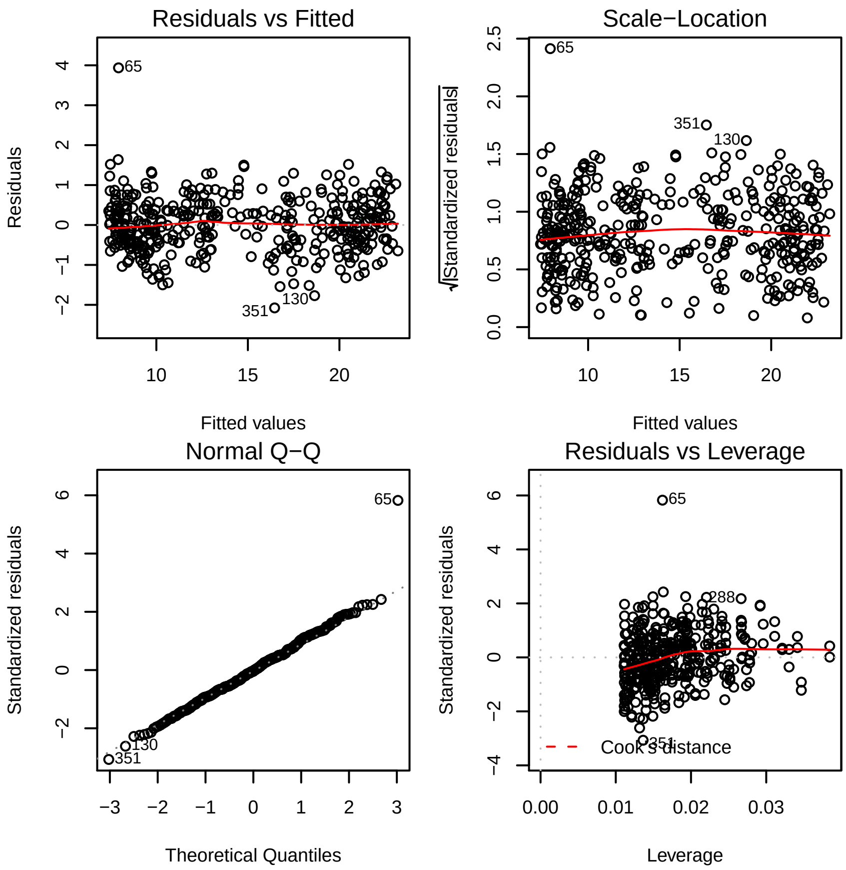

Figure D.4: *check plots provided by R to evaluate the validity of the linear piecewise model used to analyse the observed* $\hat{\Theta}_S$.

```
Residuals:
     Min       1Q   Median       3Q      Max 
-0.02718 -0.00541 -0.00046  0.00503  0.02773 

Coefficients:
                 Estimate Std. Error t value Pr(>|t|)    
(Intercept)     -0.060434   0.004765   -12.7   <2e-16 ***
methodMMLM       0.001403   0.000823     1.7     0.09 .  
freqSpread1theo  1.342207   0.016811    79.8   <2e-16 ***
Tz1theo         -0.060365   0.004335   -13.9   <2e-16 ***
---
Signif. codes:  0    ***    0.001    **    0.01    *    0.05    .    0.1   
    ⇝     1 

Residual standard error: 0.00823 on 396 degrees of freedom
Multiple R-squared: 0.945,      Adjusted R-squared: 0.944 
F-statistic: 2.26e+03 on 3 and 396 DF,  p-value: <2e-16
```

The test plots provided by *R* in Fig. D.5 shows that the model not entirely adequate. The *scale-location* plot shows that the variance do increase with the mean which conflict with the underlying hypothesis of normal errors with constant variance. However, no better model was found and the repetition of f_s in two clusters (Bretschneider or JONSWAP spectra) is blamed for this issue.

Summary of the minimal adequate model fitted to the observed $\hat{H}_{m0}$ from virtual data as explained in Section 4.6.1.1 on page 80.

```
Call:
lm(formula = Hm01 ~ method + spreadFactor1Theo + freqSpread1theo + 
    hmo1theo)

Residuals:
       Min         1Q     Median         3Q        Max 
-3.238e-03 -7.284e-04 -4.284e-05  7.765e-04  4.143e-03 

Coefficients:
                   Estimate Std. Error t value Pr(>|t|)    
(Intercept)       -1.204e-02  7.121e-04  -16.91   <2e-16 ***
methodMMLM         1.324e-03  1.145e-04   11.56   <2e-16 ***
spreadFactor1Theo  1.861e-04  9.342e-06   19.92   <2e-16 ***
```

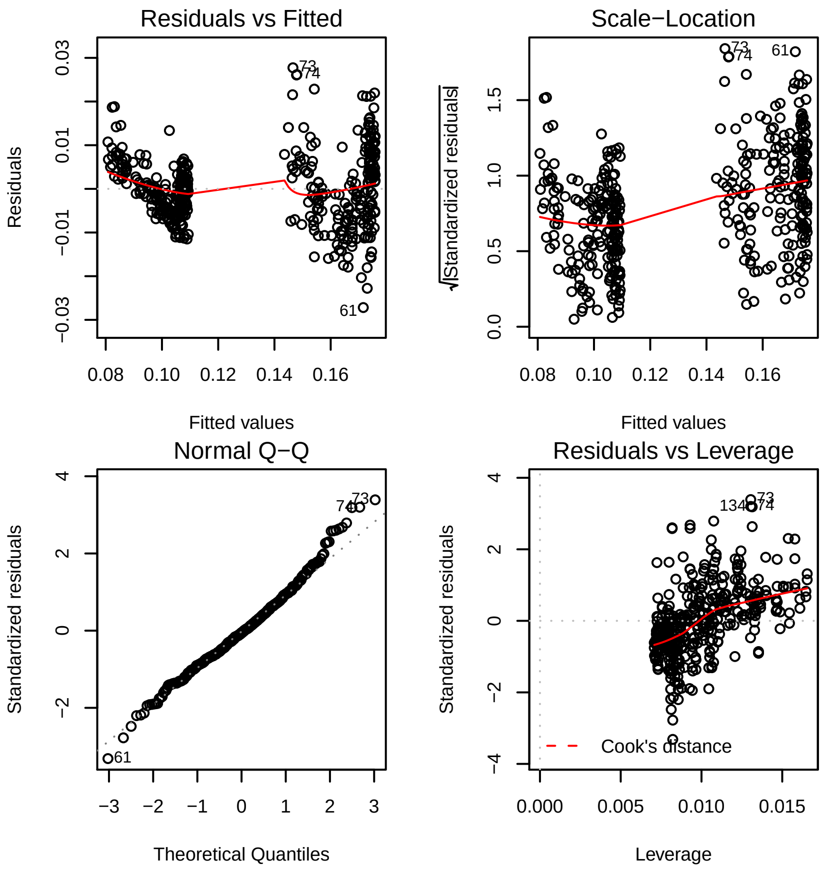

Figure D.5: *check plots provided by R to evaluate the validity of the linear model used to analyse the observed* $\hat{f}_s$.

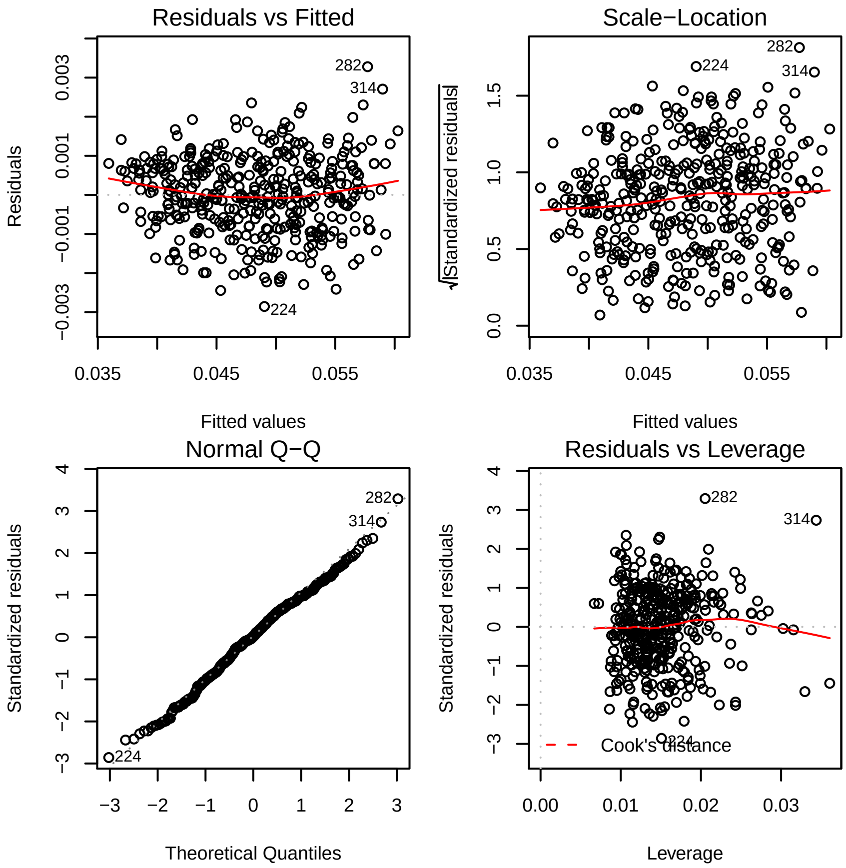

Figure D.6: *check plots provided by R to evaluate the validity of the linear model used to analyse the observed* $\hat{H}_{m0}$.

```
freqSpread1theo    4.609e-02  2.353e-03   19.59   <2e-16 ***
hmo1theo           7.777e-01  8.263e-03   94.12   <2e-16 ***
---
Signif. codes:  0    ***    0.001    **    0.01    *    0.05    .    0.1
    ⇝    1

Residual standard error: 0.001143 on 394 degrees of freedom
Multiple R-squared: 0.9594,     Adjusted R-squared: 0.9589
F-statistic:  2325 on 4 and 394 DF,  p-value: < 2.2e-16
```

The test plots provided by *R* in Fig. D.6 shows that the model fit reasonably well the data.

D.2.2 Interference parameter of bi-modal sea state

The interference parameter was introduced in an attempt to characterise the success rate of the isolation method in separating two spectra. It was thought that the level of interference between the two wave system could be a good indicator of it.

The Matlab code used to compute this parameter is presented below:

```
function inferenceFactor = computeIndeference(RStheo1,RStheo2,varargin)

[m,n] = size(RStheo1);
[m2,n2] = size(RStheo2);

if (m~=m2)||(n~=n2)
    inferenceFactor = -1;
else

    if isempty(varargin) || varargin{1}==1
        figure
        contour(RStheo1,30)
        hold on
        contour(RStheo2,30)
    end

    treshold1 = max(RStheo1) / 10;
    treshold2 = max(RStheo2) / 10;

    for i = 1:m
        for j = 1:n
            if RStheo1(i,j) >= treshold1
                RStheo1(i,j) = 1;
            else
                RStheo1(i,j) = 0;
            end
            if RStheo2(i,j) >= treshold2
                RStheo2(i,j) = 1;
            else
                RStheo2(i,j) = 0;
            end
        end
    end
    area1 = sum(sum(RStheo1));
    area2 = sum(sum(RStheo2));
    interferenceArea = sum(sum(RStheo1.*RStheo2));

    inferenceFactor = interferenceArea / min(area1,area2);
end
```

The interference is computed from the target wave spectra. The common footprint of the wave systems on the $f, \theta)$ plan is identified and the interference is estimated as the ratio between this common area and the smallest area of the two wave systems.

D.2.3 Bi-modal sea state: parameter investigation

Fig. D.7 presents a summary of the observations build with the *pairs* function of the R language. The correlation between parameters can be investigated.

D.2.4 linear models for the sensitivity analysis

The *R* summary of the multi-linear piecewise model fitted to the observed ϵ_T during the sensitivity analysis is provided below. Test plots provided by *R* shown in Fig. D.8 show that the model is a decent fit for the observed data.

```
 Call:
lm(formula = totalDifference ~ (angleNoise + (reflection < breakPointPM3_tot
    ↪) +
    reflection)^2 + (angleNoise + (reflection >= breakPointPM3_tot) +
    reflection)^2)

Residuals:
       Min         1Q     Median         3Q        Max
-0.0576119 -0.0150625 -0.0006384  0.0139508  0.1182935

Coefficients: (3 not defined because of singularities)
                                                Estimate Std. Error t value
(Intercept)                                     0.451860   0.008269  54.646
angleNoise                                      0.073351   0.015176   4.833
reflection < breakPointPM3_totTRUE             -0.224875   0.007952 -28.280
reflection                                      4.874334   0.110152  44.251
reflection >= breakPointPM3_totTRUE                   NA         NA      NA
angleNoise:reflection < breakPointPM3_totTRUE   0.014241   0.011753   1.212
angleNoise:reflection                          -0.881472   0.203772  -4.326
reflection < breakPointPM3_totTRUE:reflection   4.635314   0.132547  34.971
angleNoise:reflection >= breakPointPM3_totTRUE        NA         NA      NA
reflection:reflection >= breakPointPM3_totTRUE        NA         NA      NA
                                               Pr(>|t|)
(Intercept)                                     < 2e-16 ***
```

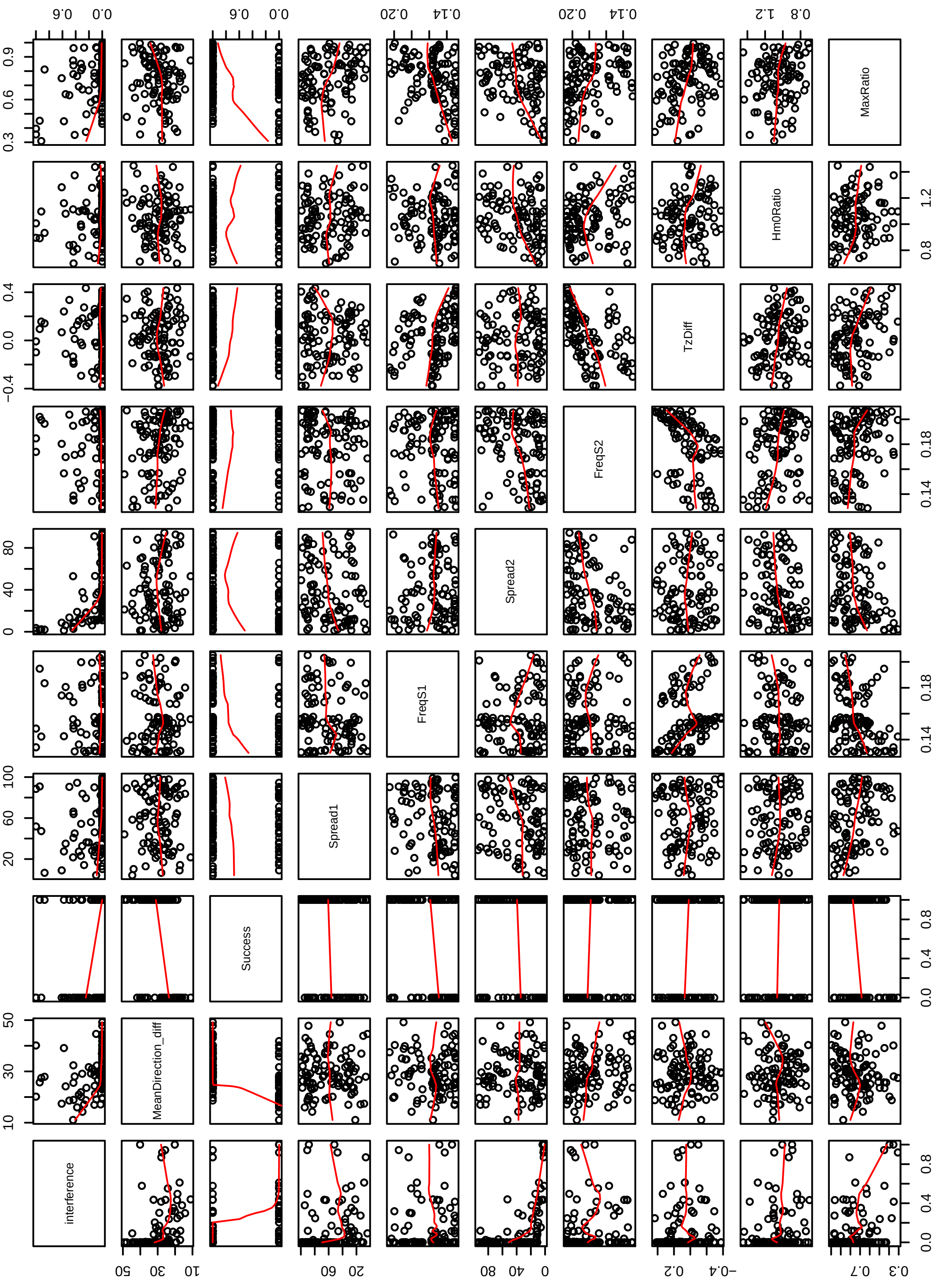

Figure D.7: *Plots produced by the pairs function of the statistical language R. I gives a fast ieda of the correlation between the variable of a dataset*

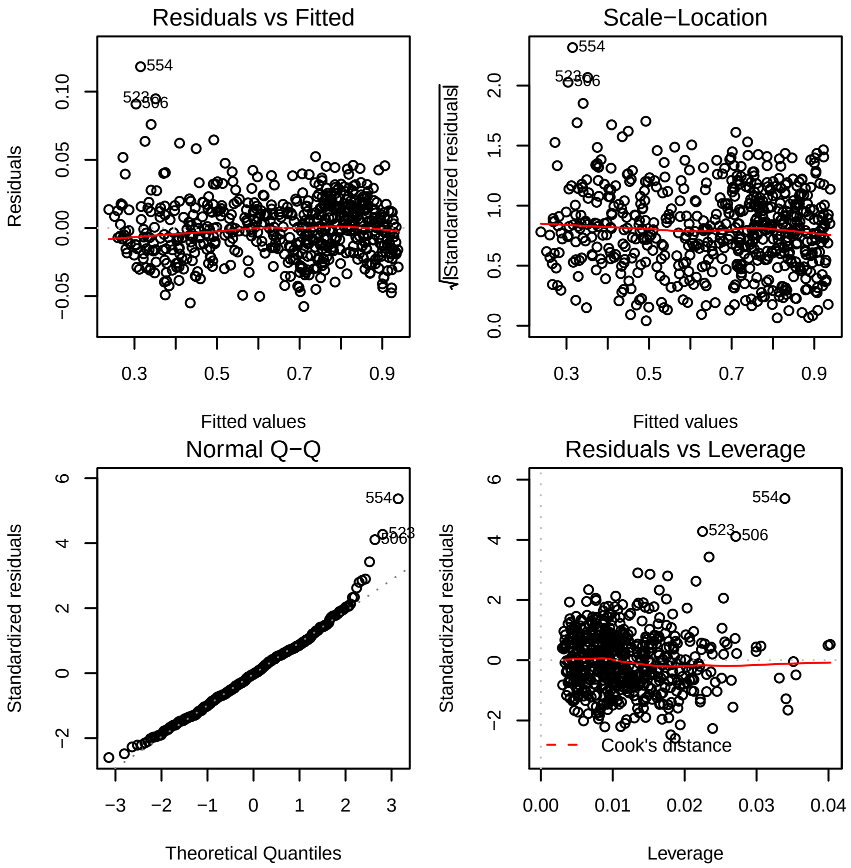

Figure D.8: *test plots provided by R to validate the multi-linear piecewise model fitted to the observed ϵ_T during the sensitivity analysis*

```
angleNoise                                    1.71e-06 ***
reflection < breakPointPM3_totTRUE             < 2e-16 ***
reflection                                     < 2e-16 ***
reflection >= breakPointPM3_totTRUE                 NA
angleNoise:reflection < breakPointPM3_totTRUE     0.226
angleNoise:reflection                         1.78e-05 ***
reflection < breakPointPM3_totTRUE:reflection  < 2e-16 ***
angleNoise:reflection >= breakPointPM3_totTRUE      NA
reflection:reflection >= breakPointPM3_totTRUE      NA
---
Signif. codes:  0   ***   0.001   **   0.01   *   0.05   .   0.1
   ↝    1

Residual standard error: 0.02241 on 593 degrees of freedom
Multiple R-squared: 0.987,     Adjusted R-squared: 0.9868
F-statistic:  7478 on 6 and 593 DF,  p-value: < 2.2e-16
```

The *R* summary of the multi-linear piecewise model fitted to the observed $\epsilon_{n,Hm0}$ during the sensitivity analysis is provided below. Test plots provided by *R* shown in Fig. D.9 show that the model is a decent fit for the observed data.

```
Call:
lm(formula = Hm0Error ˜ (angleNoise + (reflection < breakPointPM4) +
    reflection)ˆ2 + (angleNoise + (reflection >= breakPointPM4) +
    reflection)ˆ2)

Residuals:
      Min        1Q    Median        3Q       Max
-2.67e-03 -4.22e-04  3.44e-05  4.51e-04  1.89e-03

Coefficients: (3 not defined because of singularities)
                                            Estimate Std. Error t value
(Intercept)                                -0.003145   0.000341   -9.23
angleNoise                                 -0.003807   0.000457   -8.34
reflection < breakPointPM4TRUE              0.004576   0.000324   14.14
reflection                                 -0.091089   0.004188  -21.75
reflection >= breakPointPM4TRUE                   NA         NA      NA
angleNoise:reflection < breakPointPM4TRUE   0.001100   0.000318    3.46
angleNoise:reflection                       0.045520   0.005577    8.16
reflection < breakPointPM4TRUE:reflection  -0.087186   0.004157  -20.98
angleNoise:reflection >= breakPointPM4TRUE        NA         NA      NA
reflection:reflection >= breakPointPM4TRUE        NA         NA      NA
                                           Pr(>|t|)
(Intercept)                                 < 2e-16 ***
angleNoise                                  5.3e-16 ***
reflection < breakPointPM4TRUE              < 2e-16 ***
reflection                                  < 2e-16 ***
reflection >= breakPointPM4TRUE                  NA
angleNoise:reflection < breakPointPM4TRUE   0.00058 ***
angleNoise:reflection                       2.0e-15 ***
reflection < breakPointPM4TRUE:reflection   < 2e-16 ***
angleNoise:reflection >= breakPointPM4TRUE       NA
reflection:reflection >= breakPointPM4TRUE       NA
---
Signif. codes:  0    ***    0.001    **    0.01    *    0.05    .    0.1
    ⤳     1

Residual standard error: 0.000669 on 593 degrees of freedom
Multiple R-squared: 0.969,      Adjusted R-squared: 0.968
```

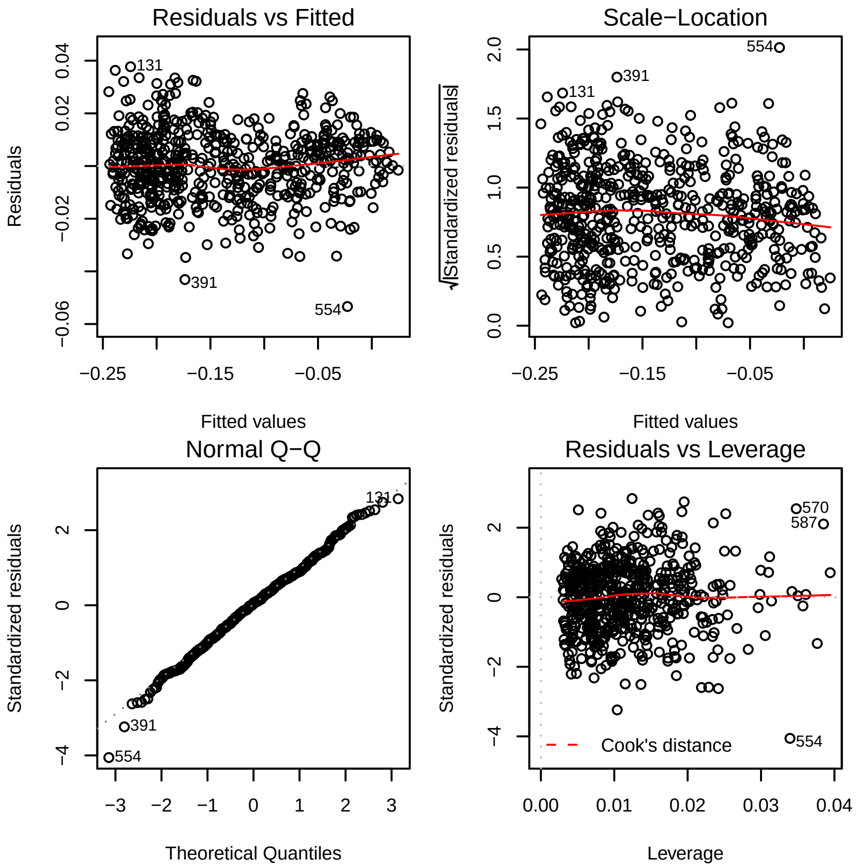

Figure D.9: *test plots provided by R to validate the multi-linear piecewise model fitted to the observed ϵ_{Hm0} during the sensitivity analysis*

```
F-statistic: 3.06e+03 on 6 and 593 DF,  p-value: <2e-16
```

The *R* summary of the gneralised linear model with poisson errors fitted to the observed $\epsilon_{n,\Theta}$ during the sensitivity analysis is provided below. Test plots provided by *R* shown in Fig. D.10 show that the model is a decent fit for the observed data.

```
Call:
glm(formula = SpreadError ˜ reflection, family = poisson, data = Data[
    ↝SpreadError >
    0, ])

Deviance Residuals:
    Min        1Q    Median        3Q       Max
-0.3937   -0.0945   -0.0240    0.0711    0.3919

Coefficients:
            Estimate Std. Error z value Pr(>|z|)
```

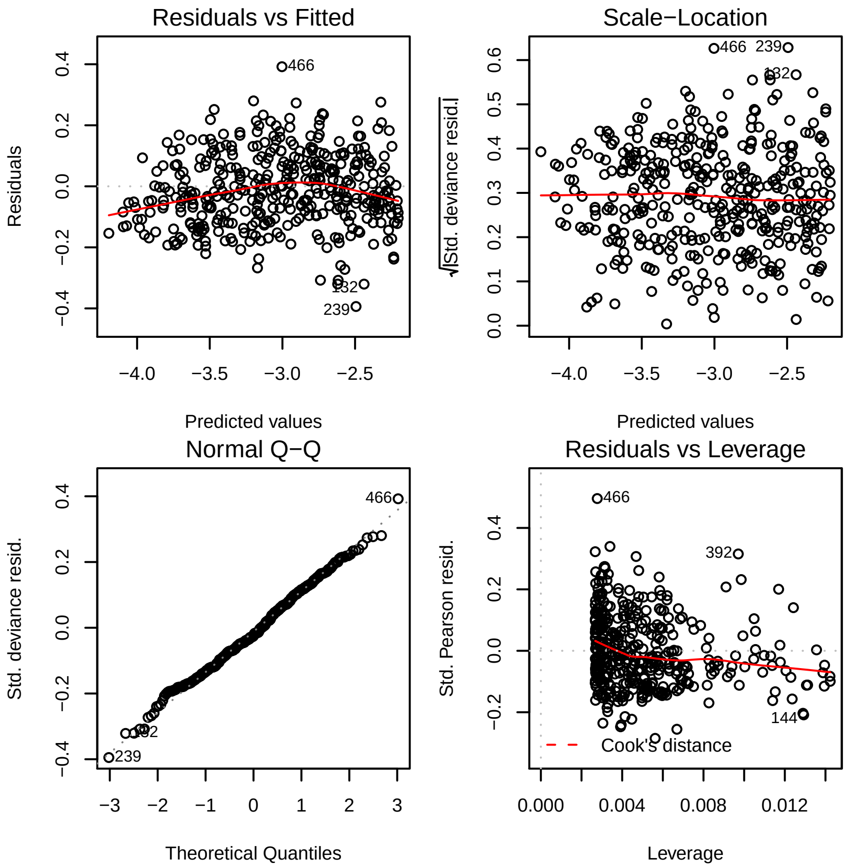

Figure D.10: *test plots provided by R to validate the gneralised linear model with poisson errors fitted to the observed* $\epsilon_{n,\Theta}$ *during the sensitivity analysis*

```
(Intercept)   -4.603      0.895   -5.14  2.7e-07 ***
reflection    23.999     11.564    2.08    0.038 *
---
Signif. codes:  0    ***   0.001    **    0.01    *    0.05    .    0.1
    ↝     1


(Dispersion parameter for poisson family taken to be 1)


    Null deviance: 10.4265  on 395  degrees of freedom
Residual deviance:  5.7279  on 394  degrees of freedom
AIC: Inf


Number of Fisher Scoring iterations: 6
```

Appendix E
Summaries of the statistical models: first phase results

E.1 The single OWC

Summary of the model fitted to the observed P^n of the single OWC during the first phase tests:

```
Call:
lm(formula = normSingleOWC ~ I(Te^2) + Hm0 + Te + freqSpread +
    spreadFactor + Te:freqSpread + Te:spreadFactor, data = singleOWC)

Residuals:
      Min        1Q    Median        3Q       Max
-0.045677 -0.015024 -0.002251  0.010293  0.101707

Coefficients:
                 Estimate Std. Error t value Pr(>|t|)
(Intercept)     -5.391442   0.219845 -24.524  < 2e-16 ***
I(Te^2)         -3.698194   0.182272 -20.289  < 2e-16 ***
Hm0             15.114941   1.978046   7.641 8.56e-12 ***
Te               9.346944   0.402213  23.239  < 2e-16 ***
freqSpread       3.495217   0.632996   5.522 2.27e-07 ***
spreadFactor    -0.013568   0.004184  -3.243  0.00157 **
Te:freqSpread   -4.718087   0.595834  -7.918 2.08e-12 ***
Te:spreadFactor  0.011714   0.003736   3.135  0.00220 **
---
Signif. codes:  0    ***    0.001    **    0.01    *    0.05    .    0.1
    ⇝     1

Residual standard error: 0.026 on 110 degrees of freedom
Multiple R-squared: 0.9833,     Adjusted R-squared: 0.9823
F-statistic: 926.2 on 7 and 110 DF,  p-value: < 2.2e-16
```

Summary of the model fitted to the observed Cw of the single OWC during the first phase tests:

```
Call:
lm(formula = captureWidthSingle ~ I(Te^2) + Hm0 + Te + freqSpread +
    Te:freqSpread, data = singleOWC)

Residuals:
     Min       1Q   Median       3Q      Max
-0.90575 -0.29436 -0.03307  0.25253  1.40303

Coefficients:
              Estimate Std. Error t value Pr(>|t|)
(Intercept)    -85.229      3.806 -22.391  < 2e-16 ***
I(Te^2)        -65.536      3.099 -21.146  < 2e-16 ***
Hm0             40.269     18.952   2.125   0.0358 *
Te             163.183      6.861  23.783  < 2e-16 ***
freqSpread      79.627     10.619   7.499 1.63e-11 ***
Te:freqSpread  -90.730      9.895  -9.169 2.73e-15 ***
---
Signif. codes:  0    ***    0.001    **    0.01    *    0.05    .    0.1
    ⇝     1

Residual standard error: 0.4604 on 112 degrees of freedom
Multiple R-squared: 0.9655,     Adjusted R-squared: 0.964
F-statistic: 627.6 on 5 and 112 DF,  p-value: < 2.2e-16
```

The test plots provided by *R* in Fig. E.1b shows that the model is adequate for the data. A few points are singled out (1, 48 and 56) and could be discarded as they exhibit larger residuals than expected for a normal distribution. However, according to the *Residual Vs Leverage* plot, they do not have a strong influence on the estimated coefficients so the model was accepted as it is.

E.2 The double OWC

Summary of the model fitted to the observed P^n of the double OWC during the first phase tests:

```
Call:
lm(formula = normDoubleOWC ~ I(Te^2) + Hm0 + Te + freqSpread +
    Te:freqSpread, data = doubleOWC)

Residuals:
       Min         1Q     Median         3Q        Max
-0.0775683 -0.0149676  0.0004785  0.0150177  0.0465718
```

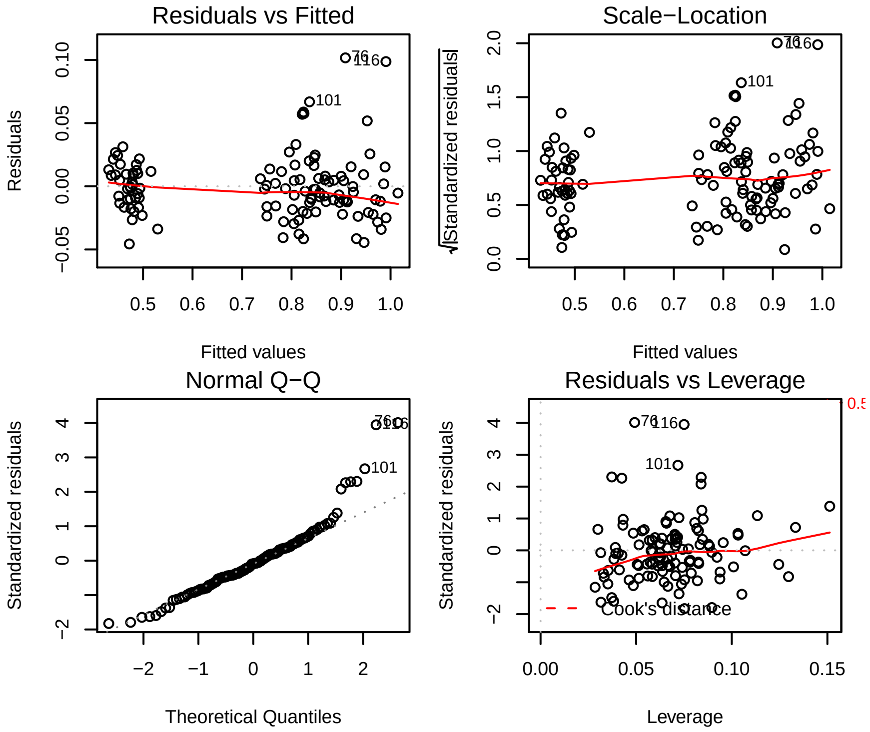

(a) test plots for P^n model

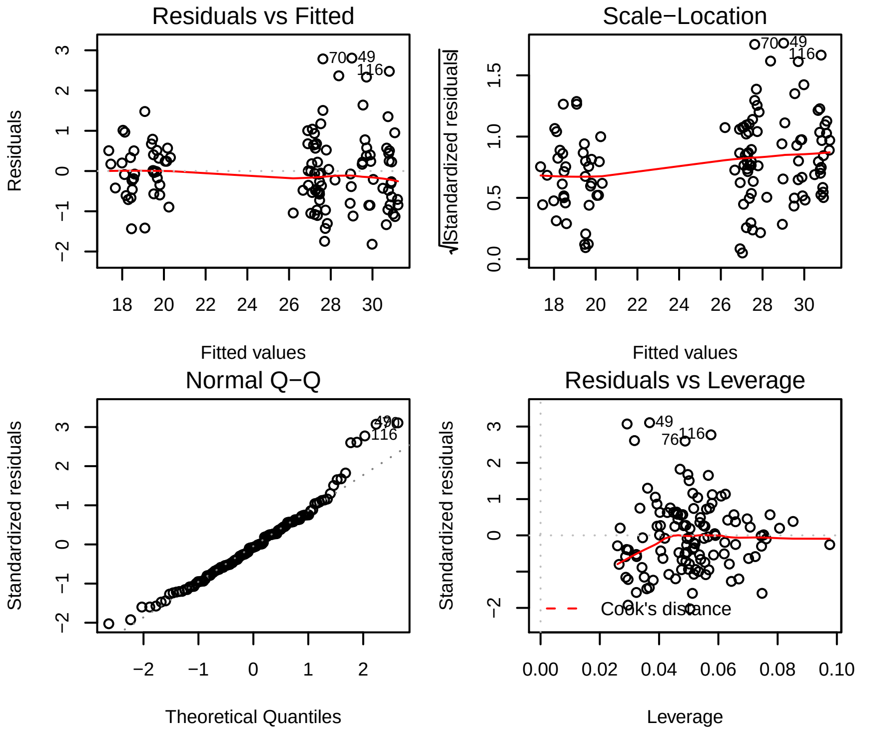

(b) test plots for Cw model

Figure E.1: *Test plots provided by R to evaluate the validity of the minimal adequate models fitted to the observed* P^n *and* Cw *of the single OWC during the* 1^{st} *test phase.*

```
Coefficients:
              Estimate Std. Error t value Pr(>|t|)
(Intercept)    -5.3449     0.2419 -22.095  < 2e-16 ***
I(Te^2)        -3.7054     0.1968 -18.832  < 2e-16 ***
Hm0             6.0045     1.2061   4.979 3.90e-06 ***
Te              9.6190     0.4383  21.948  < 2e-16 ***
freqSpread      3.1480     0.6705   4.695 1.16e-05 ***
Te:freqSpread  -4.1852     0.6282  -6.662 3.77e-09 ***
---
Signif. codes:  0    ***    0.001    **    0.01    *    0.05    .    0.1
    ⇝     1

Residual standard error: 0.02433 on 76 degrees of freedom
Multiple R-squared: 0.9876,     Adjusted R-squared: 0.9868
F-statistic:  1214 on 5 and 76 DF,  p-value: < 2.2e-16
```

The test plots provided by *R* in Fig. E.2a shows that the model is adequate for the data.

Summary of the model fitted to the observed Cw of the double OWC during the first phase tests:

```
Call:
lm(formula = captureWidthDouble ~ I(Te^2) + Hm0 + Te + freqSpread +
    Te:freqSpread, data = doubleOWC)

Residuals:
    Min      1Q  Median      3Q     Max
-7.1751 -1.5167 -0.1237  1.2352  4.5174

Coefficients:
              Estimate Std. Error t value Pr(>|t|)
(Intercept)    -312.49      21.24 -14.709  < 2e-16 ***
I(Te^2)        -247.49      17.44 -14.195  < 2e-16 ***
Hm0            -331.07     103.07  -3.212  0.00192 **
Te              623.43      38.70  16.109  < 2e-16 ***
freqSpread      305.13      59.01   5.171 1.75e-06 ***
Te:freqSpread  -336.15      55.43  -6.065 4.44e-08 ***
---
Signif. codes:  0    ***    0.001    **    0.01    *    0.05    .    0.1
    ⇝     1
```

```
Residual standard error: 2.167 on 78 degrees of freedom
Multiple R-squared: 0.9573,     Adjusted R-squared: 0.9545
F-statistic: 349.4 on 5 and 78 DF,  p-value: < 2.2e-16
```

The test plots provided by *R* in Fig. E.2b shows that the model is adequate for the data.

E.3 The Duck

Summary of the model fitted to the observed P^n of the duck during the first phase tests:

```
Call:
lm(formula = normDuck ~ Hm0 + Te + freqSpread + spreadFactor +
    Te:freqSpread, data = duckSet)

Residuals:
      Min        1Q    Median        3Q       Max
-0.199312 -0.040149  0.004363  0.027939  0.162102

Coefficients:
               Estimate Std. Error t value Pr(>|t|)
(Intercept)   -2.161255   0.274701  -7.868 1.12e-11 ***
Hm0           12.381957   4.517664   2.741  0.00749 **
Te             2.231492   0.165973  13.445  < 2e-16 ***
freqSpread     3.462315   1.598813   2.166  0.03318 *
spreadFactor  -0.007470   0.002239  -3.337  0.00126 **
Te:freqSpread -3.693548   1.501864  -2.459  0.01597 *
---
Signif. codes:  0    ***    0.001    **    0.01    *    0.05    .    0.1
    ⇝     1

Residual standard error: 0.05798 on 84 degrees of freedom
Multiple R-squared: 0.9586,     Adjusted R-squared: 0.9562
F-statistic: 389.3 on 5 and 84 DF,  p-value: < 2.2e-16
```

Tests plots are provided by *R* in Fig. E.3a to evaluate the validity of the model. The Normal Q-Q plot is not as satisfactory as the similar plots for the OWC models, but nothing extremely worrying is identified. The model is accepted as it is.

Summary of the model fitted to the observed Cw of the duck during the first phase tests:

```
Call:
```

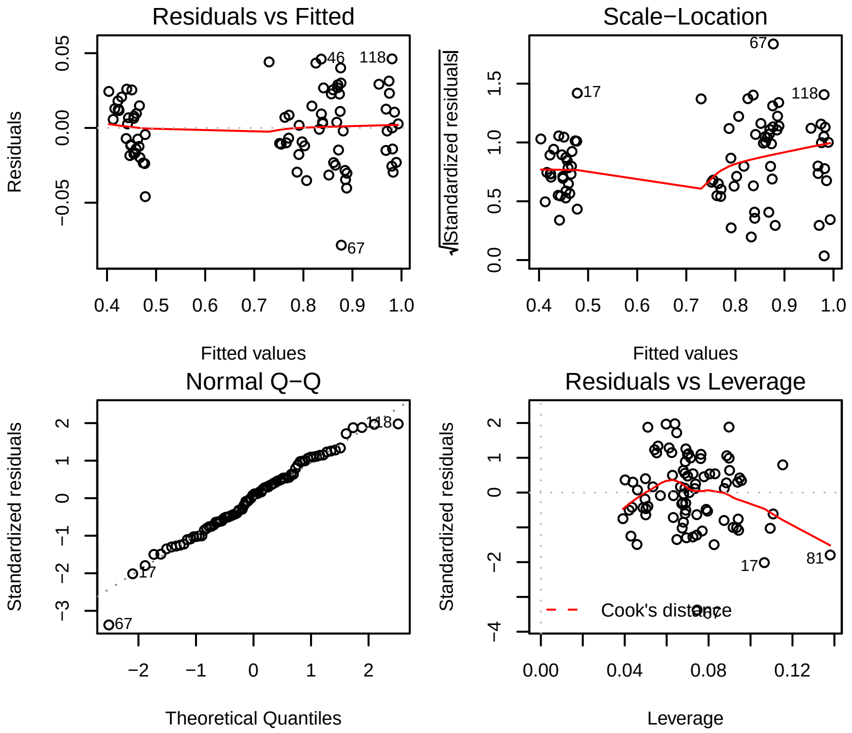

(a) test plots for P^n model

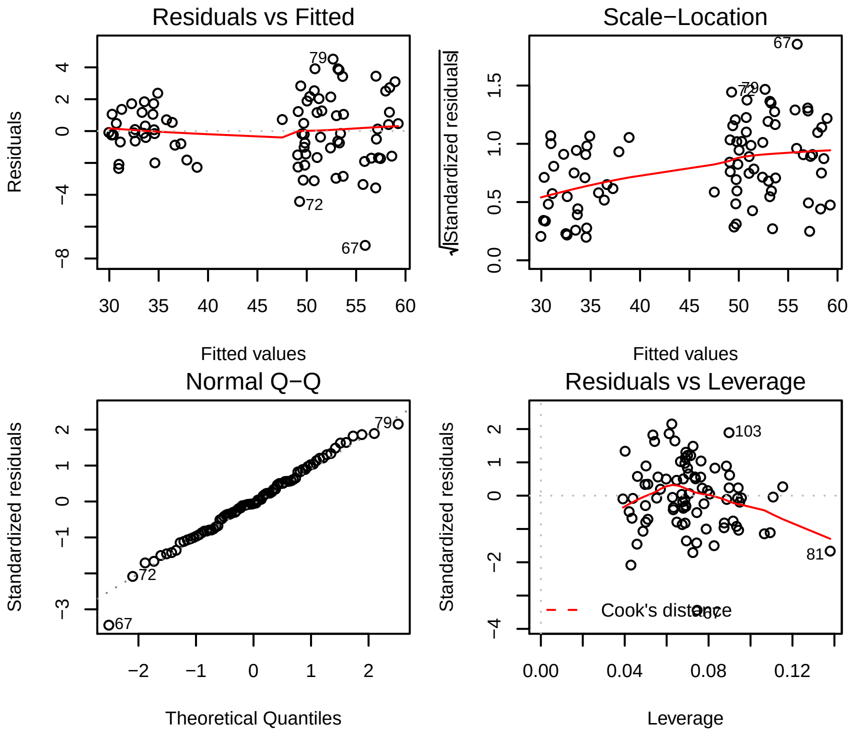

(b) test plots for Cw model

Figure E.2: *Test plots provided by R to evaluate the validity of the minimal adequate models fitted to the observed* P^n *and* Cw *of the double OWC during the* 1^{st} *test phase.*

```
lm(formula = captureWidthDuck ~ Te + spreadFactor, data = duckSet)

Residuals:
     Min       1Q   Median       3Q      Max
-7.14877 -1.16962 -0.05404  1.09160  5.74080

Coefficients:
              Estimate Std. Error t value Pr(>|t|)
(Intercept)  -34.06426    1.80922 -18.828  < 2e-16 ***
Te            51.21213    1.54757  33.092  < 2e-16 ***
spreadFactor  -0.18192    0.04704  -3.868 0.000212 ***
---
Signif. codes:  0    ***    0.001    **    0.01    *    0.05    .    0.1
    ⇝     1

Residual standard error: 2.079 on 87 degrees of freedom
Multiple R-squared: 0.9282,     Adjusted R-squared: 0.9265
F-statistic: 562.3 on 2 and 87 DF,  p-value: < 2.2e-16
```

Tests plots are provided by *R* in Fig. E.3b to evaluate the validity of the model.

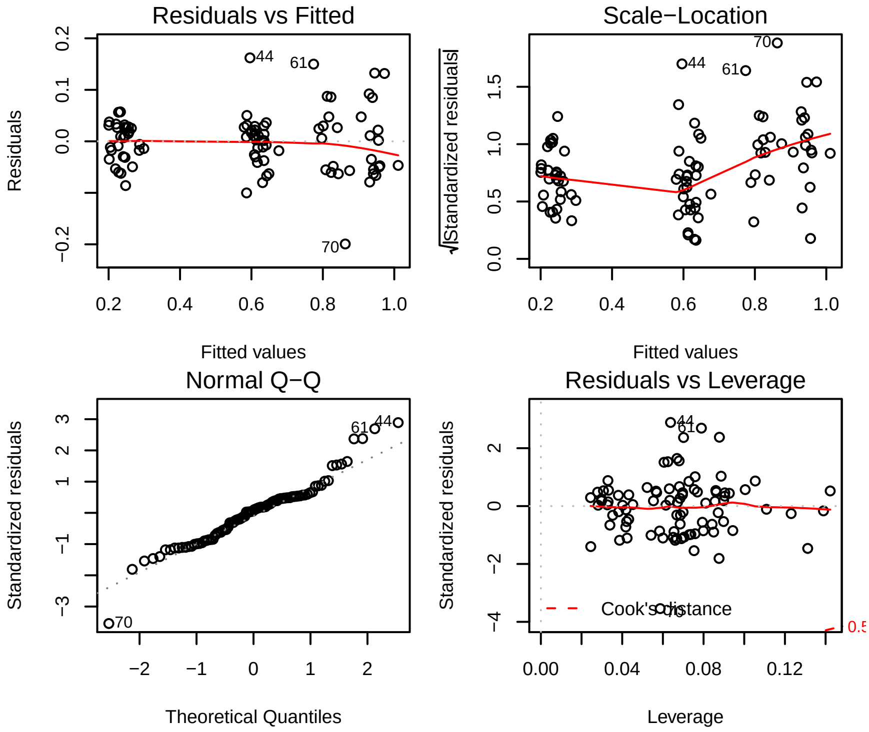

(a) test plots for P^n model

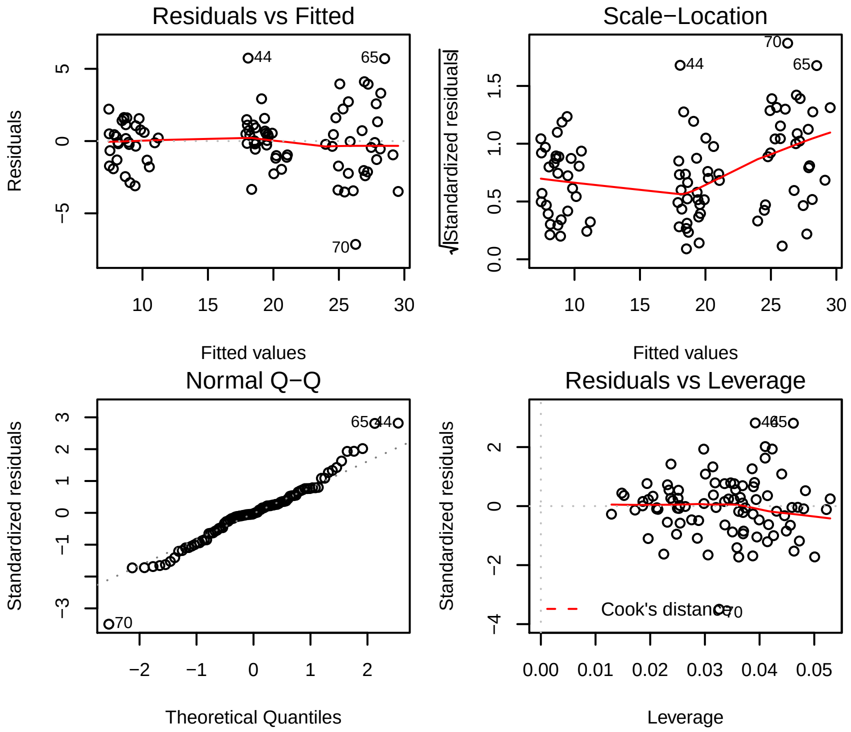

(b) test plots for Cw model

Figure E.3: *Test plots provided by R to evaluate the validity of the minimal adequate models fitted to the observed P^n and Cw of the Duck during the 1^{st} test phase.*

Appendix F
Second test phase: supplementary material

A summary of the capture width observation of the Duck and of the double OWC for the second phase of tests is presented in Fig. F.1 and Fig. F.2. The different behaviour of the devices with respect to the type of sea state (1^{st} and 2^nd group) is well marked. From these graphs, it looks like that best parameter to use would be directly the wave power P_w. However, it had been shown that the power extracted by a WEC can vary dramatically for sea states with the same energy period and significant wave height, which also mean identical wave power per meter of crest length.

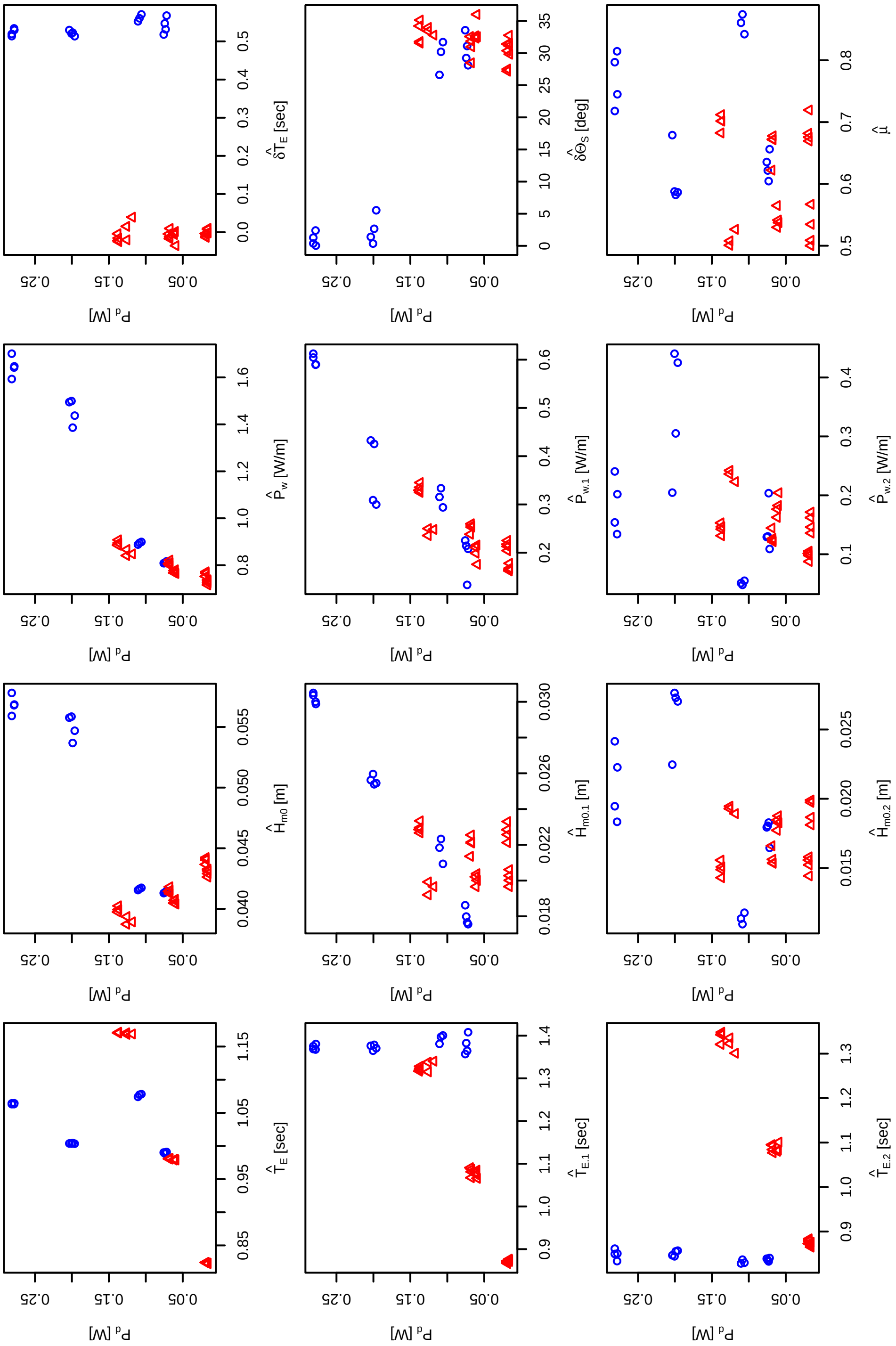

Figure F.1: *Duck average power output with respect to sea state parameters during the* 2^{nd} *phase. Results are differentiated between* 1^{st} *group (*$\delta\hat{T}_E < 0.2\,\mathrm{s}$*) represented by red triangles and* 2^{nd} *group (*$\delta\hat{T}_E > 0.2\,\mathrm{s}$*) represented in blue circles.*

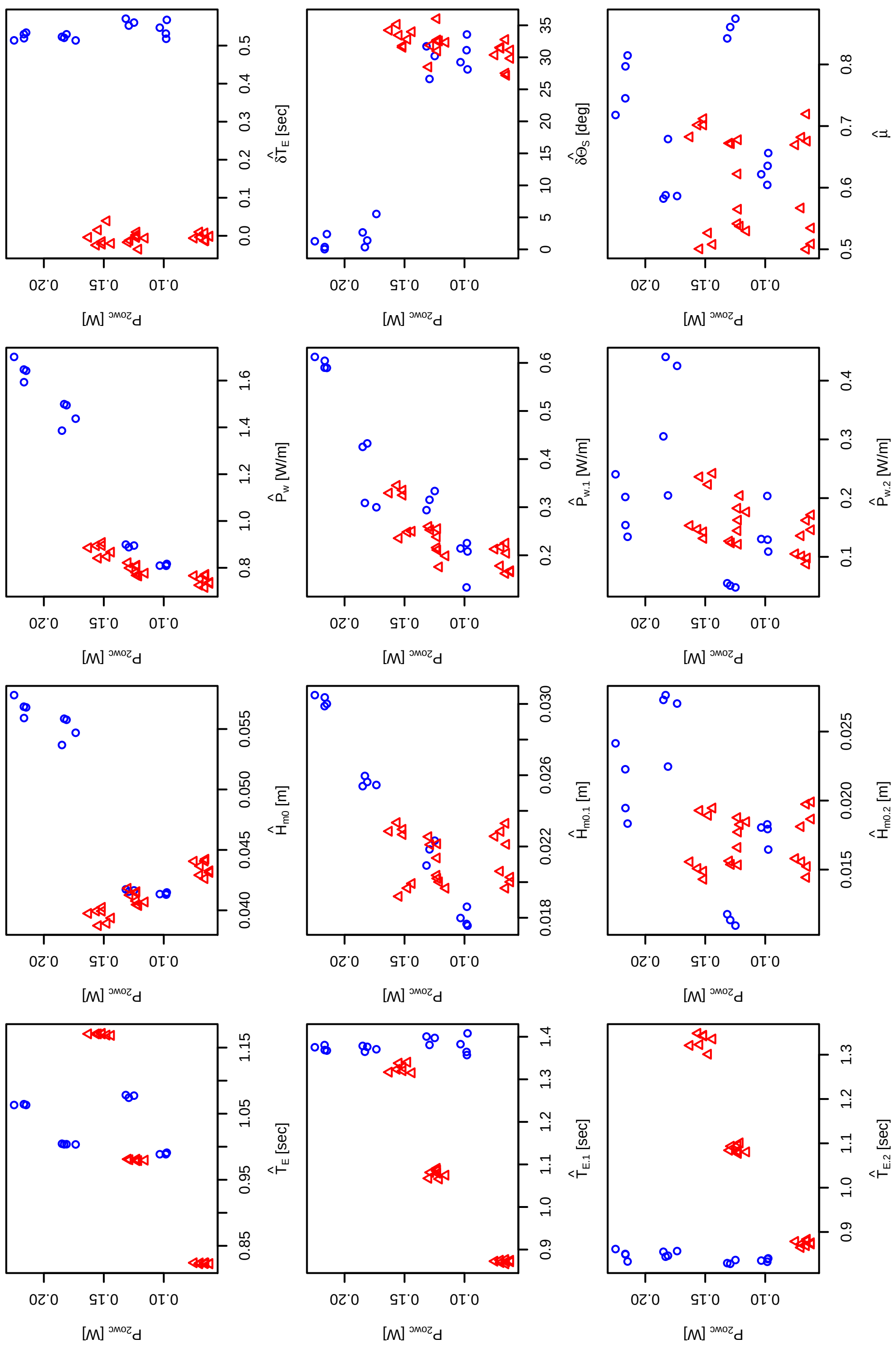

Figure F.2: *Double OWC average power output with respect to sea state parameters during the* 2^{nd} *phase. Results are differentiated between* 1^{st} *group* ($\delta\hat{T}_E < 0.2\,\mathrm{s}$) *represented by red triangles and* 2^{nd} *group* ($\delta\hat{T}_E > 0.2\,\mathrm{s}$) *represented in blue circles.*

Bibliography

Airy, G.B. 1841. Tides and waves. *Encyclopedia Metropolitana*, **241–396**. 11

Babarit, Aurélien, Benahmed, H, Clément, Alain, Debusschere, V, Duclos, G, Multon, B, & Robin, G. 2006. Simulation of electricity supply of an Atlantic island by offshore wind turbines and wave energy converters associated with a medium scale local energy storage. *Renewable Energy*, **31**(2), 153–160. 2

Babarit, Aurélien, Gilloteaux, Jean-Christophe, & Clément, Alain. 2007. Influence of wave spectrum spreading on the production of the SEAREV wave energy converter. *Pages 415–420 of: ISOPE2007 Seventeenth International Offshore and Polar Engineering Conference Proceedings and Polar Engineering Conference Proceedings*. 168

Barber, NF. 1963. The directional resolving power of an array of wave detectors. *Pages 137–150 of: Ocean wave spectra*. Easton, Maryland: Prentice-Hall. 12

Benoit, Michel, Frigaard, P, & Schaffer, H A. 1997 (Aug.). Analysing multidirectional wave spectra: A tentative classification of available methods. *Pages 131–158 of: IAHR Seminar Multidirectional Waves and their Interaction with Structures*. 12, 49, 105

Boukhanovsky, Alexander, & Guedes Soares, C. 2009. Modelling of multipeaked directional wave spectra. *Applied Ocean Research*, **31**(2), 132–141. 15

Bryden, Ian, Linfoot, Brian, & Hall, M S. 1990 (June). Computer-controlled simulation of short-crested seas. *Pages 207–224 of: Proc. Instn Civ. Engrs, Part 2*, vol. 89. 10

Capon, J., Greenfield, RJ, & Kolker, RJ. 1967. Multidimensional maximum-likelihood processing of a large aperture seismic array. *Proceedings of the IEEE*, **55**(2), 192–211. 12, 51

Cartwright, D E. 1963. The use of directional spectra in studying the output of a wave recorder on a moving ship. *Ocean wave spectra*, 203–218. 14

Child, B.F.M., & Venugopal, Vengatesan. 2010. Optimal configurations of wave energy device arrays. *Ocean Engineering*, **37**(16), 1402–1417. 164, 166

Craik, Alex D D. 2005. George Gabriel Stokes on Water Wave Theory. *Annual Review of Fluid Mechanics*, **37**, 23–42. 61

Crawley, M.J. 2007. *The R Book*. John Wiley & Sons Inc. 90, 91, 101, 150, 211, 214

Cruz, João, Pascal, Rémy, & Taylor, Jamie. 2006. Characterisation of the wave profile in the Edinburgh curved tank. *Pages 1–10 of: Proceedings of the 25th International Conference on Offshore Mechanics and Arctic Engineering*. 38

Davidson, Mark A, Huntley, David A, & Birdb, Paul A D. 1998. A practical method for the estimation of directional wave spectra in reflective wave fields. *Coastal Engineering*, **33**(2-3), 91–116. 50, 54

Davis, Russ E, & Regier, Loyd A. 1977. Methods for estimating directional wave spectra from multi-element arrays. *Journal of Marine Research*, **35**(3), 453–478. 50, 51, 52, 53, 72

Dean, R.G., & Dalrymple, R.A. 1991. *Water wave mechanics for engineers and scientists*. World Scientific Pub Co Inc. 61

Donelan, Mark A., Drennan, W M, & Magnusson, Anne Karin. 1996. Nonstationary analysis of the directional properties of propagating waves. *Journal of Physical Oceanography*, **26**(9), 1901–1914. 49

Elgar, Steve, Guza, RT, & Seymour, RJ. 1985. Wave group statistics from numerical simulations of a random sea. *Applied ocean research*, **7**(2), 93–96. 21

Fernandes, A A, Menon, H B, & Sarma, Y V B. 2000. Directional spectrum of ocean waves from array measurements using phase/time/path difference methods. *Ocean Engineering*, **27**(4), 345–363. 28, 49

Folley, Matt. 2009. The effect of sub-optimal control and the spectral wave climate on the performance of wave energy converter arrays. *Applied Ocean Research*. 164

Frigaard, P, Helm-petersen, Jacob, Klopman, G., Stansberg, C.T., Benoit, Michel, Briggs, M. J., Miles, MD, Santas, J., Schaffer, H A, & Hawkes, P. J. 1997. List of Sea State Parameters - an update for multidirectional waves from IAHR seminar. *In: Proceeding of IAHR seminar on Multidirectional Waves and their Interaction with Structures*. 17

Gilloteaux, Jean-Christophe, & Ringwood, John V. 2009. Influences of wave directionality on a generic point absorber. *Pages 979–988 of: Proceedings of the 8th European Wave and Tidal Energy Conference*. 169

Guedes Soares, C. 1984. Representation of double-peaked sea wave spectra. *Ocean Engineering*, **11**(2), 185–207. 15

Guedes Soares, C., & Nolasco, M. C. 1992. Spectral Modeling of Sea States With Multiple Wave Systems. *Journal of Offshore Mechanics and Arctic Engineering*, **114**(4), 278. 15

Hanson, Jeffrey L, & Phillips, Owen M. 2001. Automated Analysis of Ocean Surface Directional Wave Spectra. *Journal of Atmospheric and Oceanic Technology*, **18**(2), 277–293. 66

Hasselmann, D E, Dunckel, M., & Ewing, J. A. 1980. Directional wave spectra observed during JONSWAP 1973,. *Journal of Physical oceanography*, **10**, 1264–1280. 14

Hasselmann, K, Barnett, T P, Bouws, E, Carlson, H, Cartwright, D E, Eake, K, Euring, J A, Gicnapp, A, Hasselmann, D E, Kruseman, P, Meerburg, A, Mullen, P, Olbers, D J, Richren, K, Sell, W, & Walden, H. 1973. Measurements of wind-wave growth and swell decay during the Joint North Sea Wave Project (JONSWAP). *Ergnzungsheft zur Deutschen Hydrographischen Zeitschrift Reihe*, **8**(12), 95. 14

Haubrich, Richard A. 1968. Array Design. *Bulletin of the Seismological Society of America.*, **58**(June), pp. 977—-991. x, 71, 72, 79

Holmes, Brian, & Barrett, Sean. 2007 (Sept.). Sea & Swell Spectra. *In: Proceedings of the 7th European Wave and Tidal Energy Conference*. 2

Huntley, David A, & Davidson, Mark A. 1998. Estimating the Directional Spectrum of Waves Near a Reflector. *Journal of Waterway, Port, Coastal and Ocean Engineering*, **124**, 312–319. ix, 50, 56, 57

Ilic, Suzana, Chadwick, Andrew, & Helm-petersen, Jacob. 2000. An evaluation of directional analysis techniques for multidirectional, partially reflected waves. Part 1: numerical investigations. *Journal of Hydraulic Research*, **38**(4), 243–252. 65

Isobe, Masahiko, & Kondo, K. 1984. Method for estimating directional wave spectrum in incident and reflected wave field. *Pages 467–483 of: Proceedings of the 19th Conference on Coastal Engineering*, vol. 19. New York, USA: American Society of Civil Engineers. 50

J. Ploeg. 1987. Wave Analysis and Generation in Laboratory Basins. *Page 219 of: Analysis*. Lausanne, Suisse: International Association for Hydraulic Research. 20

Jefferys, E R. 1987. Directional seas should be ergodic. *Applied Ocean Research*, **9**(Oct.), 186–191. 20, 21, 22, 43

Jefferys, E R, Wareham, GT, & Ramsden, N. 1981. Measuring directional spectra with the MLM. *Pages 203–219 of:* Wiegel, Robert L. (ed), *Proceedings of the Conference on Directional Wave Spectra Applications,*. Berkeley, California: American Society of Civil Engineers. ix, 22, 23, 71

Jeffrey, D J E, Keller, Glen, Salter, Stephen H, & Taylor, Jamie. 1978 (July). *Edinburgh Wave Power Project, Fourth Year Report*. Tech. rept. The University of Edinburgh, Edinburgh, UK. 46

Keller, Glen. 1984. *Experiments on Nonlinear interaction of two wavetrains*. Tech. rept. The University of Edinburgh, Edinburgh, UK. 23

Kerbiriou, Marie-Aurélie, Prevosto, Marc, Maisondieu, Christophe, Babarit, Aurélien, & Clément, Alain. 2007a (June). Influence of an improved sea-state description on a wave energy converter production. *In: Proceedings of the 26th International Conference on Offshore Mechanics and Arctic Engineering*. 15

Kerbiriou, Marie-Aurélie, Prevosto, Marc, Maisondieu, Christophe, Clément, Alain, & Babarit, Aurélien. 2007b (Sept.). Influence of Sea-States Description on Wave Energy Production Assessment. *In: Proceedings of the 7th European Wave and Tidal Energy Conference*. 66, 123

Korteweg, D J, & De Vries, G. 1895. On the Change of Form of Long Waves advancing in a Rectangular Canal and on a New Type of Long Stationary Waves. *The London, Edinburgh and Dublin philosophical magazine and journal of science*, **39**, 422–443. 61

Lin, Chia-Po. 1999. *Experimental Studies of the Hydrodynamic Characteristics of a Sloped Wave Energy Device*. Ph.D. thesis, The University of Edinburgh. 43

Liu, Paul C. 2000. Is the wind wave frequency spectrum outdated. *Ocean Engineering*, **27**(5), 577–588. 11, 49

Lucas, Jorge. 2011. *The dynamics of a horizontal cylinder oscillating as a wave energy converter about an off-centred axis*. PhD, The University of Edinburgh. 118, 119

Lucas, Jorge, Cruz, João, Salter, Stephen H, & Taylor, Jamie. 2008 (June). Update on the design of a 1:33 scale model of a modified Edinburgh Duck WEC. *In: Proceedings of the 27th International Conference on Offshore Mechanics and Arctic Engineering*. 7, 40, 46, 50, 115, 117, 118

Lucas, Jorge, Salter, Stephen H, Cruz, João, & Taylor, Jamie. 2009. Performance optimisation of a modified Duck through optimal mass distribution. *Pages 270–279 of: Proceedings of the 8th European Wave and Tidal Energy Conference*. 7

Mackay, Edward B.L. 2011. Modelling and Description of Omnidirectional Wave Spectra. *In: Proceedings of the 9th European Wave and Tidal Energy Conference*. 15

Mansard, E P R, & Funke, E R. 1980. The measurement of incident and reflected spectra using a least squares method. *Pages 154–172 of: Proceedings of the 17th International Conference on Coastal Engineering*, vol. 1. 41

Massel, Stanislaw R. 2001. Wavelet analysis for processing of ocean surface wave records. *Ocean Engineering*, **28**(8), 957–987. 49

Masterton, S R, & Swan, C. 2008. On the accurate and efficient calibration of a 3D wave basin. *Ocean Engineering*, **35**(8-9), 763–773. 46

Miles, MD, & Funke, E R. 1989. A comparison of methods for synthesis of directional seas. *Journal of Offshore Mechanics and Arctic Engineering*, **111**(Feb.), 43. 21, 22, 28, 50

Mitsuyasu, Hisashi, Tasai, Fukuzo, Sihara, Toshiro, Minzuno, Shinjiro, Honda, Makoto Ohkusuand Tadao, & Rikiishi, Kunio. 1975. Observation of Directional Spectrum of Ocean Waves Using a Cloverleaf Buoy. *Journal of Physical Oceanography*, **5**, 750–760. 14

Newland, D E. 2005. *An Introduction to Random Vibrations, Spectral & Wavelet Analysis: Third Edition*. Mineola, New York: Dover Publication, Inc. 12

Ochi, MK. 2003. *Hurricane-generated seas*. Vol. 8. Elsevier Science. 17

Ouellet, Y, & Datta, I. 1986. A survey of wave absorbers. Revue des amortisseurs a houle. *Journal of Hydraulic Research*, **24**, 265–279. 50

Pascal, Rémy. 2006. *Wave quality assessment and Testing of a wave energy converter in the Edinburgh Curved Wave Tank*. 7, 111

Pascal, Rémy, & Bryden, Ian. 2011. Directional spectrum methods for deterministic waves. *Ocean Engineering*, **38**(13), 1382–1396. 16

Pascal, Rémy, Lucas, Jorge, Ingram, David M, & Bryden, Ian. 2009 (June). Assessing and Improving the Edinburgh Curved Wave Tank. *Pages 269–276 of: Proceedings of the 19th International Offshore and Polar Engineering Conference*. 40, 50

Pascal, Rémy, Payne, Gregory S, & Bryden, Ian. 2011. Parametric models for WEC performances. *In: Proceedings of the 9th European Wave and Tidal Energy Conference*. 16

Payne, Gregory S, Taylor, Jamie, Bruce, Tom, & Parkin, Penny. 2008. Assessment of boundary-element method for modelling a free-floating sloped wave energy device. Part 1: Numerical modelling. *Ocean Engineering*, **35**, 333–341. 169

Pierson, Willard .J., & Marks, W. 1952. The power spectrum analysis of ocean wave records. *Trans. Amer. Geophys. Union*, **33**(6). 11, 13

R Development Core Team. 2009. *R: A Language and Environment for Statistical Computing*. 45, 211

Reich, Andrew. 2010. *Calibration of a Unidirectional Wave Flume Using a Transient Focused-Wave Approach*. Master Thesis, The University of Edinburgh. 46

Rogers, Douglas, & King, Guy Bolton. 1996. *Wave generation using Ocean and wave*. 20

Salter, Stephen H. 1974. Wave power. *Nature*, **249**(3), 720–724. 115

Salter, Stephen H. 1981. Absorbing wave-makers and wide tanks. *Pages 185 – 202 of:* Wiegel, Robert L. (ed), *Proceedings of ASCE \& ECOR International Symposium on Directional Wave Spectra Applications*, vol. 81. Berkeley, California: Amer Society of Civil Engineers. 23

Salter, Stephen H, Cruz, João, Lucas, Jorge, & Pascal, Rémy. 2007. Wave powered desalination. *In: Proceedings of the International Conference on Integrated Sustainable Energy Resources in Arid Regions*. 7, 115

Saulnier, Jean-Baptiste, Ricci, Pierpaolo, Clément, Alain, & Falcão, António F. De O. 2009. Mean Power Output Estimation of WECs in Simulated Sea. *Pages 891–900 of: Proceedings of the 8th European Wave and Tidal Energy Conference*. 21

Saulnier, Jean-Baptiste, Clément, Alain, Falcão, António F. De O., Pontes, Teresa, Prevosto, Marc, & Ricci, Pierpaolo. 2010. Wave groupiness and spectral bandwidth as relevant parameters for the performance assessment of wave energy converters. *Ocean Engineering*, **38**(Nov.), 130–147. 2, 15

Smith, George H., & Taylor, Jamie. 2007. *Preliminary Wave Energy Device Performance Protocol*. Tech. rept. Heriot-Watt University, the University of Edinburgh, Edinburgh. 2

Stokes, George Gabriel. 1847. On the theory of oscillatory waves. *Trans. Camb. Phil. Soc*, **8**(441), 197–229. 10, 61

Taylor, Jamie, Rogers, Douglas, & Rea, Mathew. 2003. The Edinburgh curved tank. *Pages 307–314 of: Fifth European Wave Energy Conference*. 5

Tucker, M J, & Pitt, Edward G. 2001. *Waves in Ocean engineering*. Elsevier. 14, 16

Tucker, M J, Challenor, Peter G., & Carter, D J T. 1984. Numerical simulation of a random sea: a common error and its effect upon wave group statistics. *Applied ocean research*, **6**(2), 118–122. 21, 125

Venables, WN, & Ripley, BD. 2002. *Modern applied statistics with S*. 4th edn. Springer verlag. 150, 216

Young, I. 1994. On the measurement of directional wave spectra. *Applied Ocean Research*, **16**(5), 283–294. 71, 72, 78, 79